

Models in search of signals:

pulsar glitches, solar flares, and
continuous gravitational waves

Julian Brian Carlin

ORCID: 0000-0001-5694-0809 

MARCH, 2023

A THESIS SUBMITTED IN COMPLETE FULFILLMENT
OF THE REQUIREMENTS FOR THE DEGREE OF

DOCTOR OF PHILOSOPHY
PHYSICS
THE UNIVERSITY OF MELBOURNE

“A MEANINGFUL QUOTE OR SPECIAL DEDICATION”

Abstract

Lorem ipsum dolor sit amet, consectetuer adipiscing elit. Ut purus elit, vestibulum ut, placerat ac, adipiscing vitae, felis. Curabitur dictum gravida mauris. Nam arcu libero, nonummy eget, consectetuer id, vulputate a, magna. Donec vehicula augue eu neque. Pellentesque habitant morbi tristique senectus et netus et malesuada fames ac turpis egestas. Mauris ut leo. Cras viverra metus rhoncus sem. Nulla et lectus vestibulum urna fringilla ultrices. Phasellus eu tellus sit amet tortor gravida placerat. Integer sapien est, iaculis in, pretium quis, viverra ac, nunc. Praesent eget sem vel leo ultrices bibendum. Aenean faucibus. Morbi dolor nulla, malesuada eu, pulvinar at, mollis ac, nulla. Curabitur auctor semper nulla. Donec varius orci eget risus. Duis nibh mi, congue eu, accumsan eleifend, sagittis quis, diam. Duis eget orci sit amet orci dignissim rutrum.

Nam dui ligula, fringilla a, euismod sodales, sollicitudin vel, wisi. Morbi auctor lorem non justo. Nam lacus libero, pretium at, lobortis vitae, ultricies et, tellus. Donec aliquet, tortor sed accumsan bibendum, erat ligula aliquet magna, vitae ornare odio metus a mi. Morbi ac orci et nisl hendrerit mollis. Suspendisse ut massa. Cras nec ante. Pellentesque a nulla. Cum sociis natoque penatibus et magnis dis parturient montes, nascetur ridiculus mus. Aliquam tincidunt urna. Nulla ullamcorper vestibulum turpis. Pellentesque cursus luctus mauris.

Declaration

This page certifies that:

- This thesis contains only original work towards a Doctor of Philosophy, except where indicated in the preface
- Due acknowledgement has been made in the text to all other material used
- This thesis is fewer than 100 000 words in length, exclusive of tables, figures, bibliographies, and appendices



Julian Brian Carlin

Preface

Here and henceforth “the author” refers to the author of this thesis, Julian Brian Carlin. This thesis is an original work by the author reporting research done alone or in collaboration with other authors. This section provides a chapter-by-chapter summary of the author’s contributions and the publication status of all material.

Chapter 1 is a comprehensive literature review for the work in Chapters 2–5 written by the author for this thesis. It is an original work of the author and will not be submitted for publication.

Chapter 2 is an adaptation the work published as Carlin and Melatos [1] in the Monthly Notices of the Royal Astronomical Society. This work was written and conceived primarily by the author, with scientific input and editing from A. Melatos. Some ideas in this chapter originally appeared in the thesis submitted for the degree of Master of Science (Physics) awarded to the author in 2018. The chapter is expanded to include a broader introduction to the state-dependent Poisson process, as applied in the context of pulsar glitches, by including detailed reviews of Fulgenzi et al. [2] and Carlin and Melatos [3]. All figures and tables are the work of the author.

Chapter 3 is published as Carlin and Melatos [4] in the Monthly Notices of the Royal Astronomical Society. It was written primarily by the author, with scientific input and editing from A. Melatos. All figures and tables are the work of the author.

Chapter 4 is published as Carlin and Melatos [5] in The Astrophysical Journal. It was written primarily by the author, with scientific input and editing from A. Melatos. All figures are the work of the author.

Chapter 5 is submitted for publication in The Astrophysical Journal. It was written primarily by the author, with scientific input and editing from A. Melatos and M. Wheatland. Appendix 3.A1 was written primarily by A. Melatos, but is included in this thesis for completeness. All figures and tables are the work of the author.

Chapter 6 is a comprehensive literature review for the work in Chapter 7 written by the author for this thesis. It is an original work of the author and will not be submitted for publication.

Chapter 7 is published as LVK [6] in Physical Review D on behalf of the LIGO-Virgo-KAGRA (LVK) collaboration. It was written primarily by the author, with scientific input and editing from A. Melatos, and other members of the LVK collaboration. According to LVK policies, all members of the collaboration are listed as authors, in alphabetical order. The full author list is included as [\[TODO: insert ref to appendix here\]](#). The author was responsible for selecting the targets for the search, developing the scripts to run the search pipeline (which was first developed by Suvorova et al. [7, 8]), running the search, constructing and testing validation procedures for outliers, and calculating upper limits on detectable strain. The analysis was reviewed internally to the collaboration by Pat Meyers and Evan Goetz. All figures and tables are the work of the author.

Chapter 8 summarizes the above work. It includes some exploratory future directions for the work in this thesis. It was written by the author, with editing from A. Melatos. All figures and tables are the work of the author.

During the author's PhD they also contributed to two other publications, which are not included in this thesis but are listed here for completeness.

- Millhouse et al. [9] studies how observed glitch rates scale with the spin frequency, spin frequency derivative (and combinations thereof). The author contributed edits to the manuscript, and scientific input regarding treatment of the likelihood function and related statistics.
- Jones et al. [10] presents a guide for two follow-up procedures for continuous gravitational wave candidates. The author contributed edits to the manuscript, and scientific input regarding the effective point spread function of the matched filtering statistic.

Acknowledgments

A long list of acknowledgements, inside jokes, etc

Contents

DEDICATION	ii
ABSTRACT	iii
DECLARATION	iv
PREFACE	iv
ACKNOWLEDGMENTS	vii
LIST OF FIGURES	ix
LIST OF TABLES	x
1 LONG-TERM STATISTICS OF PULSAR GLITCHES TRIGGERED BY A BROWNIAN STRESS ACCUMULATION PROCESS	1
1.1 INTRODUCTION	1
1.2 BROWNIAN STRESS ACCUMULATION	2
1.2.1 Equation of motion	2
1.2.2 Waiting time and size distributions	3
1.2.3 Average waiting time	4
1.2.4 Comparison with the SDP meta-model	6
1.2.5 Inter-glitch spin wandering	6
1.3 OBSERVABLE LONG-TERM STATISTICS	7
1.3.1 Waiting time distribution	7
1.3.2 Correlations and memory	10
1.4 FALSIFYING THE BROWNIAN META-MODEL	11
1.4.1 PSR J0537-6910	12
1.4.2 PSR J1740-3015	13
1.4.3 PSR J0534+2200	13
1.4.4 PSR J1341-6220	14
1.4.5 PSR J0835-4510	14

1.4.6	PSR J0631+1036	14
1.5	POPULATION TRENDS	14
1.6	CONCLUSIONS	16
	APPENDIX 1.A1 ANALYTIC SOLUTION OF THE FOKKER-PLANCK EQUATION FOR THE INTER-GLITCH STRESS DISTRIBUTION	17
	APPENDIX 1.A2 CONDITIONAL WAITING TIME PDF WITHOUT THE REFLECTING BOUNDARY	18
2	LONG-TERM STATISTICS OF PULSAR GLITCHES DUE TO HISTORY-DEPENDENT AVALANCHES	20
2.1	INTRODUCTION	20
2.2	PINNING THRESHOLD DISTRIBUTION	22
2.2.1	Standard picture	22
2.2.2	Available versus occupied sites	23
2.2.3	Unpinning and repinning	24
2.2.4	Equation of motion for the distribution of occupied pinning sites	26
2.3	STATE-DEPENDENT POISSON PROCESS	28
2.3.1	Equation of motion for the stress	28
2.3.2	Monte Carlo simulations	29
2.3.3	Qualitative results	29
2.3.4	Differences from previous meta-models	33
2.3.5	Mutual friction	34
2.4	OBSERVABLE LONG-TERM STATISTICS	34
2.4.1	Waiting time and size PDFs	34
2.4.2	Cross- and autocorrelations	36
2.4.3	Aftershocks and precursors	36
2.5	ASTRONOMICAL OBSERVATIONS	39
2.6	CONCLUSION	40
	APPENDIX 2.A1 NON-MAXIMAL STRESS-CRUST COUPLING	42
	APPENDIX 2.A2 ENSEMBLE-AVERAGED STRESS THRESHOLD DISTRIBUTION AT OC- CUPIED PINNING SITES	43
	APPENDIX 2.A3 RELATION TO POINT PROCESSES AND TIME SERIES MODELING .	44
3	A STATISTICAL SEARCH FOR A UNIFORM TRIGGER THRESHOLD IN SOLAR FLARES FROM INDIVIDUAL ACTIVE REGIONS	46
3.1	INTRODUCTION	46
3.2	STATE-DEPENDENT POISSON PROCESS	47
3.2.1	Equation of motion	47
3.2.2	Monte Carlo automaton	48
3.2.3	Mapping to solar flares	49
3.3	OBSERVABLE SIGNATURES OF A RAPIDLY-DRIVEN PROCESS	50
3.3.1	Slow driver	50
3.3.2	Fast driver	51
3.3.3	Heuristic test for a threshold-driven process	52
3.4	GOES SOFT X-RAY OBSERVATIONS	52
3.4.1	Flare data	53
3.4.2	Obscuration of subsequent flares after a large flare	53
3.4.3	Aggregate size and waiting time statistics	54

3.5	DISAGGREGATED DATA IN INDIVIDUAL ACTIVE REGIONS	55
3.5.1	Waiting time and size PDFs versus flare rate	55
3.5.2	Size-waiting-time cross-correlations	58
3.5.3	Matching the shapes of the waiting time and size PDFs	60
3.5.4	Autocorrelations and longer term memory	61
3.6	CONCLUSION	63
APPENDIX 3.A1 MAGNETIC ENERGY DENSITY AS A STRESS VARIABLE IN AN ACTIVE REGION		65
APPENDIX 3.A2 HIERARCHICAL BAYESIAN FRAMEWORK		66
3.A2.1	Likelihood and Bayes' theorem	66
3.A2.2	Population-level parameter estimation	67
3.A2.3	Validation with synthetic data	68
3.A2.4	Likelihood based on the average waiting time	69
APPENDIX 3.A3 CLEANING GOES FLARE SUMMARY DATA		69
4	SEARCH FOR CONTINUOUS GRAVITATIONAL WAVES FROM 20 ACCRETING MILISECOND X-RAY PULSARS IN O3 LIGO DATA	71
4.1	INTRODUCTION	71
4.2	SEARCH ALGORITHM	72
4.2.1	HMM	73
4.2.2	\mathcal{J} -statistic	74
4.3	TARGETS	74
4.4	SEARCH PARAMETERS	77
4.4.1	Coherence time and frequency binning	77
4.4.2	Number of orbital templates	78
4.4.3	Thresholds	79
4.4.4	Computing resources	81
4.5	O3 DATA	81
4.6	VETOES	82
4.6.1	Known line veto	82
4.6.2	Single interferometer veto	82
4.6.3	Off-target veto	83
4.7	O3 SEARCH RESULTS	83
4.7.1	IGR J18245–2452	84
4.7.2	IGR J00291+5934	84
4.7.3	MAXI J0911–655	85
4.7.4	XTE J0929–314	85
4.7.5	IGR J16597–3704	85
4.7.6	IGR J17062–6143	86
4.7.7	IGR J17379–3747	86
4.7.8	SAX J1748.9–2021	86
4.7.9	NGC 6440 X–2	86
4.7.10	IGR J17494–3030	86
4.7.11	Swift J1749.4–2807	87
4.7.12	IGR J17498–2921	87
4.7.13	IGR J17511–3057	87

4.7.14	XTE J1751–305	87
4.7.15	Swift J1756.9–2508	87
4.7.16	IGR J17591–2342	87
4.7.17	XTE J1807–294	87
4.7.18	SAX J1808.4–3658	88
4.7.19	XTE J1814–338	88
4.7.20	HETE J1900.1–2455	88
4.8	TARGET-OF-OPPORTUNITY SEARCH: SAX J1808.4–3658 IN OUTBURST . . .	88
4.8.1	Search parameters	89
4.8.2	Search results	89
4.9	FREQUENTIST UPPER LIMITS	90
4.9.1	Upper limit procedure in a sub-band	90
4.9.2	Upper limits	91
4.9.3	Comparison to expected strain from AMXPs	91
4.9.4	Astrophysical implications	93
4.10	CONCLUSIONS	95
APPENDIX 4.A1 THRESHOLD SETTING		97
4.A1.1	Exponential tail method	97
4.A1.2	Percentile method	98
4.A1.3	Comparison of methods	98
4.A1.4	Off-target thresholds	99
4.A1.5	Probability that a candidate arises due to noise	99
APPENDIX 4.A2 FULL SEARCH RESULTS AND SURVIVOR FOLLOW-UP		99
4.A2.1	Additional follow-up for survivors	100
APPENDIX 4.A3 SURVIVOR FOLLOW-UP FOR TARGET-OF-OPPORTUNITY SEARCH CANDIDATE		101

List of Figures

1.1	Visual comparison of the evolution of the internal, unobservable stress, $X(t)$, for four different values of ξ/σ^2 . The red dashed line indicates the stress threshold, set to $X_c = 1$, where glitches are triggered. The same sequence of glitch sizes, drawn from a power-law $\eta(\Delta X)$ distribution, is used in each panel. The small black tick marks indicate the epoch of each glitch.	5
1.2	Comparison between two representative time series of stress (top panels) and crust angular velocity (bottom panels) from the SDP meta-model (left) and the Brownian meta-model (right). A deterministic, secular torque drives the stress between glitches in the SDP meta-model, whereas a stochastic Langevin torque drives the stress between glitches in the Brownian meta-model. Black tick marks in the top panels indicate the glitch epochs. Parameters for SDP meta-model: $\alpha = 1$, power law conditional jump distribution, as described in equations (17) and (19) of Fulgenzi et al. [2] respectively. Parameters for Brownian meta-model: $\mu = 50$, power law stress-release distribution, as in (1.15). Parameters shared between meta-models: $\delta = -1.5$, $\beta = 10^{-2}$ in (1.15).	8
1.3	Waiting time PDF, $p(\Delta t)$, for four values of μ on log-linear (left panel) and log-log (right panel) scales. The stress release distribution, $\eta(\Delta X)$, is a power law, as in (1.15), with $\delta = -1.5$ and $\beta = 10^{-2}$	8
1.4	As for Figure 1.3 but with a Gaussian $\eta(\Delta X)$, as in (1.16), with $\mu_G = 0.5$ and $\sigma_G = 0.125$	9
1.5	As for Figure 1.3 but with a log-normal $\eta(\Delta X)$, as in (1.17), with $\mu_{LN} = -1$ and $\sigma_{LN} = 0.5$	10
1.6	Spearman cross-correlation between the size of a glitch and the waiting time until the next glitch versus μ . At 200 logarithmically spaced values of μ , 10^5 waiting times and sizes are drawn from (1.8) and (1.15) respectively, using each generated size to determine the starting point for the next inter-glitch interval and hence waiting time.	11

2.1	A toy example illustrating schematically the evolution of $g(X_{\text{th}}, t)$ during a sequence of four glitches, with $X(t_1^+) < X(t_3^+) < X(t_2^+) < X_{\text{th}, \max} < X(t_4^-)$, where $g(X_{\text{th}}, t_1^-) = \phi(X_{\text{th}})$ is the uniform distribution between $0 \leq X_{\text{th}} \leq X_{\text{th}, \max}$. The colors correspond to how many glitches occur in the time elapsed since vortices unpin from pinning sites with a certain threshold. Darker colors indicate that the vortices have stayed pinned during more events.	26
2.2	Evolution of X (main panel) and $g(X_{\text{th}}, t)$ (sub-panels) across four glitches at t_1, \dots, t_4 , generated via the automaton outlined in Section 2.3.2. Parameters: $\alpha = 0.2$, $X_{\text{th}, \max} = 0.95$ (indicated in both the main panel and sub-panels with a red dashed line), $K = X_{\text{th}, \max}$. X and X_{th} are in units of X_c and t is in units of $X_c I_C / N_{\text{em}}$	30
2.3	As in Figure 2.2 but with $\alpha = 1$	31
2.4	As in Figure 2.2 but with $\alpha = 10$	31
2.5	Long-term qualitative behavior of X for three different values of $\alpha = 0.2$, 1, and 10 in the top, middle and bottom panel respectively. Parameters: $X_{\text{th}, \max} = 0.95$ (indicated with a red dashed line in each panel), $K = X_{\text{th}, \max}$	32
2.6	Fraction of glitches that reset the system as a function of α for three different values of $X_{\text{th}, \max}$. Parameters: $N = 10^5$ glitches generated at 50 logarithmically spaced values of α for each value of $X_{\text{th}, \max}$, with $K = X_{\text{th}, \max}$	33
2.7	Waiting time, Δt , and size, ΔX , PDFs on the top and bottom panel respectively. Parameters: $N = 10^7$ simulated glitches for each value of α , $X_{\text{th}, \max} = 0.95$ (indicated with a red dashed line in each panel), $K = X_{\text{th}, \max}$	35
2.8	Top panel: Forward cross-correlation, ρ_+ , and backward cross-correlation, ρ_- , as a function of α (orange and purple curves respectively). Bottom panel: Auto-correlation between waiting times, $\rho_{\Delta t}$, and sizes, $\rho_{\Delta X}$, as a function of α (red and blue curves respectively). Parameters: $N = 10^5$ glitches generated at 100 logarithmically spaced values of α , $X_{\text{th}, \max} = 0.95$, $K = X_{\text{th}, \max}$	37
2.9	Top panel: PDFs of all waiting times, Δt , waiting times just prior to a system-resetting glitch, Δt_{pre} , and waiting times just after a system-resetting glitch, Δt_{post} . Bottom panel: Corresponding PDFs for sizes. Parameters: $\alpha = 10$, $N = 10^8$ total glitches, $\sim 10^5$ of which reset the system completely, $X_{\text{th}, \max} = 0.95$, $K = X_{\text{th}, \max}$	38
2.10	Waiting time PDFs for $K = 0.6$ (left panel) and $K = 0.01$ (right panel). Parameters: $N = 10^7$ simulated glitches for each value of α , with $X_{\text{th}, \max} = 0.95$. The black dashed vertical line indicates $\Delta t = K$ in each panel.	42
2.11	Ensemble averaged PDF of occupied pinning sites $g_s(X_{\text{th}}) = \langle g(X_{\text{th}}, t) \rangle$ calculated empirically for three values of α . Parameters: 10^7 samples of $g(X_{\text{th}})$ for each value of α , $X_{\text{th}, \max} = 0.95$, with $K = X_{\text{th}, \max}$	44

3.1	Top panels: qualitative behavior of the evolution of the stress, $X(t)$, in the SDP process in the two main regimes, slowly driven (left panel, $\alpha = 10$), and rapidly driven (right panel, $\alpha = 0.1$). Bottom panels: predicted waiting time and size PDFs $p(\Delta t)$ and $p(\Delta X)$ respectively in the above regimes. For all panels we fix $\eta[\Delta X_i X(t_i^-)] \propto (\Delta X_i)^{-3/2} H[\Delta X_i - 10^{-2} X(t_i^-)]$, where the Heaviside function $H(...)$ enforces a minimum stress-release size of 1% of the stress in the system, ensuring integrability. The histograms in the bottom panels each include $N = 10^7$ events.	49
3.2	Forward, ρ_+ (solid curve), and backward, ρ_- (dashed curve), cross-correlations between event sizes and waiting times for 10^2 values of $10^{-2} \leq \alpha \leq 10^2$, with $N = 10^5$ events generated per value of α . We fix $\eta[\Delta X_i X(t_i^-)]$ to the same functional form as in Figure 3.1. A version of this figure first appeared as figure 13 in Fulgenzi et al. [2].	51
3.3	Top panel: Probability mass function of the number of flares per active region, N_k , for all active regions with $N_k \geq 5$. Regions with $0 \leq N_k \leq 4$ are excluded, as the number of samples per region is too small for the statistical tests in this paper. Bottom panel: PDF of the flare rate, λ_k , for all active regions with $N_k \geq 5$, binned into 50 uniformly spaced bins between 0 hours^{-1} and 0.5 hours^{-1}	54
3.4	Top panel: PDF $p(\Delta t)$ of waiting times (thick black stepped curve), Δt , aggregated over all active regions with $N_k \geq 5$, binned into 50 logarithmically spaced bins between the minimum and maximum Δt in the full, unmasked catalog. Overlaid are the best fit estimates of an exponential (blue dashed curve), power law (orange dotted curve), and log-normal (green dot-dashed curve) PDF. Bottom panel: As for top panel, but for sizes Δs . The grey region in the bottom panel shows the difference between the size PDFs from the masked and full catalogs (see Section 3.4.2).	56
3.5	Top panel: Proportion of active regions with waiting time PDF fitted best by three possible shapes (a power law, an exponential, and a log-normal) as determined by the AICc, as a function of the region's flare rate, λ_k . The CDF of λ_k is overlaid in black. Bottom panel: As in the top panel, but for size PDFs.	57
3.6	Top panel: PDF of forward cross-correlation, $\rho_{+,k}$ (black stepped curve), and backward cross-correlation, $\rho_{-,k}$ (black dashed curve), for all active regions with $N_k \geq 5$. Data binned into 30 uniformly spaced bins between $\rho_{\pm,k} = -1$ and $\rho_{\pm,k} = 1$. Bottom panel: Scatter plot of the forward cross-correlation, $\rho_{+,k}$, and flare rate, λ_k , for all regions with $N_k \geq 10$. The dashed grey line corresponds to $\rho_{+,k} = 0$	59
3.7	Calibrating the cross-correlation test in Section 3.5.3: two-dimensional KDEs of the relationship between ρ_+ and \mathcal{M} (top panel), and ρ_- and \mathcal{M} (bottom panel), for events simulated from the SDP model with four values of α (see legend for color code). The text in Section 3.5.3 reports details about the Monte Carlo procedure. Contours correspond to the 10%, 50%, and 90% credible intervals.	61

3.8	As for Figure 3.7 but for <i>GOES</i> data with black crosses marking all regions in the full, unmasked <i>GOES</i> catalog with $N_k \geq 10$. Red contours correspond to the 10%, 50%, and 90% credible intervals inferred from the black crosses.	62
3.9	Posterior predictive check demonstrating the recovery of injected population-level parameters. The weakly informative priors set on the hyper-parameters τ , ξ , and β are shown in green, histograms of samples from the injected population parameters are shown in red, while histograms of samples from the posterior distributions are shown in blue. See text in Appendix 3.A2.3 for details on the procedure.	68
4.1	Summary of search results across all targets and sub-bands with $\mathcal{L} > \mathcal{L}_{\text{th}}$. The different symbols correspond to candidates from different targets. The ordinate shows p_{noise} for each candidate, the probability that a search of that candidate's sub-band in pure noise would return at least one candidate at least as loud as the one seen. The color of each candidate indicates \mathcal{L} (see color bar at right). Candidates that are eliminated by the vetoes outlined in Sec. 4.6 are not shown for clarity. Details on the search results are in Sec. 4.7 and Appendix 4.A2.	84
4.2	Search results for IGR J18245–2452. Black crosses indicate the terminating frequency and \mathcal{L} for the most likely path through the sub-band for each binary template. The vertical blue dashed (green dot-dashed) lines correspond to the threshold set via Gaussian (off-target) noise realizations, $\mathcal{L}_{\text{th},G}$ ($\mathcal{L}_{\text{th},\text{OT}}$), in each sub-band. Solid red lines in the right panel indicate the peak frequency of known instrumental lines in the Hanford detector; the orange band indicates the width of the line in the detector frame and the yellow band indicates the increased effective width due to Doppler broadening, as described in Sec. 4.6.1. Multiple overlapping orange bands creates the red bands. The sub-band around 508.8 Hz is especially noisy due to test mass suspension violin mode resonances [269]. The transparency of crosses in sub-bands with many templates, is adjusted relative to the maximum \mathcal{L} in that sub-band for clarity.	85
4.3	Kernel density estimate of the PDF of the constraints on ellipticity $\epsilon^{95\%}$ (left panel) and dimensionless r -mode amplitude $\alpha^{95\%}$ (right panel) via Eqs. (4.14) and (4.15) respectively. Both PDFs are normalized to a height of one. The black dashes in both panels correspond to the individual estimates of $\epsilon^{95\%}$ or $\alpha^{95\%}$ from each target.	94

4.4	Search results for each target and sub-band, laid out as in Fig 4.2. Black crosses indicate the frequency and \mathcal{L} for the most likely path through the sub-band for each binary template. The vertical blue dashed (green dot-dashed) lines correspond to the threshold set via Gaussian (off-target) noise realizations, $\mathcal{L}_{\text{th},G}$ ($\mathcal{L}_{\text{th},OT}$), in each sub-band. Solid red lines indicate the peak frequency of known instrumental lines in the Hanford or Livingston detectors; the red band indicates the width of the line and the yellow band indicates the increased effective width due to Doppler broadening, as described in Sec. 4.6.1. Multiple overlapping orange bands creates the red bands. The transparency of crosses in sub-bands with many templates, e.g. the sub-bands of IGR J16597–3704, is adjusted relative to the maximum \mathcal{L} in that sub-band for clarity.	105
4.5	Top panels: frequency paths, $f(t)$, for candidates with $p_{\text{noise}} \leq 0.1$. The terminating frequency bin, $f(N_T)$, is subtracted and displayed in the title of each figure for clarity. Faint horizontal grey lines demarcate frequency bins of size $\Delta f = 5.787037 \times 10^{-7}$ Hz, while faint vertical grey lines demarcate chunks of length $T_{\text{drift}} = 10$ d. Bottom panels: the cumulative log-likelihood along the frequency path relative to the average sum log-likelihood needed to reach \mathcal{L}_{th} , $C\mathcal{L} \equiv \sum_{i=0}^{i=t} [\mathcal{L}(i) - \mathcal{L}_{\text{th}}/N_T]$, where $\sum_{i=0}^{i=t} \mathcal{L}(i)$ is $\ln P(Q^* O)$ from Eq. (4.2) truncated after the t -th segment. The horizontal blue dashed line corresponds to $\sum_{i=0}^{i=t} \mathcal{L}(i) = t\mathcal{L}_{\text{th}}/N_T$. The grey shaded regions in both top and bottom panels correspond to the segments which have no SFTs and are therefore filled with a uniform log-likelihood, as described in Sec. 4.5.	106
4.6	\mathcal{L} , as represented by the color of each pixel, calculated at 3721 regularly spaced sky locations in a 100 arcmin^2 patch of sky, centered on IGR J16597–3704. See text in Appendix 4.A2.1 for details.	107

List of Tables

1.1	Pulsar name, number of glitches (N), Spearman correlation coefficient between glitch size and subsequent waiting time (ρ_+), associated p-value, and the 95% confidence interval (CI). The last two columns indicate the functional form of the best-fitting distribution for glitch sizes, $p(\Delta X)$, and waiting times, $p(\Delta t)$ [14, 16, 37].	12
3.1	Anomalous active region numbers found in the GOES flare summary data by checking whether one has $\Delta t_{i,k} < 14$ days for $1 \leq i \leq N_k - 1$ for each active region. Corrected values are determined manually, by considering the context of what active regions are present at the time of the anomalous flare at a similar latitude. Corrected values of “–” indicate that we cannot identify a reasonable active region to associate with the anomalous flare.	70
4.1	Target list: position (RA and Dec), orbital period (P), projected semi-major axis in light-seconds (a_0), time of passage through the ascending node as measured near the time of the most recent outburst (T_{asc}), the time of passage through the ascending node as propagated to the start of O3 ($T_{\text{asc}, \text{O3}}$), as described in Sec. 4.4.2, and frequency of observed pulsations (f_\star). Numbers in parentheses indicate reported 1σ errors (68% confidence level), unless otherwise noted. All objects have positional uncertainty ≤ 1 s in RA and $\leq 0.5''$ in Dec.	76
4.2	Starting frequencies, f_s , for each ~ 0.61 Hz-wide sub-band, number of templates needed to cover the P and T_{asc} domains in that sub-band, N_P and $N_{T_{\text{asc}}}$ respectively, and the total number of templates for each sub-band, $N_{\text{tot}} = N_P N_{T_{\text{asc}}}$. The projected semi-major axis a_0 is known precisely enough that we have $N_{a_0} = 1$ for each sub-band.	80
4.3	Upper limits on the detectable gravitational wave strain at a 95% confidence level, $h_0^{95\%}$, in each of the sub-bands for each target. See Sec. 4.9.1 for details on how they are estimated, and the precision to which they are known. Upper limits are not estimated in sub-bands marked with a “–” as these sub-bands are highly contaminated with known noise lines.	92

4.4	Maximum expected strain from each target, as inferred from EM observations. The second column contains the best estimate for the distance to the target. Targets with “-” listed as the frequency derivative (third column), \dot{f}_\star , do not have a measured value during outburst, and also do not have a long-term (quiescent) \dot{f}_\star measured either. The labels (A) and (Q) indicate that \dot{f}_\star is measured in outburst and quiescence respectively. The scaling equations used to estimate the maximum spin-down strain (fourth column), $h_{0,\text{sd}}$, and the maximum strain assuming torque-balance (sixth column), $h_{0,\text{torque}}$, are Eqs. (4.12) and (4.13) respectively. The $h_{0,\text{sd}}$ value is calculated using the central distance and \dot{f}_\star estimates. The $h_{0,\text{torque}}$ value is calculated using the maximum bolometric X-ray flux measured during outburst (fifth column), $F_{X,\text{max}}$, which is typically measured to a precision of $\sim 10\%$. The X-ray flux of each target in quiescence is not shown, as it is only measured for half of the targets, and is usually $\sim 1 - 2$ orders of magnitude lower than $F_{X,\text{max}}$. The seventh column contains $h_0^{95\%}$ in the $2f_\star$ sub-band (fourth column of Table 4.3) to facilitate comparisons between $h_0^{95\%}$ and $h_{0,\text{torque}}$ or $h_{0,\text{sd}}$	109
4.5	Target, starting frequency, f_s , for each ~ 0.61 Hz-wide sub-band, threshold calculated using Gaussian noise realizations and the exponential tail method, $\mathcal{L}_{\text{th},G}^e$, and threshold calculated using off-target noise realizations and the percentile method, $\mathcal{L}_{\text{th},\text{OT}}^P$. All thresholds are calculated with $\alpha_{N_{\text{tot}}} = 0.3$	110
4.6	Orbital template, (P, a_0, T_{asc}) , terminating frequency bin, $f(N_T)$, log-likelihood, \mathcal{L} , and the probability that a search of the candidate’s sub-band in pure noise would return a candidate just as loud, p_{noise} , for the 16 candidates with $\mathcal{L} > \mathcal{L}_{\text{th}}$ that cannot be eliminated by any of the vetoes detailed in Sec. 4.6.	111
4.7	Orbital template, (P, a_0, T_{asc}) , frequency, f , log-likelihood, \mathcal{L} , and the probability of seeing a candidate at least this loud in pure noise, p_{noise} , for the remaining candidate from the target-of-opportunity, 24 d coherent search when SAX J1808.4–3658 was in outburst. The candidate cannot be eliminated by any of the vetoes detailed in Sec. 4.6.	111

1

CHAPTER 1

2

3

Long-term statistics of pulsar glitches triggered by a Brownian stress accumulation process

4

5

6 1.1. INTRODUCTION

7 The secular braking of rotation-powered pulsars is perturbed by two phenomena: glitches
8 and timing noise. Timing noise, or stochastic wandering of the spin frequency, shows
9 up in timing residuals as a red-noise process with an auto-correlation time-scale of days
10 to weeks [11–13]. Glitches are impulsive spin-up events that recur erratically [14–16].

11 The microphysical mechanism that triggers glitches is an open question. Candidates
12 include superfluid vortex avalanches [17, 18], starquakes [19, 20], hydrodynamic insta-
13 bilities [21–23] and more; see Haskell and Melatos [24] for a modern review. Most of
14 these mechanisms are predicated on the idea that the electromagnetic braking of the
15 crust increases stress (e.g. elastic strain or differential rotation) in the system, some
16 fraction of which is released spasmodically at each glitch. If the stress increases deter-
17 ministically between glitches, the long-term glitch activity can be described by a state-
18 dependent Poisson (SDP) process which links the instantaneous glitch rate to the stress
19 in the system; glitches become more likely as the stress approaches a threshold [2]. The
20 SDP process is a meta-model in the sense that it encompasses phenomenologically the
21 stress-release idea at the core of the mechanisms listed above without specializing to the
22 microphysics of the mechanism. It makes falsifiable statistical predictions about long-
23 term observations of the sizes and waiting times of glitches and their correlations [1–3,
24 25].

25 Pulse-to-pulse observations of a glitch in the Vela pulsar (PSR J0835–4510) were made
26 at the Mount Pleasant radio telescope in December 2016 [26]. Bayesian analysis finds
27 evidence for a rotational slowdown (“precursor”) immediately prior to the glitch [27].
28 The slowdown is of the same order as the pulse jitter, i.e. pulse-to-pulse variations in the
29 pulse profile, possibly caused by magnetospheric fluctuations unrelated to the internal
30 stress. Another possibility — certainly not unique — is that the slowdown represents a
31 random internal (e.g. hydrodynamic) fluctuation, which drives the stress above a critical

32 threshold, triggering the glitch [27]. Stochastic fluctuations in the internal stress may be
33 caused by superfluid turbulence, for example [28–30].

34 In this paper we do not seek to adjudicate on the putative link between internal
35 stochastic fluctuations and an observed rotational slowdown prior to a glitch. Nor do we
36 seek to model such a link directly. Instead, motivated partly by the Vela data, we investi-
37 giate an alternative to the SDP meta-model, wherein glitches are the result of an internal,
38 unobservable, globally averaged stress that evolves stochastically as a Brownian process,
39 until a glitch is triggered at a critical stress threshold. The Brownian meta-model dif-
40 fers from the SDP meta-model by allowing the stress to evolve stochastically between
41 glitches (instead of increasing deterministically), and triggering a glitch only when a
42 critical threshold is reached (instead of at any time before the threshold is reached).
43 Together the two meta-models encompass a large set of plausible microphysical mech-
44 anisms. Both models make falsifiable predictions about long-term statistics, a valuable
45 feature. We describe the details of the Brownian meta-model in Section 1.2. In Section
46 1.3 we explore its long-term statistical predictions. In Section 1.4 we compare data from
47 the six pulsars with the highest number of recorded glitches with the predictions of the
48 Brownian meta-model, with an eye towards falsification. An analogous study of the SDP
49 meta-model can be found elsewhere [1, 3, 25]. In Section 1.5 we discuss how population
50 trends may inform meta-model parameters.

51 1.2. BROWNIAN STRESS ACCUMULATION

52 1.2. *Equation of motion*

53 We define X to be a stochastic variable equal to the globally averaged stress in the sys-
54 tem. In the superfluid vortex avalanche picture X is proportional to the lag between the
55 angular speed of the rigid crust and the superfluid interior. In the crustquake picture X is
56 proportional to the elastic strain in the crust.

57 Between glitches we propose that $X(t)$ evolves according to a Wiener process, which
58 obeys the Langevin (Itô) equation

$$\frac{dX(t)}{dt} = \xi + \sigma B(t) , \quad (1.1)$$

59 with drift coefficient ξ (units: stress/time) and diffusion coefficient σ [units: stress/(time) $^{1/2}$],
60 and where $B(t)$ is a white noise process of zero mean and unit variance [31, 32]. We as-
61 sume both ξ and σ are constant with time. Practically, at each time step, the stress
62 increments by ξ and undergoes a random step (up or down) by σ multiplied by a ran-
63 dom number drawn from a Gaussian with zero mean and variance equal to the time step.
64 Equation (1.1) leads to the Fokker-Planck equation

$$\frac{\partial p}{\partial t} = -\xi \frac{\partial p}{\partial X} + \frac{\sigma^2}{2} \frac{\partial^2 p}{\partial X^2} , \quad (1.2)$$

65 where $p dX = p(X, t | X_0) dX$ is the probability of finding the stress in the region $(X, X +$
66 $dX)$ at time t , given that it started at $X = X_0$ after a glitch at $t = 0$, viz.

$$p(X, t = 0 | X_0) = \delta(X - X_0) . \quad (1.3)$$

67 The Brownian process terminates at $X = X_c$, i.e. X_c is the stress threshold where a
 68 glitch is triggered. The glitch decrements the stress by a random amount ΔX , drawn
 69 from a stress-release distribution, discussed in Section 1.2.2. Mathematically, the ter-
 70 mination of the Brownian process at $X = X_c$ corresponds to an absorbing boundary
 71 condition:

$$0 = p(X = X_c, t | X_0) . \quad (1.4)$$

72 We also require $X(t) \geq 0$; the stress is never negative¹. This corresponds to a reflecting
 73 boundary condition at $X = 0$:

$$0 = \frac{\partial p(X, t | X_0)}{\partial X} \Big|_{X=0} - \frac{2\xi}{\sigma^2} p(X = 0, t | X_0) . \quad (1.5)$$

74 Equations (1.2)–(1.5) are solved analytically assuming that $p(X, t | X_0)$ is separable in
 75 X and t . The solution is presented in Appendix 1.A1, following the approach in Sweet
 76 and Hardin [33]. Higher values of $\xi X_c / \sigma^2$ imply drift dominates over diffusion; lower
 77 values of $\xi X_c / \sigma^2$ imply diffusion dominates over drift. Figure 1.1 shows four representa-
 78 tive time series of the evolution of X for four different values of ξ / σ^2 , with $X_c = 1$ fixed
 79 in each panel. For $\xi / \sigma^2 = 0.1$ the process appears by eye to fluctuate randomly, with
 80 large, rapid excursions both up and down in stress. On the other hand, for $\xi / \sigma^2 = 50$, the
 81 stress accumulates steadily with small random excursions and large glitches are clearly
 82 demarcated from inter-glitch fluctuations.

83 1.2. Waiting time and size distributions

84 The stress is not observable. Instead, what we observe are sequences of glitch sizes and
 85 waiting times.

86 The conditional waiting time distribution, $g(\Delta t | X_0)$, gives the probability density
 87 function (PDF) of waiting times Δt , when the inter-glitch evolution starts at X_0 , accord-
 88 ing to (1.3). It is calculated as [31]

$$g(\Delta t | X_0) = -\frac{d}{d(\Delta t)} \left[\int_{-\infty}^{X_c} dX p(X, \Delta t | X_0) \right] . \quad (1.6)$$

89 The integral inside the square brackets, often called the survivor function, equals the
 90 probability density that the process stays in the interval $-\infty < X(t) \leq X_c$ for $0 \leq t \leq \Delta t$.

91 The starting stress X_0 is a random variable, related to the size of the previous glitch.
 92 To find the observable waiting time distribution, $p(\Delta t)$, we marginalize over the starting
 93 stress by calculating,

$$p(\Delta t) = \int_0^{X_c} dX_0 g(\Delta t | X_0) \eta(X_c - X_0) , \quad (1.7)$$

94 where $\eta(\Delta X)$ equals the probability density of releasing an amount of stress $\Delta X = X_c -$
 95 X_0 during a glitch.

¹In the vortex unpinning picture, for example, a vortex avalanche cannot ever transfer so much angular momentum, that the crust rotates faster than the pinned superfluid; see Fulgenzi et al. [2] and the output of Gross-Pitaevskii simulations [18]

96 We henceforth express t in units of $2X_c^2/\sigma^2$ and X in units of X_c , unless otherwise
97 stated. In these units, equations (1.6) and (1.26) combine to yield (see Appendix 1.A1)

$$g(\Delta t | X_0) = 2\mu \exp[\mu^2 \Delta t + \mu(1 - X_0)] \sum_{n=1}^{\infty} \exp(-\lambda_n^2 \Delta t) \frac{\lambda_n \sin[\lambda_n(1 - X_0)]}{\mu + \cos^2 \lambda_n} , \quad (1.8)$$

98 where λ_n is the n -th positive root of the transcendental equation

$$\mu \tan \lambda_n = -\lambda_n , \quad (1.9)$$

99 with

$$\mu = \xi X_c / \sigma^2 . \quad (1.10)$$

100 In this paper, we assume for simplicity that ΔX is proportional to the observed glitch
101 size, $\Delta\nu$, i.e. the observed increment in the crust's spin frequency. Glitches represent
102 small perturbations to an underlying equilibrium state, with $\Delta\nu/\nu \ll 1$, where ν is the
103 spin frequency, so it is reasonable to model them in terms of a linear response, although
104 nonlinear alternatives are certainly conceivable [34, 35]. In the vortex avalanche picture,
105 for example, where $X(t)$ equals the crust-core angular velocity lag we have [2]

$$\Delta X = -\frac{2\pi(I_c + I_s)\Delta\nu}{I_s} , \quad (1.11)$$

106 where I_c and I_s are the moments of inertia of the crust and superfluid interior respec-
107 tively. An analogous proportionality exists in the starquake picture [20, 36]. The size
108 distributions observed from individual pulsars are approximated by power-law, Gaus-
109 sian, lognormal, and exponential distributions [14, 16, 37]. Assuming $\Delta X \propto \Delta\nu$, we
110 adjust $\eta(\Delta X)$ to match the measured size PDF $p(\Delta\nu)$ of the pulsar under consideration.

111 1.2. Average waiting time

112 The average waiting time, $\langle \Delta t \rangle$, is conditional on X_0 . It can be calculated from $g(\Delta t | X_0)$
113 via

$$\langle \Delta t \rangle = \int_0^{\infty} d(\Delta t) \Delta t g(\Delta t | X_0) . \quad (1.12)$$

114 With the boundary conditions (1.4) and (1.5), we obtain (see Appendix 1.A1)

$$\langle \Delta t \rangle = 2\mu \exp[\mu(1 - X_0)] \sum_{n=1}^{\infty} (\lambda_n^2 + \mu^2)^{-2} \frac{\lambda_n \sin[\lambda_n(1 - X_0)]}{\mu + \cos^2(\lambda_n)} . \quad (1.13)$$

115 The behavior of $\langle \Delta t \rangle$ as a function of μ is complicated, even after marginalizing over
116 X_0 . Numerical tests indicate that for $\mu \lesssim 1$, $\langle \Delta t \rangle$ is roughly constant with μ , while for
117 $\mu \gtrsim 1$ it varies inversely with μ . The latter behavior can be understood with the help
118 of the approximate non-reflecting solution at large μ (see Appendix 1.A2), which has
119 $\langle \Delta t \rangle \propto \mu^{-1}$, via equation (1.29) and (1.12). The behavior at low values of μ makes sense
120 physically, as σ dominates the time to reach X_c in this regime. On the other hand, at
121 high values of μ and fixed σ , a high value of the drift coefficient ξ leads the process to
122 quickly reach X_c while a low value of ξ takes comparatively longer.

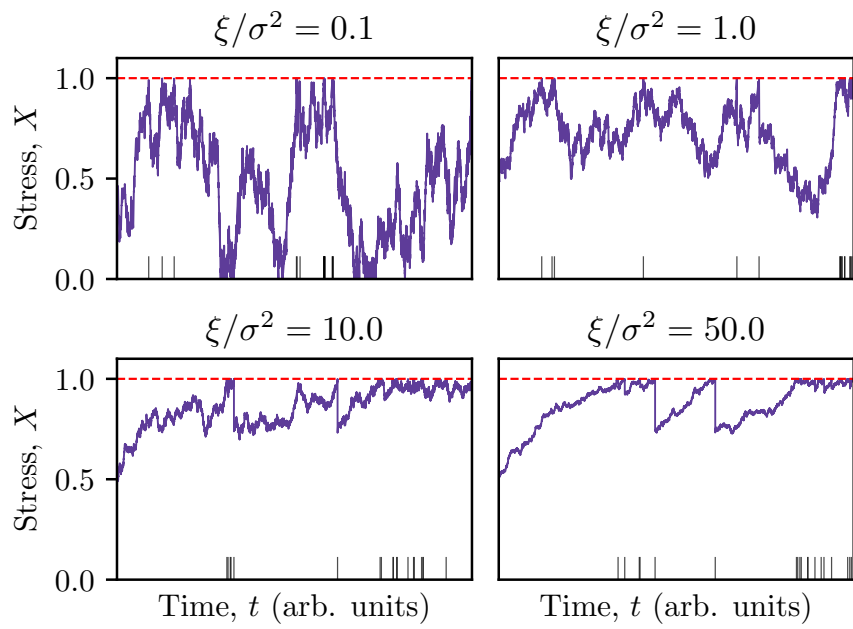


Figure 1.1: Visual comparison of the evolution of the internal, unobservable stress, $X(t)$, for four different values of ξ/σ^2 . The red dashed line indicates the stress threshold, set to $X_c = 1$, where glitches are triggered. The same sequence of glitch sizes, drawn from a power-law $\eta(\Delta X)$ distribution, is used in each panel. The small black tick marks indicate the epoch of each glitch.

123 1.2. Comparison with the SDP meta-model

124 A key goal of this paper is to create a framework for falsifying one or both of the Brownian and SDP meta-models by making quantitative predictions about long-term glitch statistics. As the two meta-models encompass a range of plausible microphysics, falsifying one or both has significant scientific value in understanding which microphysical theories are consistent with the data.

129 The Brownian meta-model shares several similarities with the SDP meta-model [1–3, 25]. Both link the observed changes in $\nu(t)$ to a globally averaged, unobservable stress, which fluctuates around marginal stability. Both are examples of a self-organized critical system [see Aschwanden et al. [38] for a review], where an external driver pushes the system towards criticality, until a glitch releases internal stress and transfers angular momentum from the core to the crust [39]. Neither meta-model assumes a specific microphysical trigger mechanism; together the two meta-models embrace a wide variety of plausible mechanisms of stress accumulation and threshold triggering.

137 The meta-models also differ in important respects. The driver in the SDP meta-model is secular; it does not vary with time. In the Brownian meta-model the driving torque is a fluctuating Langevin torque with white noise statistics, as in (1.1). The SDP process never quite reaches $X = X_c$, as glitches become increasingly likely for $X \rightarrow X_c$. In contrast, the Brownian meta-model reaches $X = X_c$ at every glitch. This has important implications regarding the “memory” of previous events, as explored in Section 1.3.2. Finally, $\eta(\Delta X)$ plays a different role in the two meta-models. As mentioned in Section 1.2.2, one has $\Delta\nu \propto \Delta X$, so $\eta(\Delta X)$ and $p(\Delta\nu)$ have the same shape in the Brownian meta-model. In the SDP meta-model $\eta(\Delta X)$ is conditional on $X(t)$ just before the glitch, so $\eta(\Delta X)$ and $p(\Delta\nu)$ have the same shape only under certain conditions; see Carlin and Melatos [3] for details.

148 The similarities and differences between the two meta-models are illustrated in Figure 1.2. Time series $X(t)$ and $\nu(t)$ are constructed by repeatedly evolving the stress in the system until a glitch is triggered (probabilistically at $X < X_c$ for the SDP meta-model, deterministically at $X = X_c$ for the Brownian meta-model), then drawing a glitch size from the stress-release PDF $\eta(\Delta X)$. Visually, with 20 glitches, the crust angular velocity evolves similarly for the two meta-models, despite the different stress evolution between glitches (deterministic for the SDP meta-model and stochastic for the Brownian meta-model). However, as we find in Section 1.3, the long-term statistical behavior of the two meta-models is different.

157 1.2. Inter-glitch spin wandering

158 Besides its influence on glitch statistics, the Brownian process may also drive stochastic spin wandering between glitches, unlike the SDP process. In principle, therefore, observations of inter-glitch timing noise in radio pulsars [11–13, 40] should place constraints 159 on the meta-model parameters ξ and σ^2 independent of the constraints derived from 160 glitches. As an illustrative special case, if ξ and X_c are held fixed, $\langle\Delta t\rangle$ decreases and the 161 inter-glitch timing noise amplitude increases simultaneously, as σ^2 increases. Hence a 162 measured upper limit on the timing noise amplitude implies a maximum value of σ^2 and 163 hence a minimum value of $\langle\Delta t\rangle$, which provides an additional, independent opportunity 164 to falsify the Brownian meta-model.

167 In practice, falsification experiments of the above kind are complicated by the un-
 168 known coupling between various components of the stellar interior. The meta-model
 169 parameters ξ and σ^2 control the statistical behavior of the internal, i.e. unobservable,
 170 stress, $X(t)$. In Sections 1.2.1 and 1.2.2 we assume that changes in $X(t)$ couple linearly
 171 to the rotational frequency of the crust, $\nu(t)$, only when a glitch occurs, via (1.11). If we
 172 relax this restriction and couple $X(t)$ linearly to the crust between glitches, we have

$$\frac{d\nu}{dt} = -A \frac{dX}{dt}, \quad (1.14)$$

173 where A is an unknown coupling constant (units: Hz per unit stress) which depends on
 174 the physical mechanism of stress accumulation and the microphysics controlling how
 175 the star's internal angular momentum reservoir is tapped in between glitches. Equation
 176 (1.14) implies that, if the crust undergoes the same type of Brownian process with drift
 177 as described by (1.1), the observable, long-term, average spin-down rate, $\langle \dot{\nu} \rangle$, is propor-
 178 tional to ξ , while the observed spin-wandering amplitude is proportional to σ^2 .

179 In the special case of $A = A_{\max}$ (its maximum allowed value) the coupling is the
 180 same as during a glitch, e.g. $A = I_s/[2\pi(I_c + I_s)]$ in the vortex avalanche picture. This is a
 181 problem for the Brownian meta-model, as we see from Figure 1.1. To distinguish glitches
 182 from stochastic wandering we need $\mu \gtrsim 50$, otherwise large Brownian fluctuations can
 183 be mistaken for glitches. For $\mu \gtrsim 50$, there should be a strong cross-correlation between
 184 glitch sizes and waiting times until the next glitch, as discussed in Section 1.3.2. We
 185 do not see this cross-correlation in most pulsars, so we can rule out the special case of
 186 $A = A_{\max}$ or the Brownian meta-model (or both).

187 On the other hand, for $A < A_{\max}$, where the inter-glitch coupling is weaker than
 188 during a glitch, the problem outlined above is alleviated. Another scenario is that A is not
 189 constant, i.e. it varies with time or the stress in the system. These scenarios are motivated
 190 by the observations of the “precursor” slowdown in the Vela pulsar immediately prior
 191 to the 2016 glitch [27], and by studies of non-linear coupling mechanisms [35, 41]. A
 192 detailed study of the microphysical implications of inter-glitch spin wandering for the
 193 coupling mechanism between the stress reservoir and the crust is left for future work.
 194 For simplicity, we assume henceforth that coupling only occurs at a glitch, via (1.11).

195 1.3. OBSERVABLE LONG-TERM STATISTICS

196 To prepare for comparing the Brownian meta-model to data, we study how changing
 197 the input parameters affects the long-term statistical predictions.

198 1.3. Waiting time distribution

199 The long-term waiting time PDF, $p(\Delta t)$, constructed after many glitches are observed, is
 200 calculated from (1.7) given μ and $\eta(\Delta X)$. Figure 1.3 shows $p(\Delta t)$ for four representative
 201 values of μ when $\eta(\Delta X)$ is a power law of the form

$$\eta(\Delta X) \propto \Delta X^{-\delta} H(1 - \Delta X) H(\Delta X - \beta), \quad (1.15)$$

202 where the proportionality constant is fixed by $1 = \int_0^1 d(\Delta X) \eta(\Delta X)$, δ is the power-law
 203 index, β is the lower cut-off to ensure normalisability, and H is the Heaviside function

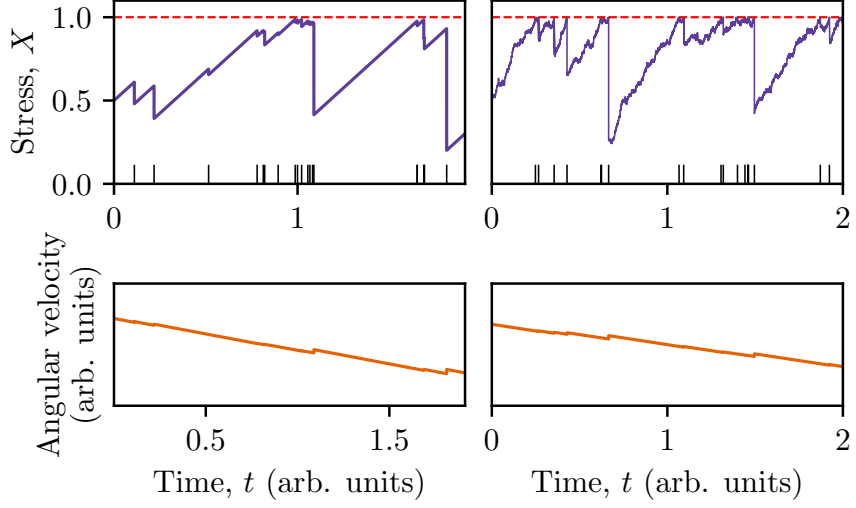


Figure 1.2: Comparison between two representative time series of stress (top panels) and crust angular velocity (bottom panels) from the SDP meta-model (left) and the Brownian meta-model (right). A deterministic, secular torque drives the stress between glitches in the SDP meta-model, whereas a stochastic Langevin torque drives the stress between glitches in the Brownian meta-model. Black tick marks in the top panels indicate the glitch epochs. Parameters for SDP meta-model: $\alpha = 1$, power law conditional jump distribution, as described in equations (17) and (19) of Fulgenzi et al. [2] respectively. Parameters for Brownian meta-model: $\mu = 50$, power law stress-release distribution, as in (1.15). Parameters shared between meta-models: $\delta = -1.5$, $\beta = 10^{-2}$ in (1.15).

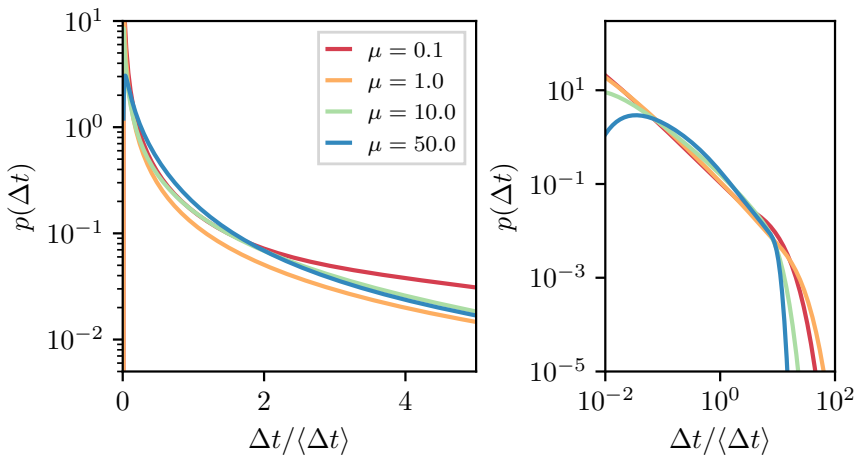


Figure 1.3: Waiting time PDF, $p(\Delta t)$, for four values of μ on log-linear (left panel) and log-log (right panel) scales. The stress release distribution, $\eta(\Delta X)$, is a power law, as in (1.15), with $\delta = -1.5$ and $\beta = 10^{-2}$.

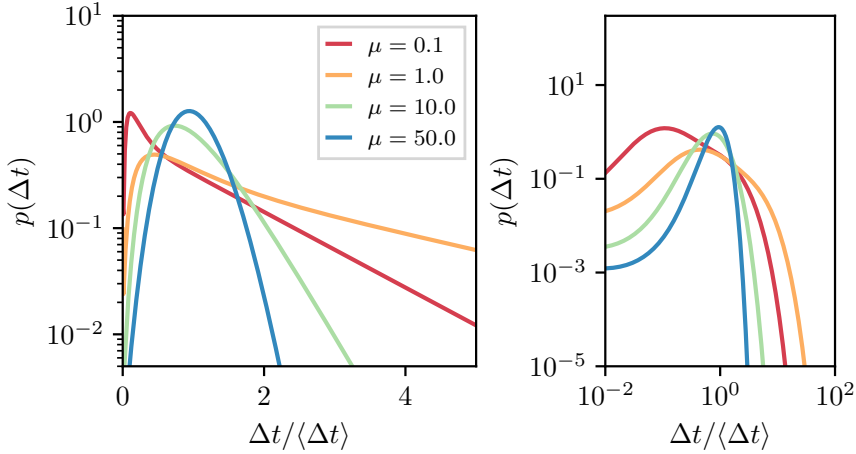


Figure 1.4: As for Figure 1.3 but with a Gaussian $\eta(\Delta X)$, as in (1.16), with $\mu_G = 0.5$ and $\sigma_G = 0.125$.

($\beta \leq \Delta X \leq 1$ implies $0 \leq X \leq 1$ at all times). The abscissae are normalized by $\langle \Delta t \rangle$ to highlight how the shape of $p(\Delta t)$ evolves with μ . On the log-log axes (right panel) $p(\Delta t)$ resembles a power law over at least 3 decades, with a cut-off at $\Delta t \approx 10\langle \Delta t \rangle$. The cut-off steepens as μ grows. The shape of $p(\Delta t)$ depends weakly on δ and β for $\mu \lesssim 10$, but depends strongly for $\mu \gtrsim 10$. For example, for $\mu \gtrsim 10$ and $\beta = 10^{-1}$, $p(\Delta t)$ becomes unimodal, as small waiting times become less likely when each glitch reduces the stress by $\Delta X \geq \beta$.

What about other functional forms of $\eta(\Delta X)$? Figure 1.4 shows $p(\Delta t)$ for four representative values of μ , with a Gaussian $\eta(\Delta X)$, viz.

$$\eta(\Delta X) \propto \exp\left[\frac{-(\Delta X - \mu_G)^2}{2\sigma_G^2}\right] H(1 - \Delta X) H(\Delta X) , \quad (1.16)$$

where the proportionality constant is fixed to normalize $\eta(\Delta X)$, μ_G is the mean, and σ_G is the standard deviation. For $\mu \lesssim 1$, $p(\Delta t)$ resembles an exponential distribution, if the smallest waiting times with $\Delta t \lesssim 0.25\langle \Delta t \rangle$ are ignored. For $\mu \gtrsim 1$, $p(\Delta t)$ is unimodal. Increasing the size of the average ΔX , via increasing μ_G , reduces the variance in $p(\Delta t)$ for all μ , whereas reducing μ_G makes $p(\Delta t)$ resemble the results for a power law $\eta(\Delta X)$. Reducing the variance of each stress-release event by reducing σ_G also reduces the variance of $p(\Delta t)$, as expected.

The third functional form of $\eta(\Delta X)$ that we test is a log-normal distribution,

$$\eta(\Delta X) \propto \frac{1}{\Delta X} \exp\left[\frac{-(\log \Delta X - \mu_{LN})^2}{2\sigma_{LN}^2}\right] H(1 - \Delta X) H(\Delta X) , \quad (1.17)$$

where μ_{LN} and σ_{LN} are the mean and standard deviation, and the proportionality constant is set by normalization. Figure 1.5 shows that the general shape of $p(\Delta t)$ with a log-normal $\eta(\Delta X)$ is similar to what is seen with a Gaussian $\eta(\Delta X)$. There are fewer small waiting times for a given μ . If the average stress release is increased, by increasing μ_{LN} , the same response is seen as with a Gaussian $\eta(\Delta X)$, i.e. the variance of $p(\Delta t)$ drops. If we increase σ_{LN} , $p(\Delta t)$ resembles what is seen with a uniform $\eta(\Delta X)$.

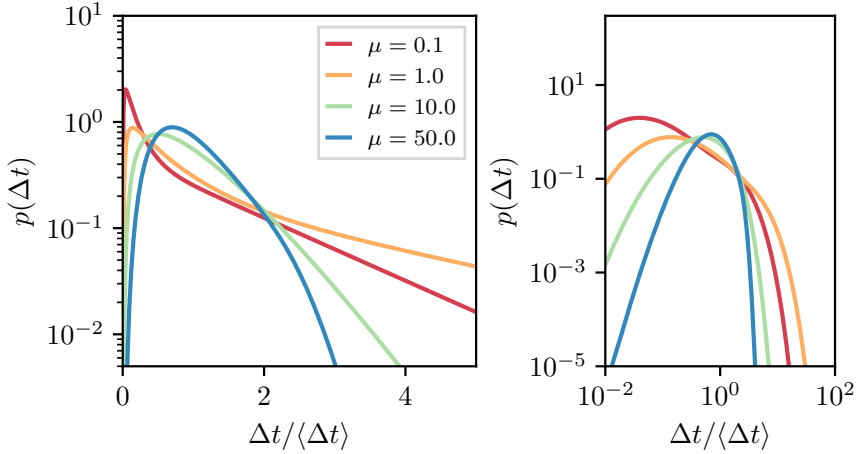


Figure 1.5: As for Figure 1.3 but with a log-normal $\eta(\Delta X)$, as in (1.17), with $\mu_{LN} = -1$ and $\sigma_{LN} = 0.5$.

An analogous study of $p(\Delta t)$ for the SDP meta-model, with $\eta(\Delta X)$ taken to be a power law, Gaussian, and a variety of other functional forms, is presented by Carlin and Melatos [3].

1.3. Correlations and memory

The meta-model in Section 1.2.1 predicts whether we should see a correlation between the size of a glitch and the subsequent waiting time, which we call a forward cross-correlation. As the glitch size is independent of the history of the stress evolution, there is no backward cross-correlation between the size of a glitch and the previous waiting time in the Brownian meta-model. Forward and backward cross-correlations have been investigated previously in the context of the SDP meta-model, and numerous falsifiable predictions are made [1, 3, 25].

Figure 1.6 shows the Spearman correlation coefficient for the forward cross-correlation, ρ_+ , for $5 \times 10^{-2} \leq \mu \leq 5 \times 10^3$. The cross-correlation is always positive and increases from $\rho_+ \approx 0.25$ for $\mu \lesssim 1$ to $\rho_+ \approx 1$ for $\mu \gg 1$. Figure 1.6 is generated with $\eta(\Delta X)$ as a power law, but the result is insensitive to the form of $\eta(\Delta X)$. The trend in Figure 1.6 is intuitive. The size of the stress release in a glitch dictates how much stress must be accumulated before the next glitch occurs. For μ high, the diffusion of the Brownian process is negligible compared to the secular drift, and so the waiting time is determined almost completely by the size of the previous glitch. For μ low, the diffusion randomizes the waiting time and decouples it from the size, while still maintaining a slight forward cross-correlation; even a process with zero drift is more likely to reach the threshold faster, if X_0 is closer to X_c .

The Brownian meta-model predicts zero autocorrelations between glitch sizes, or between waiting times. The threshold at $X = 1$ is reached before every glitch in the Brownian meta-model, removing “memory” in the system of the behavior of the stress prior to reaching that threshold. In contrast, the SDP meta-model predicts sizable auto-correlations in certain regimes [1].

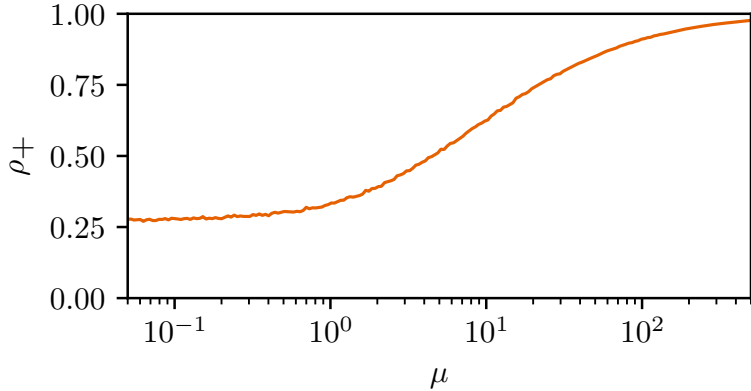


Figure 1.6: Spearman cross-correlation between the size of a glitch and the waiting time until the next glitch versus μ . At 200 logarithmically spaced values of μ , 10^5 waiting times and sizes are drawn from (1.8) and (1.15) respectively, using each generated size to determine the starting point for the next inter-glitch interval and hence waiting time.

254 1.4. FALSIFYING THE BROWNIAN META-MODEL

255 There are six pulsars with more than 15 recorded glitches². Their names, the number of
 256 recorded glitches, the forward Spearman cross-correlation coefficient (along with asso-
 257 ciated p-value and 95% confidence interval), as well as the best-fitting size and waiting
 258 time distributions are listed in Table 1.1. The Spearman correlation coefficient minimizes
 259 the impact of outliers by testing for monotonic correlations, as opposed to the strictly
 260 linear correlations which the standard Pearson correlation coefficient describes. The
 261 confidence interval is calculated as described in Section 4 of Carlin and Melatos [1]. The
 262 best-fitting PDFs are copied from Fuentes et al. [16] and are selected based on the Akaike
 263 Information Criterion [43]. These shapes are broadly consistent with previous analyses
 264 using different techniques, although there are minor individual differences [14, 37]. We
 265 note that PDF shape fitting is uncertain when the sample size is small. Often the best
 266 one can do in the glitch context is to distinguish between a monotonic (e.g. exponential,
 267 power law) and unimodal (e.g. Gaussian) PDF, without tying down the functional form.
 268 Even then some functional forms (e.g. Weibull) straddle both categories [44]. Further
 269 shape-fitting studies should be carried out in the future, as the data sets grow.

270 Although not listed in Table 1.1, we note that the backward cross-correlation, the
 271 autocorrelation between glitch sizes, and the autocorrelation between waiting times are
 272 all consistent with zero, at a 95% confidence level for all six objects [1, 16, 25].

273 One virtue of the Brownian meta-model, like the SDP meta-model studied elsewhere
 274 [1–3, 25], is that it makes specific, quantitative predictions about PDFs and correlations.
 275 These predictions are open to falsification using existing and future data. With an eye to
 276 falsifying the meta-model presented in Sections 1.2 and 1.3 we now ask whether existing
 277 long-term observations of the pulsars in Table 1.1 can be adequately explained. In doing

²Up-to-date online catalogues of pulsar glitches are available through the Jodrell Bank Centre of Astrophysics at <http://www.jb.man.ac.uk/pulsar/glitches.html> [15], and the Australian National Telescope Facility at <https://www.atnf.csiro.au/research/pulsar/psrcat> [42]

Table 1.1: Pulsar name, number of glitches (N), Spearman correlation coefficient between glitch size and subsequent waiting time (ρ_+), associated p-value, and the 95% confidence interval (CI). The last two columns indicate the functional form of the best-fitting distribution for glitch sizes, $p(\Delta X)$, and waiting times, $p(\Delta t)$ [14, 16, 37].

Name (PSR J)	N	ρ_+	p-value	95% CI	$p(\Delta X)$	$p(\Delta t)$
0537–6910	42*	0.93	10^{-18}	(0.84, 0.97)	Gaussian	Gaussian
1740–3015	36	0.29	0.091	(−0.06, 0.58)	Power law	Exponential
0534+2200	25†	−0.060	0.78	(−0.45, 0.35)	Log-normal	Exponential
1341–6220	23	0.58	0.0048	(0.13, 0.83)	Log-normal	Exponential
0835–4510	21	0.30	0.20	(−0.19, 0.67)	Gaussian	Gaussian
0631+1036	17	0.21	0.44	(−0.33, 0.65)	Power law	Exponential

*The number and parameters of glitches in PSR J0537–6910 vary between Middleditch et al. [20], Antonopoulou et al. [44], and Ferdman et al. [45]. We include in our analysis glitches that appear in two out of three sources.

†The first four PSR J0534+2200 glitches in the Jodrell Bank catalogue occurred before daily monitoring commenced and are excluded from the analysis [46].

so, we caution that there is debate about whether the existing glitch catalogues are complete and accurate. Espinoza et al. [47] claimed that all glitches in the Crab pulsar (PSR J0534+2200) are detected. Yu and Liu [48] used a Monte Carlo study to confirm that the Yu et al. [49] analysis of 165 pulsars observed between 1990 and 2011 using the Parkes Observatory has “detected all detectable glitches in the data” (verbatim quote). However, as the cadence of observations for most pulsars is not constant [50], post-glitch recovery time-scales vary [51, 52], and glitch detections still rely on human intervention [48], it remains uncertain whether or not we are seeing the smallest glitches, or resolving glitches that happen in quick succession.

1.4. PSR J0537–6910

PSR J0537–6910 has the most recorded glitches and the highest forward cross-correlation amongst all the prolific glitching pulsars. In the context of the Brownian meta-model, these properties place PSR J0537–6910 in the $\mu \gtrsim 10^2$ regime, via Figure 1.6. The glitch size distribution for PSR J0537–6910 is approximately Gaussian [16]. Looking at Figure 1.4, where $\eta(\Delta X)$ is a Gaussian, we note that $p(\Delta t)$ should also be a Gaussian, with $\mu \gtrsim 10^2$, in accord with observations. Therefore, the main features of the long-term statistics of this pulsar conform to the Brownian meta-model, if $\eta(\Delta X)$ is a Gaussian, and one has $\mu \gtrsim 10^2$.

We note that the waiting time distribution for PSR J0537–6910 is also well described by a Weibull distribution [44], a more general functional form, which includes the exponential and a skewed Gaussian as special cases.

299 1.4. *PSR J1740–3015*

300 PSR J1740–3015 has a forward cross-correlation that is consistent with zero. However
301 the 95% confidence interval is broad enough to encompass ρ_+ up to 0.58. According to
302 Figure 1.6 this means PSR J1740–3015 has $\mu \lesssim 10$, in the context of the Brownian meta-
303 model. As PSR J1740–3015 has a power-law size PDF [16], we look to Figure 1.3, where
304 $\eta(\Delta X)$ is a power law. For $\mu \lesssim 10$ the Brownian meta-model predicts that $p(\Delta t)$ is a
305 power law with a cut-off at large Δt . Therefore, as $p(\Delta t)$ is observed to be exponential
306 in this object, the long-term statistics are not explained by the Brownian meta-model
307 with any set of input parameters.

308 Power-law and log-normal distributions are often hard to distinguish for such small
309 sample sizes. If $\eta(\Delta X)$ is actually a log-normal distribution for this object, then we look
310 at Figure 1.5. With $\mu \lesssim 10$ we note that $p(\Delta t)$ should be an exponential, if the small-
311 est waiting times are not observed. Therefore, as $p(\Delta t)$ is observed to be exponential
312 in this object, it is consistent with the Brownian meta-model, if we are unable to ob-
313 serve glitches with $\Delta t \lesssim 0.25\langle\Delta t\rangle$. Note that $\langle\Delta t\rangle$ refers to the true underlying average
314 waiting time, rather than the estimate from the sample of glitches we have observed.

315 1.4. *PSR J0534+2200*

316 PSR J0534+2200 has a forward cross-correlation that is consistent with zero, with $\rho_+ \leq$
317 0.35 at 95% confidence. This limits PSR J0534+2200 to $\mu \lesssim 2$, according to Figure 1.6.
318 PSR J0534+2200 has a log-normal size distribution [16]. Taking $\eta(\Delta X)$ to be log-normal,
319 as in Figure 1.5, we see that $p(\Delta t)$ should be an exponential, if the smallest waiting
320 times are not observed. Therefore, as $p(\Delta t)$ is observed to be exponential in this object,
321 it is consistent with the Brownian meta-model, if we are unable to observe glitches with
322 $\Delta t \lesssim 0.25\langle\Delta t\rangle$. If we do see all glitches in PSR J0534+2200, as claimed by Espinoza et al.
323 [47], then the observations are inconsistent with the Brownian meta-model.

324 We note that the semi-autonomous glitch-finding algorithm of Espinoza et al. [47]
325 may miss closely spaced glitches occasionally. For example, it missed one glitch, at epoch
326 MJD 52146.8 with a size of $\Delta\nu = 0.27 \mu\text{Hz}$, which occurred $\Delta t \approx 63\text{ d}$ after the previous
327 glitch with Espinoza et al. [47] noting that the likely cause is “influence of the recovery
328 from the previous glitch” (verbatim quote). If we take 63 d as the minimum resolvable
329 waiting time, the true underlying average waiting time is $\langle\Delta t\rangle \approx 63\text{ d}/0.25 = 252\text{ d}$, in
330 order for the long-term statistics to be consistent with the Brownian meta-model. The
331 observed average waiting time is 501 d, while the median waiting time is 284 d. On the
332 other hand, the Brownian meta-model may be ruled out, and the minimum resolvable
333 waiting time may be shorter than 63 d. More work is needed to clarify these issues,
334 including systematic studies of the false alarm and false dismissal probabilities of glitch-
335 finding algorithms [40, 48, 50, 53].

336 1.4. *PSR J1341–6220*

337 PSR J1341–6220 has a forward cross-correlation that is significantly positive. However
338 the 95% confidence interval is broad, allowing $0.13 \leq \rho_+ \leq 0.83$. According to Figure
339 1.6 this limits μ to $\mu \lesssim 10^2$. PSR J1341–6220 has a log-normal size distribution [16],
340 and so like PSR J0534+2200 is consistent with Brownian the meta-model, only if we do

341 not detect glitches with $\Delta t \lesssim 0.25\langle\Delta t\rangle$. The observed waiting time distribution is an
342 exponential.

343 1.4. PSR J0835–4510

344 PSR J0835–4510 has a forward cross-correlation that is consistent with zero. The 95%
345 confidence interval encompasses ρ_+ up to 0.67, consistent with $\mu \lesssim 30$, according to Fig-
346 ure 1.6. The size PDF, and hence $\eta(\Delta X)$, for PSR J0835–4510 is approximately Gaussian
347 [16]. Therefore according to Figure 1.4 the meta-model predicts $p(\Delta t)$ to be an expo-
348 nential (for $\mu \lesssim 5$) or a skewed Gaussian (for $5 \lesssim \mu \lesssim 30$). The observed $p(\Delta t)$ is a
349 Gaussian, not an exponential. Therefore, the observations are currently consistent with
350 the Brownian meta-model for $5 \lesssim \mu \lesssim 30$, if $\eta(\Delta X)$ is a Gaussian.

351 The somewhat strict constraints on μ imply that, with more glitches, the measured
352 forward cross-correlation should increase to $0.4 \lesssim \rho_+ \lesssim 0.6$. If ρ_+ stays outside this
353 range, PSR J0835–4510 will become another counterexample to the Brownian meta-
354 model.

355 1.4. PSR J0631+1036

356 PSR J0631+1036 has roughly half the recorded glitches of PSR J1740–3015 but is other-
357 wise similar statistically. Hence the same conclusion holds: as long as the size distri-
358 bution is a power law [16], the Brownian meta-model does not adequately explain the
359 observations, as exponential waiting times cannot be generated if $\eta(\Delta X)$ is a power law.

360 As with PSR J1740–3015, if $\eta(\Delta X)$ is actually a log-normal distribution, instead of a
361 power law, the conclusion is different: the observations are consistent with the predic-
362 tions of the Brownian meta-model, if we do not resolve glitches with $\Delta t \lesssim 0.25\langle\Delta t\rangle$.

363 1.5. POPULATION TRENDS

364 The primary goal of this paper is to formulate rigorously and then falsify (if possible)
365 the Brownian meta-model, rather than engage in a parameter estimation exercise. Nev-
366 ertheless the results in Section 1.4 do carry some interesting preliminary implications
367 concerning the parameters of the Brownian meta-model, in the event that it survives
368 falsification in the future. In this section, we touch briefly on two population trends that
369 are consistent with (albeit not guaranteed by) the results in Section 1.4: why do $\eta(\Delta X)$
370 and μ seem to vary significantly among the six pulsars in Table 1.1?

371 Regarding $\eta(\Delta X)$, laboratory studies of self-organized critical systems with avalanche
372 dynamics, like sand piles, reveal that $\eta(\Delta X)$ is power-law-like when the driver is “slow”,
373 and Gaussian-like when the driver is “fast” [39]. In the former regime, avalanches occur
374 sporadically at well-separated points within the system, so consecutive avalanches are
375 independent and scale invariant: they can have any size, ranging from a solitary nearest-
376 neighbor interaction to a catastrophic collapse of the whole system. In the latter regime,
377 consecutive avalanches “trip over one another” (i.e. are correlated, not independent) and
378 involve most of the system every time, so they all have comparable sizes, and $\eta(\Delta X)$ is
379 unimodal. Broadly speaking the foregoing physics may suggest a correlation between
380 the shape of $\eta(\Delta X)$ and $\langle\dot{\nu}\rangle$, and it will be interesting to test for such a correlation in the

future, as more data are gathered. However, one must approach such a test with caution. The demarcation between “slow” and “fast” drivers is a subtle and unsolved question in idealized systems like sand piles, let alone in neutron stars where the microphysics is complicated and unknown (e.g. vortex avalanches, starquakes). Moreover observables like $\langle \dot{v} \rangle$ cannot be related easily to the behavior of the stress reservoir, e.g. due to uncertain coupling between multiple components of the star’s interior, as discussed in Section 1.2.5.

To understand how $\mu = \xi X_c / \sigma^2$ could vary pulsar-to-pulsar we need to unpack the various internal parameters, and relate them to potential observables. In the standard picture, $\langle \dot{v} \rangle$ is set by the spin-down torque, N_{ext} , and moment of inertia of the crust, I_c . As discussed in Section 1.2.5, one can invoke a linear coupling between the internal stress and observed behavior of the crust. Linear coupling faces many issues, as we discuss in Section 1.2.5, but taking it to be valid for the moment, we find $\xi \propto \langle \dot{v} \rangle \approx N_{\text{ext}}/I_c$, where the proportionality constant controls the strength of the coupling. For the six objects discussed in this paper, $N_{\text{ext}} \propto B^2 v^3$ (where B is the strength of the dipole magnetic field at the surface) varies across three orders of magnitude, using values of B and v from the ATNF pulsar catalogue³. The other factor is I_c . There are two popular scenarios for this quantity, as discussed in Section 3 of Melatos et al. [54]: (a) if the crust is a thin crystalline lattice and the rest of the star is composed of a superfluid we have $I_c/I_0 \sim 10^{-2}$, where I_0 is the total moment of inertia of the star [55, 56]; (b) if the crust has most of the interior superfluid pinned and co-rotating with it (via magnetic flux tubes or charged particles), with only a bit of the inner crust superfluid decoupled, we have $I_c/I_0 \sim 1$ [15, 57, 58]. We do not explore which of these scenarios is more likely, as both have strong support in the literature. We do note that the difference between these scenarios widens the possible range of ξ by another two orders of magnitude. The other factors in μ are σ and X_c . Again, as discussed in Section 1.2.5, σ is proportional to the observed spin-wandering amplitude, if we assume a linear coupling. The spin-wandering amplitude in the six objects considered in this paper is not well quantified in the literature. However, Shannon and Cordes [59] found that for a general population of “canonical pulsars”, the timing noise strength, σ_{TN} , spans three orders of magnitude. Finally, the critical stress X_c may vary from object to object, as it is a complex combination of microphysical (e.g. pinning potential) and thermodynamic (e.g. equation of state) parameters [60]. Hence, even for linear coupling (which is already ruled out by looking at inter-glitch spin wandering, as discussed in Section 1.2.5), the possible range of μ inferred from external observables spans more than eight orders of magnitude, comfortably encompassing the range of μ which the meta-model considers.

417 1.6. CONCLUSIONS

418 The physical mechanism that triggers pulsar glitches is unknown. Phenomenological
419 meta-models offer one way to link — and potentially falsify — broad classes of plausi-
420 ble microphysical mechanisms with measurements of long-term glitch statistics. The
421 SDP meta-model [2] describes microphysical mechanisms in which glitches are trig-
422 gered probabilistically, while the stress in the system rises secularly, becoming more

³<https://www.atnf.csiro.au/research/pulsar/psrcat/> [42]

likely as the stress increases. It makes falsifiable, quantitative predictions for size and waiting-time cross-correlations [25], autocorrelations [1], and PDFs [3]. However, the SDP meta-model does not allow the stress to fluctuate stochastically in between glitches due to random processes in the stellar interior, e.g. superfluid vortex motion [18], superfluid turbulence [29, 61], or crust cracking [62].

Motivated partly by recent observations of PSR J0835–4510 [27], we introduce an alternative meta-model, where the stress evolves between glitches according to a Brownian process with drift and diffusion components, and where glitches are triggered deterministically once the stress surmounts a threshold. The rotational slowdown observed by Ashton et al. [27] just prior to the glitch may be a coincidentally large instance of pulse jitter, but it may also indicate a large, stochastic fluctuation in the internal stress, which briefly couples the magnetosphere to the interior and triggers the glitch. While we do not model the microphysics in detail, the Brownian meta-model encompasses such a trigger mechanism. We show in Section 1.4 and Carlin and Melatos [1] that the glitch statistics of PSR J0835–4510 are consistent with the predictions of both the Brownian and SDP meta-models.

We find that the Brownian meta-model predicts various long-term statistical fingerprints. If the glitch size distribution is not a power law, and diffusion dominates drift (i.e. $\mu \lesssim 1$), the waiting time PDF is predicted to be an exponential, if glitches that occur soon after one another are not resolved. As μ increases, the observed waiting time PDF resembles more closely the glitch size PDF. The Spearman cross-correlation coefficient between glitch size and waiting time until the next glitch is predicted to be at least 0.25 for all pulsars.

Current observations of the long-term glitch statistics in all six of the pulsars with the most recorded glitches cannot be explained adequately by the Brownian meta-model. The two “quasi-periodic” glitchers (PSR J0537–6910 and PSR J0835–4510) with Gaussian size and waiting time distributions [16, 37] can be explained with the Brownian meta-model, while PSR J1740–3015 and PSR J0631+1036 cannot (regardless of input parameters), unless their glitch sizes are distributed as a log-normal instead of a power law [16]. PSR J0534+2200 and PSR J1341–6220 are consistent with the meta-model, if there are many glitches with small waiting times that we do not resolve. More data could falsify the Brownian meta-model as it applies to individual pulsars in several ways: i) if the measured forward cross-correlation is statistically inconsistent with $\rho_+ \geq 0.25$; ii) if a non-zero backward cross-correlation is measured; or iii) if the size or waiting time auto-correlations are nonzero. Additionally, measurements of the forward cross-correlation, combined with the size and waiting time PDFs, further constrain the meta-model parameters.

We note that i) the SDP meta-model is broadly consistent with the long-term statistics in the six pulsars with the most recorded glitches [1, 3], and ii) it predicts a different set of long-term statistics. Thus, over time we can distinguish between the two meta-models and falsify one, the other, or both. We remind the reader that most plausible microphysical mechanisms contemplated in the literature (e.g. superfluid vortex avalanches, starquakes, hydrodynamic instabilities and turbulence) fit broadly within one or both of the Brownian and SDP meta-models.

467 **ACKNOWLEDGEMENTS**

468 Parts of this research are supported by the Australian Research Council (ARC) Centre of
 469 Excellence for Gravitational Wave Discovery (OzGrav) (project number CE170100004)
 470 and ARC Discovery Project DP170103625. JBC is supported by an Australian Postgrad-
 471 uate Award. We thank the anonymous referee for pointing out that inter-glitch spin
 472 wandering places independent constraints on the Brownian meta-model in principle, as
 473 discussed in Section 1.2.5.

474 **1.A1. ANALYTIC SOLUTION OF THE FOKKER-PLANCK EQUA-
 475 TION FOR THE INTER-GLITCH STRESS DISTRIBUTION**

476 The Fokker-Planck equation for the globally averaged stress variable, X , together with
 477 the initial and boundary conditions, (1.3)–(1.5), constitute a standard diffusion problem.
 478 Namely, equation (1.2) is a parabolic partial differential equation with constant coeffi-
 479 cients solved on the finite interval $0 \leq X \leq X_c$, subject to mixed Dirichlet-Neumann (also
 480 called Robin) boundary conditions. The problem can be solved analytically by expanding
 481 the solution in eigenfunctions on the interval $0 \leq X \leq X_c$ [33].

482 We assume a separable ansatz

$$p(X, t) = Y(X)T(t) , \quad (1.18)$$

483 which converts (1.2) into two coupled ordinary differential equations,

$$\frac{2}{\sigma^2 T} \frac{dT}{dt} = -\alpha^2 , \quad (1.19)$$

$$\frac{1}{Y} \left(\frac{-2\xi}{\sigma^2} \frac{dY}{dX} + \frac{d^2 Y}{dX^2} \right) = -\alpha^2 , \quad (1.20)$$

484 for some constant α . Equation (1.20) has exponential solutions of the form

$$Y(X) \propto \exp \left[\left(\frac{\xi}{\sigma^2} \pm \sqrt{-\lambda^2} \right) X \right] , \quad (1.21)$$

485 with $\lambda^2 = \alpha^2 - \xi^2/\sigma^4$.

486 As (1.2) is linear, we apply the boundary conditions to the eigenfunctions defined in
 487 (1.21) independently, then sum over the eigenvalues using the principle of superposition.
 488 For $\lambda^2 \leq 0$, $Y(X)$ becomes a linear combination of $\sinh(\lambda X)$ and $\cosh(\lambda X)$. The bound-
 489 ary conditions imply $\tanh(\lambda X) \propto -\lambda$, whose only solution $\lambda = 0$ leads to the trivial
 490 result $Y(X) = 0$. We therefore restrict our attention to $\lambda^2 > 0$ and hence

$$Y(X) = \exp \left(\frac{\xi}{\sigma^2} X \right) (A \sin \lambda X + B \cos \lambda X) , \quad (1.22)$$

491 where A and B are constants. The reflecting boundary condition (1.5) implies

$$B = \frac{\lambda \sigma^2}{\xi} A , \quad (1.23)$$

⁴⁹² while the absorbing boundary condition (1.4) fixes the eigenvalues, λ , via

$$\tan(\lambda X_c) = -\frac{\lambda \sigma^2}{\xi} . \quad (1.24)$$

⁴⁹³ Hence we write the full solution for $P(X, t)$ as

$$P(X, t) = \exp\left(\frac{\xi}{\sigma^2}X\right) \sum_{n=1}^{\infty} A_n \exp\left[-t\left(\frac{\lambda_n^2 \sigma^2}{2} + \frac{\xi^2}{2\sigma^2}\right)\right] \left[\sin(\lambda_n X) + \frac{\lambda_n \sigma^2}{\xi} \cos(\lambda_n X) \right] \quad (1.25)$$

⁴⁹⁴ or equivalently

$$P(X, t) = \exp\left(\frac{\xi}{\sigma^2}X\right) \sum_{n=1}^{\infty} A'_n \exp\left[-t\left(\frac{\lambda_n^2 \sigma^2}{2} + \frac{\xi^2}{2\sigma^2}\right)\right] \sin[\lambda_n(X - X_c)] , \quad (1.26)$$

⁴⁹⁵ where λ_n is the n -th positive root of (1.24), and the A'_n constant coefficients are to be
⁴⁹⁶ determined.

⁴⁹⁷ We find the A'_n factors by applying the initial condition (1.3) and noting that the
⁴⁹⁸ eigenfunctions are orthogonal on $0 \leq X \leq X_c$ (not the standard Fourier domain $0 \leq X \leq$
⁴⁹⁹ 2π) as a consequence of Sturm-Liouville theory [63]. Orthogonality implies

$$A'_n = \frac{\int_0^{X_c} dX \exp(-\xi X / \sigma^2) \sin[\lambda_n(X - X_c)] p(X, t=0)}{\int_0^{X_c} dX \sin^2[\lambda_n(X - X_c)]} \quad (1.27)$$

$$= 2 \exp(-\xi X_0 / \sigma^2) \sin[\lambda_n(X_0 - X_c)] \frac{\xi / \sigma^2}{\xi X_c / \sigma^2 + \cos^2(\lambda_n X_c)} . \quad (1.28)$$

⁵⁰⁰ The full solution is given by (1.24), (1.26), and (1.28).

⁵⁰¹ 1.A2. CONDITIONAL WAITING TIME PDF WITHOUT THE RE- ⁵⁰² FLECTING BOUNDARY

⁵⁰³ If the reflecting boundary condition (1.5) is relaxed, such that the process operates on
⁵⁰⁴ the semi-infinite domain $X < X_c$, the conditional waiting time distribution is an inverse
⁵⁰⁵ Gaussian [31],

$$g(\Delta t | X_0) = \frac{X_c - X_0}{\sigma \sqrt{2\pi \Delta t^3}} \exp\left[\frac{-(X_c - X_0 - \xi \Delta t)^2}{2\sigma^2 \Delta t}\right] . \quad (1.29)$$

⁵⁰⁶ For $\xi/\sigma^2 \gtrsim 10$, numerical tests show that (1.29) agrees with (1.8) to within 1% for $0 \leq$
⁵⁰⁷ $\Delta t \leq 5\langle\Delta t\rangle$. This makes intuitive sense, as the process is driven strongly away from
⁵⁰⁸ $X = 0$ for large $\xi/\sigma^2 > 0$. We use (1.29) instead of (1.8) for $\xi/\sigma^2 \gtrsim 10$, because (1.8)
⁵⁰⁹ converges slowly in the latter regime.

CHAPTER 2

Long-term statistics of pulsar glitches due to history-dependent avalanches

2.1. INTRODUCTION

More than 500 rotational glitches have been detected in radio pulsars¹. The sample is large enough that it is meaningful to disaggregate the data and study the long-term statistics of glitch activity in some individual objects with enough recorded glitches. Quantities of interest include waiting time and size cross-correlations, autocorrelations, and probability density functions (PDFs) [1, 3, 14–16, 25, 37].

Given measurements of the above quantities, one can falsify popular phenomenological meta-models describing glitch activity as a stress-relax process, wherein stress accumulates between glitches and relaxes partially at a glitch. A meta-model unifies a broad class of stochastic processes under its umbrella while remaining agnostic about the specific microphysics and the physical nature of the stress. It makes concrete, falsifiable predictions about long-term glitch statistics. The pay-offs from falsifiability are considerable and have driven work in this area recently. For example, existing data have been used to discriminate between the state-dependent Poisson (SDP) and Brownian stress accumulation (BSA) meta-models in six objects with high glitch activity [4]. In the SDP meta-model, glitches are triggered stochastically via a Poisson process with a stress-dependent rate, while the stress increases deterministically between glitches [2, 64]. In the BSA meta-model, glitches are triggered deterministically when the stress reaches a threshold, while the stress evolves stochastically via a Brownian process between glitches [4]. Both meta-models are consistent with various flavors of microphysics in the literature, e.g. superfluid vortex avalanches [17, 18], starquakes [19, 20], and hydrodynamic instabilities [21–23], but they embody important physical differences in how the stress accumulates and when the relaxation events are triggered.

¹Up-to-date online catalogues are maintained at the Jodrell Bank Centre of Astrophysics, <http://www.jb.man.ac.uk/pulsar/glitches.html> [15], and the Australian National Telescope Facility, <https://www.atnf.csiro.au/research/pulsar/psrcat/> [42]

538 The roughly scale invariant glitch size PDFs observed in some pulsars suggest that
 539 the stress relaxes via an *avalanche process*, i.e. a relaxation event triggered somewhere in
 540 the star propagates to adjacent regions via some knock-on mechanism [14, 39]. “Chain
 541 reactions” of this kind are observed in Gross-Pitaevskii simulations [18, 64–66] and
 542 mean-field or N-body simulations [67, 68] of superfluid vortex avalanches. They are
 543 typical of other systems cited as analogues of pulsar glitches in the literature, e.g. self-
 544 organized critical systems like sand piles, earthquakes, and magnetic fluxoids in type
 545 II superconductors [38, 39, 69]. In the meta-models published to date, a key input is
 546 the *conditional distribution of avalanche sizes*, $\eta[\Delta X^{(n)} | X(t_n^-)]$, specifically the PDF of
 547 the spatially averaged stress released during the n -th avalanche, $\Delta X^{(n)}$, if the stress
 548 just prior to the avalanche is $X(t_n^-)$. There is no way to infer the functional form of
 549 $\eta[\Delta X^{(n)} | X(t_n^-)]$ uniquely from neutron star data, although one can get a rough idea
 550 from the observed glitch size distribution. Quantities of interest, such as size and wait-
 551 ing time PDFs, cross-correlations, and autocorrelations all depend jointly on the form of
 552 $\eta[\Delta X^{(n)} | X(t_n^-)]$, however, opening the door to falsifiability [1, 3, 4].

553 In this paper, we generalize the successful SDP meta-model by adding a recipe to cal-
 554 culate $\eta[\Delta X^{(n)} | X(t_n^-)]$ endogenously instead of stipulating it exogenously by fiat. We
 555 refer to this generalization as the endogenous- η meta-model. The recipe makes con-
 556 crete the following key idea, which underpins the traditional picture of superfluid vortex
 557 avalanches in the literature: i) the vortex pinning strength varies randomly from one lo-
 558 cation to the next within the star; ii) the stress $\Delta X^{(n)}$ released in a glitch is proportional
 559 to the number of locations where the stress X exceeds a threshold, when the glitch is trig-
 560 gered; and iii) the unpinned vortices are reassigned randomly to new pinning locations
 561 after the glitch. In other words, as time passes, the distribution of occupied pinning sites
 562 is continually revised in a history-dependent fashion, as the star spins down secularly
 563 and glitches occur stochastically. This idea is based on the “coherent noise” meta-model
 564 introduced by Sneppen and Newman [70] to describe sand piles [71], earthquakes [71],
 565 and biological extinctions [72]². It has been repurposed successfully as a pulsar glitch
 566 meta-model in previous work [73].

567 Haskell [74] investigated a meta-model that connects the “snowplow” mechanism
 568 for hydrodynamically triggered glitches [75] to simulations of vortex unpinning and
 569 re-pinning in a two-component fluid framework [76]. It differs from the meta-model
 570 considered here in two fundamental ways: i) it unpins a random fraction of vortices
 571 at each avalanche event, independent of the past avalanche history; and ii) it assumes
 572 event waiting times are exponentially distributed (i.e. the waiting times do not depend
 573 on the stress, as in the SDP meta-model). However it does explicitly consider the mutual
 574 friction between the different fluid components, and shows that these hydrodynamic
 575 considerations produce deviations from power-law size distributions and exponential
 576 waiting time distributions.

577 We emphasize that we do not elect to analyze the endogenous- η meta-model because
 578 we favor it over other options. True, it is reasonable from a physical standpoint, but so
 579 too are other options. The main motivation is that it formalizes the dominant (albeit
 580 idealized) idea in the literature about how vortex unpinning leads to glitches. We there-

²The term “coherent noise” is not perfectly apt in the context of pulsar glitches, where the stress is coherent, while the noise, namely thermal creep, acts incoherently throughout the star. We retain the original terminology for consistency with previous literature [70, 73].

fore quantify for the first time the long-term statistics predicted by the broad consensus behind what determines $\eta[\Delta X^{(n)} | X(t_n^-)]$ in the superfluid vortex avalanche picture. As we show below, the long-term statistics are somewhat inconsistent with observations to date, although the conclusion is not final; more data are needed. As a matter of fact the exogenous SDP meta-model, where $\eta[\Delta X^{(n)} | X(t_n^-)]$ is stipulated by fiat instead of being calculated self-consistently, seems to be more consistent with the data. It is unclear what this result implies more broadly, but it is intriguing and likely to inspire more investigations. It serves as a reminder of the value of falsification of physically-motivated meta-models.

The paper is structured as follows: in Section 2.2 we specify how $\Delta X^{(n)}$ is decided at each glitch. In Section 2.3 we connect this method of determining $\Delta X^{(n)}$ at a glitch to the SDP meta-model. In Section 2.4 we explore the long-term statistical observables predicted by the endogenous- η meta-model, and discuss how they compare to current glitch observations in Section 2.5. We conclude in Section 2.6.

2.2. PINNING THRESHOLD DISTRIBUTION

We start by formalizing an idealized version of how the coherent stress mechanism may operate, which reflects standard ideas in the literature about stress accumulation and relaxation in pulsar glitches; see Haskell and Melatos [24] for a recent review. As argued below, there are at least three reasons why the simple version may not be what is truly occurring: i) it introduces a cross-correlation between sizes and waiting times, which is largely absent from the data; ii) it struggles to generate exponentially distributed waiting times, which are seen in some pulsars; and iii) it assumes a spatially uniform stress distribution which is qualitatively different to the spatially correlated stress distribution observed in Gross-Pitaevskii [18, 66] and N-body simulations [68] of superfluid vortex avalanches. Nonetheless it is important to study the simple version first, partly to falsify it if possible, and partly because it highlights the key idea that the stress distribution is history-dependent. As in previous papers, we develop the meta-model in the context of superfluid vortex avalanches for concreteness. Adapting it to the context of other microphysics, e.g. starquakes, is possible but outside the scope of this paper [71].

2.2. Standard picture

To fix ideas, suppose that the region of the stellar interior where glitch activity occurs is divided into “sites”. In the vortex avalanche picture, for example, the sites are nucleons or interstices in the nuclear lattice, where a superfluid vortex may pin [77–79]; in the starquake picture, the sites are segments of a fault or other tectonic element of the rigid crust [20, 36, 80]. At an arbitrary site located at \mathbf{r} , there is a local stress $X(\mathbf{r}, t)$ at time t , which evolves in response to the global driver and local relaxation physics. In the vortex avalanche picture, $X(\mathbf{r}, t)$ is proportional to the Magnus force; in the starquake picture, $X(\mathbf{r}, t)$ is proportional to the elastic stress (or equivalently the strain in the linear regime).

Let $X_{\text{th}}(\mathbf{r})$ denote the stress threshold at \mathbf{r} , which is assumed to be constant on the time-scales of interest (see below). Whenever the stress satisfies $X(\mathbf{r}, t) \geq X_{\text{th}}(\mathbf{r})$, and a glitch is triggered, the stress relaxes locally and is redistributed to nearby sites. In the

vortex avalanche picture, a vortex at a site unpins when it escapes the nuclear pinning potential; in the starquake picture, the crustal lattice fails locally when the breaking strain is exceeded. On the other hand, if the stress satisfies $X(\mathbf{r}, t) < X_{\text{th}}(\mathbf{r})$, it remains supported stably at \mathbf{r} during a glitch. A group of contiguous sites with $X(\mathbf{r}, t) < X_{\text{th}}(\mathbf{r})$ form a stress reservoir or capacitive domain [81]. Note that $X(\mathbf{r}, t) > X_{\text{th}}(\mathbf{r})$ can be supported metastably for some time before a glitch is triggered.

The coarse-grained stress threshold is assumed to be spatially uniform, because the length-scale of vortex avalanches or starquakes (inferred from the size of observed glitches) is smaller than the length-scale over which the nuclear lattice is stratified (typically $\sim 10^2 \text{ m}$) [82]. However the fine-grained stress threshold varies randomly from one site to the next, due to defects and microscopic compositional gradients in the lattice.

2.2. Available versus occupied sites

When describing the pinning thresholds statistically, it is essential to distinguish between their “available” distribution (defined without reference to any vortices) and their “occupied” distribution (defined with reference only to those pinning sites where a vortex is pinned). These are not the same in general. The available distribution is governed by the physics of the nuclear lattice. The occupied distribution is governed by a combination of the available distribution and the history-dependent vortex dynamics; vortices may congregate preferentially in deeper pinning potentials, for example.

Let $\phi(X_{\text{th}})$ denote the PDF of the thresholds at all available pinning sites. We assume that $\phi(X_{\text{th}})$ is constant in time, because the nuclear properties of the star evolve slowly (e.g. on the cooling time-scale $\sim 10^5 \text{ yr}$) compared to the inter-glitch waiting time and the length of glitch monitoring campaigns to date. Let $X_{\text{th}, \text{max}} = \max_{X_{\text{th}}} X_{\text{th}}$ denote the maximum pinning threshold in the star. In the superfluid vortex picture, for example, $X_{\text{th}, \text{max}}$ corresponds to the nuclear site with the deepest pinning potential; if a uniform stress satisfying $X \geq X_{\text{th}, \text{max}}$ is applied to the system, every vortex unpins when a glitch is triggered. The functional form of $\phi(X_{\text{th}})$ is unknown from first principles, but theoretical calculations suggest that it is broad, with standard deviation comparable to the mean [77–79], and $X_{\text{th}, \text{max}}$ is certain to be finite as stipulated by quantum mechanics. In this work we assume $\phi(X_{\text{th}})$ has compact support on the interval $0 = X_{\text{th}, \text{min}} \leq X_{\text{th}} \leq X_{\text{th}, \text{max}}$ for simplicity, but the results carry over straightforwardly to the case $X_{\text{th}, \text{min}} \neq 0$ without changing qualitatively. We emphasize that $X_{\text{th}, \text{max}}$ need not equal X_c , the critical stress at which a glitch is certain in either the SDP or BSA meta-models. This subtle point is discussed further in Section 2.3.3.

What is the PDF $g(X_{\text{th}}, t)$ of the stress thresholds at pinning sites actually occupied by vortices at time t ? In the absence of a global driver, we have $g(X_{\text{th}}, t) = \phi(X_{\text{th}})$ in the limit $t \rightarrow \infty$, after initial transients die away. In the presence of a persistent global driver, however, $g(X_{\text{th}}, t)$ depends on time and does not equal $\phi(X_{\text{th}})$ for any t in general (except perhaps $t = 0$, or in the special situation where all vortices unpin at once, resetting the system back to $g(X_{\text{th}}, t) = \phi(X_{\text{th}})$, as described in Section 2.2.3). Whenever a glitch occurs, vortices unpin from relatively shallow pinning sites and repin randomly, changing the relative occupation of sites with lower and higher X_{th} . Thus $g(X_{\text{th}}, t)$ is not only time- and history-dependent but also stochastic; it depends on the random sequence of glitch sizes and waiting times up to the instant t .

667 How $g(X_{\text{th}}, t)$ evolves depends, among other things, on whether one treats the sys-
 668 tem as spatially uniform or nonuniform. In self-organized critical systems like sand
 669 piles, for example, long-range spatial correlations exist between the stress at different
 670 locations \mathbf{r} and \mathbf{r}' , with $|\langle X(\mathbf{r}, t)X(\mathbf{r}', t) \rangle - \langle X(\mathbf{r}, t) \rangle \langle X(\mathbf{r}', t) \rangle| \propto |\mathbf{r} - \mathbf{r}'|^{-a}$ and $a > 0$ typ-
 671 ically [38, 39]. The system self-organizes through spatial gradients to produce scale-
 672 invariant dynamics (e.g. power-law avalanche size PDFs). A strong case can be made,
 673 through Gross-Pitaevskii and N-body simulations, that superfluid vortex avalanches or
 674 starquakes in a neutron star are self-organized critical systems too [14, 24, 68]. How-
 675 ever, the theoretical treatment of a far-from-equilibrium system with correlated spatial
 676 gradients is a notoriously challenging (and unsolved) problem in statistical mechanics
 677 [39]. In this paper, therefore, we derive an equation of motion for $g(X_{\text{th}}, t)$ under the
 678 assumption that every pinning site in the star experiences the same, spatially-averaged
 679 stress, $X(\mathbf{r}, t) = X(t)$. This mean-field approximation [2, 67] has been employed success-
 680 fully in the analysis of pulsar glitch observational data on size and waiting time PDFs,
 681 cross-correlations, and autocorrelations in the context of the SDP and BSA meta-models
 682 [1–4, 25, 83] as well as in previous work on “coherent noise” models of pulsar glitches
 683 [see footnote 2 and Melatos and Warszawski [73]].

684 2.2. *Unpinning and repinning*

685 Consider two consecutive glitches that occur at times t_n and t_{n+1} . Let t_n^\pm denote the
 686 instants infinitesimally after (+) and before (−) the event at $t = t_n$ ³. During the inter-
 687 val $t_n^+ \leq t \leq t_{n+1}^-$, the vortices are pinned, so the occupied sites do not change, and
 688 neither does $g(X_{\text{th}}, t)$. That is, we have $g(X_{\text{th}}, t) = g(X_{\text{th}}, t_n^+)$ for $t_n^+ \leq t \leq t_{n+1}^-$. We
 689 also have $g(X_{\text{th}}, t) = 0$ for $X_{\text{th}} \leq X(t_n^+)$, because vortices repin exclusively at sites with
 690 $X_{\text{th}} > X(t_n^+)$, when the avalanche at $t = t_n$ occurs; they cannot get stuck at sites where
 691 the stress exceeds the local threshold, while they are moving freely. Simultaneously,
 692 $X(t)$ evolves during the interval $t_n^+ \leq t \leq t_{n+1}^-$ (deterministically in the SDP process,
 693 stochastically in the BSA process). By the time the instant $t = t_{n+1}$ is reached, we have
 694 $X(t_{n+1}^-) \geq X_{\text{th}}$ at many sites; the corresponding vortices are pinned metastably and are
 695 ready to unpin when provoked by some minuscule statistical (e.g. thermal) fluctuation.
 696 When they do unpin, they are assumed to do so instantaneously at $t = t_{n+1}$. The instan-
 697 taneous approximation is justified amply by Gross-Pitaevskii simulations, where vortex
 698 avalanches are observed to occur on a time-scale shorter than one rotation period, and
 699 by high-time-resolution radio timing observations, which reveal that the spin up during
 700 a glitch takes less than ~ 30 s [26, 27, 84, 85]. Both these time-scales are much shorter
 701 than the typical inter-glitch waiting time of weeks to months.

702 How many vortices unpin at $t = t_{n+1}$? In the mean-field approximation, the answer
 703 is all of them pinned in sites that satisfy $X_{\text{th}} \leq X(t_{n+1}^-)$, which represent a fraction, F , of

3It is important to distinguish t_n from t_n^\pm , because the glitch is assumed to occur instantaneously, as in
 previous work.

704 the total, with

$$F = \int_0^{X(t_{n+1}^-)} dX'_{\text{th}} g(X'_{\text{th}}, t_{n+1}^-) \quad (2.1)$$

$$= \int_{X(t_n^+)}^{X(t_{n+1}^-)} dX'_{\text{th}} g(X'_{\text{th}}, t_n^+) . \quad (2.2)$$

705 The unpinned vortices move radially outward by a distance Δr comparable to one inter-
706 vortex (Feynman) separation λ_F before repinning (as seen in Gross-Pitaevskii and N-
707 body simulations), reducing the angular momentum of the superfluid in proportion to
708 Δr and their number. By angular momentum conservation, the crust spins up, and the
709 crust-superfluid angular velocity lag (i.e. the spatially averaged stress) decreases. That
710 is, we have

$$X(t_{n+1}^+) - X(t_{n+1}^-) = -KF , \quad (2.3)$$

711 where $K > 0$ is a constant measured in units of stress. To ensure $X(t) \geq 0$ we require
712 $K \leq X_{\text{th}, \max}$.

713 In the vortex avalanche picture, where X is the crust-core differential angular velocity,
714 angular momentum conservation implies [2, 54]

$$KF = \frac{2\pi(I_C + I_S)\Delta\nu}{I_S} \quad (2.4)$$

715 or equivalently

$$K = \frac{2\pi(I_C + I_S)}{I_C} \frac{\nu\Delta r}{R} , \quad (2.5)$$

716 where ν is the rotational frequency of the rigid crust (with $X \ll \nu$), $\Delta\nu$ is the increase in
717 ν at the glitch, I_S and I_C are moments of inertia of the superfluid and crust respectively,
718 and R is the neutron star radius. For $\Delta r \sim \lambda_F = 4.1 \times 10^{-2}(\nu/10\text{Hz})^{-1/2}$ cm, we estimate

$$K \sim 10^{-7} \left(\frac{I_C + I_S}{I_C} \right) \left(\frac{\nu}{10\text{Hz}} \right)^{1/2} \left(\frac{R}{10\text{km}} \right)^{-1} \text{Hz.} \quad (2.6)$$

719 The factor $(I_C + I_S)/I_C$ amounts to $\sim 10^2$ if the crust is a thin crystalline lattice while the
720 rest of the star is composed of a superfluid [55, 56] or ~ 1 if the crust is coupled tightly to
721 most of the neutrons and protons throughout the star, e.g. by pinning between neutron
722 vortices and magnetic fluxoids of the superfluid [15, 57, 58, 86]. As discussed in Section
723 2.5 of Carlin and Melatos [4] the coupling between the rotation of the superfluid and
724 the crust may be imperfect [87]. In light of the uncertainty, we allow K to remain a free
725 parameter in the meta-model.

726 The unpinned vortices repin instantaneously. The number of pinning sites per unit
727 area is $\sim 10^{20}$ times the number of vortices per unit area, so there is no reason for a
728 vortex to pin preferentially to a shallower or deeper pinning site, as it circulates freely
729 during an avalanche. Hence the probability that a vortex repins at a site with stress
730 threshold X_{th} is simply proportional to the number of such sites present in the crustal

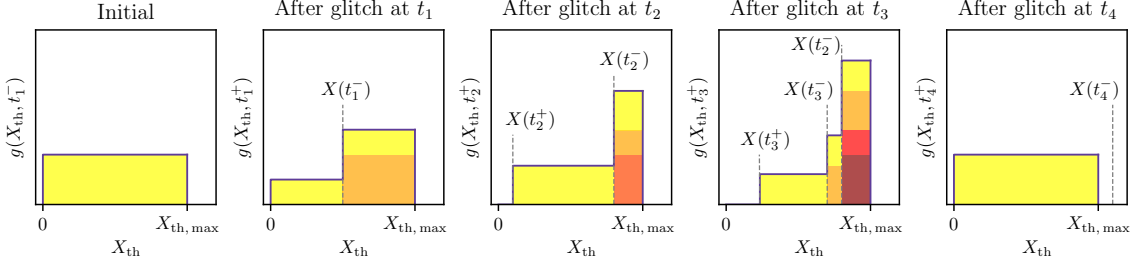


Figure 2.1: A toy example illustrating schematically the evolution of $g(X_{\text{th}}, t)$ during a sequence of four glitches, with $X(t_1^+) < X(t_3^+) < X(t_2^+) < X_{\text{th}, \text{max}} < X(t_4^-)$, where $g(X_{\text{th}}, t^-) = \phi(X_{\text{th}})$ is the uniform distribution between $0 \leq X_{\text{th}} \leq X_{\text{th}, \text{max}}$. The colors correspond to how many glitches occur in the time elapsed since vortices unpin from pinning sites with a certain threshold. Darker colors indicate that the vortices have stayed pinned during more events.

lattice, i.e. the fraction of the total sites with threshold X_{th} . Therefore the distribution of thresholds at which the vortices repin satisfies $g_{\text{repin}}(X_{\text{th}}, t_{n+1}^+) \propto \phi(X_{\text{th}})^4$. Of course, freely moving vortices cannot repin at a site whose threshold is lower than the global stress, as discussed above, so we have

$$g_{\text{repin}}(X_{\text{th}}, t_{n+1}^+) = A \phi(X_{\text{th}}) H[X_{\text{th}} - X(t_{n+1}^+)], \quad (2.7)$$

where $H(\dots)$ denotes the Heaviside function. The constant A is determined by normalization with respect to the unpinned fraction and is given by

$$A = \left[\int_{X(t_{n+1}^+)}^{X_{\text{th}, \text{max}}} dX'_{\text{th}} \phi(X'_{\text{th}}) \right]^{-1} F. \quad (2.8)$$

2.2. Equation of motion for the distribution of occupied pinning sites

We are now in a position to combine the results on unpinning and repinning in Section 2.2.3 to write down the equation of motion for $g(X_{\text{th}}, t)$. We remind the reader that $g(X_{\text{th}}, t)$ does not evolve at all during the inter-glitch interval $t_n^+ \leq t \leq t_{n+1}^-$, while vortices are pinned. Its evolution is described completely, in the above approximation, by discontinuous adjustments at each glitch. That is, at $t = t_{n+1}$, the following things happen to the stress threshold PDF:

- i) we start with $g(X_{\text{th}}, t_{n+1}^-) = g(X_{\text{th}}, t_n^+)$, which is nonzero for $X_{\text{th}} > X(t_n^+)$;
- ii) we calculate the change in stress $-KF$ in equation (2.3) by integrating $g(X_{\text{th}}, t_n^+)$ according to equation (2.2);

⁴In other words, as there are many more pinning sites than vortices, the distribution of thresholds of pinning sites at which a free vortex may repin is equal to the distribution of thresholds of pinning sites in general. A free vortex is not biased towards pinning sites with higher or lower thresholds. It pins indiscriminately to any site, whose threshold exceeds the global stress [88].

747 iii) we set $g(X_{\text{th}}, t_{n+1}^-)$ to zero in the range $X(t_n^+) \leq X_{\text{th}} \leq X(t_{n+1}^-)$, because the vortices
 748 therein unpin;

749 iv) we reassign the unpinned vortices to sites with thresholds in the range $X(t_{n+1}^+) <$
 750 $X_{\text{th}} \leq X_{\text{th}, \text{max}}$ according to equations (2.7) and (2.8).

751 Putting steps i)–iv) together yields

$$g(X_{\text{th}}, t_{n+1}^+) = g(X_{\text{th}}, t_{n+1}^-) H[X_{\text{th}} - X(t_{n+1}^-)] + \left[\int_{X(t_{n+1}^+)}^{X_{\text{th}, \text{max}}} dX'_{\text{th}} \phi(X'_{\text{th}}) \right]^{-1} F \phi(X_{\text{th}}) H[X_{\text{th}} - X(t_{n+1}^+)] \quad (2.9)$$

752 It is easy to check that this normalizes correctly with $1 = \int_0^{X_{\text{th}, \text{max}}} dX'_{\text{th}} g(X'_{\text{th}}, t_{n+1}^+)$.
 753 Note that $g(X_{\text{th}}, t_{n+1}^+)$ depends on $g(X_{\text{th}}, t_n^+)$ implicitly through F . It also depends on
 754 $X(t_{n+1}^-)$ and $X(t_n^+)$ independently, because the evolution of $X(t)$ during the interval $t_n^+ \leq$
 755 $t \leq t_{n+1}^-$ is controlled by the stress accumulation process, which does not depend on the
 756 unpinning and repinning physics.

757 Equation (2.9) resembles, but is not the same as, the equations of motion in Snep-
 758 pen and Newman [70] and Melatos and Warszawski [73]. The foregoing papers treat
 759 unpinning and repinning similarly, i.e. by nullifying the unpinned portion of $g(X_{\text{th}}, t)$
 760 and reassigning it elsewhere $\propto \phi(X_{\text{th}})$ ⁵. However neither paper evolves $g(X_{\text{th}}, t)$. It is
 761 assumed that $g(X_{\text{th}}, t)$ converges rapidly to its steady-state form, $g(X_{\text{th}}, t) = g(X_{\text{th}})$, i.e.
 762 the system establishes detailed balance between unpinning and repinning at each indi-
 763 vidual value of X_{th} [see equations (3) and (4) in Melatos and Warszawski [73]]. This
 764 approach is perfectly defensible, when the goal is to calculate the statistically stationary
 765 size and waiting time PDFs, but it does not contain enough information to study the
 766 cross- and autocorrelations we are interested in here [1, 3, 25].

767 To build intuition, Figure 2.1 illustrates schematically the evolution of $g(X_{\text{th}}, t)$ over
 768 the course of four hypothetical glitches at t_1 , t_2 , t_3 , and t_4 . For simplicity we choose
 769 $\phi(X_{\text{th}})$ to be uniform in the range $0 \leq X_{\text{th}} \leq X_{\text{th}, \text{max}}$, with $K = X_{\text{th}, \text{max}}$. The system
 770 starts with $g(X_{\text{th}}, t_1^-) = \phi(X_{\text{th}})$. In this particular realization we choose $X(t_1^+) < X(t_3^+) <$
 771 $X(t_2^+) < X_{\text{th}, \text{max}} < X(t_4^-)$ for illustrative purposes. The first glitch, at t_1 , unpins half of
 772 the vortices, and they are reassigned according to equation (2.7). The second glitch, at t_2 ,
 773 unpins more than half of the vortices, but due to the previous glitch we have $X(t_2^+) \neq 0$,
 774 as $g(X_{\text{th}}, t)$ is no longer uniform. The third glitch, at t_3 , occurs with $X(t_3^-) < X(t_2^-)$,
 775 demonstrating that the memory of the previous stress in the system is imprinted on
 776 $g(X_{\text{th}}, t)$, i.e. $g(X_{\text{th}}, t_3^+)$ depends on $X(t_2^-)$, not just $X(t_3^\pm)$. The fourth glitch, at t_4 , resets
 777 the system back to $\phi(X_{\text{th}})$ because we have $X(t_4^-) > X_{\text{th}, \text{max}}$, and so all vortices unpin.

778 Note that there is a complex feedback loop at play which relates the glitch sizes and
 779 waiting times to $g(X_{\text{th}}, t)$. If chance produces a long sequence of frequent glitches, i.e.
 780 the stress does not increase much before another glitch is triggered, vortices pile up at
 781 larger values of X_{th} near $X_{\text{th}, \text{max}}$. Then, when there is a long delay, which gives the
 782 stress time to reach $X \approx X_{\text{th}, \text{max}}$, the vortex pile pinned at sites with $X_{\text{th}} \approx X_{\text{th}, \text{max}}$
 783 unpins all at once to produce a relatively large glitch resetting the system. By contrast,

⁵They also include an optional thermal unpinning process independent of X_{th} , which is not essential and is omitted in this paper.

784 a similarly long delay produces a smaller glitch, if it is preceded by a glitch sequence
785 which does not pile up vortices at $X_{\text{th}} \approx X_{\text{th,max}}$.

786 2.3. STATE-DEPENDENT POISSON PROCESS

787 The above recipe for updating $g(X_{\text{th}}, t)$ must be combined with a compatible recipe for
788 choosing the waiting times between glitches. Two approaches have been explored pre-
789 viously, in the SDP [2, 3] and BSA meta-models [4]. In the BSA meta-model the stress
790 accumulates stochastically to a fixed threshold, whereupon a glitch is triggered deter-
791 ministically. In the SDP meta-model glitches are triggered probabilistically, at an instan-
792 taneous rate which depends on the stress in the system. If $X(t_n^-) = X_c$ is identical for
793 each glitch as in the BSA meta-model, the system does not produce glitches of differ-
794 ent sizes, as the same fraction of vortices would unpin every time, and repopulate the
795 same distribution of pinning sites. To avoid this trivial behavior, which is inconsistent
796 with pulsar data, we henceforth adopt the SDP meta-model to pick waiting times, and
797 therefore determine $X(t_{n+1}^-)$, given $X(t_n^+)$.

798 We position the SDP and related meta-models in the broader context of point pro-
799 cesses and time series modeling in Appendix 2.A3.

800 2.3. *Equation of motion for the stress*

801 The stress, $X(t)$, in the star evolves according to

$$X(t) = X(0) + t + \sum_{n=1}^{N(t)} \Delta X^{(n)}, \quad (2.10)$$

802 where X and t are here and henceforth expressed in dimensionless units of X_c (the crit-
803 ical stress at which a glitch becomes certain) and $X_c I_C / N_{\text{em}}$ respectively, where N_{em} is
804 the electromagnetic torque acting on the crust, and $X(0)$ is an arbitrary initial condition.
805 The number of glitches up to time t , $N(t)$, is a random variable, implicitly determined
806 by the waiting times between each glitch. The size $\Delta X^{(n)}$ of the n -th relaxation event
807 is a deterministic function of the fluctuating PDF $g(X_{\text{th}}, t)$. The recipe for determining
808 $\Delta X^{(n)} = -KF$ is outlined in Section 2.2.3, specifically equations (2.2) and (2.3).

809 One key assumption of the SDP meta-model is that the instantaneous glitch rate, $\lambda(t)$,
810 is a function of the spatially-averaged stress, $X(t)$. We assume $\lambda[X(t)]$ grows monoton-
811 ically between glitches according to

$$\lambda[X(t)] = \frac{\alpha}{1 - X(t)}, \quad (2.11)$$

812 where

$$\alpha = \frac{I_C X_c \lambda_0}{N_{\text{em}}} \quad (2.12)$$

813 is a dimensionless control parameter, and λ_0 is a reference rate defined as $\lambda_0 = \lambda(1/2)/2$.
814 The exact functional form of $\lambda[X(t)]$ does not significantly change the long-term dynam-
815 ics, as long as the rate diverges as $X \rightarrow X_c$ [2, 3].

816 The PDF of waiting times after the n -th glitch is [2, 89]

$$p[\Delta t | X(t_n^+)] = \lambda[X(t_n^+) + \Delta t] \exp \left\{ - \int_{t_n^+}^{t_n^+ + \Delta t} dt' \lambda[X(t_n^+) + t'] \right\}. \quad (2.13)$$

817 2.3. *Monte Carlo simulations*

818 The evolution of $X(t)$ and $g(X_{\text{th}}, t)$ is jointly modeled with a simple Monte Carlo au-
819 tomaton.

- 820 1. Initialize the system at $t = 0$ with $g(X_{\text{th}}, 0) = \phi(X_{\text{th}})$, and $X = X(0)$.
- 821 2. Pick a random Δt from equation (2.13), given the current stress X .
- 822 3. Update the stress to $X + \Delta t$ to account for the deterministic evolution up to the
823 glitch.
- 824 4. Evaluate $\Delta X = -KF$ deterministically via equations (2.2) and (2.3), given $g(X_{\text{th}}, t)$
825 and X .
- 826 5. Update $g(X_{\text{th}}, t)$ according to equation (2.9).
- 827 6. Update X by adding ΔX according to equation (2.10).
- 828 7. Repeat from step 2.

829 Random numbers for step 2 are picked using the standard inverse cumulative algorithm
830 [90]. As $\phi(X_{\text{th}})$ is chosen to be a uniform distribution between $0 \leq X_{\text{th}} \leq X_{\text{th},\text{max}}$,
831 $g(X_{\text{th}}, t)$ is a piecewise-constant function. Hence, we efficiently update it by storing the
832 heights at change-points X_{th} in memory, as opposed to sampling $g(X_{\text{th}}, t)$ on a grid of
833 X_{th} values.

834 2.3. *Qualitative results*

835 There are three control parameters in the dimensionless meta-model: α , $X_{\text{th},\text{max}}$, and
836 K . We fix $\phi(X_{\text{th}})$ to be a uniform distribution between 0 and $X_{\text{th},\text{max}}$. For simplicity,
837 we assume $K = X_{\text{th},\text{max}}$ (its maximal value) for the rest of this work. Appendix 2.A1
838 contains a brief exploration of the impact $K < X_{\text{th},\text{max}}$ has on long-term observables.
839 Figures 2.2–2.4 illustrate the qualitative impact of α on the evolution of X and $g(X_{\text{th}}, t)$,
840 given $X_{\text{th},\text{max}} = 0.95X_c$. Figure 2.2 shows that at low values $\alpha \lesssim 0.5$, longer waiting
841 times are more likely, and the stress often exceeds $X_{\text{th},\text{max}}$ before each glitch, resetting
842 the system. Therefore one finds $g(X_{\text{th}}, t) \approx \phi(X_{\text{th}})$, i.e. there is little long-term memory
843 in the system. In Figure 2.4 high values $\alpha \gtrsim 5$ produce shorter waiting times. Thus
844 long sequences of small glitches unfold before rare, large events reset the system once
845 the stress finally accumulates to $X \gtrsim X_{\text{th},\text{max}}$. Figure 2.3 shows that for intermediate
846 values of α between the above two extremes the behavior of both the stress $X(t)$ and
847 the evolution of $g(X_{\text{th}}, t)$ is complex.

848 The qualitative long-term behavior of X is shown in Figure 2.5. In the top panel with
849 $\alpha = 0.2$, the stress often exceeds $X_{\text{th},\text{max}}$ due to the long waiting times between glitches,

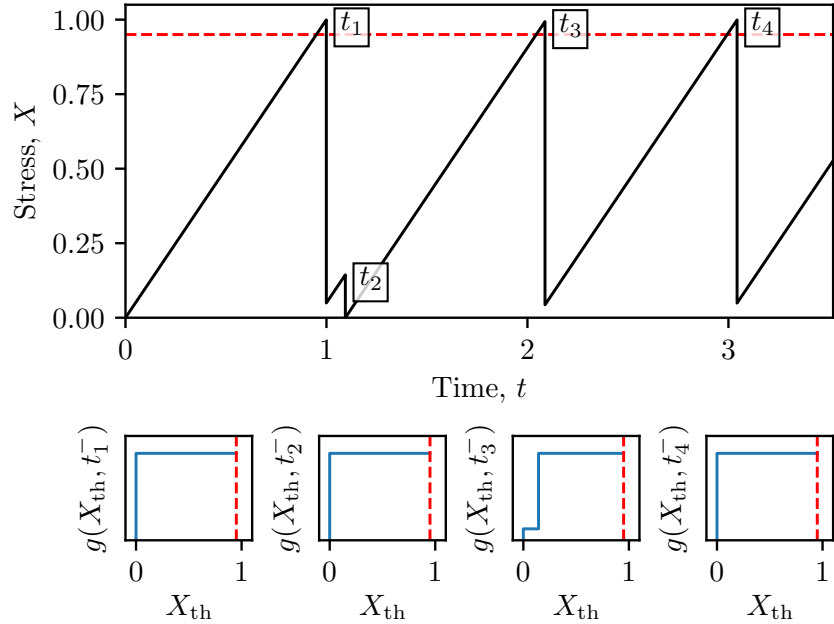


Figure 2.2: Evolution of X (main panel) and $g(X_{\text{th}}, t)$ (sub-panels) across four glitches at t_1, \dots, t_4 , generated via the automaton outlined in Section 2.3.2. Parameters: $\alpha = 0.2$, $X_{\text{th}, \text{max}} = 0.95$ (indicated in both the main panel and sub-panels with a red dashed line), $K = X_{\text{th}, \text{max}}$. X and X_{th} are in units of X_c and t is in units of $X_c I_C / N_{\text{em}}$.

resetting the system and keeping the average stress around $X \sim 0.5$. In the middle panel with $\alpha = 1$, the average stress climbs stochastically until finally a longer than average waiting time allows $X > X_{\text{th}, \text{max}}$, resetting the system. In the bottom panel with $\alpha = 10$, waiting times are short and the stress builds asymptotically towards $X = X_{\text{th}, \text{max}}$. For $\alpha \gtrsim 1$ the automaton takes some time to stabilize such that the memory of the arbitrary initial conditions $X(t = 0) = 0$ and $g(X_{\text{th}}, t = 0) = \phi(X_{\text{th}})$ is lost. When calculating long-term statistics predicted by the meta-model in Section 2.4 we throw away the first $\lfloor 100\alpha \rfloor$ glitches generated.

Figures 2.2–2.4 demonstrate that how often the system completely resets is closely linked to the dynamics of how X and $g(X_{\text{th}}, t)$ evolve, and therefore observables such as waiting times and glitch sizes. The fraction of glitches that fully reset the system, i.e. result in $g(X_{\text{th}}, t_n^+) = \phi(X_{\text{th}})$ after a glitch at time t_n , is plotted as a function of α and $X_{\text{th}, \text{max}}$ in Figure 2.6. The smallest value of α where over half the glitches reset the system shifts from 0.5 to 0.3 to 0.15 as $X_{\text{th}, \text{max}}$ decreases from 0.99 to 0.95 to 0.8 respectively. This is intuitive, as lower α results in longer waiting times, all else being equal, and the stress is more likely to exceed $X_{\text{th}, \text{max}}$ by the time a glitch is triggered.

For $X_{\text{th}, \text{max}} \geq 1$, X never exceeds $X_{\text{th}, \text{max}}$, and the system never completely resets. That is, the repinning step in equation (2.7) assigns vortices to pinning potentials with $X_{\text{th}} \geq 1$, which never unpin. The system stagnates eventually, with all vortices pinned at sites whose stress thresholds cannot be reached. Melatos and Warszawski [73] ameliorated this stagnation by allowing a “thermal creep” term, whereby a small fraction of vortices at sites with $X_{\text{th}} > X$ unpin randomly at a glitch [70].

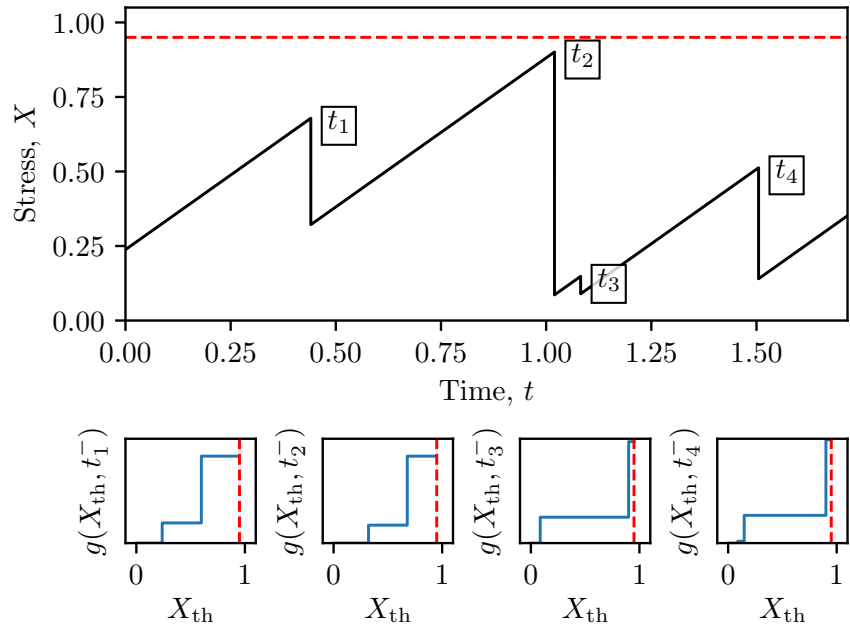


Figure 2.3: As in Figure 2.2 but with $\alpha = 1$.

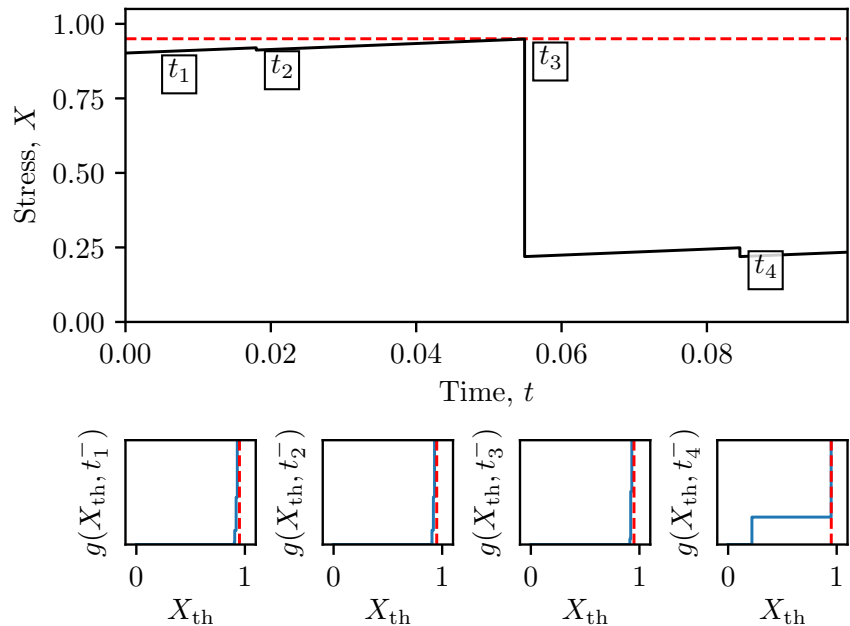


Figure 2.4: As in Figure 2.2 but with $\alpha = 10$.

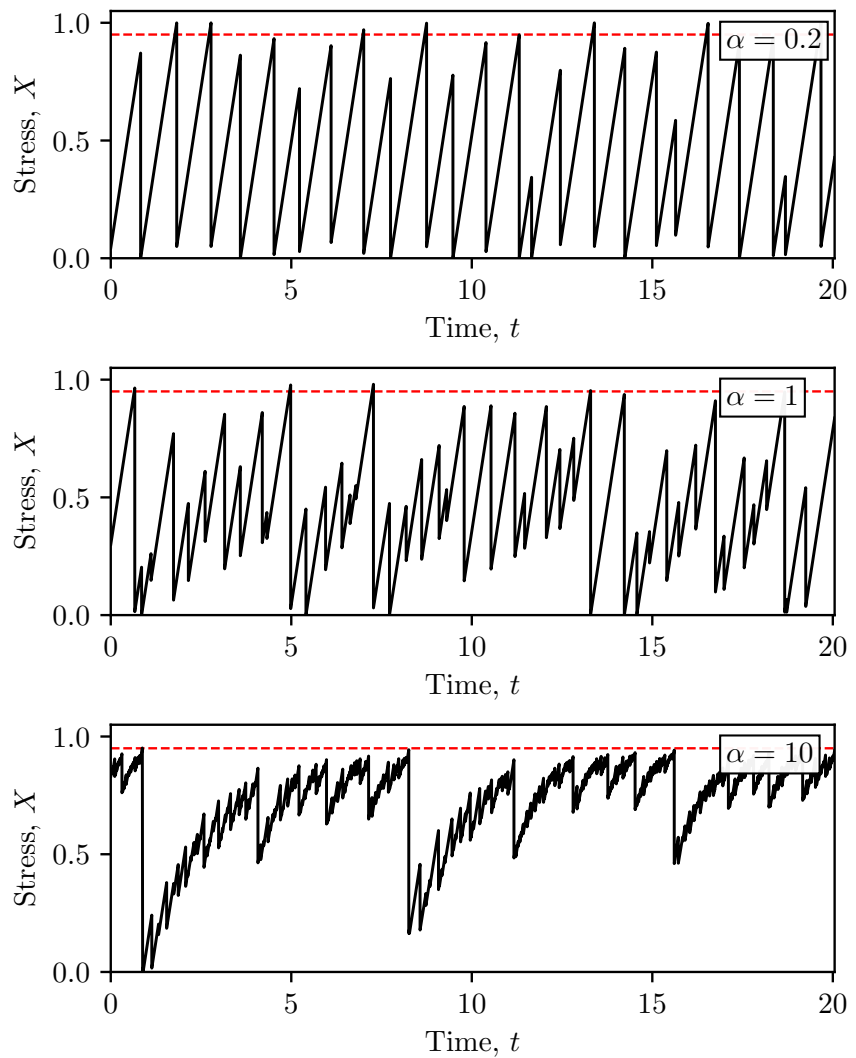


Figure 2.5: Long-term qualitative behavior of X for three different values of $\alpha = 0.2, 1$, and 10 in the top, middle and bottom panel respectively. Parameters: $X_{\text{th}, \text{max}} = 0.95$ (indicated with a red dashed line in each panel), $K = X_{\text{th}, \text{max}}$.

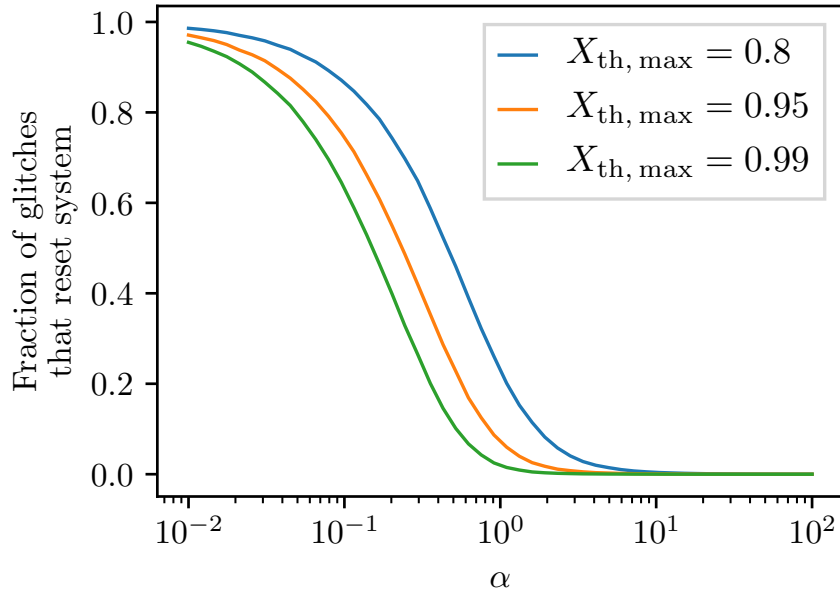


Figure 2.6: Fraction of glitches that reset the system as a function of α for three different values of $X_{\text{th}, \text{max}}$. Parameters: $N = 10^5$ glitches generated at 50 logarithmically spaced values of α for each value of $X_{\text{th}, \text{max}}$, with $K = X_{\text{th}, \text{max}}$.

872 2.3. Differences from previous meta-models

873 The recipe for updating $g(X_{\text{th}}, t)$ and hence generating $\Delta X^{(n)}$ differs fundamentally from
 874 the recipe in previous meta-models [2–4]. Firstly $\Delta X^{(n)}$ is generated from $g(X_{\text{th}}, t)$,
 875 which is a new step. In the SDP and BSA meta-models, $\Delta X^{(n)}$ is drawn from an exoge-
 876 nously defined conditional jump distribution, $\eta[\Delta X^{(n)} | X(t_n^-)]$, which makes no refer-
 877 ence to which pinning sites are occupied. Secondly, $\Delta X^{(n)}$ is generated deterministically;
 878 once $g(X_{\text{th}}, t_n^+)$ and $X(t_{n+1}^-)$ are known, so is $\Delta X^{(n)}$ without rolling dice. This fundamen-
 879 tally alters the meta-model from a doubly stochastic process, where the waiting time Δt
 880 and avalanche size $\Delta X^{(n)}$ are drawn randomly from independent PDFs (inhomogeneous
 881 Poisson and $\eta[\Delta X^{(n)} | X(t_n^-)]$ respectively), to a singly stochastic process, where only Δt
 882 is drawn randomly, according to the stress accumulation process of choice.

883 With that said, the sequence of avalanche sizes is still unpredictable in a long-term
 884 sense in the endogenous- η meta-model, because it is driven by stochastic draws of Δt .
 885 Furthermore, the ensemble average $g_s(X_{\text{th}}) = \langle g(X_{\text{th}}, t_n^+) \rangle$, is analogous to the statisti-
 886 cally stationary global stress PDF $p(X)$ discussed in Section 6 of Fulgenzi et al. [2]. From
 887 $g_s(X_{\text{th}})$, it is possible to calculate an effective $\eta[\Delta X^{(n)} | X(t_n^-)]$, which is also statistically
 888 stationary. We do so in Appendix 2.A2. If the goal of the theory is to predict the station-
 889 ary glitch size and waiting time PDFs, then running the SDP meta-model as developed in
 890 previous papers and drawing randomly from $\eta[\Delta X^{(n)} | X(t_n^-)]$ derived from $g_s(X_{\text{th}})$ as in
 891 Appendix 2.A2 is adequate. However, if the exact temporal sequence of sizes and waiting
 892 times is of interest, e.g. to investigate cross- and autocorrelations, then the evolution of
 893 $g(X_{\text{th}}, t)$ must be tracked according to equation (2.9) or some variant thereof.

894 2.3. *Mutual friction*

895 In hydrodynamical multi-component models, the coupling between the inviscid and vis-
896 cos components is called the mutual friction [91–93]. The strength and functional form
897 of the mutual friction is fundamentally linked to how the vortices transfer angular mo-
898 mentum from the unobservable stress reservoir and the observable crust [41, 93, 94]. The
899 SDP meta-model, and endogenous- η extension considered in this paper, tacitly assume
900 that mutual friction is weak between glitches as the stress grows linearly, irrespective of
901 its absolute magnitude, until a glitch is triggered. These meta-models align qualitatively
902 with phenomenological models that abruptly change the form (and usually weaken the
903 strength) of the mutual friction when a glitch occurs, due to a phase transition between
904 turbulent and laminar flow states [95–97]. We note that the meta-model treats glitches as
905 impulsive events and has nothing to say in its present form about post-glitch recoveries,
906 where hydrodynamic effects are likely to play a role.

907 2.4. OBSERVABLE LONG-TERM STATISTICS

908 Following the steps outlined in Section 2.3.2 one can generate sequences of waiting times
909 and sizes of arbitrary length, given α , K , and $X_{\text{th},\text{max}}$. From these sequences, observ-
910 able long-term statistics are predictable. They offer a baseline for falsification studies
911 involving astronomical observations [1, 3, 25]. As stated in equation (2.4), we have
912 $\Delta X = -KF \propto \Delta\nu$, implying the shape of the event size PDF $p(\Delta X)$ is the same as the
913 observed glitch size PDF $p(\Delta\nu)$.

914 2.4. *Waiting time and size PDFs*

915 Figure 2.7 shows the waiting time PDF, $p(\Delta t)$, and size PDF, $p(\Delta X)$, for three values
916 of α on a log-linear scale. For $\alpha \lesssim 0.5$, $p(\Delta t)$ has two peaks, one at $\Delta t = X_{\text{th},\text{max}}$ and
917 one at $\Delta t = 1$, and increases monotonically for $\Delta t < X_{\text{th},\text{max}}$. In the low- α regime X
918 regularly exceeds $X_{\text{th},\text{max}}$, triggering a glitch of size $\Delta X = X_{\text{th},\text{max}}$. With $X \approx 1$ before
919 the glitch, and $X \approx 1 - X_{\text{th},\text{max}}$ after, the maximum Δt until the next glitch is $X_{\text{th},\text{max}}$. As
920 equation (2.13) increases monotonically with Δt for $\alpha < 1$, the maximum Δt allowed by
921 equation (2.13) is the most likely waiting time. When plotted on a log-log scale, we see
922 that for $\alpha \gtrsim 3$, $p(\Delta t)$ is well approximated by a power-law distribution, with a turn-off
923 at $\Delta t \lesssim 10^{-2}$ (in units of $X_c I_C / N_{\text{em}}$). Where this turn-off occurs depends on both α
924 and $X_{\text{th},\text{max}}$. The slope of the power-law component of $p(\Delta t)$ is approximately -3 for
925 $\alpha = 10$ and decreases to -4 for $\alpha = 50$. In the intermediate regime $0.5 \lesssim \alpha \lesssim 3$, $p(\Delta t)$
926 is approximately uniform.

927 The size PDFs also display distinctive features in the low- and high- α regimes. For
928 $\alpha \lesssim 0.5$, $p(\Delta X)$ increases monotonically, with a significant fraction of the probability
929 mass close to $\Delta X = X_{\text{th},\text{max}}$. The latter events correspond to the glitches that completely
930 reset the system, if one has $X \geq X_{\text{th},\text{max}}$ prior to the glitch. On a log-log scale, we see
931 that for $\alpha \gtrsim 3$, $p(\Delta X)$ can be approximated as a broken power law distribution, with a
932 smooth turn-over at $\Delta X \approx 10^{-2}$ (in units of X_c). The location of this turn-over depends
933 on α and $X_{\text{th},\text{max}}$. The slope of $p(\Delta X)$ for $\Delta X \gtrsim 10^{-2}$ is approximately -2 for $\alpha = 10$,
934 and decreases to -2.5 for $\alpha = 50$. For $0.5 \lesssim \alpha \lesssim 3$, $p(\Delta X)$ is approximately uniform,

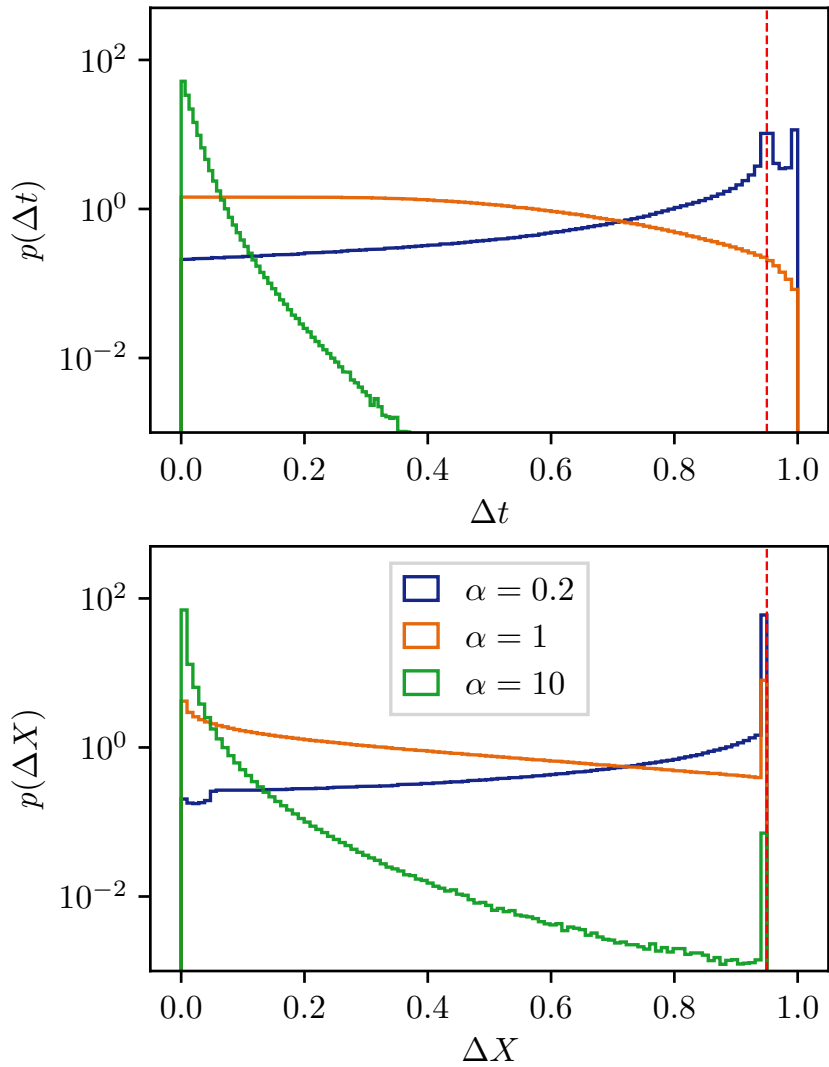


Figure 2.7: Waiting time, Δt , and size, ΔX , PDFs on the top and bottom panel respectively. Parameters: $N = 10^7$ simulated glitches for each value of α , $X_{\text{th},\text{max}} = 0.95$ (indicated with a red dashed line in each panel), $K = X_{\text{th},\text{max}}$.

935 with a spike at $\Delta X = X_{\text{th}, \max}$, again corresponding to glitches that completely reset the
936 system.

937 In summary, in the low- α regime $p(\Delta t)$ is bimodal with peaks at $\Delta t = X_{\text{th}, \max}$ and
938 $\Delta t = 1$, while $p(\Delta X)$ is monotonically increasing until $\Delta X = X_{\text{th}, \max}$ where there is a
939 spike in the PDF then a sharp cut-off. In the high- α regime both $p(\Delta t)$ and $p(\Delta X)$ are
940 approximately power-law distributed, with low-end turn-offs at $\Delta t \approx 10^{-2}$ and $\Delta X \approx$
941 10^{-2} .

942 2.4. Cross- and autocorrelations

943 The time-ordered nature of waiting times and relaxation events invites investigation into
944 what relationships exist between events that happen consecutively. For example, in the
945 SDP meta-model certain combinations of observables, such as the rate of spin-down and
946 average waiting time, predict the cross-correlation between waiting times and the next
947 glitch size [25]. In the SDP and BSA meta-models combinations of cross-correlations and
948 autocorrelations restrict possible values of meta-model control parameters in individual
949 glitching pulsars [1, 4].

950 Figure 2.8 shows the Spearman correlation coefficients for the forward cross-correlation,
951 ρ_+ , i.e. the correlation between the size of the previous glitch and the next waiting time;
952 the backward cross-correlation, ρ_- , i.e. the correlation between the size of the glitch
953 and the preceding waiting time; as well as the autocorrelations between consecutive
954 waiting times, $\rho_{\Delta t}$, and sizes, $\rho_{\Delta X}$. It is clear that ρ_+ is high for all but the smallest
955 values of α . The longer the waiting time, the larger the upper terminal in equation
956 (2.2), and thus a greater fraction of the vortices unpin. At small values $\alpha \lesssim 10^{-2}$ most
957 glitches completely reset the system, and the forward cross-correlation is lower. The
958 backward cross-correlation, ρ_- , is small and negative for $\alpha \lesssim 0.2$, but small and positive
959 for $\alpha \gtrsim 0.2$. Size autocorrelations, $\rho_{\Delta X}$, are negligible for all α . Waiting time autocorre-
960 lations satisfy $\rho_{\Delta t} \sim -0.5$ for $\alpha \lesssim 0.1$, but are negligible for $\alpha \gtrsim 0.2$.

961 The impact of decreasing $X_{\text{th}, \max}$ on Figure 2.8 is minimal; the magnitudes of the
962 Spearman correlation coefficients decrease marginally, and the Spearman correlation co-
963 efficients as functions of α shift towards the right a small amount. As $X_{\text{th}, \max}$ decreases,
964 Figure 2.6 shows that more glitches reset the system, at a fixed value of α .

965 2.4. Aftershocks and precursors

966 Aftershocks occur after a large event, when subsequent events are larger and more fre-
967 quent than usual. They are common in spatially correlated knock-on processes such as
968 avalanches and earthquakes [39, 98, 99]. Naively, one might expect that the endogenous-
969 η meta-model should not exhibit aftershocks, as it does not include spatial correlations,
970 due to the assumption that each pinning site experiences the same spatially-averaged
971 stress. Aftershocks are not discussed in the context of the SDP or BSA meta-models,
972 as large events in those meta-models do not correspond to a rearrangement of occu-
973 pied pinning sites. A large event does not impact the next waiting time or size, beyond
974 reducing the stress in the system.

975 We investigate whether the above naive expectation holds for the endogenous- η
976 meta-model by calculating the conditional waiting time and size PDFs for glitches im-

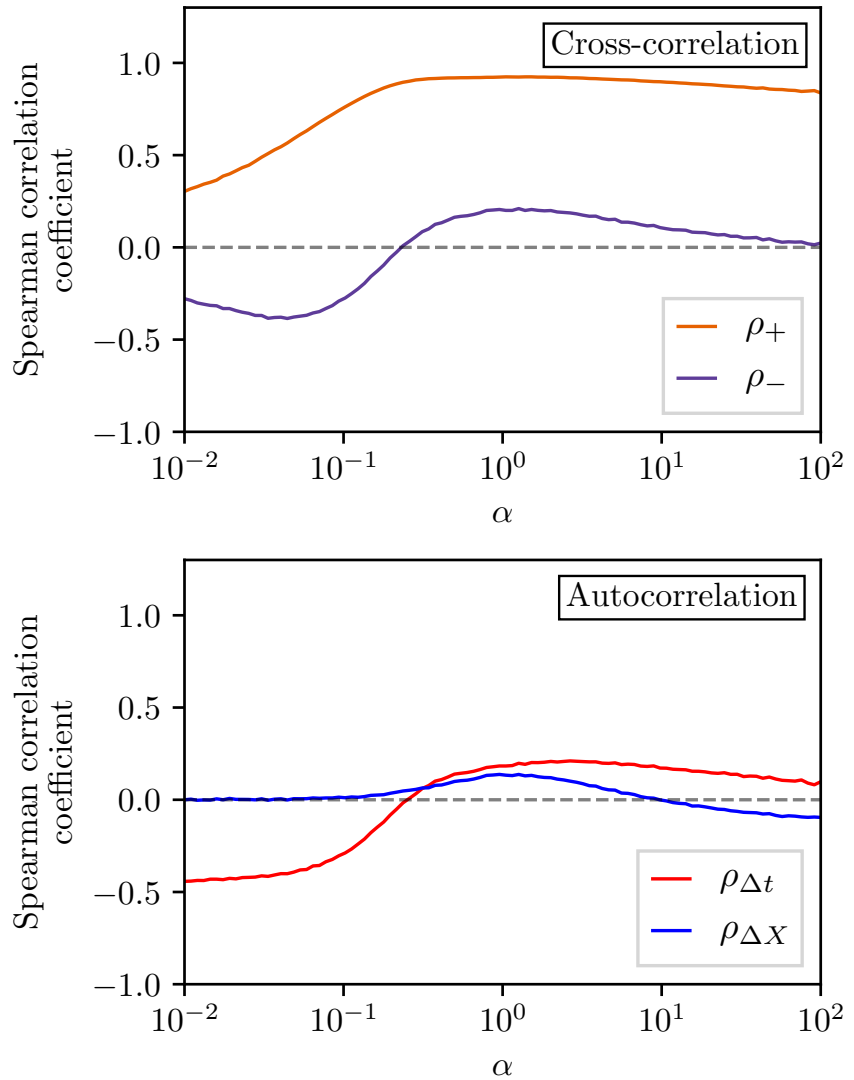


Figure 2.8: Top panel: Forward cross-correlation, ρ_+ , and backward cross-correlation, ρ_- , as a function of α (orange and purple curves respectively). Bottom panel: Auto-correlation between waiting times, $\rho_{\Delta t}$, and sizes, $\rho_{\Delta X}$, as a function of α (red and blue curves respectively). Parameters: $N = 10^5$ glitches generated at 100 logarithmically spaced values of α , $X_{\text{th},\max} = 0.95$, $K = X_{\text{th},\max}$.

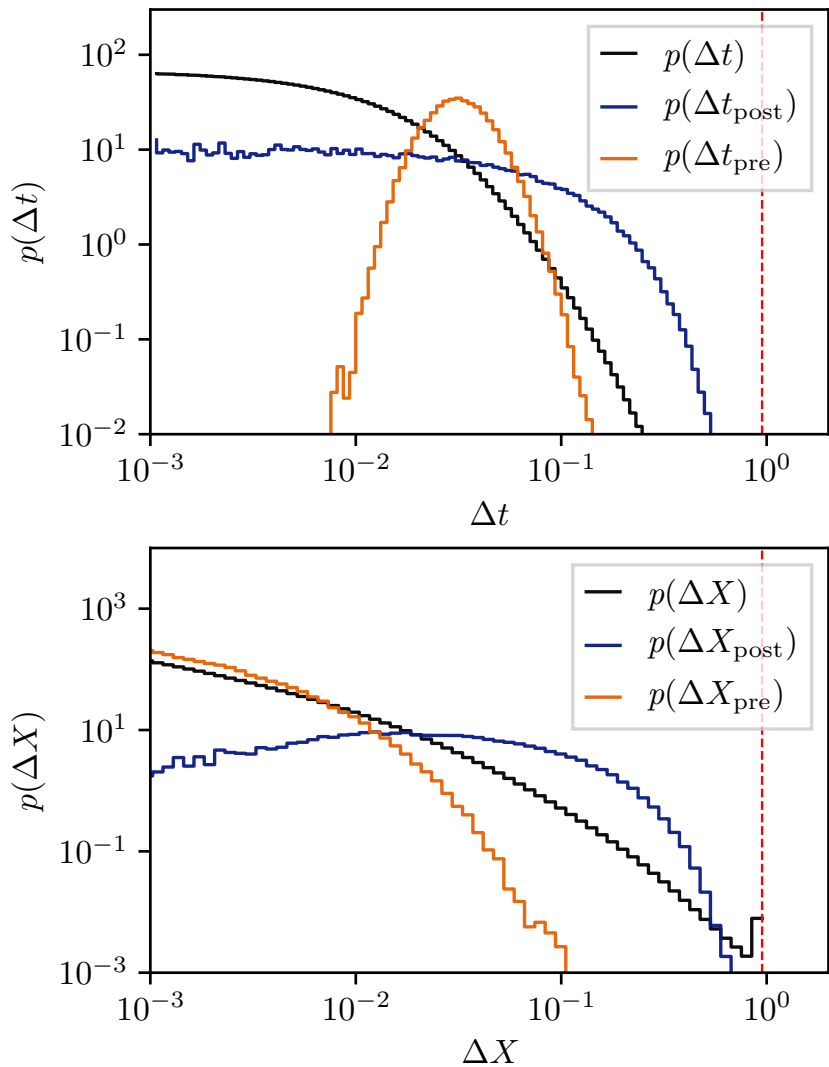


Figure 2.9: Top panel: PDFs of all waiting times, Δt , waiting times just prior to a system-resetting glitch, Δt_{pre} , and waiting times just after a system-resetting glitch, Δt_{post} . Bottom panel: Corresponding PDFs for sizes. Parameters: $\alpha = 10$, $N = 10^8$ total glitches, $\sim 10^5$ of which reset the system completely, $X_{\text{th}, \max} = 0.95$, $K = X_{\text{th}, \max}$.

977 mediate following a glitch that completely resets the system, $p(\Delta t_{\text{post}})$ and $p(\Delta X_{\text{post}})$
 978 respectively. Figure 2.9 shows these PDFs, and the waiting time and size PDFs of events
 979 just prior to a glitch that completely resets the system, $p(\Delta t_{\text{pre}})$ and $p(\Delta X_{\text{pre}})$ respec-
 980 tively. There is an excess of longer waiting times in $p(\Delta t_{\text{post}})$ compared to $p(\Delta t)$, as
 981 the system takes some time to build up stress before another glitch is likely, after such
 982 a system-resetting glitch. There is a corresponding excess of larger sizes in $p(\Delta X_{\text{post}})$
 983 compared to $p(\Delta X)$. The precursor waiting times, Δt_{pre} , are distributed as a log-normal
 984 distribution, with $\langle \Delta t_{\text{pre}} \rangle > \langle \Delta t \rangle$. There are relatively few small Δt_{pre} events, because
 985 the system-resetting condition $\Delta X \geq X_{\text{th}, \text{max}}$ occurs only if enough stress accumulates
 986 before the glitch. There are few large glitches in $p(\Delta X_{\text{pre}})$ compared to $p(\Delta X)$, as large
 987 glitches place the system in a configuration which is unlikely to fully reset at the next
 988 glitch, as X is low.

989 The behavior of aftershocks and precursors in Figure 2.9 is replicated qualitatively
 990 for other values of $\alpha \neq 10$ and $X_{\text{th}, \text{max}} \neq 0.95$. That is, there is always an excess of
 991 longer waiting times, and larger glitches, following a system-resetting glitch, while the
 992 precursor waiting times are longer than average. For $\alpha \lesssim 0.2$ these features in the PDFs
 993 are less prominent, as the system resets after almost every event.

994 2.5. ASTRONOMICAL OBSERVATIONS

995 How do the long-term statistical predictions in Section 2.4 compare to what we currently
 996 see in glitching pulsars? This question has been answered previously in the context of
 997 the SDP [1, 3, 25], and BSA [4] meta-models. For the five pulsars with the most recorded
 998 glitches, there are regimes of parameter space in the SDP meta-model which adequately
 999 explain observations. For example, PSR J0537–6910 is consistent with the SDP meta-
 1000 model if $\alpha \lesssim 0.1$ [1]. However this is not the case for the BSA meta-model, for which
 1001 two pulsars, namely PSR J0534+2200 and PSR J1341–6220, are consistent with the meta-
 1002 model only if there exists an undetected population of frequent small glitches.

1003 The endogenous- η meta-model presented here is falsifiable using the same approach:
 1004 the meta-model must predict simultaneously, with one set of input parameters, the long-
 1005 term $p(\Delta t)$, $p(\Delta X)$, cross-correlations, and autocorrelations, otherwise it is rejected. In
 1006 principle we have one additional potential observable in this meta-model, the after-
 1007 shocks and precursors discussed in Section 2.4.3. However, due to the small number
 1008 of glitches recorded in individual pulsars ($N < 50$), it is not yet clear whether we have
 1009 witnessed any large, system-resetting glitches in astronomical data, and so we cannot
 1010 compare to the aftershock or precursor predictions of Section 2.4.3.

1011 Current observations of glitch waiting time and size distributions [16, 37] do not
 1012 show clear signs of a sharp cut-off at the upper end, as the meta-model predicts in Figure
 1013 2.7 for $\alpha \lesssim 5$. For $\alpha \gtrsim 5$, where the distributions are steeper, the sharp cut-off may have
 1014 escaped detection until now due to the paucity of recorded glitches. Even so, if most
 1015 glitching pulsars fall in the $\alpha \gtrsim 5$ regime we should expect to see significant forward
 1016 cross-correlations, $\rho_+ \gtrsim 0.8$, in more pulsars, as seen in Figure 2.8. Yet only two pulsars,
 1017 PSR J0537–6910 and PSR J1341–6220 have ρ_+ significantly different from zero, at 95%
 1018 confidence. Neither of these objects favor a power-law glitch size distribution, as the
 1019 model predicts for $\alpha \gtrsim 5$. We therefore conclude provisionally that the endogenous- η
 1020 meta-model is incompatible with existing pulsar observations, although more data are

needed to be confident of course. This is an important result, because the endogenous- η meta-model codifies the traditional, popular understanding in the literature regarding how vortex pinning and unpinning occurs stochastically, as explained in Sections 2.1–2.3.

Model parameters such as α , the dimensionless control parameter that determines the speed at which stress accumulates, and K , the coupling constant between changes in stress and the observable change in frequency, may be partially informed by independent (i.e. non-glitch) observations of pulsars. As discussed in Section 3 of Melatos et al. [25], and Section 5 of Carlin and Melatos [4], we have

$$\alpha \approx \frac{X_c}{\langle \Delta t \rangle \dot{\nu}}, \quad (2.14)$$

up to a factor of order unity, where $\langle \Delta t \rangle$ is the mean waiting time between glitches, and $\dot{\nu}$ is the long-term spin-down rate of the pulsar, after correcting for glitches and timing noise. The critical stress at which a glitch becomes certain, X_c , depends on the equation of state and is unknown in general [60, 78]. Nevertheless, the denominator in Equation (2.14) varies between pulsars by many orders of magnitude; see Table 2 of Melatos et al. [25], for example. The coupling constant K has even more uncertainties surrounding it, as described in Section 2.2.3. If a linear coupling between the crust and the stress is assumed at a glitch, we recover Equation (2.5), however non-linear couplings are also plausible, and may easily change the dependence of K on observables [41, 87, 100]. A preliminary exploration of how K impacts the endogenous- η meta-model is presented in Appendix 2.A1.

Direct comparisons of the meta-model predictions to long-term statistics derived from glitch catalogues are predicated on the assumption that all glitches are detected, i.e. that the datasets are complete. Espinoza et al. [47] and Espinoza et al. [101] claimed that this assumption is true for PSR J0534+2200 and PSR0835–4510 respectively. Monte Carlo injection studies have been published which seek to quantify completeness, but they are hampered by human intervention in traditional glitch finding algorithms [48, 50]. Autonomous glitch finding algorithms, such as those based on hidden Markov models [102] and nested sampling [40, 53, 103], will probe this question quantitatively for more pulsars, especially as more pulsars are regularly timed.

2.6. CONCLUSION

The long-term predictions from meta-models of stress-relax processes are avenues to falsify otherwise plausible microphysical mechanisms that the meta-model encompasses. The SDP meta-model [2] encompasses mechanisms wherein glitches are triggered probabilistically, and are more likely to occur when the system-wide stress is higher. The falsifiable predictions such as size and waiting-time cross-correlations [25], and auto-correlations [1], depend on the functional form of the conditional avalanche size PDF, $\eta[\Delta X^{(n)}|X(t_n^-)]$ [3]. Previously, this PDF was fixed exogenously to be a power law [2, 25, 83], motivated by Gross-Pitaevskii simulations of vortex avalanches [18], and the sizes of stress-release avalanches in other self-organized critical systems [39]. However, when $\eta[\Delta X^{(n)}|X(t_n^-)]$ is a power law, the SDP meta-model does not explain the quasiperiodic waiting times and unimodal size PDF seen in some pulsars [37]. This is ameliorated

1062 by adjusting “by hand” $\eta[\Delta X^{(n)} | X(t_n^-)]$ to a unimodal distribution, whereupon the SDP
1063 meta-model remains consistent with the data [3].

1064 In this paper, we generalize the SDP meta-model so that $\eta[\Delta X^{(n)} | X(t_n^-)]$ is generated
1065 endogenously via the coherent stress mechanism [70, 73]. The coherent stress mecha-
1066 nism encapsulates the traditional understanding of how superfluid vortex pinning and
1067 unpinning proceeds stochastically in a neutron star. The memory of previous glitches is
1068 imprinted on the PDF of occupied pinning sites, $g(X_{\text{th}}, t)$, which we emphasize does not
1069 equal the distribution of available sites $\phi(X_{\text{th}})$ in general. Vortices pinned at sites with
1070 thresholds below the stress at a glitch unpin when a glitch is triggered, repinning at sites
1071 with thresholds above the stress after the glitch. The size of the glitch is proportional to
1072 the fraction of vortices unpinned in this manner.

1073 The endogenous- η meta-model produces a broad phenomenology of observable wait-
1074 ing time and size PDFs, conditional on the choice of control parameters. In all circum-
1075 stance, though, it produces high forward cross-correlations between glitch sizes and sub-
1076 sequent waiting times ($\rho_+ \gtrsim 0.8$), which are largely absent from observational data. It
1077 also predicts that either i) the system stagnates, for $X_{\text{th}, \max} \geq X_c$, or ii) there is an excess
1078 of the largest waiting times and sizes, corresponding to events which completely reset
1079 the system by unpinning all vortices. Associated with these system-resetting events are
1080 aftershocks, which are larger and occur later than an average glitch, and precursors,
1081 which are smaller than an average glitch. There is no evidence for such large, system-
1082 resetting events in the size or waiting time PDFs of any glitching pulsar. We therefore
1083 conclude provisionally that the endogenous- η version of the SDP meta-model is falsified
1084 by existing data, although more data are needed to be sure.

1085 The provisional falsification of the endogenous- η version of the SDP meta-model is
1086 important. The coherent stress process is not just any process; it embodies the tradi-
1087 tional understanding of how vortex pinning and unpinning works throughout the liter-
1088 ature [24]. Moreover it is intriguing that the version of the SDP meta-model in which
1089 $\eta[\Delta X^{(n)} | X(t_n^-)]$ is specified exogenously is not falsified by existing pulsar data. What
1090 are we to make of this situation? Is it a hint that some microphysics other than super-
1091 fluid vortex avalanches is at work? Is the success (at escaping falsification) of the
1092 SDP meta-model with exogenous $\eta[\Delta X^{(n)} | X(t_n^-)]$ thanks simply to the flexibility it af-
1093 fords, when choosing $\eta[\Delta X^{(n)} | X(t_n^-)]$ selectively to suit every individual pulsar? It is
1094 too early to say. The endogenous- η meta-model is still an idealized, phenomenological
1095 representation of what happens inside a pulsar during a superfluid vortex avalanche. For
1096 example, recent N -body point-vortex simulations of collective, glitch-like vortex motion
1097 indicates that the stress is spatially correlated [68]. Spatial correlations are notoriously
1098 hard to treat theoretically, but it is known that they can alter the observable statistics of
1099 a far-from-equilibrium system comprehensively, e.g. in self-organized critical systems
1100 [38, 39]. Larger and more complete glitch catalogs generated by the latest generation
1101 of glitch monitoring campaigns at radio wavelengths are likely to play a central role in
1102 resolving some of the physical puzzles above [103, 104].

1103 ACKNOWLEDGEMENTS

1104 Parts of this research are supported by the Australian Research Council (ARC) Centre of
1105 Excellence for Gravitational Wave Discovery (OzGrav) (project number CE170100004)

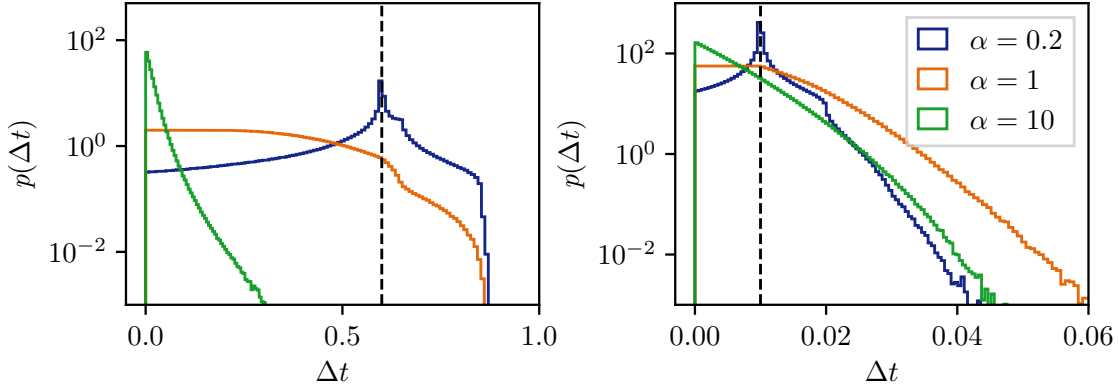


Figure 2.10: Waiting time PDFs for $K = 0.6$ (left panel) and $K = 0.01$ (right panel). Parameters: $N = 10^7$ simulated glitches for each value of α , with $X_{\text{th},\text{max}} = 0.95$. The black dashed vertical line indicates $\Delta t = K$ in each panel.

1106 and ARC Discovery Project DP170103625. JBC is supported by an Australian Postgrad-
1107 uate Award.

1108 2.A1. NON-MAXIMAL STRESS-CRUST COUPLING

1109 The coupling factor K defined in equation (2.3) and appearing in equations (2.4) and (2.5)
1110 relates changes in the stress variable X to the angular velocity $2\pi\nu$ of the crust. The
1111 long-term observables in Section 4 are predicted assuming K takes its maximum value,
1112 $X_{\text{th},\text{max}}$. Somewhat counter-intuitively, the long-term statistics do change – modestly,
1113 but meaningfully – when non-maximal coupling is considered.

1114 One always has $K \leq X_{\text{th},\text{max}}$ to ensure $X(t) \geq 0$. In Section 2.2.3, we specialize to
1115 $K = X_{\text{th},\text{max}}$ for the sake of definiteness. In this appendix we briefly check the case
1116 $K < X_{\text{th},\text{max}}$. Figure 2.10 shows the PDF of waiting times, $p(\Delta t)$, for two representative
1117 values of $K < X_{\text{th},\text{max}} = 0.95$. For $K = 0.6$, $p(\Delta t)$ looks broadly similar to the top panel of
1118 Figure 2.7 ($K = X_{\text{th},\text{max}}$), except for $\alpha = 0.2$, which no longer has a peak at $\Delta t = 1$. Long
1119 waiting times are suppressed as K sets the maximum event size in equation (2.4). Smaller
1120 K increases the minimum stress in the system, as less stress is released at the largest
1121 glitches (i.e. when $F = 1$). For $K = 0.01$ and $\alpha \gtrsim 1$, $p(\Delta t)$ is exponentially distributed.
1122 For $\alpha \lesssim 1$, $p(\Delta t)$ is peaked around $\Delta t = K$, but has an exponential tail. The size PDFs,
1123 $p(\Delta X)$, are broadly the same shape as in the bottom panel of Figure 2.7 ($K = X_{\text{th},\text{max}}$),
1124 but for $K < X_{\text{th},\text{max}}$ and $\alpha \lesssim 1$ they are more strongly peaked around $\Delta X = K$, and for
1125 $\alpha \gtrsim 1$ they are power-law distributed over many decades, with a small peak at $\Delta X = K$.
1126 In summary, if $K < X_{\text{th},\text{max}}$, in the high- α regime $p(\Delta t)$ is exponentially distributed and
1127 $p(\Delta X)$ is power-law distributed, while in the low- α regime $p(\Delta t)$ is unimodal around a
1128 peak at $\Delta t = K$ and $p(\Delta X)$ is sharply peaked at $\Delta X = K$.

1129 The behavior of the cross-correlations and autocorrelations as a function of α does
1130 not change for $K < X_{\text{th},\text{max}}$ compared to $K = X_{\text{th},\text{max}}$, beyond shifting the features seen
1131 in Figure 2.8 to the right, e.g. for $K = 0.1$ the peak in ρ_+ occurs at $\alpha \approx 10$ instead of
1132 $\alpha \approx 0.5$. Reducing K has a similar impact as reducing $X_{\text{th},\text{max}}$ on the fraction of events
1133 that completely reset the system, as shown in Figure 2.6. At a fixed α , reducing K reduces

1134 the amount of stress released. Hence we reach $X \geq X_{\text{th}, \max}$ more often by the time the
 1135 next glitch is triggered.

1136 2.A2. ENSEMBLE-AVERAGED STRESS THRESHOLD DISTRIBUTION 1137 AT OCCUPIED PINNING SITES

1138 The PDF $g(X_{\text{th}}, t)$ is a stochastically fluctuating function, dependent on the random se-
 1139 quence of waiting times drawn up to time t , as described in Section 2.2.4. A stationary
 1140 analogue, $g_s(X_{\text{th}})$, would allow for a priori prediction of long-term statistics that do not
 1141 depend on the exact time-ordered nature of events, such as $p(\Delta t)$ and $p(\Delta X)$ [70, 73].

1142 Following the notation in Daly and Porporato [105] and Fulgenzi et al. [2], $p(\Delta t)$ and
 1143 $p(\Delta X)$ are related to the PDFs $p_e(Y)dY$ and $p_s(X)dX$, the probabilities that the stress
 1144 is in $(Y, Y + dY)$ just before a glitch and in $(X, X + dX)$ just after a glitch respectively.
 1145 With these definitions we obtain

$$p(\Delta t) = \int_0^{1-\Delta t} dY p_s(Y) \lambda(Y + \Delta t) \exp[-\Lambda(Y + \Delta t) \Lambda(Y)], \quad (2.15)$$

1146 and

$$p(\Delta X) = \int_{\Delta X}^1 dY p_e(Y) \eta(\Delta X | Y), \quad (2.16)$$

1147 with $\Lambda(x) = \int_0^x dx' \lambda(x')$, and $\Delta X = Y - X$. In the endogenous- η meta-model $\eta(\Delta X | Y)$,
 1148 is a deterministic function of the occupied pinning site PDF, $g(X_{\text{th}})$, as discussed in Sec-
 1149 tion 2.2.3. The relationship becomes probabilistic again, as in the SDP meta-model, if
 1150 we consider the statistically stationary PDF, $g_s(X_{\text{th}}) = \langle g(X_{\text{th}}, t) \rangle$, where the brackets
 1151 indicate an ensemble average. The PDF $g_s(X_{\text{th}})$ is related to $\eta(\Delta X | Y)$ via

$$\eta(\Delta X | Y) = K \int_0^{p_e(Y)} dX_{\text{th}} g_s(X_{\text{th}}). \quad (2.17)$$

1152 Solving equations (2.15)–(2.17) analytically for $g_s(X_{\text{th}})$ is outside the scope of this paper.
 1153 Instead, we show an estimate of $g_s(X_{\text{th}})$ at three values of α in Figure 2.11, calculated
 1154 by running the automaton outlined in Section 2.3.2 and sampling $g(X_{\text{th}}, t)$ after every
 1155 glitch. As expected, $g_s(X_{\text{th}})$ is a strictly increasing function of X_{th} , i.e. sites with a
 1156 higher threshold are occupied more often than those with a lower threshold. For $\alpha \lesssim 1$,
 1157 $g_s(X_{\text{th}})$ is well approximated by a power law with upper and lower cut-offs, i.e. $g_s(X_{\text{th}}) \propto$
 1158 $X_{\text{th}}^\gamma H(X_{\text{th}})H(X_{\text{th}, \max} - X_{\text{th}})$, with $0 < \gamma \lesssim 3$, and γ growing with α .

1159 2.A3. RELATION TO POINT PROCESSES AND TIME SERIES MOD- 1160 ELING

1161 The endogenous- η meta-model in this paper and its exogenous- η alternatives, such as
 1162 the SDP [2] and BSA [4] meta-models, are examples of stochastic time series with jumps.

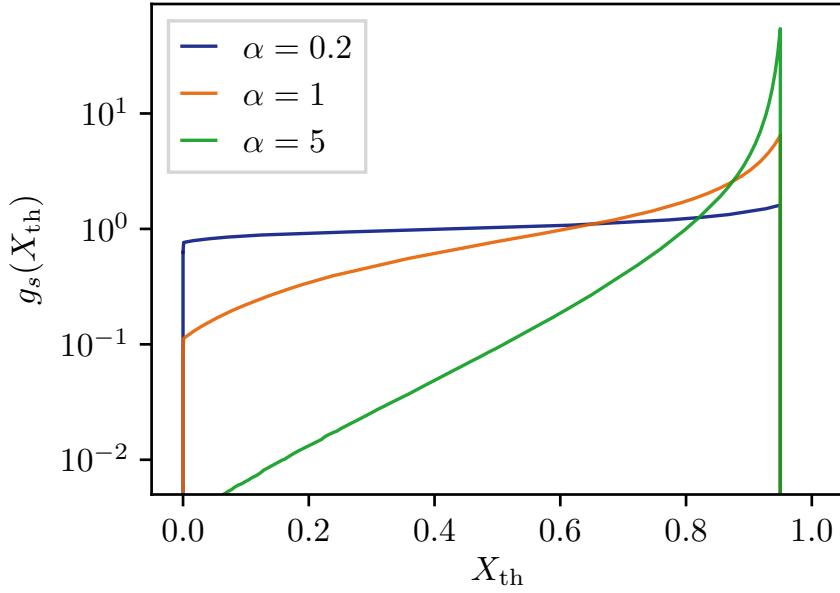


Figure 2.11: Ensemble averaged PDF of occupied pinning sites $g_s(X_{\text{th}}) = \langle g(X_{\text{th}}, t) \rangle$ calculated empirically for three values of α . Parameters: 10^7 samples of $g(X_{\text{th}})$ for each value of α , $X_{\text{th}, \max} = 0.95$, with $K = X_{\text{th}, \max}$.

We observe the jumps as a point process. In this appendix, we situate the endogenous- η meta-model within canonical classification schemes for such processes. The classification schemes are not unique.

The SDP meta-model is an example of a doubly stochastic, marked point process [2, 106, 107]. It is a one-dimensional point process because it is a sequence of instantaneous events ordered in time. Marked refers to additional information (i.e. the event size) that is associated with the epoch of each event. It is doubly stochastic as both the event sizes and the waiting times between events are random processes. The endogenous- η meta-model is not doubly stochastic, as the event sizes are deterministic, after the waiting time is chosen (given a certain history of past avalanches), as described in Section 2.2. For both the SDP and endogenous- η meta-models, the state of the system jumps discontinuously at each event making them examples of a jump process. The SDP meta-model is Markovian, the current state only depends on the immediately previous state. However the endogenous- η meta-model is not, as the threshold distribution of occupied pinning sites contains a long-lasting memory of states before the one immediately previous.

The analysis of point processes from a statistical perspective is often presented alongside time series modeling [108, 109]. Autoregressive models, such as the autoregressive integrated moving average (ARIMA) model, can be used to model a wide variety of astronomical time series data [110]. Adopting the formalism of autoregressive models unlocks a large, well-tested literature for common tasks such as maximum likelihood parameter estimation, model comparison, and model validation [109]. Recent advances in filters for hidden semi-Markov models are another intriguing avenue, as these models are explicitly designed to track a process that jumps between states at irregularly spaced intervals [111].

In this paper and others investigating glitch meta-models, we elect not to analyze

the problem in terms of autoregressive models for three reasons. i) Glitch sample sizes are small ($N \lesssim 50$), so there is no practical imperative to exploit the computational efficiency offered by autoregressive models. ii) We are motivated by the astrophysical goal of exploring the long-term statistical behavior of an automaton which formalizes directly the popular intuitive picture of glitches as a stick-slip, stress-relax phenomenon. It is possible in principle to formulate the stress-relax dynamics less directly in the language of an autoregressive model, and we leave that for future work. iii) Some work has been done on parameter estimation by Markov chain Monte Carlo methods for the SDP meta-model [83]. Extending this work to other meta-models or larger data sets may benefit from the computational efficiency of autoregressive modeling, but is outside the scope of this work.

CHAPTER 3

1200

1201 A statistical search for a uniform trigger threshold in solar
1202 flares from individual active regions

1203

1204 3.1. INTRODUCTION

1205 Broad consensus exists that the micro-physical process triggering individual solar flares
1206 is magnetic reconnection in the corona. A reconnection event becomes more likely to
1207 occur, the more magnetic energy accumulates in the time between flares [112, 113]. This
1208 phenomenological class of stress-relax model, was popularized by Rosner and Vaiana
1209 [114], and expounded by Wheatland and Glukhov [115], Wheatland [116, 117], Kanazir
1210 and Wheatland [118], and Hudson [119], among others. A complementary phenomeno-
1211 logical description is the avalanche or self-organized criticality model [120–122], in-
1212 spired by the canonical sandpiles of Bak et al. [123, 124]. These two classes of model
1213 are broadly compatible, but make different predictions about some long-term statistical
1214 observables [116, 125–129].

1215 Upon aggregating historical datasets, the probability density function (PDF) of the
1216 energy released in solar flares is found to be a power law or log-normal over multiple
1217 decades [114, 120, 130]. The PDF of time intervals between successive flares in the same
1218 active region, henceforth termed waiting times, is less clear-cut. Wheatland [131] found
1219 evidence that the power-law-like shape of the tail of the waiting time PDF found by
1220 Boffetta et al. [126] is explained by a sum of exponentials, with individual rates them-
1221 selves drawn from an exponential PDF. This interpretation is further developed by As-
1222 chwanden et al. [132]. Non-stationary flaring rates are also noted by Lepreti et al. [133]
1223 and Gorobets and Messerotti [134]. Cross-correlations between the size of a flare and
1224 the subsequent (preceding) waiting time, henceforth termed forward (backward) cross-
1225 correlations, are a key differentiator between the stress-relax and avalanche descriptions
1226 — the latter predicts no size–waiting-time cross-correlations [39]. Forward and back-
1227 ward correlations are broadly absent from solar flares datasets [116, 135–137], with the
1228 exception of strong forward cross-correlations found in two active regions [119].

1229 Rotational glitches in rotation-powered pulsars [24, 138] are an analogous astrophys-

1230 ical phenomenon to solar flares, in the limited sense that they are consistent with a
 1231 stress-relax process even though they do not involve magnetic reconnection as far as
 1232 one knows [38]. While the exact process that triggers a glitch is unknown, most models
 1233 are encompassed by the fundamental idea that “stress” (possibly differential rotation or
 1234 elastic deformation) builds up secularly between glitches, and is released sporadically
 1235 and partially at a glitch. The instantaneous glitch rate is assumed to grow with the
 1236 stress in the system. This idea is formalized phenomenologically in the state-dependent
 1237 Poisson (SDP) process popularized by Fulgenzi et al. [2]. Precise, falsifiable predictions
 1238 about size and waiting time PDFs, auto-, and cross-correlations, as well as comparisons
 1239 to current datasets, show the power and flexibility of the SDP model in the neutron star
 1240 context [1, 3, 25, 83]. The same falsifiable predictions also deliver new physical insights
 1241 when applied to solar flare data, as we show in this paper.

1242 Our goal in this paper is to search the *Geostationary Operational Environmental Satellite*
 1243 (*GOES*) soft X-ray flare database for signatures of a threshold-driven stress-relax pro-
 1244 cess. We do this by de-aggregating the data from different active regions, and studying
 1245 summary statistics of flare waiting times and sizes. In Section 3.2 we outline the SDP
 1246 framework, and how it maps to solar flares. In Section 3.3 we explore various regimes
 1247 of the SDP process. We also specify precise, falsifiable tests for the question of whether
 1248 solar flares are triggered once the energy reaches a static threshold, if it obeys a stress-
 1249 relax process. The *GOES* soft X-ray dataset to which we apply these tests is described
 1250 in Section 3.4. In Section 3.5 we look for associations between matching waiting time
 1251 and size PDFs and high size–waiting-time cross-correlations, as predicted for the SDP
 1252 process. We conclude with a discussion of the microphysical implications of the data
 1253 analysis in Section 3.6.

1254 3.2. STATE-DEPENDENT POISSON PROCESS

1255 3.2. *Equation of motion*

1256 The SDP process is a doubly stochastic renewal process which models the “stress” in the
 1257 system as a function of time, $X(t)$, as

$$X(t) = X(0) + t - \sum_{i=0}^{N(t)} \Delta X_i, \quad (3.1)$$

1258 where X and t are expressed respectively in dimensionless units of X_c (the critical stress
 1259 in the system at which a stress-release event becomes certain), and τ (the time taken
 1260 for the system to accumulate the critical stress X_c , in the absence of any stress-release
 1261 events). We attach a physical interpretation to $X(t)$ in the solar flare context in Sec-
 1262 tion 3.2.3 and Appendix 3.A1. The amount of stress released at the i -th event, ΔX_i , is
 1263 a random variable, drawn from a user-specified PDF, $\eta[\Delta X_i | X(t_i^-)]$, where $X(t_i^-)$ is the
 1264 stress in the system immediately prior to the i -th event. In the standard configuration,
 1265 $\eta[\Delta X_i | X(t_i^-)]$ is fixed as a power law, but other options exist [3, 5]. Conditioning η
 1266 on $X(t_i^-)$ is necessary to ensure that the stress remains positive-definite and is plausi-
 1267 ble physically. The second random variable in Equation (3.1) is $N(t)$, a Poisson counting

function of the number of events up to time t . It is determined iteratively via the waiting time between each event.

We assume the instantaneous event rate is a monotonically increasing function of the stress in the system, viz.

$$\lambda[X(t)] = \frac{\alpha}{1 - X(t)}, \quad (3.2)$$

where $\alpha = \lambda_0\tau$ is a dimensionless control parameter, and $\lambda_0 = \lambda(X = 1/2)/2$ is a reference rate. The long-term statistical output of the SDP process does not depend strongly on the functional form of $\lambda[X(t)]$, so long as it diverges in the limit $X \rightarrow 1$ as in Equation (3.2) [2, 3]. As the stress increases deterministically between events, the PDF of waiting times Δt following the i -th event is that of a variable-rate Poisson process [2, 89]

$$p[\Delta t | X(t_i^+)] = \lambda[X(t_i^+) + \Delta t] \exp \left\{ - \int_{t_i^+}^{t_i^+ + \Delta t} dt' \lambda[X(t')] \right\}, \quad (3.3)$$

where $X(t_i^+)$ is the stress immediately following the event at time t_i .

3.2. Monte Carlo automaton

Analytically solving the coupled equations (3.1)–(3.3) to calculate the PDFs of event waiting times or sizes is usually not feasible, except for particular choices of $\eta[\Delta X_i | X(t_i^-)]$; see section 6 of Fulgenzi et al. [2] for an example. Instead, it is simple to run the following automaton to generate numerical solutions:

1. Pick Δt from Equation (3.3), given the current stress X .
2. Update the stress to $X + \Delta t$ to account for the deterministic evolution.
3. Pick ΔX from $\eta[\Delta X | X + \Delta t]$, and subtract it from the stress.
4. Repeat from step 1.

Given α and $\eta[\Delta X_i | X(t_i^-)]$ the automaton generates a time-ordered sequence of waiting times and sizes. From the sequence we can calculate the long-term PDFs for waiting times and sizes [2, 3], as well as the cross-correlation [3, 25], autocorrelations [1], and other observables.

3.2. Mapping to solar flares

We identify the stress that accumulates between flares and relaxes at a flare with the spatially-averaged magnetic energy density in a given active region. One could equally choose a different physical quantity, such as the magnetic shear, depending on the particular microphysics of the flare trigger. We assume that active regions have independent stress reservoirs, i.e. the coronal magnetic fields of different active regions do not interact strongly, and all flares from the same active region extract energy from one reservoir. An idealized toy model relating the foregoing definition of stress to magnetic energy

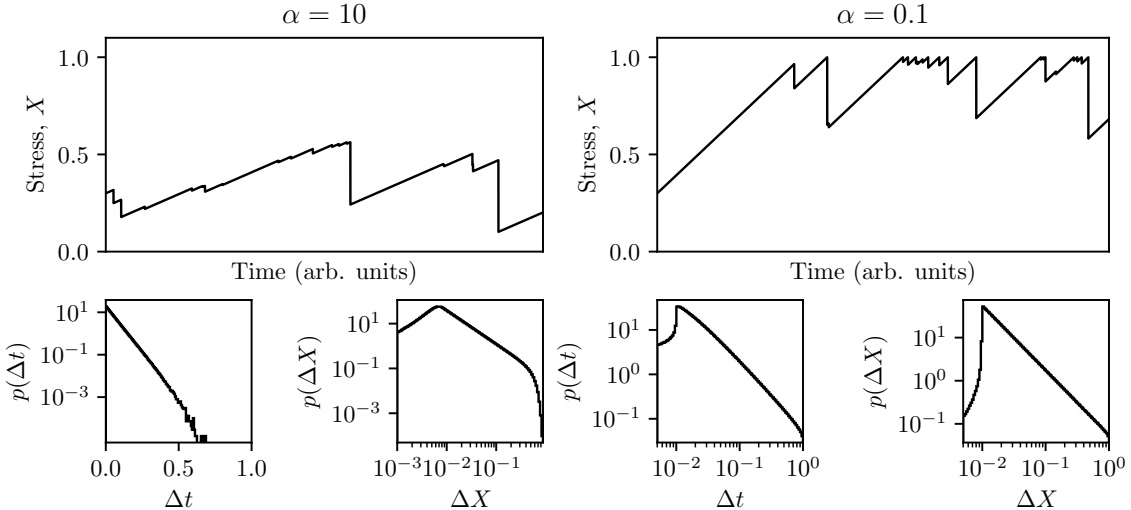


Figure 3.1: Top panels: qualitative behavior of the evolution of the stress, $X(t)$, in the SDP process in the two main regimes, slowly driven (left panel, $\alpha = 10$), and rapidly driven (right panel, $\alpha = 0.1$). Bottom panels: predicted waiting time and size PDFs $p(\Delta t)$ and $p(\Delta X)$ respectively in the above regimes. For all panels we fix $\eta[\Delta X_i | X(t_i^-)] \propto (\Delta X_i)^{-3/2} H[\Delta X_i - 10^{-2} X(t_i^-)]$, where the Heaviside function $H(...)$ enforces a minimum stress-release size of 1% of the stress in the system, ensuring integrability. The histograms in the bottom panels each include $N = 10^7$ events.

input from the photosphere is outlined in Appendix 3.A1, as a simplified but concrete illustration of the physical picture under consideration.

Two major simplifying assumptions are that the rate at which energy is fed into the reservoir, τ^{-1} , is constant in time, and so is the critical, spatially-averaged magnetic energy density, X_c , for a given active region. These assumptions are motivated in Appendix 3.A1, but a key goal of the paper is to test their veracity. We also assume that flares reduce $X(t)$ instantaneously. This assumption is defensible as the typical time between flares (typically hours) is much larger than the typical duration of flaring events (typically minutes) [139]. In what follows we do not prescribe a particular functional form for $\eta[\Delta X_i | X(t_i^-)]$, to keep the SDP process as flexible as possible.

The SDP process generates sequences of dimensionless waiting times, $\{\Delta t_i^{\text{SDP}}\}$ and sizes, $\{\Delta X_i^{\text{SDP}}\}$. It is natural to ask how they correspond to directly observable sequences of waiting times, $\{\Delta t_i^{\text{obs}}\}$ and sizes, $\{\Delta s_i\}$. The waiting times satisfy

$$\Delta t_i^{\text{obs}} = \Delta t_i^{\text{SDP}} \tau, \quad (3.4)$$

where τ is unknown a priori but can be estimated, as discussed in Appendix 3.A2. The sizes are related in a more complicated way, because some energy is released through channels that are not directly observed. We make the simplifying assumption that the peak soft X-ray flux multiplied by the duration of the flare (henceforth Δs_i for the i -th flare in a given active region) is proportional to the stress released from the reservoir. This implies

$$\Delta s_i \propto \Delta X_i^{\text{SDP}} X_c. \quad (3.5)$$

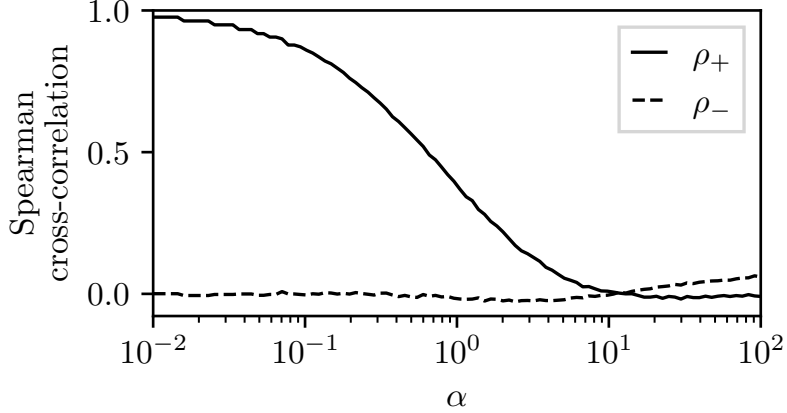


Figure 3.2: Forward, ρ_+ (solid curve), and backward, ρ_- (dashed curve), cross-correlations between event sizes and waiting times for 10^2 values of $10^{-2} \leq \alpha \leq 10^2$, with $N = 10^5$ events generated per value of α . We fix $\eta[\Delta X_i | X(t_i^-)]$ to the same functional form as in Figure 3.1. A version of this figure first appeared as figure 13 in Fulgenzi et al. [2].

1319 The unknown constant of proportionality in Equation (3.5) hampers direct parameter
 1320 estimation of X_c from an observed size PDF.

1321 Full parameter estimation for the SDP process given a set of observed waiting times
 1322 and sizes is discussed in Melatos and Drummond [83]. It lies outside the scope of this
 1323 paper. In Appendix 3.A2 we also describe for completeness an alternative parameter
 1324 estimation procedure using a hierarchical Bayesian scheme. The advantage of the hier-
 1325 archical scheme is that it clarifies as a matter of principle the information content and
 1326 flow in the estimation problem, i.e. the parameter combinations that can be estimated
 1327 uniquely, and the data components that inform each parameter estimate. The disad-
 1328 vantage is that it can be implemented in practice only if $\eta[\Delta X_i | X(t_i^-)]$ is drawn from
 1329 a certain class of mathematical functions. The favored class produces waiting time and
 1330 size PDFs which do not match solar flare observations (see Section 3.5), so the hierar-
 1331 chical scheme is not applied to real data in this paper. Nonetheless, it is included for the
 1332 benefit of the reader, who may wish to develop it further for solar flare analysis in the
 1333 future.

1334 3.3. OBSERVABLE SIGNATURES OF A RAPIDLY-DRIVEN PROCESS

1335 Broadly speaking, an SDP process operates in one of two regimes: slowly-driven, with
 1336 $\alpha \gg 1$, and rapidly-driven, with $\alpha \ll 1$. In this section we identify the key dynamics in
 1337 both regimes, in Sections 3.3.1 and 3.3.2 respectively. We then infer, in Section 3.3.3, a
 1338 set of observable signatures, which if absent rule out the operation of a rapidly-driven
 1339 process of the form described in Section 3.3.2.

1340 3.3. *Slow driver*

1341 When the system is slowly driven, we have $X(t) \ll 1$, as events are usually triggered
1342 before the stress accumulates to near the threshold. When $\eta[\Delta X_i | X(t_i^-)]$ is a power
1343 law, the predicted waiting time PDF $p(\Delta t)$ is an exponential, and the predicted size PDF
1344 $p(\Delta X)$ is a power law over multiple decades. We show the qualitative behavior of the
1345 stress in the slowly driven regime in the top-left panel of Figure 3.1, where for the se-
1346 quence of 20 stress-release events shown we have $0.1 < X(t) < 0.6$. In the bottom-left
1347 panels of the same figure we show the predicted waiting time and size PDFs. The size
1348 PDF $p(\Delta X)$ has a turn-over in logarithmic slope at $\Delta X \approx 10^{-2}$ due to the particular
1349 choice of $\eta[\Delta X_i | X(t_i^-)]$ (see caption for the functional form).

1350 Depending on the choice of $\eta[\Delta X_i | X(t_i^-)]$, there may be detectable backward cross-
1351 correlations (i.e. a correlation between the size of an event and the waiting time since
1352 the preceding event). This is because the size of an event cannot exceed the amount of
1353 stress in the system, so longer periods of stress-accumulation allow for the possibility of
1354 larger events. This backward cross-correlation is especially pronounced with the choice
1355 $\eta[\Delta X_i | X(t_i^-)] \propto \delta[\Delta X - X(t_i^-)]$, where $\delta(\dots)$ is the Dirac-delta function. This choice
1356 forces the stress reservoir to empty at each event, and collapses the SDP process to
1357 other stochastic processes in the literature, e.g. forest fire models [140]. In the solar flare
1358 context, a backward cross-correlation is a long-standing prediction of the Rosner and
1359 Vaiana [114] stress build-up model; and the “reset” model of Hudson [119] and Hudson
1360 et al. [136]. If instead $\eta[\Delta X_i | X(t_i^-)]$ prefers small stress-release events, e.g. if it is a
1361 power law [2], the backward cross-correlation is small.

1362 3.3. *Fast driver*

1363 When the system is rapidly driven, we have $X(t_i^-) \lesssim 1$, i.e. the stress is driven close to
1364 the threshold before each event. As the dynamics of the system are strongly influenced
1365 by the presence of the threshold, we sometimes call this regime “threshold-driven”. A
1366 prediction of the SDP process in this regime is that the size and waiting time PDFs should
1367 “match”, i.e. they should be the same distribution, up to a linear scaling [2]. For example,
1368 if $\eta[\Delta X_i | X(t_i^-)]$ is a power law, both the waiting time and size PDFs are power laws. We
1369 show this in the bottom-right panels of Figure 3.1. We also show the qualitative behavior
1370 of the stress versus time in this regime in the top-right panel of the same figure, where
1371 we see $X(t) \rightarrow 1$ (i.e. unit critical stress) before every stress-release event.

1372 A strong forward cross-correlation (i.e. a correlation between the size of an event
1373 and the waiting time to the next event) is observed in this regime. This is because a
1374 large stress-release event results in a longer delay before the system accumulates enough
1375 stress to approach the threshold. In the solar flares context, this cross-correlation is
1376 predicted by the “saturation” model of Hudson et al. [136] and Hudson [119]. The smooth
1377 transition between the fast-driven regime ($\alpha \ll 1$), with high forward cross-correlations,
1378 and the slow-driven regime ($\alpha \gg 1$), is shown in Figure 3.2.

1379 3.3. *Heuristic test for a threshold-driven process*

1380 Ideally, we fit the parameters of the SDP process (τ , X_c , λ_0 , and $\eta[\Delta X_i | X(t_i^-)]$) to a
1381 paired sequence of solar flare sizes and waiting times, and infer what regime applies. In
1382 practice, however, at least some of these parameters vary between active regions, which
1383 limits us to sequences of length $N \lesssim 50$ (typical active regions have at most dozens of
1384 events; see Section 3.4), which are insufficient to infer four or more parameters. Instead,
1385 we combine the results in Sections 3.3.1 and 3.3.2 to deduce qualitative features, which
1386 must be present in multiple observables simultaneously (e.g. PDFs, cross-correlations), if
1387 the SDP process operates in a particular α regime or indeed operates at all. Specifically,
1388 we summarize the behavior in Sections 3.3.1 and 3.3.2 into the following observation-
1389 ally testable prediction. If solar flares are well-modeled with a rapidly-driven process
1390 (e.g. the SDP process with $\alpha \ll 1$), then we should see large forward cross-correlations,
1391 accompanied by waiting time and size PDFs with the same shape in individual active
1392 regions. This coincident signature should become more prominent as α (or a proxy
1393 thereof) decreases. We quantify this prediction in Section 3.5.2.

1394 With the test above we also ameliorate the impact of a potentially mis-specified
1395 model. Although it is agnostic about the microphysics, the SDP process is not the only
1396 possible prescription of stress accumulation and release. If some of the assumptions
1397 outlined in Section 3.2.3 do not hold, a different underlying model may underpin solar
1398 flares. For example, one may build a model in which stress accumulates according to
1399 a Brownian random walk with some underlying drift, until a threshold is breached, at
1400 which point a stress-release event is triggered [4]. In the Brownian stress accumulation
1401 model, $X(t)$ is always driven to the threshold before each event. If drift occurs faster
1402 than diffusion, we predict the same coincident signature as for the SDP process: large
1403 forward cross-correlations are accompanied by matching waiting time and size PDFs.

1404 3.4. *GOES SOFT X-RAY OBSERVATIONS*

1405 The X-ray Sensor (XRS) on the *Geostationary Operational Environmental Satellites* (GOES)
1406 has continuously monitored the Sun in soft X-rays (0.5 to 8 Å) since 1975. In Section 3.4.1
1407 we introduce the flare summary data analyzed in this paper. In Section 3.4.2 we remind
1408 the reader of the obscuration effect described in Wheatland [141], and explain how it
1409 affects our analysis. In Section 3.4.3 we analyze aggregated waiting time and size PDFs
1410 across all active regions.

1411 3.4. *Flare data*

1412 We use the publicly available flare summary data hosted by the National Geophysical
1413 Data Center (NGDC)¹ for flares before June 29 2015, and by the Space Weather Prediction
1414 Center (SWPC)² for flares after June 28 2015. We combine these two data sources into a
1415 homogeneous, cleaned database (henceforth “catalog”), with some anomalies corrected
1416 as described in Appendix 3.A3. These data are collated with the flare start epochs, t^s ,

¹<ftp://ftp.ngdc.noaa.gov/STP/space-weather/solar-data/solar-features/solar-flares/x-rays/GOES/xrs/>

²<ftp://ftp.swpc.noaa.gov/pub/indices/events/>

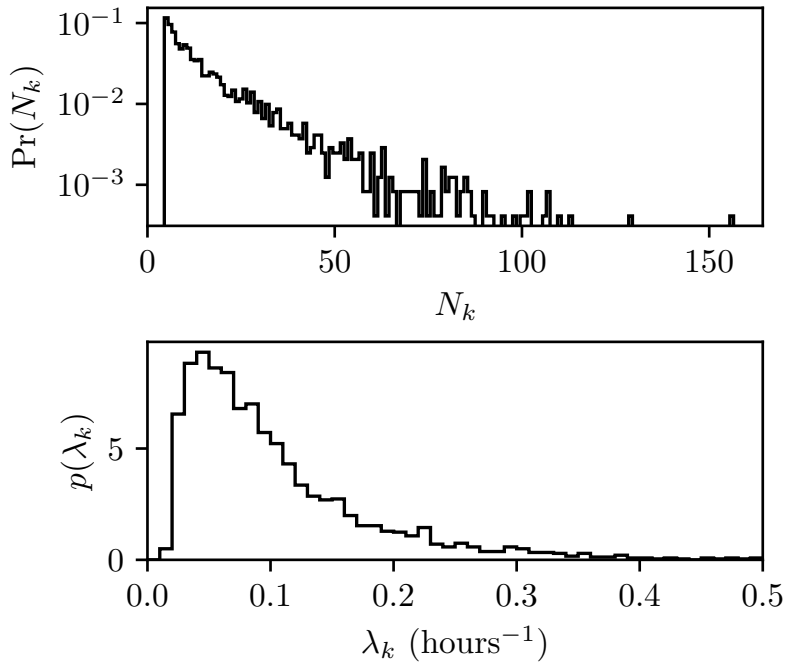


Figure 3.3: Top panel: Probability mass function of the number of flares per active region, N_k , for all active regions with $N_k \geq 5$. Regions with $0 \leq N_k \leq 4$ are excluded, as the number of samples per region is too small for the statistical tests in this paper. Bottom panel: PDF of the flare rate, λ_k , for all active regions with $N_k \geq 5$, binned into 50 uniformly spaced bins between 0 hours $^{-1}$ and 0.5 hours $^{-1}$.

peak epochs, t^P , and end epochs, t^e . The peak flux (irradiance) of each flare, f^P , is calculated with reference to the recorded flare class, in units of W m $^{-2}$. The longitude and latitude of the flare are also often available, if the flare is associated with an active region. For clarity, we henceforth denote as $x_{i,k}$ an arbitrary measurement of the variable x in the i -th flare from the k -th active region.

We define the waiting time between two flare epochs as $\Delta t_{i,k} = t_{i+1,k}^s - t_{i,k}^s$. One could equally use the flare peak or end epochs to define the waiting time. We define the flare size as $\Delta s_{i,k} = f_{i,k}^P (t_{i,k}^e - t_{i,k}^s)$; that is, we multiply the irradiance by the duration of the flare to obtain a flare size with dimensions of energy per unit area. The duration of an active region is $\Delta T_k = t_{N_k,k}^e - t_{1,k}^s$, where there are N_k flares in the region. The average flare rate in an active region is $\lambda_k = N_k / \Delta T_k$. The average λ_k overestimates systematically the true flare rate, as the duration ΔT_k is between two flare epochs, both of which are counted in N_k . An unbiased estimate would take ΔT_k as the difference between the epochs when the active region appears and disappears, but neither epoch is recorded in the GOES flare summary data³. A concern we touch on further in Section 3.4.3 is that $\lambda_k = N_k / \Delta T_k$ assumes that the flare catalog is complete, i.e. all flares from a given region are detected and correctly attributed to that region.

As of September 1 2022, there are 83283 flares in the catalog, 49328 of which are associated with an active region. There are 2429 active regions with $N_k \geq 5$, accounting

³The epochs when the active region appears and disappears may be extracted from other records in some instances. Such an analysis lies outside the scope of this paper.

for 42982 flares. The median number of flares in an active region (when considering only regions with $N_k \geq 5$) is 12, but the average is 17.7, as the distribution is peaked at $N_k = 5$ and monotonically decreases with N_k . We show the probability mass function of the number of flares in an active region, $\text{Pr}(N_k)$, in the top panel of Figure 3.3 for regions with $N_k \geq 5$. The PDF of observed flare rates, $p(\lambda_k)$, across all active regions with $N_k \geq 5$, is displayed in the bottom panel of the same figure. The distribution of λ_k is well-described by a log-normal, with mean 0.08 hours⁻¹, and standard deviation 0.7 hours⁻¹. Henceforth, we typically only include regions with $N_k \geq 5$ in our analysis unless stated otherwise, as many of the subsequent statistical tests, such as the cross-correlation(s), have low statistical power with smaller sample sizes.

3.4. Obscuration of subsequent flares after a large flare

As described in section 2.2 of Wheatland [141], the GOES flare detection algorithm involves a selection effect that obscures the detection of flares following a large flare, due to the enhanced background soft X-ray flux. To detect a flare, the flux must monotonically increase for four consecutive minutes, with the last value 1.4 times the value three minutes earlier. Hence a flare must produce a 40% increase above the background flux. However, while flares typically rise rapidly to peak flux, the soft X-ray emission is observed to decay on the timescales of hours [113]. Thus, even large flares may be obscured by the enhanced background flux following, say, an X1 ($f^P = 10^{-4} \text{ W m}^{-2}$) class flare.

A comprehensive re-analysis of the soft X-ray flux time-series may reveal flares that were not detected with the original flare detection algorithm. Such a re-analysis lies outside the scope of this paper. Acknowledging that the GOES catalog is incomplete, we mitigate the impact on our analysis by creating a secondary masked catalog that only includes flares with $f^P \geq 10^{-6} \text{ W m}^{-2}$ (i.e. class C1 and higher), where we know the fraction of missed flares is smaller. This masked catalog is used in Sections 3.4.3 and 3.5.1 when we perform comparative studies and parametric fits for the waiting time and size PDFs.

3.4. Aggregate size and waiting time statistics

When we aggregate flare waiting times and sizes across all active regions with $N_k \geq 5$, we obtain the PDFs shown in the top and bottom panels of Figure 3.4 respectively. The data are shown as the black histograms. The grey region in the bottom panel shows the flare sizes that are not included in the masked catalog, as described in Section 3.4.2. The difference between the masked and full catalog is not visible in the top panel as the effect on $p(\Delta t)$ is minimal.

Three empirical trial distributions with common analytic forms are overlaid on each PDF for the masked catalog. The overlaid distributions have parameters fixed to their maximum likelihood values, given the data. By eye, it is clear that the log-normal distribution best describes both the aggregated waiting time PDF, $p(\Delta t)$, and the aggregated size PDF, $p(\Delta s)$. We formalize this comparison using the corrected Akaike Information Criterion (AICc) [43, 142]. The AICc calculates the model, among a set of possible models, which minimizes the information loss, while accounting for potential bias due to the number of model parameters and the sample size. When calculated for $p(\Delta t)$, the

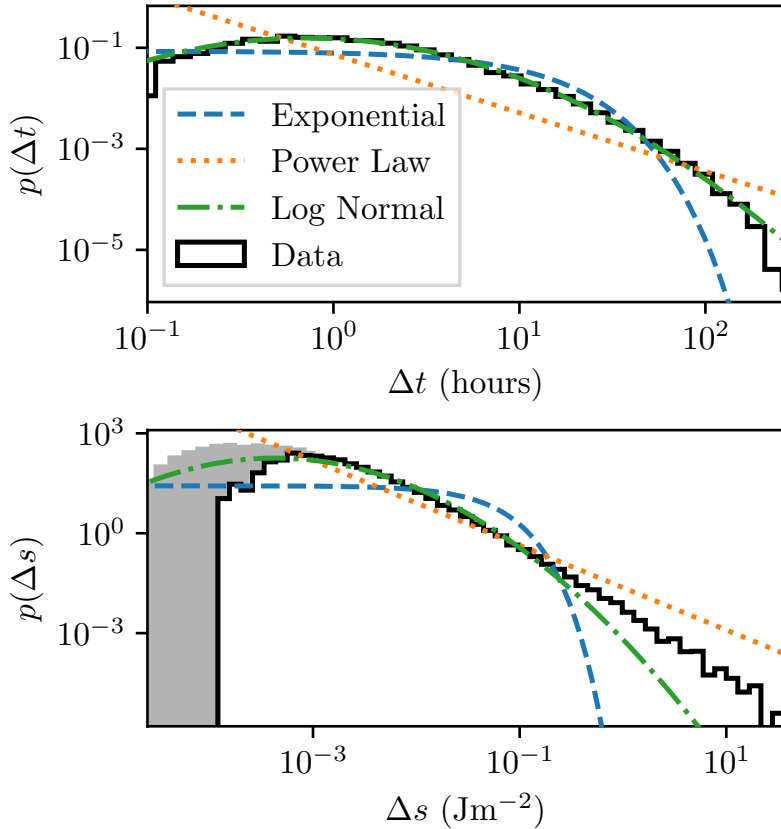


Figure 3.4: Top panel: PDF $p(\Delta t)$ of waiting times (thick black stepped curve), Δt , aggregated over all active regions with $N_k \geq 5$, binned into 50 logarithmically spaced bins between the minimum and maximum Δt in the full, unmasked catalog. Overlaid are the best fit estimates of an exponential (blue dashed curve), power law (orange dotted curve), and log-normal (green dot-dashed curve) PDF. Bottom panel: As for top panel, but for sizes Δs . The grey region in the bottom panel shows the difference between the size PDFs from the masked and full catalogs (see Section 3.4.2).

relative probability for a log-normal describing the data over an exponential or a power law is $e^{4 \times 10^3}$ and $e^{3 \times 10^4}$ respectively. When calculated for $p(\Delta s)$, the relative probability for a log-normal describing the data over an exponential or a power law is $e^{4 \times 10^4}$ and $e^{1 \times 10^4}$ respectively. The preference the data show for a log-normal over a power law is also noted in Verbeeck et al. [130]. The preference arises because of the small number of flares in the masked catalog with $10^{-4} < \Delta s / \text{J m}^{-2} \lesssim 10^{-3}$. If we fit the full, unmasked catalog (i.e. include the flares shaded in grey in the bottom panel of Figure 3.4) we find that $p(\Delta s)$ is again fitted best with a log-normal. If instead we only include flares with $\Delta s \geq 10^{-3} \text{ J m}^{-2}$ we find that $p(\Delta s)$ is fitted best with a power law.

If we assume that the same α and $\eta[\Delta X_i | X(t_i^-)]$ apply to all regions, Figure 3.4 is consistent with the SDP framework for $\alpha \lesssim 10$ and if $\eta[\Delta X_i | X(t_i^-)]$ is a log-normal. However, as we discuss in Section 3.2.3, there is good reason to believe that α (and perhaps even $\eta[\Delta X_i | X(t_i^-)]$) may vary region-to-region.

1491 3.5. DISAGGREGATED DATA IN INDIVIDUAL ACTIVE REGIONS

1492 The goal of this section is to search for signatures of a threshold-driven SDP process in
1493 individual active regions, rather than considering all flares in aggregate. In Section 3.5.1
1494 we consider only waiting time and size PDFs, without regard to their potential cross-
1495 correlation. In Section 3.5.2 we calculate these cross-correlations, and in Section 3.5.3 we
1496 apply the test outlined in Section 3.3.3 by searching for an association between matching
1497 waiting time and size PDFs and the cross-correlation, in individual active regions. In
1498 Section 3.5.4 we perform a preliminary investigation of the longer-term memory in the
1499 system by calculating the autocorrelation between subsequent waiting times and sub-
1500 sequent sizes. The analysis in Section 3.5.1 involves parametric fitting of the size PDFs,
1501 so we use the masked catalog described in Section 3.4.2. However in Sections 3.5.2–
1502 3.5.4 we use the full, unmasked catalog, as the tests performed in these sections are
1503 non-parametric.

1504 3.5. *Waiting time and size PDFs versus flare rate*

1505 For regions with $N_k \geq 5$ we disaggregate the data, and ask what PDF shape best char-
1506 acterizes each region’s waiting time and size PDFs, rather than considering only the
1507 aggregated dataset as in Section 3.4.3. Using the AICc, we find that for waiting time
1508 PDFs, 60% of regions are fitted best with an exponential distribution, 23% with a log-
1509 normal, and the remainder with a power law. For size PDFs, 41% of regions are fitted
1510 best with a power law distribution, 34% with an exponential, and the remainder with a
1511 log-normal. This is broadly consistent with the aggregate results above, i.e. that the ag-
1512 gregated $p(\Delta t)$ is fitted best with a log-normal, while the aggregated $p(\Delta s)$ is fitted best
1513 with either a log-normal or a power law, depending on how you attempt to mitigate the
1514 selection effect described in Section 3.4.2. However individual regions can occasionally
1515 be better represented with power law or exponential distributions, especially in regions
1516 with lower N_k .

1517 One may reasonably ask whether there are clear trends, or predictors, for the waiting
1518 time and size PDFs in any given region. An exhaustive search for predictors, e.g. with
1519 a multiple regression analysis, lies outside the scope of this paper, but one sensible first
1520 step is to see if the shape that fits best evolves with λ_k . This test is performed for the
1521 waiting time and size PDFs in the top and bottom panels of Figure 3.5 respectively. This
1522 figure is constructed by binning all active regions with $N_k \geq 5$ into 20 uniformly spaced
1523 bins between $\lambda_k = 0.025 \text{ hours}^{-1}$ and $\lambda_k = 0.3 \text{ hours}^{-1}$, then calculating which distri-
1524 bution fits best the waiting times and sizes using the AICc. For the waiting time PDFs,
1525 the proportion of regions fitted best with a power law stays roughly constant as λ_k in-
1526 creases, at around 15%, while the proportion of regions fitted best with a log-normal
1527 grows with λ_k , at the expense of the exponential. For the size PDFs we see a similar
1528 trend, with the proportion of regions fitted best with a power law staying roughly con-
1529 stant as λ_k increases, this time at around 40%, while the proportion of regions fitted best
1530 with a log-normal grows with λ_k , at the expense of the exponential. In both panels we
1531 plot the cumulative distribution function (CDF) of λ_k to remind the reader that each
1532 λ_k bin does not contain the same number of regions; 80% of regions with $N_k \geq 5$ have
1533 $0.033 < \lambda_k < 0.21$.

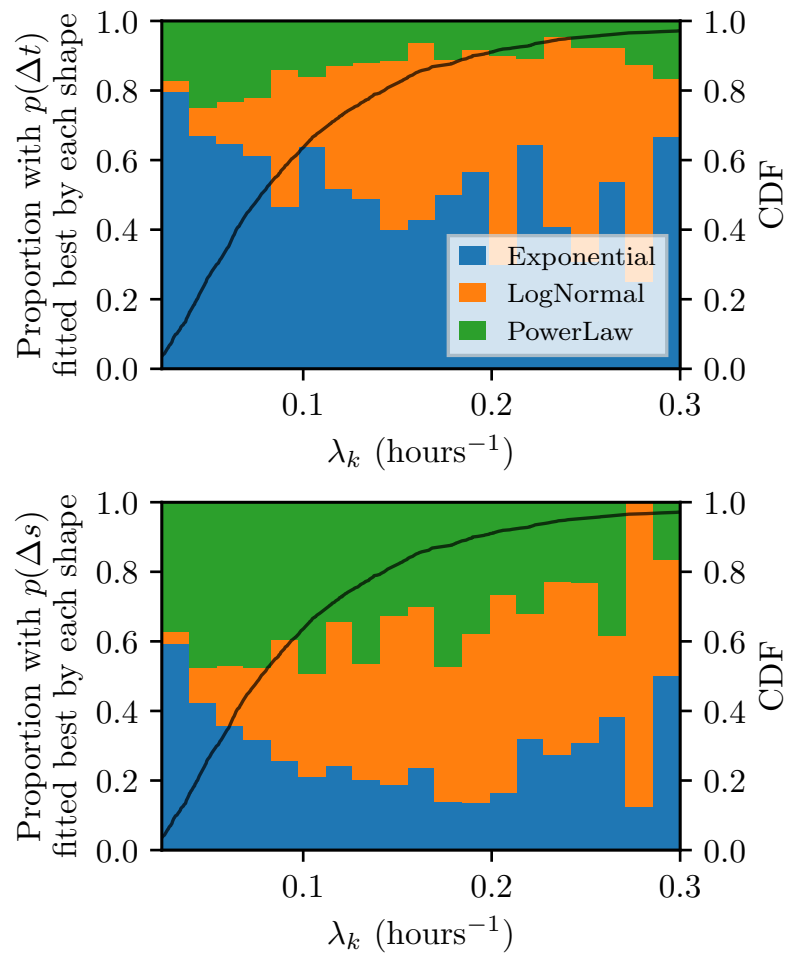


Figure 3.5: Top panel: Proportion of active regions with waiting time PDF fitted best by three possible shapes (a power law, an exponential, and a log-normal) as determined by the AICc, as a function of the region's flare rate, λ_k . The CDF of λ_k is overlaid in black. Bottom panel: As in the top panel, but for size PDFs.

1534 Can the evolution of the proportion of each shape versus λ_k be explained with the
 1535 SDP model? Under the assumption that λ_k is a tracer of the driving rate, i.e. $\lambda_k \propto \alpha^{-1}$,
 1536 we expect to see a greater proportion of exponentially distributed waiting times at low
 1537 λ_k (high α). This is the regime in which the stress does not approach the threshold at
 1538 $X = X_c$ before each event, so waiting times are un-correlated with sizes and are (broadly)
 1539 Poissonian, i.e. the waiting times are exponentially distributed. This expectation broadly
 1540 conforms with what we see in the top panel of Figure 3.5.

1541 The evolution versus λ_k in the bottom panel of Figure 3.5 is harder to explain with
 1542 the SDP model, if each region has the same $\eta [\Delta X_i | X(t_i^-)]$. We expect $p(\Delta s) \propto \eta$, when
 1543 α is low, but we see an almost even split between the three possible shapes at the highest
 1544 values of λ_k . This implies at least one of the following: i) η truly varies from one region
 1545 to the next, which implies different stress-release mechanisms are at play in different
 1546 regions; or ii) $\lambda_k \gtrsim 0.2 \text{ hours}^{-1}$ does not correspond to $\alpha \ll 1$, and hence $p(\Delta s) \propto \eta$; or
 1547 iii) the small sample size of events in each region results in the AICc not favoring the
 1548 “true” size distribution; or iv) the obscuration effect described in Section 3.4.2 is stronger
 1549 with higher λ_k , due to the enhanced background flux in regions that have many flares in
 1550 a short period of time. To test iii), we generate Figure 3.5 again for regions with $N_k \geq 10$,
 1551 instead of $N_k \geq 5$. For both the waiting times and sizes, the proportion fitted best by
 1552 an exponential drops by $\sim 10\%$ in each λ_k bin, while the proportion fitted best by a
 1553 log-normal increases. Qualitatively, however, the evolution with λ_k remains consistent
 1554 with what is seen in Figure 3.5.

1555 3.5. Size–waiting-time cross-correlations

1556 The correlation between flare sizes and subsequent waiting times, i.e. the “forward”
 1557 cross-correlation, is denoted as $\rho_{+,k}$, while the correlation between flare sizes and the
 1558 preceding waiting times, i.e. the “backward” cross-correlation, is denoted as $\rho_{-,k}$. We
 1559 calculate these correlations using the Spearman correlation coefficient [143].

1560 The PDFs of forward and backward cross-correlations measured in all active regions
 1561 with $N_k \geq 5$ are displayed in the top panel of Figure 3.6. The PDFs are broad, mostly
 1562 because the median N_k is 12 (i.e. small). However, $p(\rho_{+,k})$ and $p(\rho_{-,k})$ are different; the
 1563 latter has a median of $\rho_{-,k} = -0.02$, while the former has a median of $\rho_{+,k} = 0.10$. A
 1564 Kolmogorov-Smirnov (KS) two-sample test provides quantitative evidence of the differ-
 1565 ence, returning a p -value of 10^{-28} .

1566 The SDP process predicts a high forward cross-correlation for $\alpha \ll 1$, as discussed in
 1567 Section 3.3.2. The data neither show evidence in favor of nor against such a correlation.
 1568 In the bottom panel of Figure 3.6 we do not see a clear visual trend between $\rho_{+,k}$ and
 1569 λ_k (for regions with $N_k \geq 10$), although a Spearman correlation test returns a small but
 1570 non-zero correlation of 8×10^{-2} (p -value of 2×10^{-3}). We remind the reader that both
 1571 $\rho_{+,k}$ and λ_k are empirical estimates for each active region, and the number of events per
 1572 region is small. We do not plot uncertainties in the bottom panel of Figure 3.6, but they
 1573 are typically comparable to the central value. These results imply that either i) all active
 1574 regions have $\alpha \gtrsim 1$, where no forward cross-correlation is expected, i.e. $\lambda_k \gtrsim 0.2 \text{ hours}^{-1}$
 1575 does not correspond to the threshold-limited regime; or ii) some active regions have
 1576 $\alpha \ll 1$, but either the trigger threshold or the driving rate is not constant with time,
 1577 i.e. the random process triggering flares does not conform to the assumptions made in

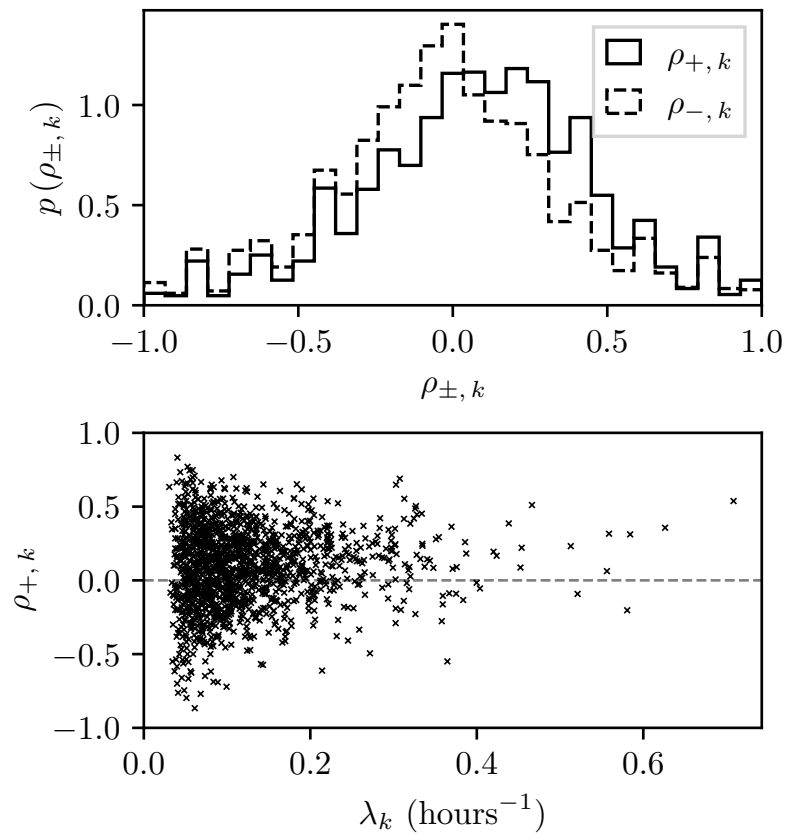


Figure 3.6: Top panel: PDF of forward cross-correlation, $\rho_{+, k}$ (black stepped curve), and backward cross-correlation, $\rho_{-, k}$ (black dashed curve), for all active regions with $N_k \geq 5$. Data binned into 30 uniformly spaced bins between $\rho_{\pm, k} = -1$ and $\rho_{\pm, k} = 1$. Bottom panel: Scatter plot of the forward cross-correlation, $\rho_{+, k}$, and flare rate, λ_k , for all regions with $N_k \geq 10$. The dashed grey line corresponds to $\rho_{+, k} = 0$.

1578 the SDP framework.

1579 As described in Section 3.4.2 the *GOES* catalog is not complete, i.e. while a given
1580 active region is visible, not all flares that occur are recorded. Wheatland [116] noted
1581 that the obscuration in Section 3.4.2 creates an artificial forward cross-correlation, which
1582 explains why the median $\rho_{+,k}$ is positive.

1583 3.5. Matching the shapes of the waiting time and size PDFs

1584 Another way to probe these data is to ask whether regions with relatively high $\rho_{+,k}$
1585 exhibit “matching” functional forms for $p(\Delta t)$ and $p(\Delta s)$, as the SDP model predicts
1586 for $\alpha \lesssim 1$. We quantify the degree to which the PDFs match via the p -value \mathcal{M}_k of
1587 the KS two-sample test applied to the sampled PDFs, $\{\Delta t_{i,k}\}$ and $\{\Delta s_{i,k}\}$. To calibrate,
1588 we perform a Monte Carlo simulation using sequences of events drawn from the SDP
1589 model. For each value of α we simulate 10^5 “regions”. For each region we generate
1590 M events, where M is a random number drawn from $p(N_k)$, restricted to values $N_k \geq$
1591 10, as empirically measured for the *GOES* regions (the distribution for $N_k \geq 5$ shown
1592 in Figure 3.3). From these M events we calculate summary statistics, e.g. \mathcal{M} and ρ_+ .
1593 This results in 10^5 pairs of (\mathcal{M}, ρ_+) , from which we construct a two-dimensional kernel
1594 density estimate (KDE) [144]. The KDE estimates the true joint PDF $p(\mathcal{M}, \rho_+)$, and is
1595 qualitatively equivalent to a smoothed, two-dimensional histogram.

1596 The result of this procedure for four values of α is shown in the top panel of Figure
1597 3.7. For $\alpha = 0.01$ (dark orange lines) the 10% and 50% credible interval contours are
1598 invisible in the top-right corner of the panel, as the vast majority of simulated regions
1599 have $\rho_+ \approx 1$ and $\mathcal{M} \approx 1$. For $\alpha = 0.1$ the KDE spreads out slightly, with the 50% credible
1600 interval reaching $\rho_+ \approx 0.8$ and $\mathcal{M} \approx 0.9$. For $\alpha = 1$, the PDF shifts such that the 50%
1601 credible interval contour stretches from $\mathcal{M} = 1$ to $\mathcal{M} \approx 0.8$, while we have $0 \lesssim \rho_+ \lesssim 0.8$.
1602 For $\alpha = 10$ we find ρ_+ centered around zero, while the 50% credible interval of \mathcal{M} ex-
1603 tends to $\mathcal{M} \approx 0.3$. The bottom panel of Figure 3.7 repeats the exercise for the backward
1604 cross-correlation. It confirms that ρ_- and \mathcal{M} are uncorrelated, as predicted elsewhere
1605 [1–3]. Integrating over ρ_\pm the reader would find that the marginal distribution of \mathcal{M} is
1606 broad in both panels, for $\alpha \gtrsim 1$, as it is difficult to confidently reject the null hypothesis
1607 that two sets of samples are from the same distribution, when dealing with small sample
1608 sizes.

1609 Monte Carlo calibration in hand, we present the equivalent data for all regions in
1610 the *GOES* catalog with $N_k \geq 10$ in Figure 3.8. To compute \mathcal{M}_k for each region we first
1611 normalize both the waiting times and the sizes by their respective means for that re-
1612 gion, before applying the KS two-sample test. In the top (bottom) panel we see no clear
1613 relationship between $\rho_{+,k}$ ($\rho_{-,k}$) and \mathcal{M}_k . Marginalizing over \mathcal{M}_k we recover the PDFs
1614 of $\rho_{+,k}$ and $\rho_{-,k}$, shown in the top panel of Figure 3.6. If, for the sake of argument, we
1615 assume that all regions have the same value of α , we can compare the KDEs in Figure 3.8
1616 to those in Figure 3.7. Under this assumption we are pushed into the regime $1 \lesssim \alpha \lesssim 10$,
1617 as the $p(\rho_{+,k}, \mathcal{M}_k)$ KDE is slightly off-set from the horizontal axis (i.e. median $\rho_{+,k} > 0$),
1618 but the 50% credible interval for \mathcal{M}_k only extends to $\mathcal{M}_k \lesssim 0.4$. Even if α is not exactly
1619 the same in each region, we can interpret the above result as ruling out that a large pro-
1620 portion of regions have $\alpha \lesssim 1$, as if that were the case we would see higher values of
1621 \mathcal{M}_k associated with higher $\rho_{+,k}$ more often than in Figure 3.8.

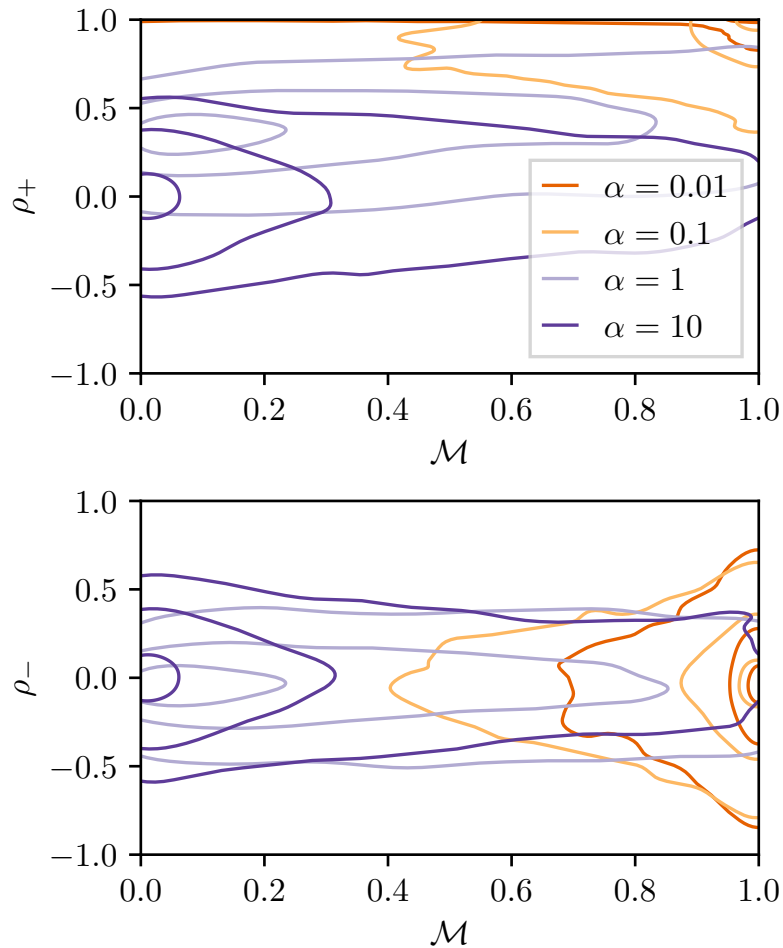


Figure 3.7: Calibrating the cross-correlation test in Section 3.5.3: two-dimensional KDEs of the relationship between ρ_+ and \mathcal{M} (top panel), and ρ_- and \mathcal{M} (bottom panel), for events simulated from the SDP model with four values of α (see legend for color code). The text in Section 3.5.3 reports details about the Monte Carlo procedure. Contours correspond to the 10%, 50%, and 90% credible intervals.

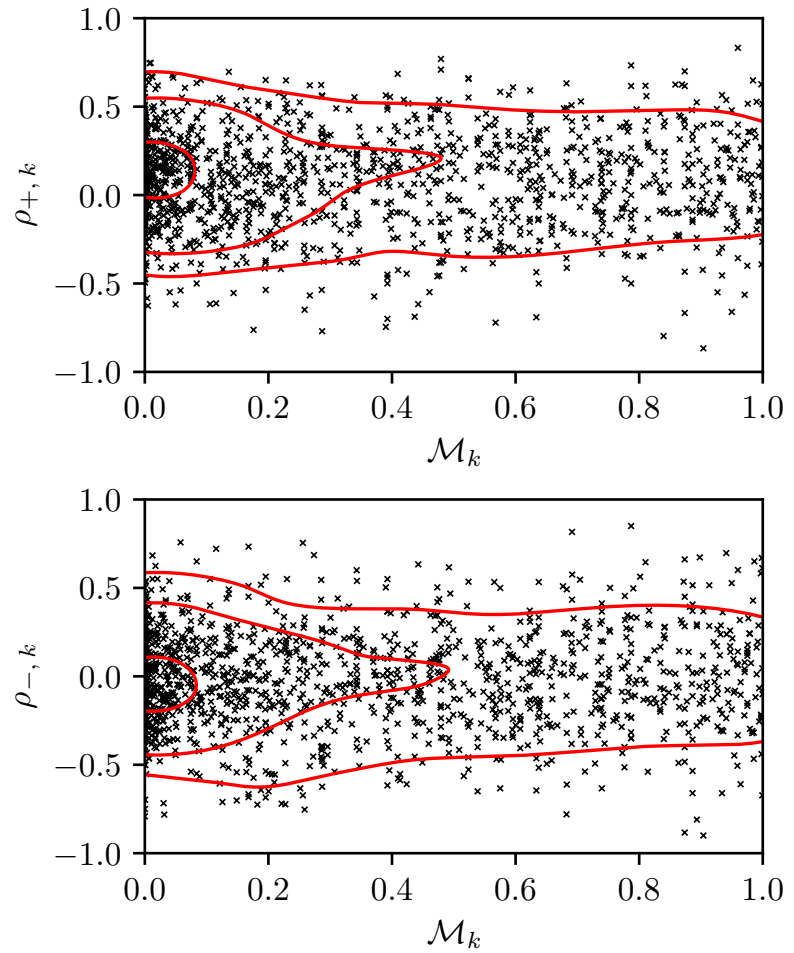


Figure 3.8: As for Figure 3.7 but for GOES data with black crosses marking all regions in the full, unmasked GOES catalog with $N_k \geq 10$. Red contours correspond to the 10%, 50%, and 90% credible intervals inferred from the black crosses.

1622 3.5. *Autocorrelations and longer term memory*

1623 While there is a wealth of information available in flare waiting time and size PDFs,
1624 as in Section 3.5.1, and cross-correlations, as in Sections 3.5.2 and 3.5.3, one may also
1625 consider statistics that quantify the longer term memory of the stress in the system.
1626 For example, as in the context of neutron star glitches [1], studying the autocorrelation
1627 between consecutive waiting times, $\rho_{\Delta t}$, or between consecutive sizes, $\rho_{\Delta s}$, allows one
1628 to place constraints on applicable SDP model parameters. In the fast-driven regime,
1629 $\alpha \ll 1$, we predict $\rho_{\Delta t} = 0$ and $\rho_{\Delta s} = 0$, as we have $X(t) \rightarrow X_c$ before every stress-
1630 release event resulting in the system resetting at every event. If we have $\eta[\Delta X_i | X(t_i^-)] \propto$
1631 $\delta[X(t_i^-)]$, i.e. all stress in the system is released at each event, the same prediction of no
1632 autocorrelations holds — again the system is reset at every event. Observations of non-
1633 zero autocorrelations therefore rule out certain regimes in the SDP framework.

1634 When we calculate $\rho_{\Delta t, k}$ and $\rho_{\Delta s, k}$ for all regions in the GOES catalog with $N_k \geq$
1635 10, we find that the PDFs $p(\rho_{\Delta t, k})$ and $p(\rho_{\Delta s, k})$ are broad, akin to $p(\rho_{+, k})$ shown in
1636 Figure 3.6. The medians are 0.11 and 0.10 respectively. This result is incongruent with
1637 the assumption $\alpha \ll 1$ in all regions, as $\alpha \ll 1$ implies both PDFs should have a median
1638 of zero. These results likely stem from the obscuration effect described in Section 3.4.2.
1639 One tentative physical interpretation of a positive $\rho_{\Delta t}$ and $\rho_{\Delta s}$ is via analogy to terrestrial
1640 earthquakes which exhibit aftershocks, i.e. large events are often followed by larger-
1641 than-average events, with smaller-than-average waiting times [99]. In the context of
1642 solar flares, aftershock-like features are noted in the extreme ultraviolet in so-called
1643 “late-phase” flares [145].

1644 3.6. CONCLUSION

1645 In this paper, we revisit the long-standing question of whether solar flares in different
1646 active regions are triggered by a stress-relax process with a trigger threshold which is
1647 constant in time. We do so by mapping the flaring process to a SDP process, which
1648 operates independently in each active region. The SDP framework has been applied
1649 in related contexts to forest fires [140] and solar flares [117], before being extended in
1650 the context of neutron star glitches [1–3, 25]. If one assumes a constant driving rate,
1651 and a constant “stress” threshold at which relaxation events are guaranteed to occur,
1652 the model makes precise, falsifiable predictions regarding the statistics of sequences of
1653 waiting times and sizes, such as their PDFs, and cross-correlations. It is agnostic about
1654 the underlying microphysical mechanism.

1655 Analyzing the historical GOES soft X-ray flare catalog, using data from 1975 until
1656 2022, we systematically search all active regions for signatures that flares are consistent
1657 with the SDP model with $\alpha \ll 1$ (rapidly driven). We find no evidence that this is the
1658 case. Specifically, when considering just the waiting time and size PDFs of each active
1659 region we find that either i) the conditional PDF of stress-release sizes, $\eta[\Delta X_i | X(t_i^-)]$,
1660 varies from one region to another, or ii) a flare rate of $\lambda_k \gtrsim 0.2 \text{ hours}^{-1}$ does not corre-
1661 spond to $\alpha \ll 1$ (assuming that λ_k traces α). The analysis takes into account the selection
1662 effect that obscures the detection of flares following a large flare due to enhancement of
1663 the soft X-ray background.

1664 On the other hand, if many active regions house a SDP process driven rapidly to-
1665 wards a static-in-time threshold before each event, i.e. have $\alpha \ll 1$, then those regions
1666 that have large cross-correlations between event sizes and subsequent waiting times
1667 should also have waiting time and size PDFs of the same shape. This prediction is not
1668 supported by the data, as proved clearly by Figure 3.8. The match between $p(\Delta t)$ and
1669 $p(\Delta s)$, quantified by \mathcal{M}_k (the p -value from a KS two-sample test) for the k -th active
1670 region, does not correlate with the forward cross-correlation, $\rho_{+,k}$. If we assume each
1671 region has the same α , this test implies $1 \lesssim \alpha \lesssim 10$.

1672 We emphasize that the prediction that \mathcal{M}_k should correlate with $\rho_{+,k}$ for a process
1673 driven to a threshold does not rely on the specific details of the SDP framework, such as
1674 the relationship between flare rate and stress in Equation (3.2), nor the functional form of
1675 $\eta[\Delta X_i | X(t_i^-)]$. Any stochastic process that drives the stress towards a static threshold
1676 before each event would predict an equivalent observable, for example the Brownian
1677 stress-accumulation model [4].

1678 There are many ways to interpret the results in Sections 3.4.3 and 3.5: i) solar flares
1679 may not be triggered by stress (e.g. magnetic energy density) breaching a threshold; a
1680 completely different process may trigger a flare. ii) The GOES flare catalog is incomplete;
1681 flares that occur in the aftermath of large flares are not recorded, creating an artificial
1682 cross-correlation. iii) The threshold at which a glitch is triggered and/or iv) the driving
1683 rate at which stress accumulates may vary with time; either of options iii) and iv) could
1684 wash out the observable signature. Untangling these explanations entails exploiting the
1685 entire wealth of data available in the flare catalog(s), rather than focussing on individual
1686 special flares or regions.

1687 In closing, we touch on the following question: if option iii) above is true, is a thresh-
1688 old that varies with time compatible with any plausible microphysical flare triggers?
1689 The question falls outside the scope of this paper, which focuses on the microphysics-
1690 agnostic analysis in Sections 3.4 and 3.5, so we limit ourselves to the following brief
1691 remark. Magnetohydrodynamic instabilities relevant to solar flare activity are triggered
1692 above a threshold, which typically depends on the detailed geometry of a flaring mag-
1693 netic loop, not just its bulk properties (e.g. magnetic energy density). The geometry of
1694 a flaring loop does vary with time in general. For example, the ideal kink instability
1695 occurs, when the total twist $\Phi = lB_\phi(r)/[rB_z(r)]$ satisfies $\Phi > \Phi_{\text{cr}}(a) \sim 10$, where l
1696 and r are the length and minor radius of the current-carrying loop, $B_\phi(r)$ and $B_z(r)$ are
1697 the toroidal and axial magnetic field components, and a is the loop aspect ratio [146].
1698 As sub-photospheric turbulence perturbs randomly the footpoints of a magnetic flux
1699 tube, the variables a and hence $\Phi_{\text{cr}}(a)$ fluctuate stochastically. Quantifying the ampli-
1700 tude (drift and diffusion) of the fluctuations is a task for detailed magnetohydrodynamic
1701 simulations and lies well outside the scope of this paper, but it is conceivable that the
1702 amplitude is sufficiently large to render option iii) above viable.

1703 ACKNOWLEDGEMENTS

1704 We acknowledge helpful discussions with Kai Yang in the early stages of this paper. JBC,
1705 AM, and MSW are supported by the Australian Research Council (ARC) Centre of Ex-
1706 cellence for Gravitational Wave Discovery (OzGrav) (project number CE170100004) and

1707 ARC Discovery Project DP220102201. JBC is supported by an Australian Postgraduate
1708 Award.

1709 *Software:* Numpy [147], Scipy [148], Matplotlib [149], and stan [150] through
1710 the cmdstanpy interface.

1711 3.A1. MAGNETIC ENERGY DENSITY AS A STRESS VARIABLE IN 1712 AN ACTIVE REGION

1713 The SDP framework described in Sections 3.2 and 3.3 is agnostic about the microphysics
1714 of solar flares, beyond the general assumption that the flaring rate increases with the
1715 stress in the system and diverges at a stress threshold. In this appendix, we sketch briefly
1716 one possible mapping between the SDP model and a specific microphysical flare model,
1717 in which the stress variable is the spatially-averaged magnetic energy density in an ac-
1718 tive region. We emphasize that the model is phenomenological and highly idealized. We
1719 do not favor it over the many alternatives; it is merely one possible illustration of how
1720 such a mapping may work, as a guide to the interested reader.

1721 Let $X(t)$ correspond to the spatially-averaged magnetic energy density in an ac-
1722 tive region. The spatial average is taken in order to package the stress into a single
1723 variable, noting that the magnetic energy density is nonuniform in reality. Let the ac-
1724 tive region have characteristic linear dimension L . Let S be the magnetohydrodynamic
1725 Poynting flux through the photosphere. We assume that the Poynting flux deposits mag-
1726 netic energy into the active region without losses and at a constant rate, so that one has
1727 $X(t) = X(t_i^+) + St/L$ between flares ($t_i^+ \leq t \leq t_{i+1}^-$). Recent vector magnetogram measure-
1728 ments allow direct observation of the Poynting flux, and the magnetic energy density of
1729 an active region, which are at-odds with our assumption that S is steady in time [151–
1730 154]. Putting aside the latter consideration for the moment, we can write the control
1731 parameter α as

$$\alpha = \frac{\lambda_0 S}{X_c L}, \quad (3.6)$$

1732 where X_{cr} is the magnetic energy density threshold for a magnetohydrodynamic insta-
1733 bility, for example, and λ_0 is the instability’s trigger reference rate.

1734 Several plausible magnetohydrodynamic instabilities have been suggested as solar
1735 flare triggers in the literature [155]. Some of them do not involve a magnetic energy
1736 density threshold at all. For example, the kink instability discussed at the end of Sec-
1737 tion 3.6 is triggered when the field-line twist Φ exceeds a threshold $\Phi_{\text{cr}}(a)$, whose value
1738 depends on the aspect ratio a of the flaring loop [146]. However, instabilities triggered
1739 by a magnetic energy density threshold do exist. One example is plasmoid-induced mag-
1740 netic reconnection via tearing modes in a fractal current sheet [156], whose threshold
1741 depends on fractional powers of the Alfvén speed (or equivalently the Lundquist num-
1742 ber) and hence on the magnetic energy density; see Ji and Daughton [155] or section 5 in
1743 Shibata and Tanuma [156] for example. In the latter reference, the threshold condition
1744 also depends on the aspect ratio a (width divided by length) of the current sheet, which
1745 can vary with time, as a flaring loop responds to sub-photospheric turbulence.

1746 What are the time-scales on which S and X_c vary? In the SDP picture, both variables
1747 are steady, but the GOES analysis in Section 3.5 implies that one or both may vary in re-

1748 ability (although other scenarios are possible too, as discussed in Section 3.6). As far as S
 1749 is concerned, one expects to find statistical fluctuations on the eddy turnover time-scale
 1750 of sub-photospheric turbulence and flux emergence, τ_{flux} , as observed with vector mag-
 1751 netograms and Doppler measurements [151]. Magnetohydrodynamic simulations and
 1752 G-band radiative signatures suggest $\tau_{\text{flux}} \sim \text{minutes}$ for magnetic features associated
 1753 with solar granulation, with peak-to-peak fluctuation amplitude $\lesssim 30\%$ [157–159]. As
 1754 far as X_c is concerned, in the plasmoid-induced reconnection picture as one illustrative
 1755 example, the magnetic energy density threshold for a Sweet-Parker current sheet to un-
 1756 dergo secondary tearing depends not only on the magnetic diffusivity, which fluctuates
 1757 on the same time-scale as the local temperature, but also on a and L , which fluctuate on
 1758 the turnover time-scale τ_{flux} , e.g. equation (15) in [156]. Flare waiting times are typically
 1759 comparable to or longer than τ_{flux} , so it is conceivable that the constant- X_c approxima-
 1760 tion in the SDP theory does not apply to every active region.

1761 We emphasize again that the mapping in this appendix is idealized and illustrative.
 1762 None of the statistical analysis in Sections 3.4.3 and 3.5 is predicated on the microphysics
 1763 in this appendix.

1764 3.A2. HIERARCHICAL BAYESIAN FRAMEWORK

1765 This appendix lays out a complementary approach to the heuristic tests with which we
 1766 analyze individual active regions in Section 3.5. We first write down the likelihood for a
 1767 set of observed waiting times and sizes in an individual region, given a set of model pa-
 1768 rameters, in Appendix 3.A2.1. We introduce the hierarchical Bayesian framework which
 1769 combines inference in different regions to estimate population-level parameters, in Ap-
 1770 pendix 3.A2.2. In Appendix 3.A2.3 we test the efficacy of this approach with synthetic
 1771 data, and explain why it is not appropriate in this paper to apply this framework to the
 1772 real GOES catalog despite its efficacy. Finally, in Appendix 3.A2.4 we propose an alter-
 1773 native approach using only the average waiting time in each region, as a motivation for
 1774 future studies. The recipes in this appendix are included for completeness and as a start-
 1775 ing point for readers, who wish to develop hierarchical methods of solar flare analysis
 1776 further.

1777 3.A2. Likelihood and Bayes' theorem

1778 Solving Equations (3.1)–(3.3) for the long-term observable PDFs, $p(\Delta t)$ and $p(\Delta X)$, is
 1779 intractable analytically for most choices of $\eta[\Delta X_i | X(t_i^-)]$. However, for the special case

$$\eta[\Delta X_i | X(t_i^-)] \propto [X(t_i^-) - \Delta X_i]^\delta, \quad (3.7)$$

1780 we obtain the analytic result

$$p(z) = (\alpha + \delta + 1)(1 - z)^{\alpha + \delta}, \quad (3.8)$$

1781 where the variable z is either Δt or ΔX , i.e. the waiting time and size PDFs are identical
 1782 [2]. In Equation (3.7) we have $\delta > 0$ and the constant of proportionality is set by the
 1783 condition that η must integrate to unity between $\Delta X_i = 0$ and $\Delta X_i = X(t_i^-)$; see section

6 and appendix D of Fulgenzi et al. [2] for a full derivation. Equation (3.7) is a monotonically decreasing function of ΔX_i , i.e. small stress-release events are preferred over large events. Its specific functional form is reasonable but arbitrary; it is not inferred from solar flare data. We adopt it here as a pedagogical device to illustrate the advantages and disadvantages of a hierarchical Bayesian approach to analyzing flare data.

When we restore the dimensions to Equation (3.8), and consider the set of observations in the k -th active region, $D_k = \{\Delta t_{i,k}, \Delta s_{i,k}\}$, with $1 \leq i \leq N_k$, we can write the likelihood

$$\mathcal{L}(D_k | \boldsymbol{\theta}_k) = \prod_{i=1}^{N_k-1} p(\Delta t_{i,k} | \boldsymbol{\theta}_k) \prod_{i=1}^{N_k} p(\Delta s_{i,k} | \boldsymbol{\theta}_k) \quad (3.9)$$

$$= \tau_k^{1-N_k} \xi_k^{-N_k} (\beta_k + 1)^{2N_k-1} \prod_{i=1}^{N_k-1} \left(1 - \frac{\Delta t_{i,k}}{\tau_k}\right)^{\beta_k} \prod_{i=1}^{N_k} \left(1 - \frac{\Delta s_{i,k}}{\xi_k}\right)^{\beta_k} \quad (3.10)$$

where ξ_k is the constant of proportionality in Equation (3.5) which translates the drop in magnetic energy density ΔX to the observed flare size, Δs , and one has $\beta_k = \lambda_{0,k} \tau_k + \delta_k$. While there are N_k flare sizes in the region, there are only $N_k - 1$ waiting times. The three model parameters $\boldsymbol{\theta}_k = \{\tau_k, \xi_k, \beta_k\}$ are assumed constant in time for the lifetime of the active region. Bayes' theorem calculates the posterior probability distribution (henceforth "posterior"), $p(\boldsymbol{\theta}_k | D_k)$, i.e. the probability density of parameter vector $\boldsymbol{\theta}_k$ given the data D_k , using the prior probability distribution (henceforth "prior"), $\pi(\boldsymbol{\theta}_k)$, viz.

$$p(\boldsymbol{\theta}_k | D_k) \propto \mathcal{L}(D_k | \boldsymbol{\theta}_k) \pi(\boldsymbol{\theta}_k). \quad (3.11)$$

The normalizing constant of proportionality is often called the evidence and, while essential for model comparison, is not relevant for the parameter estimation exercise below [160].

3.A2. Population-level parameter estimation

Suppose, for the sake of illustration, that X_c , λ_0 , and every component of $\boldsymbol{\theta}_k$ are approximately the same in all active regions. In the language of hierarchical Bayesian inference, this corresponds to assuming that the value of $\boldsymbol{\theta}_k$ for each region is a random number drawn from a population-level distribution known as a "hyper-prior", with narrow extent. For concreteness, we assume the hyper-prior for each model parameter is a Gaussian with mean and standard deviation μ_a and σ_a respectively, with $a \in \{\tau, \xi, \beta\}$. While β_k does depend on τ_k , the inference remains accurate so long as the covariance between τ_k , $\lambda_{0,k}$, and δ_k is minimal. The marginal posterior distribution for the parameters describing the hyper-priors is calculated as

$$p(\boldsymbol{\Lambda} | \mathcal{D}) \propto \pi(\boldsymbol{\Lambda}) \prod_k^M \int d\boldsymbol{\theta}_k \mathcal{L}(D_k | \boldsymbol{\theta}_k) \pi(\boldsymbol{\theta}_k | \boldsymbol{\Lambda}), \quad (3.12)$$

with $\boldsymbol{\Lambda} = \{\mu_a, \sigma_a\}$. In Equation (3.12), $\pi(\boldsymbol{\Lambda})$ is the prior on $\boldsymbol{\Lambda}$, and $\mathcal{D} = \{D_1, \dots, D_k, \dots, D_M\}$ is the set of all data, D_k , from M different active regions.

In practice, we can use a Monte Carlo sampler to estimate Equation (3.12), and thus infer the posterior predictive distributions, $p(\boldsymbol{\theta})$, where we drop the subscript k to signify

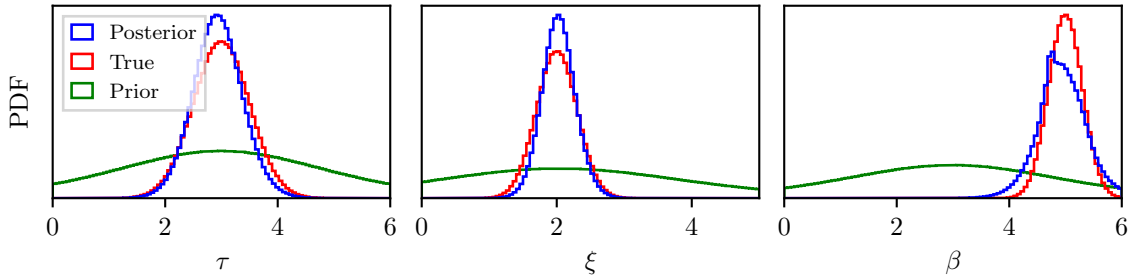


Figure 3.9: Posterior predictive check demonstrating the recovery of injected population-level parameters. The weakly informative priors set on the hyper-parameters τ , ξ , and β are shown in green, histograms of samples from the injected population parameters are shown in red, while histograms of samples from the posterior distributions are shown in blue. See text in Appendix 3.A2.3 for details on the procedure.

that these distributions bring together information from all active regions to inform the inference. We opt to sample using a Hamiltonian Monte Carlo No U-Turn Sampler [161], as implemented in the Stan programming language [150].

3.A2. Validation with synthetic data

To estimate the efficacy of the scheme in Appendix 3.A2.2 to infer population-level parameters, we first apply it to a set of synthetic data generated directly from the model. That is, we generate $M = 50$ fake “active regions”, each with $N_k = 100$ events, with flare sizes and waiting times generated from the SDP framework with $\eta[\Delta X_i | X(t_i^-)]$ as in Equation (3.7). In what follows we use the compact notation $x \sim \mathcal{N}(\mu, \sigma)$ to denote that the random variable x is drawn from a Gaussian distribution with mean μ and standard deviation σ . To generate the data for each region we select a value $\tau_k \sim \mathcal{N}(\mu_\tau = 3 \text{ day}, \sigma_\tau = 0.5 \text{ day})$, a value $\xi_k \sim \mathcal{N}(\mu_\xi = 2 \text{ arb. units}, \sigma_\xi = 0.3 \text{ arb. units})$, and a value $\beta_k \sim \mathcal{N}(\mu_\beta = 5, \sigma_\beta = 0.3)$. Each Gaussian is truncated such that all variates are positive.

After running the sampler with the synthetic data we perform a posterior predictive check, i.e. compare the samples from our posterior distributions $p(\tau)$, $p(\xi)$, and $p(\beta)$ with the injected distributions and the priors on the hyper-parameters. We show the results in Figure 3.9. We see that the posterior samples (blue) appropriately overlap with the injected ground truth (red) for τ , ξ , and β .

Despite the encouraging results in Figure 3.9, we do not apply this hierarchical Bayesian scheme to the GOES catalog in this paper. This is because in most regions neither the waiting time nor the size PDFs follow the functional form in Equation (3.8). When we include Equation (3.8) in the set of options available for the AICc to select between, as in Section 3.5.1, fewer than 0.1% of active regions are fitted best with Equation (3.8). Therefore Equation (3.10) is not an appropriate likelihood for the data. Other choices of the jump distribution in Equation (3.7) may alleviate this problem but they lie outside the scope of this paper.

1844 3.A2. *Likelihood based on the average waiting time*

1845 An alternative approach is to build the likelihood out of a summary statistic, such as the
 1846 average waiting time in a given region, $\langle \Delta t \rangle_k$, rather than each observed waiting time
 1847 and/or size. In the SDP framework, we find [2, 9]

$$\langle \Delta t \rangle^{\text{SDP}} = \frac{1}{\alpha + \alpha_0}, \quad (3.13)$$

1848 where $\alpha_0 \sim 1$ is a dimensionless constant, whose exact value depends on the particular
 1849 form of $\eta[\Delta X_i | X(t_i^-)]$. Restoring the dimensions to Equation (3.13) we can write the
 1850 likelihood as

$$\mathcal{L}(\langle \Delta t \rangle_k | \boldsymbol{\theta}_k) = \frac{1}{\sqrt{2\pi}\sigma_k} \exp\left[\frac{-\left(\langle \Delta t \rangle_k - \frac{\tau_k}{\lambda_{0,k}\tau_k + \alpha_{0,k}}\right)^2}{2\sigma_k^2} \right], \quad (3.14)$$

1851 with $\boldsymbol{\theta}_k = \{\tau_k, \lambda_{0,k}, \alpha_{0,k}, \sigma_k\}$, where we assume the residual of $\langle \Delta t \rangle_k$ with the model
 1852 subtracted is normally distributed, with zero mean and standard deviation σ_k . With the
 1853 likelihood in Equation (3.14) one could perform population-level parameter estimation,
 1854 as described in Section 3.A2.2. We leave this, and an exploration of how $\boldsymbol{\theta}_k$ depends on
 1855 parameters intrinsic to each active region, to future work.

1856 3.A3. CLEANING GOES FLARE SUMMARY DATA

1857 The SWPC and NGDC File Transfer Protocol servers that host the *GOES* flare summary
 1858 data, as well as other data portals such as the Heliophysics Event Knowledgebase⁴, con-
 1859 tain numerous typographical anomalies found when collating the data into a homo-
 1860 geneous catalog. These anomalies are found in the recorded active region number by
 1861 checking whether one has $\Delta t_{i,k} < 14$ days for $1 \leq i \leq N_k - 1$ for each active region. The
 1862 limit of 14 days applies because active regions are typically only visible for two weeks
 1863 due to the rotation period of the Sun. The one exception in the *GOES* flare summary
 1864 data is eight flares that occurred on 2002-11-02, and are assigned to active region num-
 1865 ber 10198. Two weeks later the active region appears on the eastern limb of the Sun,
 1866 and 33 additional flares are assigned to active region number 10198, from 2002-11-17
 1867 until 2002-11-28. We opt not to consider the former eight flares as part of active region
 1868 number 10198, and do not include them in the catalog.

1869 The anomalies, and hand-corrected values, are tabulated in Table 3.1. The corrected
 1870 values are determined manually by referring to the context of surrounding flares in the
 1871 database. For example, the flare starting at 1981-07-18 11:46 is recorded with active re-
 1872 gion number 3121. Yet the other 11 flares associated with the latter region occurred be-
 1873 tween 1981-05-24 and 1981-06-01, while active region number 3221 has 32 flares recorded
 1874 between 1981-07-17 and 1981-07-29, indicating that the anomalous flare should be as-
 1875 sociated with the latter active region. The latitude of the anomalous flare is also within
 1876 $\pm 5^\circ$ of other flares from active region number 3221, while flares in active region number
 1877 3121 are $\gtrsim 10^\circ$ higher in latitude.

⁴ Accessible through http://hec.helio-vo.eu/hec/hec_gui.php.

Table 3.1: Anomalous active region numbers found in the GOES flare summary data by checking whether one has $\Delta t_{i,k} < 14$ days for $1 \leq i \leq N_k - 1$ for each active region. Corrected values are determined manually, by considering the context of what active regions are present at the time of the anomalous flare at a similar latitude. Corrected values of “—” indicate that we cannot identify a reasonable active region to associate with the anomalous flare.

Flare start time	Anomalous active region number	Corrected active region number
1978-05-30 06:19	1000	1134
1981-07-18 11:46	3121	3221
1981-08-22 06:58	366	3266
1983-03-01 18:24	2102	4102
1983-03-01 18:54	2102	4102
1983-07-04 06:09	4135	4235
1983-07-29 03:53	4236	4263
1993-09-27 01:35	7500	7590
2000-11-09 21:13	9125	—
2002-06-14 20:18	1	10001
2003-07-31 07:59	422	10422
2003-12-21 04:10	10000	—
2011-12-22 13:04	11281	11381
2017-07-11 01:09	12655	12665
2017-07-16 10:25	12655	12665
2021-05-10 23:46	12282	12822
2021-09-01 03:03	12680	12860
2021-09-01 04:27	12680	12860
2021-11-06 22:01	12984	12894
2021-12-18 11:17	12807	12907
2021-12-18 17:27	12807	12907

CHAPTER 4

1878

1879

1880 Search for continuous gravitational waves from 20 accreting 1881 millisecond x-ray pulsars in O3 LIGO data

1882

1883 4.1. INTRODUCTION

1884 Second generation, ground-based gravitational wave detectors, specifically the Advanced
1885 Laser Interferometer Gravitational wave Observatory (Advanced LIGO) [162] and Ad-
1886 vanced Virgo [163], have detected more than 50 compact binary coalescence events in
1887 recent years [164–166]. Continuous gravitational waves from rapidly-rotating neutron
1888 stars are also potential sources, e.g. a non-axisymmetry due to mountains on the surface,
1889 or stellar oscillation modes in the interior [167–169]. There are no reported detections of
1890 continuous gravitational waves to date, despite a number of searches in Advanced LIGO
1891 and Advanced Virgo data [170–191].

1892 Low-mass X-ray binaries (LMXBs) are a high-priority target for continuous gravita-
1893 tional wave searches. LMXBs are composed of a compact object, such as a neutron star¹,
1894 which accretes matter from a stellar-mass ($\lesssim 1M_{\odot}$) companion [192]. The accretion
1895 exerts a torque that may spin up the compact object. Electromagnetic (EM) observa-
1896 tions show that even the pulsar with the highest known frequency, PSR J1748–2446ad
1897 at 716 Hz [193], rotates well below the centrifugal break-up frequency, estimated at
1898 ~ 1400 Hz [194]. Gravitational wave emission may provide the balancing torque in
1899 binary systems such as these, stopping the neutron star from spinning up to the break-
1900 up frequency [195, 196]. If so, there should thus be a correlation between accretion rate
1901 (which is inferred via X-ray flux) and the strength of the continuous gravitational wave
1902 emission [195–198]. The LMXB Scorpius X-1 is the brightest extra-Solar X-ray source in
1903 the sky, making it a prime target for searches for continuous gravitational waves [171,
1904 185, 199, 200].

1905 Some LMXBs have EM observations of pulsations during “outburst” events lasting
1906 days to months, which allow for measurement of their rotational frequency, f_* , to an ac-

¹LMXBs in which the compact object is a stellar-mass black hole are not expected to function as con-
tinuous gravitational wave sources and are not discussed in this paper.

curacy of $\sim 10^{-8}$ Hz, and measurement of their binary ephemerides [192, 201]. LMXBs that are observed to go into outburst and have measurable pulsations with millisecond periods are sometimes called accreting millisecond X-ray pulsars (AMXPs). If the rotational frequency is known, computationally cheap narrowband searches are possible. Six AMXPs were previously searched for continuous gravitational waves, one in Science Run 6 (S6) using the TwoSpect algorithm [202, 203], and five in Observing Run 2 (O2) using the same Hidden Markov Model (HMM) algorithm we use in this work [8, 186]. No significant candidates were found in either search. Searches for continuous gravitational waves from LMXBs are difficult as the rotation frequency may wander stochastically on timescales of $\lesssim 1$ yr [204], limiting the duration of coherent integration. A HMM tracks a wandering signal, and is the search algorithm we use here, following Refs. [7, 8, 185, 186].

Advanced LIGO and Advanced Virgo began the third Observing Run (O3) on April 1 2019, 15:00 UTC. There was a month-long commissioning break between October 1 2019, 15:00 UTC, and November 1 2019, 15:00 UTC, after which observations resumed until March 27, 2020, 17:00 UTC. This month-long break divides O3 into two segments: O3a and O3b. In this work we search the full O3 data set for continuous gravitational wave signals from AMXPs with known rotational frequencies. The search is a more sensitive version of an analogous search in O2 data [186], with an expanded target list. We briefly review the algorithm and O2 search in Sec. 4.2. In Secs. 4.3 and 4.4 we describe the targets and the parameter space respectively. We discuss the data used in Sec. 4.5. In Sec. 4.6 we describe the vetoes applied to discriminate between terrestrial and astrophysical candidates. In Sec. 4.7 we present the results of the search. In Sec. 4.8 we describe an additional target-of-opportunity search performed for one of the targets that was in outburst during O3a. We provide upper limits for the detectable wave-strain, and astrophysical implications thereof, in Sec. 4.9. We conclude in Sec. 4.10.

4.2. SEARCH ALGORITHM

The search in this paper follows the same prescription as the O2 searches for Scorpius X-1 [185] and LMXBs with known rotational frequency [186]. It is composed of two parts: a HMM which uses the Viterbi algorithm to efficiently track the most likely spin history, and the \mathcal{J} -statistic, which calculates the likelihood a gravitational wave is present given the detector data, and the orbital parameters of both the Earth and the LMXB. The HMM formalism is identical to that used in Refs. [7, 8, 185, 186, 199], and the \mathcal{J} -statistic was first introduced in Ref. [8]. Below, we provide a brief review of both the HMM and the \mathcal{J} -statistic.

4.2.1. HMM

In a Markov process, the probability of finding the system in the current state depends only on the previous state. In a hidden Markov process the states are not directly observable and must be inferred from noisy data. In this paper, the hidden state of interest is the gravitational wave frequency $f(t)$. Although the rotation frequency $f_\star(t)$ of every target in this search is measured accurately from EM pulsations, we allow $f(t) \neq f_\star(t)$ in general for three reasons: i) different emission mechanisms emit at different multiples

of f_\star [205]; ii) a small, fluctuating drift may arise between $f(t)$ and $f_\star(t)$, if the star's core (where the gravitational-wave-emitting mass or current quadrupole may reside) decouples partially from the crust (to which EM pulsations are locked) [7, 206]; and, iii) the rotational frequency of the crust may also drift stochastically due to a fluctuating accretion torque [192, 204]. The gravitational-wave frequency is therefore hidden even though the EM measurement of f_\star helps restrict the searched frequency space, as described in Sec. 4.4.

Following the notation of Refs. [185, 186] we label the hidden state variable as $q(t)$. In our model, it transitions between a discrete set of allowed values $\{q_1, \dots, q_{N_Q}\}$ at discrete times $\{t_0, \dots, t_{N_T}\}$. The probability of the state transitioning from q_i at time t_n to q_j at time t_{n+1} is determined by the transition matrix $A_{q_j q_i}$. In this search, as in previous searches of LMXBs [185, 186, 199], the transition matrix is

$$A_{q_j q_i} = \frac{1}{3} (\delta_{q_j q_{i+1}} + \delta_{q_j q_i} + \delta_{q_j q_{i-1}}), \quad (4.1)$$

where δ_{ij} is the Kronecker delta. Eq. (4.1) corresponds to allowing $f(t)$ to move 0, or ± 1 frequency bins, with equal probability, at each discrete transition. It implicitly defines the signal model for $f(t)$ to be a piece-wise constant function, with jumps in frequency allowed at the discrete times $\{t_0, \dots, t_{N_T}\}$. This is a well-tested approximation for an unbiased random walk [7, 8].

The total duration of the search is T_{obs} , which we split into N_T coherent equal chunks of length T_{drift} , where $N_T = \lfloor T_{\text{obs}}/T_{\text{drift}} \rfloor$, and $\lfloor \dots \rfloor$ indicates rounding down to the nearest integer. We justify our choice of T_{drift} in Sec. 4.4. In essence, it needs to be short enough to ensure that $f_\star(t)$ does not wander by more than one frequency bin during each time segment, but ideally no shorter in order to maximize the signal-to-noise ratio in each segment. For each time segment the likelihood that the observation o_j is related to the hidden state q_i is given by the emission matrix $L_{o_j q_i}$. We calculate $L_{o_j q_i}$ from the data via a frequency domain estimator, e.g. the \mathcal{J} -statistic, as discussed in Sec. 4.2.2.

The probability that the hidden path is $Q = \{q(t_0), \dots, q(t_{N_T})\}$ given a set of observations $O = \{o(t_0), \dots, o(t_{N_T})\}$ is

$$\begin{aligned} P(Q|O) &= \Pi_{q(t_0)} A_{q(t_1)q(t_0)} L_{o(t_1)q(t_1)} \dots \\ &\quad \times A_{q(t_{N_T})q(t_{N_T-1})} L_{o(t_{N_T})q(t_{N_T})}, \end{aligned} \quad (4.2)$$

where $\Pi_{q(t_0)}$ is the prior probability of starting in the state $q(t_0)$, and is taken to be uniform within a certain range guided by EM measurements of f_\star . The Viterbi algorithm is a computationally efficient way to find the path Q^* that maximizes Eq. (4.2) [207].

The detection statistic we use in this work is $\mathcal{L} = \ln P(Q^*|O)$, i.e. the log-likelihood of the most likely path given the data. The search outputs one $P(Q^*|O)$ value per frequency bin, corresponding to the optimal path Q^* terminating in that frequency bin.

4.2. \mathcal{J} -statistic

Any long-lived gravitational wave signal from an LMXB observed by the detectors is Doppler modulated by the orbital motion of the detectors around the Solar System barycenter, and by the orbital motion of the compact object in its binary. The \mathcal{F} -statistic is a

frequency domain estimator originally designed for isolated neutron stars, and accounts for the Earth’s annual orbital motion (as well as the amplitude modulation caused by the Earth’s diurnal rotation) [208]. Algorithms that implement the \mathcal{F} -statistic, such as `lalapps_ComputeFstatistic_v2` [209], have subsequently added functionality to account for modulation of the signal due to binary motion.

The \mathcal{J} -statistic accounts for the binary modulation via a Jacobi-Anger expansion of the orbit [8]. It ingests \mathcal{F} -statistic “atoms” as calculated for an isolated source as an input, assumes the binary is in a circular orbit², and requires three binary orbital parameters: the period P , the projected semi-major axis a_0 , and the time of passage of the ascending node T_{asc} . We use the \mathcal{J} -statistic as the frequency domain estimator $L_{o_j q_i}$ in this paper, as in Refs. [185, 186]. The \mathcal{J} -statistic is a computationally efficient algorithm, as it re-uses \mathcal{F} -statistic atoms when searching over a template bank of binary orbital parameters.

4.3. TARGETS

The AMXPs chosen as targets for this search, along with their positions, orbital elements, and pulsation frequencies are listed in Table 4.1. These 20 targets constitute all known AMXPs with observed coherent pulsations and precisely measured orbital elements as of April 2021³. For details on the relevant EM observations, principally in the X-ray band, see Refs. [192, 201, 212, 213].

Most AMXPs are transient, with “active” (outburst) and “quiescent” phases. Pulsations, and therefore f_\star , are only observed during the active phase. Active phases are typically associated with accretion onto the neutron star, however accretion can also happen during quiescence [214]. The frequency derivatives, \dot{f}_\star , in the active phase and in the quiescent phase are set by the accretion torque and magnetic dipole braking respectively [214, 215]. The value of \dot{f}_\star has implications for the continuous gravitational wave signal strength (see Sec. 4.9.3), as well as the choice of T_{drift} (see Sec. 4.4.1).

One target, SAX J1808.4–3658, went into outburst during O3a [216–218]. It may be the case that continuous gravitational waves are only emitted when an AMXP is in outburst [219]. If so, we increase our signal-to-noise ratio by searching only data from the times that it was in outburst, compared to searching the entirety of O3 data. To investigate this possibility, we perform in Sec. 4.8 an additional target-of-opportunity search for continuous gravitational waves from SAX J1808.4–3658 while it is in outburst.

²This assumption is justified as none of the targets described in Sec. 4.3 have measurable eccentricity with sufficient precision [192, 201].

³We do not include the AMXP Aquila X-1 [210, 211] in our target list as there is a large uncertainty on all three binary orbital elements, compared to the other 20 AMXPs. One would need to search $> 10^{10}$ binary orbital templates, an order of magnitude more than the rest of the targets combined. The number of binary orbital templates is calculated as a function of the uncertainty in orbital elements in Sec. 4.4.2.

Table 4.1: Target list: position (RA and Dec), orbital period (P), projected semi-major axis in light-seconds (a_0), time of passage through the ascending node as measured near the time of the most recent outburst (T_{asc}), the time of passage through the ascending node as propagated to the start of O3 ($T_{\text{asc}, \text{O3}}$), as described in Sec. 4.4.2, and frequency of observed pulsations (f_\star). Numbers in parentheses indicate reported 1σ errors (68% confidence level), unless otherwise noted. All objects have positional uncertainty ≤ 1 s in RA and $\leq 0.5''$ in Dec.

Target	RA	Dec	P/s	$a_0/\text{lt-s}$	$T_{\text{asc}}/\text{GPS time}$	$T_{\text{asc}, \text{O3}}/\text{GPS time}$	f_\star/Hz	Ref.
IGR J00291+5934	00h29m03.05s	+59°34'18.93''	8844.07673(9)	0.064993(2)	1122149932.93(5)	1238157687(1)	598.89213099(6)	[2]
MAXI J0911–655	09h12m02.46s	-64°52'06.37''	2659.93312(47)	0.017595(9)	1145507148.0(9)	1238165918(16)	339.9750123(3)	[2]
XTE J0929–314	09h29m20.19s	-31°23'03.2''	2614.746(3)	0.006290(9)	705152406.1(9)	1238165763(612)	185.105254297(9)	[2]
IGR J16597–3704	16h59m32.902s	-37°07'14.3''	2758.2(3)	0.00480(3)	1193053416(9)	1238163777(4907)	105.1758271(3)	[2]
IGR J17062–6143	17h06m16.29s	-61°42'40.6''	2278.21124(2)	0.003963(6)	1239389342(4)	1238165942(4)	163.656110049(9)	[2]
IGR J17379–3747	17h37m58.836s	-37°46'18.35''	6765.8388(17)	0.076979(14)	1206573046.6(3)	1238162748(8)	468.083266605(7)	[2]
SAX J1748.9–2021	17h48m52.161s	-20°21'32.406''	31555.300(3)	0.38757(2)	1109500772.5(8)	1238151731(12)	442.3610957(2)	[2]
NGC 6440 X–2	17h48m52.76s	-20°21'24.0''	3457.8929(7)	0.00614(1)	956797704(2)	1238166449(57)	205.89221(2)	[2]
IGR J17494–3030	17h49m23.62s	-30°29'58.999''	4496.67(3)	0.015186(12)	1287797911(1)	1238163668(331)	376.05017022(4)	[2]
Swift J1749.4–2807	17h49m31.728s	-28°08'05.064''	31740.8417(27)	1.899568(11)	1298634645.85(12)	1238136602(5)	517.92001385(6)	[2]
IGR J17498–2921	17h49m56.02s	-29°19'20.7''	13835.619(1)	0.365165(5)	997147537.43(7)	1238164020(6)	400.99018734(9)	[2]
IGR J17511–3057	17h51m08.66s	-30°57'41.0''	12487.5121(4)	0.2751952(18)	936924316.03(3)	1238160570(10)	244.83395145(9)	[2]
XTE J1751–305	17h51m13.49s	-30°37'23.4''	2545.3414(38)	0.010125(5)	701914663.57(3)	1238164644(487)	435.31799357(3)	[2]
Swift J1756.9–2508	17h56m57.43s	-25°06'27.4''	3282.40(4)	0.00596(2)	1207196675(9)	1238166119(378)	182.06580377(11)	[2]
IGR J17591–2342	17h59m02.86s	-23°43'08.3''	31684.7503(5)	1.227714(4)	1218341207.72(8)	1238144176.7(3)	527.425700578(9)	[2]
XTE J1807–294	18h06m59.8s	-29°24'30''	2404.4163(3)	0.004830(3)	732384720.7(3)	1238165711(63)	190.62350702(4)	[2]
SAX J1808.4–3658	18h08m27.647s	-36°58'43.90''	7249.155(3)	0.062809(7)	1250296258.5(2)	1238161173(5)	400.97521037(1)	[2]
XTE J1814–338	18h13m39.02s	-33°46'22.3''	15388.7229(2)	0.390633(9)	739049147.41(8)	1238151597(4)	314.35610879(1)	[2]
IGR J18245–2452	18h24m32.51s	-24°52'07.9''	39692.812(7)	0.76591(1)	1049865088.37(9)	1238128096(33)	254.3330310(1)	[2]
HETE J1900.1–2455	19h00m08.65s	-24°55'13.7''	4995.2630(5)	0.01844(2)	803963262.3(8)	1238161513(43)	377.296171971(5)	[2]

90% confidence level

3σ error

2017 4.4. SEARCH PARAMETERS

2018 The \mathcal{J} -statistic matched filter requires specification of the source sky position [right ascension (RA) and declination (Dec)], the orbital period P , the projected semi-major axis
 2019 a_0 , and the orbital phase ϕ_a at the start of the search. The orbital phase can be equivalently specified via a time of passage through the ascending node, T_{asc} . EM observations
 2020 constrain all of these parameters, as well as the spin frequency f_\star . These measurements,
 2021 along with their associated uncertainties, are listed in Table 4.1.

2024 There are several mechanisms that could lead to continuous gravitational wave emission
 2025 from an AMXP, in its active or quiescent phase. “Mountains” on the neutron star
 2026 surface, be they magnetically or elastically supported, emit at $2f_\star$ and potentially f_\star
 2027 [256]. The dominant continuous gravitational wave emission from r -mode oscillations
 2028 (Rossby waves excited by radiation-reaction instabilities) is predicted to be at $\sim 4f_\star/3$
 2029 [257–260]. Thus, we search frequency sub-bands centered on $\{1, 4/3, 2\} f_\star$ for each target.
 2030 As in Refs. [185, 186] we choose a sub-band width of $\sim 0.61 \text{ Hz}^4$.

2031 Recent work indicates that the continuous gravitational wave signal from r -modes
 2032 could emit at a frequency far from $4f_\star/3$ due to equation-of-state-dependent relativistic
 2033 corrections, and so comprehensive searches for r -modes may need to cover hundreds of
 2034 Hz for the targets listed in Table 4.1 [262, 263]. The exact range of frequencies to search
 2035 is a non-linear function of f_\star , and does not necessarily include $4f_\star/3$ (see equation (17)
 2036 of Ref. [263]). However, these estimates are still uncertain. We deliberately search \sim
 2037 0.61 Hz sub-bands centered on $4f_\star/3$, as an exhaustive broadband search lies outside the
 2038 scope of this paper, which aims to conduct fast, narrowband searches at astrophysically
 2039 motivated harmonics of f_\star while accommodating frequency wandering within those
 2040 sub-bands, a challenge in its own right.

2041 4.4. Coherence time and frequency binning

2042 Another key parameter for the search algorithm described in Sec. 4.2 is the coherence
 2043 time T_{drift} . As in Refs. [185, 186] we fix $T_{\text{drift}} = 10 \text{ d}$ for each target⁵. This choice of T_{drift}
 2044 is guided by observations of Scorpius X-1 [204]. Quantitative studies of how X-ray flux
 2045 variability in AMXPs impacts searches for continuous gravitational waves are absent
 2046 from the literature. The choice to use $T_{\text{drift}} = 10 \text{ d}$ balances the increased sensitivity
 2047 achieved via longer coherence times with the knowledge that the gravitational wave
 2048 frequency may wander stochastically, e.g. due to fluctuations in the mass accretion rate.
 2049 The particular value $T_{\text{drift}} = 10 \text{ d}$ has been adopted in all previous Viterbi LMXB searches
 2050 [185, 186, 199] and is justified approximately with reference to a simple random-walk
 2051 interpretation of fluctuations in the X-ray flux of Scorpius X-1 [204, 264, 265], but other
 2052 values are reasonable too.

2053 We remind the reader that the choice of T_{drift} implicitly fixes the proposed signal
 2054 model as one in which the frequency may wander step-wise zero, plus or minus one

⁴Other narrowband searches, such as Refs. [181, 261], search sub-bands whose width, $\sim 10^{-3} f$, scales with frequency. We note that 0.61 Hz is comparable to $10^{-3} f$ for the harmonics of f_\star that we search in this paper, but is $2^{20} \Delta f$, where Δf is the frequency bin size defined in Sec. 4.4.1. Having the number of frequency bins in the sub-band equal a power of two speeds up the Fourier transform [185].

⁵We consider additional T_{drift} durations for the target-of-opportunity search for continuous gravitational waves from SAX J1808.4–3658 during its O3a outburst in Sec. 4.8.

frequency bin every $T_{\text{drift}} = 10$ d. The size of the frequency bins, Δf , is fixed by the resolution implied by the coherence time, i.e. $\Delta f = 1/(2 T_{\text{drift}}) = 5.787037 \times 10^{-7}$ Hz, for $T_{\text{drift}} = 10$ d. As Δf depends on T_{drift} , changing the coherence time explicitly changes the signal model, e.g. if T_{drift} is halved and T_{obs} is kept constant, then both N_T and Δf double; thus the signal can move up to a factor of four more in frequency in the same T_{obs} . The connection between the coherence time and signal model features in all semi-coherent search methods. However, for a HMM-based search such as this, the choice of coherence time is not limited by computational cost, as it is in all-sky searches or searches based on the \mathcal{F} -statistic [191, 266].

This analysis does not search over any frequency derivatives. The maximum absolute frequency derivative, $|\dot{f}_{\text{max}}|$, that does not change the frequency more than one frequency bin over the course of one coherent chunk is

$$|\dot{f}_{\text{max}}| = \frac{\Delta f}{T_{\text{drift}}} \approx 6.7 \times 10^{-13} \text{ Hz s}^{-1}. \quad (4.3)$$

When measured, the long-term secular frequency derivative is well below this value for all of our targets, see Sec. 4.9.3 for details.

4.4. Number of orbital templates

The orbital elements are known to high precision, with the uncertainty in P satisfying $\sigma_P \lesssim 10^{-3}$ s, the uncertainty in a_0 satisfying $\sigma_{a_0} \lesssim 10^{-4}$ light-seconds (lt-s), and the uncertainty in T_{asc} satisfying $\sigma_{T_{\text{asc}}} \lesssim 1$ s. However, T_{asc} is measured relative to the target's most recent outburst, which is often years before the start of O3 ($T_{\text{O3,start}} = 1238166483$ GPS time). We need to propagate it forward in time. This propagation compounds the uncertainty in T_{asc} , viz. [185, 186, 200]

$$\sigma_{T_{\text{asc,O3}}} = \left[\sigma_{T_{\text{asc}}}^2 + (N_{\text{orb}} \sigma_P)^2 \right]^{1/2}, \quad (4.4)$$

where N_{orb} is the number of orbits between the observed T_{asc} and $T_{\text{asc,O3}}$. Henceforth T_{asc} and $\sigma_{T_{\text{asc}}}$ symbolize their values when propagated to $T_{\text{O3,start}}$.

To conduct the search over the orbital elements for each target and sub-band we construct a rectangular grid in the parameter space defined by $(P \pm 3\sigma_P, a_0 \pm 3\sigma_{a_0}, T_{\text{asc}} \pm 3\sigma_{T_{\text{asc}}})$. For three targets, XTE J0929–314, IGR J16597–3704, and IGR J17494–3030, the range $(T_{\text{asc}} \pm P/2)$ is smaller than $(T_{\text{asc}} \pm 3\sigma_{T_{\text{asc}}})$ and we use the former. We assume that P and a_0 remain within the same bin for the entire search. While some targets have a non-zero measurement of $\dot{P} T_{\text{obs}}$ ($\dot{a}_0 T_{\text{obs}}$), in all cases it is much smaller than the template spacing in P (a_0) [221, 228, 267].

It is unlikely that the true source parameters lie exactly on a grid point in the parameter space. Thus the grid is spaced such that the maximum mismatch, μ_{max} , is never more than an acceptable level. The mismatch is defined as the fractional loss in signal-to-noise ratio between the search executed at the true parameters and at the nearest grid point [268]. We calculate the number of grid points required for P , a_0 and T_{asc} using Eq. (71)

2090 of Ref. [268], i.e.

$$N_P = \pi^2 \sqrt{6} \mu_{\max}^{-1/2} f a_0 \frac{\gamma T_{\text{drift}}}{P^2} \sigma_P, \quad (4.5)$$

$$N_{a_0} = 3\pi \sqrt{2} \mu_{\max}^{-1/2} f \sigma_{a_0}, \quad (4.6)$$

$$N_{T_{\text{asc}}} = 6\pi^2 \sqrt{2} \mu_{\max}^{-1/2} f a_0 \frac{1}{P} \sigma_{T_{\text{asc}}}, \quad (4.7)$$

2091 where γ is a refinement factor defined in general in Eq. (67) of Ref. [268]. In the case of
 2092 O3, the semi-coherent segments are contiguous so we have $\gamma = N_T = 36$. We fix $\mu_{\max} =$
 2093 0.1. A set of software injections into O3 data verifies that a template grid constructed
 2094 with $\mu_{\max} = 0.1$ results in a maximum fractional loss in signal-to-noise ratio of 10%. We
 2095 make the conservative choice of rounding N_P , N_{a_0} , and $N_{T_{\text{asc}}}$ up to the nearest integer,
 2096 after setting f to the highest frequency in each 0.61 Hz sub-band. As in Ref. [186] we find
 2097 $N_{a_0} = 1$ for each target and sub-band, and so hold a_0 constant at its central value while
 2098 searching over P and T_{asc} . Table 4.2 shows N_P , $N_{T_{\text{asc}}}$, and $N_{\text{tot}} = N_P N_{T_{\text{asc}}}$ for each target
 2099 and sub-band. When Eq. (4.5) or (4.7) predicts only two templates for a given sub-band
 2100 we round up to three, ensuring that the central value of P or T_{asc} from EM observations
 2101 is included in the template bank. Note that the EM observations are sufficiently precise
 2102 that $< 5 \times 10^4$ templates are required across all targets and sub-bands. This is in contrast
 2103 to the O2 search for continuous gravitational waves from Scorpius X-1, for which $\sim 10^9$
 2104 templates were needed, mainly due to the large uncertainty in a_0 , and the unknown
 2105 rotation frequency [185].

2106 4.4. Thresholds

2107 The output of the search algorithm outlined in Sec. 4.2 is a \mathcal{L} value corresponding to
 2108 the most likely path through each sub-band for each orbital template (P, a_0, T_{asc}) . We
 2109 flag a template for further follow-up if \mathcal{L} exceeds a threshold, \mathcal{L}_{th} , given an acceptable
 2110 probability of false alarm. To determine \mathcal{L}_{th} we need to know how often pure noise
 2111 yields $\mathcal{L} > \mathcal{L}_{\text{th}}$. The distribution of \mathcal{L} in noise-only data is unknown analytically, but
 2112 depends on P , a_0 , and the frequency, so Monte-Carlo simulations are used to determine
 2113 \mathcal{L}_{th} in each sub-band for each target.

2114 We estimate the distribution of \mathcal{L} in noise via two methods: i) using realizations of
 2115 synthetic Gaussian noise generated using the `lalapps_Makefakedata_v5` program in
 2116 the LIGO Scientific Collaboration Algorithm Library (LALSuite) [209], and ii) searching
 2117 O3 data in off-target locations to simulate different realizations of true detector noise.
 2118 As in Refs. [185, 186] we generate realizations for each target and sub-band, and apply
 2119 the search algorithm described in Sec. 4.2 to each realization to recover samples from the
 2120 noise-only distribution of \mathcal{L} . Details on how we use these samples to find \mathcal{L}_{th} for each
 2121 sub-band are given in Appendix 4.A1. Unless otherwise noted, \mathcal{L}_{th} refers to the lower of
 2122 the two thresholds derived from the methods listed above to minimize false dismissals.

2123 To define \mathcal{L}_{th} we must also account for a “trials factor” due to the number of templates
 2124 searched in each sub-band. We assume that in noise-only data the spacing between
 2125 templates is sufficiently large such that each template returns a statistically independent
 2126 \mathcal{L} . We can therefore relate the false alarm probability for a search of a sub-band with

Table 4.2: Starting frequencies, f_s , for each ~ 0.61 Hz-wide sub-band, number of templates needed to cover the P and T_{asc} domains in that sub-band, N_P and $N_{T_{\text{asc}}}$ respectively, and the total number of templates for each sub-band, $N_{\text{tot}} = N_P N_{T_{\text{asc}}}$. The projected semi-major axis a_0 is known precisely enough that we have $N_{a_0} = 1$ for each sub-band.

Target	f_s (Hz)	N_P	$N_{T_{\text{asc}}}$	N_{tot}	Target	f_s (Hz)	N_P	$N_{T_{\text{asc}}}$	N_{tot}
IGR J00291+5934	598.6	1	3	3	IGR J17498–2921	400.7			
	798.5	1	3	3		534.7			
	1197.8	1	3	3		802.0			
MAXI J0911–655	339.7	1	10	10	IGR J17511–3057	244.5			
	453.3	3	14	42		326.4			
	679.9	3	20	60		489.7			
XTE J0929–314	184.8	3	52	156	XTE J1751–305	435.0			
	246.8	3	69	207		580.4			
	370.2	3	104	312		870.6			
IGR J16597–3704	104.9	49	23	1127	Swift J1756.9–2508	181.8			
	140.2	65	31	2015		242.8			
	210.4	97	46	4462		364.1			
IGR J17062–6143	163.4	1	1	1	IGR J17591–2342	527.1			
	218.2	1	1	1		703.2			
	327.3	1	1	1		1054.9			
IGR J17379–3747	467.8	4	12	48	XTE J1807–294	190.3			
	624.1	5	15	75		254.2			
	936.2	7	23	161		381.2			
SAX J1748.9–2021	442.1	3	18	54	SAX J1808.4–3658	400.7			
	589.8	3	24	72		534.6			
	884.7	3	36	108		802.0			
NGC 6440 X–2	205.6	1	6	6	XTE J1814–338	314.1			
	274.5	1	8	8		419.1			
	411.8	1	12	12		628.7			
IGR J17494–3030	375.7	21	112	2352	IGR J18245–2452	254.0			
	501.4	27	150	4050		339.1			
	752.1	41	224	9184		508.7			
Swift J1749.4–2807	517.6	7	43	301	HETE J1900.1–2455	377.0			
	690.6	9	57	513		503.1			
	1035.8	13	85	1105		754.6			

2127 N_{tot} templates, $\alpha_{N_{\text{tot}}}$, to the probability of a false alarm for a single template, α , viz.

$$\alpha_{N_{\text{tot}}} = 1 - (1 - \alpha)^{N_{\text{tot}}}. \quad (4.8)$$

2128 Previous comparable searches have set $\alpha_{N_{\text{tot}}}$ between 0.01 and 0.3 [185, 186, 199, 200].
2129 In this search, we fix $\alpha_{N_{\text{tot}}} = 0.3$, i.e. set the acceptable probability of false alarm at 30%
2130 per sub-band. As we search a total of $20 \times 3 = 60$ sub-bands, we expect ~ 18 candidates
2131 above \mathcal{L}_{th} due to noise alone (i.e. false alarms), a reasonable number on which to perform
2132 more exhaustive follow-up. Looking ahead to the results in Sec. 4.7 we recover 4611
2133 candidates above \mathcal{L}_{th} . While this number is much higher than the ~ 18 false alarms
2134 expected, almost all of these candidates are non-Gaussian noise artifacts in one (or both)
2135 of the detectors. All but 16 of the 4611 candidates are eliminated by the vetoes outlined
2136 in Sec. 4.6. We reiterate that \mathcal{L}_{th} in each sub-band is the lower of the two thresholds
2137 described in Appendix 4.A1, lowering conservatively the probability of false dismissal.

2138 4.4. Computing resources

2139 A mix of central processing unit (CPU) and graphical processing unit (GPU) resources are
2140 used. The GPU implementation of the \mathcal{J} -statistic is identical to that used in Refs. [185,
2141 186]. The entire search across all targets and sub-bands takes ~ 30 CPU-hours and
2142 ~ 40 GPU-hours when using compute nodes equipped with Xeon Gold 6140 CPUs
2143 and NVIDIA P100 12GB PCIe GPUs. Producing \mathcal{L}_{th} for each sub-band, as described in
2144 Sec. 4.4.3, takes an additional $\sim 5 \times 10^2$ CPU-hours and $\sim 4 \times 10^3$ GPU-hours to perform
2145 the search on different noise realizations. The additional follow-up in Appendix 4.A2.1
2146 requires an additional $\sim 10^3$ CPU-hours and $\sim 10^2$ GPU-hours.

2147 4.5. O3 DATA

2148 We use the full dataset from O3, spanning from April 1, 2019, 15:00 UTC to March 27,
2149 2020, 17:00 UTC, from the LIGO Livingston and Hanford observatories. We do not use
2150 any data from the Virgo interferometer in this analysis, due to its lower sensitivity com-
2151 pared to the two LIGO observatories in the frequency sub-bands over which we search
2152 [269]. The data products ingested by the search algorithm described in Sec. 4.2 are short
2153 Fourier transforms (SFTs) lasting 1800 s. Times when the detectors were offline, poorly
2154 calibrated, or were impacted by egregious noise, are excluded from analysis by using
2155 “Category 1” vetoes as defined in section 5.2 of Ref. [269]. The SFTs are generated from
2156 the “C01 calibrated self-gated” dataset, which is the calibrated strain data with loud tran-
2157 sient glitches removed [270]. Transient glitches otherwise impact the noise floor, as de-
2158 scribed in section 6.1 of Ref. [269]. The median systematic error of the strain magnitude
2159 across O3 is $< 2\%$ [271, 272].

2160 The coherence time $T_{\text{drift}} = 10$ d splits the data into $N_T = 36$ segments. However,
2161 due to the month-long commissioning break between O3a and O3b there are two seg-
2162 ments without any SFTs. These two segments, starting at October 8, 2019, 15:00 UTC
2163 and October 15, 2019, 15:00 UTC, are replaced with a uniform log-likelihood for all fre-
2164 quency bins, which allows the HMM to effectively skip over them while still allowing
2165 spin wandering. When generating synthetic data in Secs. 4.4.3 and 4.9 the same two data
2166 segments are also replaced with uniform log-likelihoods to emulate the real search.

2167 4.6. VETOES

2168 When a candidate is returned with $\mathcal{L} > \mathcal{L}_{\text{th}}$ we must decide whether there are reasonable
 2169 grounds to veto the candidate as non-astrophysical. We use three of the vetoes from
 2170 Ref. [186]: the known line veto, detailed in Sec. 4.6.1, the single interferometer veto,
 2171 detailed in Sec. 4.6.2, and the off-target veto, detailed in Sec. 4.6.3. The false dismissal
 2172 rate of these vetoes is less than 5% (see detailed safety investigations in section IVB of
 2173 Ref. [199] and section IVB of Ref. [185]).

2174 4.6. *Known line veto*

2175 As part of the detector characterization process many harmonic features are identified
 2176 as instrumental “known lines” [269, 273]. However, the exact source of these harmonic
 2177 features is sometimes unidentified, and their impact cannot always be mitigated through
 2178 isolating hardware components or post-processing the data [269, 273]. We use the vetted
 2179 known lines list in Ref. [274].

2180 Any candidate close to a known line at frequency f_{line} is vetoed. Precisely, if for any
 2181 time $0 \leq t \leq T_{\text{obs}}$ the candidate’s frequency path $f(t)$ satisfies

$$|f(t) - f_{\text{line}}| < 2\pi a_0 f_{\text{line}}/P, \quad (4.9)$$

2182 then the candidate is vetoed⁶.

2183 4.6. *Single interferometer veto*

2184 An instrumental artifact is unlikely to be coincident in both detectors, so the candidate’s
 2185 \mathcal{L} should be dominated by only one of the detectors if the signal is non-astrophysical.
 2186 On the other hand, an astrophysical signal may need data from both detectors to be
 2187 detected, or if it is particularly strong may be seen in both detectors individually.

2188 We label the original log-likelihood as \mathcal{L}_{\cup} , and we also calculate the two single inter-
 2189 ferometer log-likelihoods \mathcal{L}_a and \mathcal{L}_b (where the higher \mathcal{L} is labeled with b for defi-
 2190 niteness). There are four possible outcomes for this veto:

- 2191 i) If the \mathcal{L} value in one detector is sub-threshold, while the other is above the two-
 2192 detector \mathcal{L} value, i.e. one has $\mathcal{L}_a < \mathcal{L}_{\text{th}}$ and $\mathcal{L}_b > \mathcal{L}_{\cup}$ and $f_b(t)$, the frequency path
 2193 associated with \mathcal{L}_b , is close to the frequency path of the candidate when using data
 2194 from both detectors, $f_{\cup}(t)$, i.e.

$$|f_{\cup}(t) - f_b(t)| < 2\pi a_0 f_{\cup}/P, \quad (4.10)$$

2195 then the candidate is likely to be a noise artifact in detector b , and is vetoed.

⁶One might consider an additional Doppler broadening factor of $2\pi a_{\oplus}/1 \text{ yr}$, where a_{\oplus} is the mean Earth-Sun distance, as stationary lines in the detector frame get Doppler shifted when transforming the data to the frame of reference of the source. We opt not to apply this factor for simplicity in this search, as the exact pattern of Doppler modulation depends strongly on the sky location of the target. Looking ahead to the results in Sec. 4.7, we note that none of the 16 surviving candidates is within $2\pi f a_{\oplus}/1 \text{ yr}$ of any known line.

- 2196 ii) If one has $\mathcal{L}_a < \mathcal{L}_{\text{th}}$ and $\mathcal{L}_b > \mathcal{L}_{\cup}$, but Eq. (4.10) does not hold then the candidate
 2197 signal cannot be vetoed, as the single-interferometer searches did not find the
 2198 same candidate. This could indicate that the candidate is a weak astrophysical
 2199 signal that needs data from both detectors to be detectable.
- 2200 iii) If one has $\mathcal{L}_a > \mathcal{L}_{\text{th}}$ and $\mathcal{L}_b > \mathcal{L}_{\text{th}}$, the candidate could represent a strong astro-
 2201 physical signal that is visible in data from both detectors independently, or it could
 2202 represent a common noise source. Candidates in this category cannot be vetoed.
- 2203 iv) If one has $\mathcal{L}_a < \mathcal{L}_{\text{th}}$ and $\mathcal{L}_b < \mathcal{L}_{\cup}$, data from both detectors is needed for the
 2204 candidate to be above threshold, possibly indicating a weak astrophysical signal.
 2205 Candidates in this category cannot be vetoed.

2206 **4.6. Off-target veto**

2207 The third veto we apply to a candidate is to search an off-target sky position with the
 2208 same orbital template. If the off-target search returns $\mathcal{L} > \mathcal{L}_{\text{th}}$ then the candidate is likely
 2209 instrumental rather than astrophysical. For this veto, off-target corresponds to shifting
 2210 the target sky position +40 m in RA and +10° in Dec.

2211 **4.7. O3 SEARCH RESULTS**

2212 The results of the search of all 20 targets are summarized in Fig. 4.1, with $\alpha_{N_{\text{tot}}} = 0.3$,
 2213 i.e. a nominal probability of false alarm per sub-band of 30%. Each symbol indicates, for
 2214 all templates with $\mathcal{L} > \mathcal{L}_{\text{th}}$, the terminating frequency bin and p_{noise} , the probability that
 2215 a search of that candidate’s sub-band in pure noise would return at least one candidate at
 2216 least as loud as the one seen. Equation (4.21) in Appendix 4.A1.5 defines p_{noise} explicitly.
 2217 Each candidate is colored according to \mathcal{L} . We note that high \mathcal{L} does not always corre-
 2218 spond to low p_{noise} due to the differing “trials factors” in each sub-band, as accounted for
 2219 when calculating \mathcal{L}_{th} via Eq. (4.8). A low value of p_{noise} corresponds to a higher prob-
 2220 ability that the candidate is a true astrophysical signal. Targets not listed in the legend
 2221 return zero candidates above threshold. We do not display in Fig. 4.1 candidates that are
 2222 eliminated by any of the vetoes described in Sec. 4.6 for clarity.

2223 In total, across all targets and sub-bands, there are 4611 candidates with $\mathcal{L} > \mathcal{L}_{\text{th}}$,
 2224 before the vetoes are applied. All but 100 are eliminated by veto A (known line veto). A
 2225 further 84 candidates are eliminated by veto B (single interferometer veto). None of the
 2226 remaining candidates are eliminated by veto C (off-target veto), leaving 16 candidates
 2227 passing all of the vetoes outlined in Sec. 4.6. None of the surviving candidates from
 2228 the O3 search coincide in their orbital template and terminating frequency bin with the
 2229 seven above- or sub-threshold candidates from the O2 search (c.f. Table VI of Ref. [186]).
 2230 If we set $\alpha_{N_{\text{tot}}} = 0.01$, i.e. set the probability of false alarm per sub-band to 1%, the search
 2231 does not return any candidates with $\mathcal{L} > \mathcal{L}_{\text{th}}$ for any target or sub-band, after vetoes are
 2232 applied.

2233 In Secs. 4.7.1–4.7.20 we summarize the search results for each of the 20 targets. To
 2234 guide the reader, and not clutter the main body of the paper, the full search results for
 2235 one target, IGR J18245–2452, are shown in Fig. 4.2, while the full search results for the

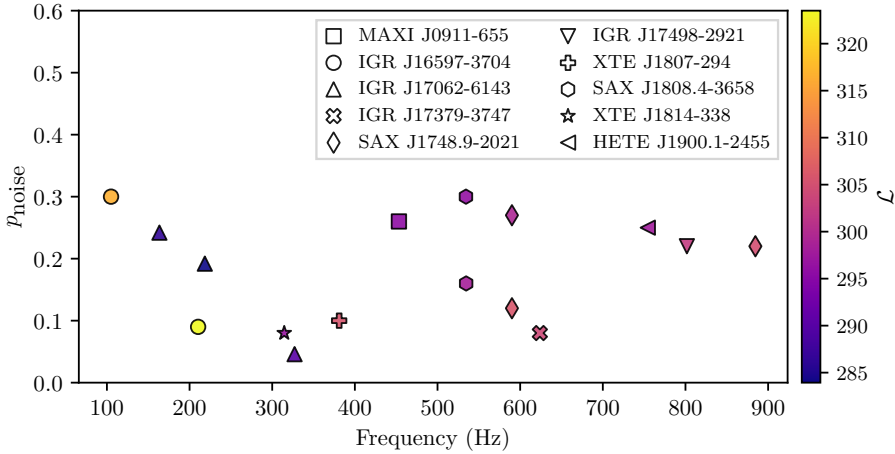


Figure 4.1: Summary of search results across all targets and sub-bands with $\mathcal{L} > \mathcal{L}_{\text{th}}$. The different symbols correspond to candidates from different targets. The ordinate shows p_{noise} for each candidate, the probability that a search of that candidate's sub-band in pure noise would return at least one candidate at least as loud as the one seen. The color of each candidate indicates \mathcal{L} (see color bar at right). Candidates that are eliminated by the vetoes outlined in Sec. 4.6 are not shown for clarity. Details on the search results are in Sec. 4.7 and Appendix 4.A2.

other 19 targets are shown in Figs. 4.4a–4.4s in Appendix 4.A2. The orbital template, terminating frequency bin, \mathcal{L} , and p_{noise} for all 16 candidates with $\mathcal{L} > \mathcal{L}_{\text{th}}$ are collated in Table 4.6 in Appendix 4.A2. We present further follow-up of the 16 candidates in Appendix 4.A2.1. We find no convincing evidence that any are a true astrophysical signal.

4.7. *IGR J18245–2452*

The search results for IGR J18245–2452 are presented in Fig. 4.2. Each marker in Fig. 4.2 shows the terminating frequency and associated \mathcal{L} of the most likely path through the sub-band for a given template, i.e. choice of P and T_{asc} . The vertical blue dashed (green dot-dashed) lines correspond to the threshold set via Gaussian (off-target) noise realizations, $\mathcal{L}_{\text{th},G}$ ($\mathcal{L}_{\text{th},OT}$), in each sub-band, with $\alpha_{N_{\text{tot}}} = 0.3$. See Appendix 4.A1 for details on how we set thresholds in each sub-band. The horizontal red lines indicate known instrumental lines in the detector with bandwidth indicated by the shading. There are zero above-threshold candidates in the f_{\star} and $4f_{\star}/3$ sub-bands. There are 435 above-threshold candidates in the $2f_{\star}$ sub-band, which are all coincident with known noise lines in both the Livingston and Hanford detectors, and are therefore eliminated by veto A. The sub-band around 508 Hz is especially noisy due to violin mode resonances [269].

4.7. *IGR J00291+5934*

The search results for IGR J00291+5934 are shown in Fig. 4.4a, which is laid out identically to Fig. 4.2. There are zero above-threshold candidates in the $4f_{\star}/3$ and $2f_{\star}$ sub-bands. There are three above-threshold candidates in the f_{\star} sub-band, however all three of these candidates are coincident with known noise lines in the Hanford detector, and

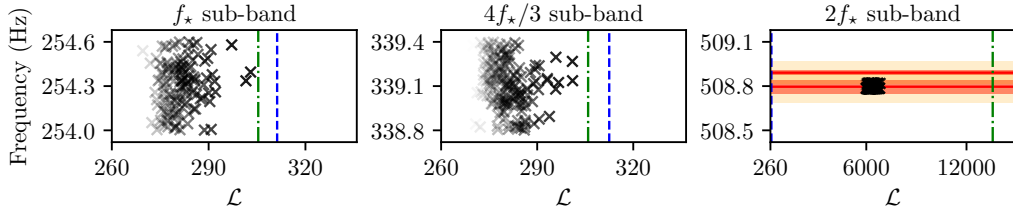


Figure 4.2: Search results for IGR J18245–2452. Black crosses indicate the terminating frequency and \mathcal{L} for the most likely path through the sub-band for each binary template. The vertical blue dashed (green dot-dashed) lines correspond to the threshold set via Gaussian (off-target) noise realizations, $\mathcal{L}_{\text{th},G}$ ($\mathcal{L}_{\text{th},\text{OT}}$), in each sub-band. Solid red lines in the right panel indicate the peak frequency of known instrumental lines in the Hanford detector; the orange band indicates the width of the line in the detector frame and the yellow band indicates the increased effective width due to Doppler broadening, as described in Sec. 4.6.1. Multiple overlapping orange bands creates the red bands. The sub-band around 508.8Hz is especially noisy due to test mass suspension violin mode resonances [269]. The transparency of crosses in sub-bands with many templates, is adjusted relative to the maximum \mathcal{L} in that sub-band for clarity.

2257 are therefore eliminated with veto A.

2258 4.7. MAXI J0911–655

2259 The search results for MAXI J0911–655 are shown in Fig. 4.4b, which is laid out identically
 2260 to Fig. 4.2. There are zero above-threshold candidates in the f_* and $2f_*$ sub-bands.
 2261 There is one above-threshold candidate in the $4f_*/3$ sub-band which survives all of the
 2262 vetoes and has $p_{\text{noise}} = 0.26$. Additional follow-up, presented in Appendix 4.A2.1, does
 2263 not provide any evidence that this candidate is a true astrophysical signal.

2264 4.7. XTE J0929–314

2265 The search results for XTE J0929–314 are shown in Fig. 4.4c, which is laid out identically
 2266 to Fig. 4.2. There are zero above-threshold candidates across all three sub-bands.

2267 4.7. IGR J16597–3704

2268 The search results for IGR J16597–3704 are shown in Fig. 4.4d, which is laid out identically
 2269 to Fig. 4.2. Each sub-band for this target is contaminated with known noise lines.
 2270 There are 84 above-threshold candidates in the $4f_*/3$ sub-band, however they are all
 2271 eliminated by veto B. One above-threshold candidate is returned in each of the f_* and
 2272 $2f_*$ sub-bands. Both of these candidates survive all of the vetoes, and have $p_{\text{noise}} = 0.30$
 2273 and $p_{\text{noise}} = 0.09$ respectively. Further follow-up, including the frequency path and cu-
 2274 mulative log-likelihood for the latter candidate, is presented in Appendix 4.A2.1. This
 2275 follow-up does not provide any evidence that either candidate is a true astrophysical
 2276 signal.

2277 4.7. *IGR J17062–6143*

2278 The search results for IGR J17062–6143 are shown in Fig. 4.4e, which is laid out identically to Fig. 4.2. Given the long-term timing presented in Ref. [228] there is only one template needed in each of the three sub-bands for this target. The template returns 2280 $\mathcal{L} > \mathcal{L}_{\text{th}}$ in all three of the f_{\star} , $4f_{\star}/3$, and $2f_{\star}$ sub-bands. All of these candidates survive 2281 all of the vetoes, and have $p_{\text{noise}} = 0.24$, $p_{\text{noise}} = 0.19$, and $p_{\text{noise}} = 0.05$ respectively. 2282 Further follow-up, including the frequency path and cumulative log-likelihood for the 2283 candidate with $p_{\text{noise}} = 0.05$, is presented in Appendix 4.A2.1. This follow-up does not 2284 provide any evidence that any of the three candidates are a true astrophysical signal. 2285

2286 4.7. *IGR J17379–3747*

2287 The search results for IGR J17379–3747 are shown in Fig. 4.4f, which is laid out identically 2288 to Fig. 4.2. There are zero above-threshold candidates in the f_{\star} and $2f_{\star}$ sub-bands. There 2289 is one above-threshold candidate in the $4f_{\star}/3$ sub-band which survives all of the vetoes 2290 and has $p_{\text{noise}} = 0.08$. Further follow-up, including the frequency path and cumulative 2291 log-likelihood, for this candidate is presented in Appendix 4.A2.1. This follow-up does 2292 not provide any evidence that the candidate is a true astrophysical signal.

2293 4.7. *SAX J1748.9–2021*

2294 The search results for SAX J1748.9–2021 are shown in Fig. 4.4g, which is laid out identically 2295 to Fig. 4.2. There are zero above-threshold candidates in the f_{\star} sub-band. There 2296 are two above-threshold candidates in the $4f_{\star}/3$ sub-band which survive all of the ve- 2297 toes and have $p_{\text{noise}} = 0.12$ and $p_{\text{noise}} = 0.27$. There is one above-threshold candidate 2298 in the $2f_{\star}$ sub-band which survives all of the vetoes and has $p_{\text{noise}} = 0.22$. Additional 2299 follow-up, presented in Appendix 4.A2.1, does not provide any evidence that any of the 2300 three candidates are a true astrophysical signal.

2301 4.7. *NGC 6440 X–2*

2302 The search results for NGC 6440 X–2 are shown in Fig. 4.4h, which is laid out identically 2303 to Fig. 4.2. There are zero above-threshold candidates across all three sub-bands.

2304 4.7. *IGR J17494–3030*

2305 The search results for IGR J17494–3030 are shown in Fig. 4.4i, which is laid out identi- 2306 cally to Fig. 4.2. There are zero above-threshold candidates in the f_{\star} and $2f_{\star}$ sub-bands. 2307 All 4050 candidates in the $4f_{\star}/3$ sub-band are above threshold, however all of them are 2308 coincident with a known noise line in the Hanford detector, and are therefore elimi- 2309 nated with veto A. The sub-band around 501.7Hz is especially noisy due to violin mode 2310 resonances [269].

2311 4.7. *Swift* J1749.4–2807

2312 The search results for Swift J1749.4–2807 are shown in Fig. 4.4j, which is laid out identi-
2313 cally to Fig. 4.2. There are zero above-threshold candidates in the f_\star and $4f_\star/3$ sub-bands.
2314 There is one above threshold candidate in the $2f_\star$ sub-band. However it is coincident
2315 with a known noise line in the Hanford detector, and is therefore eliminated by veto A.

2316 4.7. *IGR* J17498–2921

2317 The search results for IGR J17498–2921 are shown in Fig. 4.4k, which is laid out iden-
2318 tically to Fig. 4.2. There are zero above-threshold candidates in the f_\star , and $4f_\star/3$ sub-
2319 bands. There is one above-threshold candidate in the $2f_\star$ sub-band which survives all of
2320 the vetoes and has $p_{\text{noise}} = 0.22$. Additional follow-up, presented in Appendix 4.A2.1,
2321 does not provide any evidence that this candidate is a true astrophysical signal.

2322 4.7. *IGR* J17511–3057

2323 The search results for IGR J17511–3057 are shown in Fig. 4.4l, which is laid out identically
2324 to Fig. 4.2. There are zero above-threshold candidates across all three sub-bands.

2325 4.7. *XTE* J1751–305

2326 The search results for XTE J1751–305 are shown in Fig. 4.4m, which is laid out identically
2327 to Fig. 4.2. There are zero above-threshold candidates across all three sub-bands.

2328 4.7. *Swift* J1756.9–2508

2329 The search results for Swift J1756.9–2508 are shown in Fig. 4.4n, which is laid out iden-
2330 tically to Fig. 4.2. There are zero above-threshold candidates across all three sub-bands.

2331 4.7. *IGR* J17591–2342

2332 The search results for IGR J17591–2342 are shown in Fig. 4.4o, which is laid out identi-
2333 cally to Fig. 4.2. There are zero above-threshold candidates across all three sub-bands.

2334 4.7. *XTE* J1807–294

2335 The search results for XTE J1807–294 are shown in Fig. 4.4p, which is laid out iden-
2336 tically to Fig. 4.2. There are zero above-threshold candidates in the f_\star and $4f_\star/3$ sub-
2337 bands. There is one above-threshold candidate in the $2f_\star$ sub-band which survives all
2338 of the vetoes and has $p_{\text{noise}} = 0.10$. Further follow-up, including the frequency path
2339 and cumulative log-likelihood, for this candidate is presented in Appendix 4.A2.1. This
2340 follow-up does not provide any evidence that the candidate is a true astrophysical signal.

2341 4.7. *SAX J1808.4–3658*

2342 The search results for SAX J1808.4–3658 are shown in Fig. 4.4q, which is laid out identically to Fig. 4.2. There are zero above-threshold candidates in the f_\star and $2f_\star$ sub-bands.
2343 There are two above-threshold candidates in the $4f_\star/3$ sub-band which survive all of the
2344 vetoes and have $p_{\text{noise}} = 0.16$ and $p_{\text{noise}} = 0.30$. Additional follow-up, presented in Ap-
2345 pendix 4.A2.1, does not provide any evidence that either candidate is a true astrophysical
2346 signal.
2347

2348 SAX J1808.4–3658 was observed in outburst in August 2019, during O3a [217, 218].
2349 This allows us to perform an additional target-of-opportunity search during only its
2350 active phase. If the target only emits continuous gravitational waves during outburst,
2351 searching a shorter duration of data increases the probability of detection by increasing
2352 the signal-to-noise ratio. The details and results of this target-of-opportunity search are
2353 in Sec. 4.8. In summary, after searching with three separate coherence times of $T_{\text{drift}} =$
2354 1 d, $T_{\text{drift}} = 8$ d, and $T_{\text{drift}} = 24$ d, only one candidate is above threshold and survives
2355 all of the vetoes. The candidate is found using $T_{\text{drift}} = 24$ d in the f_\star sub-band, and has
2356 $p_{\text{noise}} = 0.02$. Additional follow-up does not reveal any informative features that would
2357 distinguish between an astrophysical signal and noise. It does not coincide with either
2358 of the two candidates in the $4f_\star/3$ sub-band found in the semi-coherent search using the
2359 full O3 data set.

2360 4.7. *XTE J1814–338*

2361 The search results for XTE J1814–338 are shown in Fig. 4.4r, which is laid out identically
2362 to Fig. 4.2. There are zero above-threshold candidates in the $4f_\star/3$ and $2f_\star$ sub-bands.
2363 There is one above-threshold candidate in the f_\star sub-band which survives all of the ve-
2364 toes and has $p_{\text{noise}} = 0.08$. Further follow-up, including the frequency path and cumu-
2365 lative log-likelihood, for this candidate is presented in Appendix 4.A2.1. This follow-up
2366 does not provide any evidence that the candidate is a true astrophysical signal.

2367 4.7. *HETE J1900.1–2455*

2368 The search results for HETE J1900.1–2455 are shown in Fig. 4.4s, which is laid out iden-
2369 tically to Fig. 4.2. There are zero above-threshold candidates in the f_\star sub-band. All 22
2370 templates in the $4f_\star/3$ sub-band return candidates above \mathcal{L}_{th} , however these candidates
2371 are all coincident with known noise lines in the Hanford detector, and are summarily
2372 eliminated with veto A. The sub-band around 503 Hz is especially noisy due to violin
2373 mode resonances [269]. There is one above-threshold candidate in the $2f_\star$ sub-band
2374 which survives all of the vetoes and has $p_{\text{noise}} = 0.25$. Additional follow-up, presented
2375 in Appendix 4.A2.1, does not provide any evidence that this candidate is a true astro-
2376 physical signal.
2377

2377 4.8. TARGET-OF-OPPORTUNITY SEARCH: SAX J1808.4–3658 IN
2378 OUTBURST

2379 On August 7 2019 SAX J1808.4–3658 went into outburst [216]. The Neutron star Interior
2380 Composition Explorer (NICER) team undertook a high-cadence monitoring campaign,
2381 and performed a timing analysis of the pulsations [217]. The outburst lasted for roughly
2382 24 days, with enhanced X-ray flux observed between August 7 2019 and August 31 2019
2383 (see Fig. 1 of Ref. [217]). We note that the *Swift* X-ray Telescope observed increased
2384 X-ray activity from August 6 2019, and observations in the optical i' -band with the Las
2385 Cumbres Observatory network detected an increased flux from July 25 2019 [218].

2386 Outburst events are attributed to in-falling plasma that is channeled by the magne-
2387 tosphere onto a localized region on the neutron star surface, creating a hot spot that
2388 rotates with the star [275]. As the observed X-ray flux is assumed to be linearly propor-
2389 tional to the mass accretion rate, an outburst could result in a larger mountain on the
2390 neutron star surface (or excite r -modes in the interior), compared to when the AMXP is
2391 in quiescence [219, 276].

2392 If continuous gravitational waves are only emitted from SAX J1808.4–3658 when it
2393 is in outburst, searching all of the O3 data decreases the signal-to-noise ratio, as com-
2394 pared to only searching data from the outburst. To protect against this possibility, we do
2395 an additional search for continuous gravitational waves from SAX J1808.4–3658 using
2396 data from both LIGO observatories between 1249171218 GPS time (August 7 2019) and
2397 1251244818 GPS time (August 31 2019), rather than data from the entirety of O3, as in
2398 Sec. 4.7.18.

2399 4.8. *Search parameters*

2400 The search algorithm is laid out in Sec. 4.2. We run the search using three different
2401 coherence times, setting $T_{\text{drift}} = 1 \text{ d}$, $T_{\text{drift}} = 8 \text{ d}$, and $T_{\text{drift}} = 24 \text{ d}$. We search three sub-
2402 bands centered on $\{1, 4/3, 2\}f_\star$, for each T_{drift} . The width of the sub-band depends on
2403 T_{drift} . It is $\sim 0.76 \text{ Hz}$ for the searches with $T_{\text{drift}} = 1 \text{ d}$ and 8 d , and is $\sim 1.01 \text{ Hz}$ for the
2404 search with $T_{\text{drift}} = 24 \text{ d}$. Given the precise timing achieved during the outburst in 2019
2405 [217], and the shorter search duration, only one $\{P, T_{\text{asc}}, a_0\}$ template is required for
2406 each sub-band, according to Eqs. (4.5)–(4.7). Due to the different values of T_{drift} , shorter
2407 total duration, and different number of templates, we re-calculate \mathcal{L}_{th} for each sub-band
2408 and value of T_{drift} , using the procedure outlined in Sec. 4.4.3 and Appendix 4.A1. As in
2409 the full O3 search, we set the probability of false alarm in each sub-band at $\alpha_{N_{\text{tot}}} = 0.3$.
2410 For all candidates that have $\mathcal{L} > \mathcal{L}_{\text{th}}$ we apply the three vetoes described in 4.6.

2411 4.8. *Search results*

2412 For $T_{\text{drift}} = 1 \text{ d}$, the search in the f_\star sub-band returns one candidate above \mathcal{L}_{th} . The
2413 candidate survives both veto A (known line) and veto B (single interferometer), but fails
2414 veto C (off-target). The searches in the $4/3f_\star$ and $2f_\star$ sub-bands do not return any
2415 candidates above \mathcal{L}_{th} .

2416 For $T_{\text{drift}} = 8 \text{ d}$, there are no candidates above \mathcal{L}_{th} in any of the three sub-bands.

2417 For $T_{\text{drift}} = 24$ d, the searches in the $4f_\star/3$ and $2f_\star$ sub-bands do not return any
 2418 candidates above \mathcal{L}_{th} . The search in the f_\star sub-band does return one candidate above
 2419 \mathcal{L}_{th} . This candidate survives all of the vetoes outlined in Sec. 4.6. We remind the reader
 2420 that with $\alpha_{N_{\text{tot}}} = 0.3$ and nine sub-bands searched (three for each of the three choices
 2421 of T_{drift}), we should expect ~ 3 candidates above threshold purely due to noise. The
 2422 probability that we would see a value of \mathcal{L} at least this large if this sub-band is pure
 2423 noise, p_{noise} , is 0.02. The template and frequency of the candidate are not coincident
 2424 with any candidate from the full O3 search (see Table 4.6) or the sub-threshold candidate
 2425 found in the search of this sub-band in O2 data [186]. By setting $T_{\text{drift}} = T_{\text{obs}} = 24$ d we
 2426 perform a fully coherent search across this time period, with a frequency bin size of
 2427 $\Delta f = 2.4 \times 10^{-7}$ Hz. We describe in Appendix 4.A3 further follow-up of this candidate.
 2428 In summary, we find no significant evidence that it is an astrophysical signal rather than
 2429 a noise fluctuation.

2430 4.9. FREQUENTIST UPPER LIMITS

2431 If we assume that the remaining candidates reported in Sec. 4.7 and Appendix 4.A2 are
 2432 false alarms, we can place an upper limit on the wave strain that is detectable at a confi-
 2433 dence level of 95%, $h_0^{95\%}$, in a sub-band. The value of $h_0^{95\%}$ is a function of our algorithm,
 2434 the detector configuration during O3, and our assumptions about the signal model. We
 2435 describe the method used to estimate $h_0^{95\%}$ in Sec. 4.9.1, present the upper limits in each
 2436 sub-band in Sec. 4.9.2, and compare the results to indirect methods that calculate the
 2437 expected strain in the $2f_\star$ sub-band in Sec. 4.9.3. The astrophysical implications are
 2438 discussed in Sec. 4.9.4.

2439 4.9. *Upper limit procedure in a sub-band*

2440 We set empirical frequentist upper limits in each sub-band using a sequence of injections
 2441 into O3 SFTs. For each sub-band we inject $N_{\text{trials}} = 100$ simulated binary signals at 12–
 2442 15 fixed values of h_0 using `1a1apps_MakefakeData_v5` [209]. For each of the N_{trials}
 2443 injections at a fixed h_0 we select a constant injection frequency, f_{inj} , uniformly from the
 2444 sub-band. While the injected signal has zero spin-wandering, we still use $T_{\text{drift}} = 10$ d in
 2445 the search algorithm outlined in Sec. 4.2 to mimic the real search. The injected period,
 2446 P_{inj} , and time of ascension, $T_{\text{asc,inj}}$ are chosen uniformly from the ranges $[P - 3\sigma_P, P +$
 2447 $3\sigma_P]$ and $[T_{\text{asc}} - 3\sigma_{T_{\text{asc}}}, T_{\text{asc}} + 3\sigma_{T_{\text{asc}}}]$ respectively. We keep a_0 fixed at the precisely known
 2448 value for each target. The polarization, ψ , is chosen uniformly from the range $[0, 2\pi]$.
 2449 The cosine of the projected inclination angle of the neutron star spin axis with our line of
 2450 sight, $\cos \iota$, is chosen uniformly from the range $[-1, 1]$ ⁷. We then search for the injected
 2451 signal with the template in this sub-band’s template grid that is nearest to $\{P_{\text{inj}}, T_{\text{asc,inj}}\}$.
 2452 We re-calculate \mathcal{L}_{th} such that the probability of false alarm in each sub-band is $\alpha_{N_{\text{tot}}} =$
 2453 0.01. This allows us to set conservative upper limits, even in sub-bands where we have
 2454 marginal candidates above a threshold corresponding to a probability of false alarm of

7While the inclination angle of the binary with respect to our line of sight is restricted via EM obser-
 vations for some of our targets, we opt to marginalize over $\cos \iota$ as the neutron star spin axis may not
 necessarily align with the orbital axis of the binary. It is possible to scale our results via equation (19) of
 Ref. [265], if one wishes to fix $\cos \iota$.

30% per sub-band. By recording the fraction of injected signals we recover at each h_0 with $\mathcal{L} > \mathcal{L}_{\text{th}}$ we estimate the efficiency, ε , as a function of h_0 . We then perform a logistic regression [160] to obtain a sigmoid fit to $\varepsilon(h_0)$, and solve

$$\varepsilon(h_0^{95\%}) = 0.95 , \quad (4.11)$$

to find an estimate of $h_0^{95\%}$ in the given sub-band.

One might reasonably ask, how precise is this estimate of $h_0^{95\%}$? The main factors impacting the precision are: i) the precision of the most likely parameters of the sigmoid, as estimated via logistic regression, when solving Eq. (4.11) for $h_0^{95\%}$, given the N_{trials} injections done at 12–15 values of h_0 ; and ii) the assumption that the strain data (and hence the SFTs) are perfectly calibrated. We investigate the impact of (i) by drawing alternative sigmoid fits of $\varepsilon(h_0)$ using the covariance matrix of the parameters returned by the logistic regression. We find that inverting these alternative fits through Eq. (4.11) results in a value of $h_0^{95\%}$ that varies by less than 5% from the value calculated via the most likely parameters (at the 95% confidence level). The impact of (ii) is trickier to quantify. As described in Refs. [271, 272] the median systematic error in the magnitude of the strain is less than 2% in the 20–2000 Hz frequency band across O3a. The statistical uncertainty around the measurement of calibration bias means that in the worst case the true magnitude of the calibration bias may be as large as 7%. However, the calibration bias at a given frequency is not correlated between the detectors (see Figures 16 and 17 in Ref. [271]), and so the impact on a continuous gravitational wave search that combines data from both detectors is likely to be less than 7%.

In light of the above considerations we quote $h_0^{95\%}$ to a precision of two significant figures, but we emphasize that estimating $h_0^{95\%}$ involves many (potentially compounding) uncertainties. Subsequent conclusions about the physical system that are drawn from estimates of $h_0^{95\%}$ cannot be more precise than the estimate of $h_0^{95\%}$ itself.

4.9. Upper limits

The estimates of $h_0^{95\%}$ for each target and sub-band are listed in Table 4.3. Dashes correspond to sub-bands that are highly contaminated with noise lines, which preclude the procedure described in Sec. 4.9.1, as one always finds $\mathcal{L} > \mathcal{L}_{\text{th}}$, regardless of h_0 . The most sensitive sub-bands are for IGR J17062–6143 with $h_0^{95\%} = 4.7 \times 10^{-26}$ in both the $4f_\star/3$ and $2f_\star$ sub-bands (centered around 218.2 Hz and 327.6 Hz respectively). These sub-bands lie in the most sensitive band of the detector, and the binary elements are known to high precision [228], so only one template is needed in each sub-band, corresponding to a relatively lower \mathcal{L}_{th} at fixed probability of false alarm.

No estimates of $h_0^{95\%}$ were established in Ref. [186] for the five targets therein. The search of XTE J1751–305 in S6 data estimated $h_0^{95\%} \approx 3.3 \times 10^{-24}$, 4.7×10^{-24} , and 7.8×10^{-24} in three sub-bands corresponding to f_\star , an r -mode frequency, and $2f_\star$ respectively [203]. Our estimates of $h_0^{95\%}$ for XTE J1751–305 improve these results by two orders of magnitude, because the detector is more sensitive, and T_{drift} is longer.

Table 4.3: Upper limits on the detectable gravitational wave strain at a 95% confidence level, $h_0^{95\%}$, in each of the sub-bands for each target. See Sec. 4.9.1 for details on how they are estimated, and the precision to which they are known. Upper limits are not estimated in sub-bands marked with a “–” as these sub-bands are highly contaminated with known noise lines.

Target	$h_0^{95\%}$ in each sub-band ($\times 10^{-26}$)		
	f_\star	$4f_\star/3$	$2f_\star$
IGR J00291+5934	–	7.6	11
MAXI J0911–655	7.7	6.4	7.3
XTE J0929–314	5.1	5.3	6.4
IGR J16597–3704	7.5	–	5.6
IGR J17062–6143	8.1	4.7	4.7
IGR J17379–3747	8.5	7.4	10
SAX J1748.9–2021	9.2	7.7	10
NGC 6440 X–2	6.2	7.2	5.8
IGR J17494–3030	8.3	–	9.0
Swift J1749.4–2807	11	17	24
IGR J17498–2921	7.0	6.6	8.4
IGR J17511–3057	7.5	5.5	6.6
XTE J1751–305	10	8.3	9.7
Swift J1756.9–2508	8.1	8.8	6.3
IGR J17591–2342	9.5	11	14
XTE J1807–294	6.1	5.0	5.6
SAX J1808.4–3658	6.4	6.9	8.8
XTE J1814–338	9.4	6.0	6.9
IGR J18245–2452	9.0	6.3	–
HETE J1900.1–2455	5.6	–	8.4

2493 4.9. Comparison to expected strain from AMXPs

2494 It is valuable to consider how strong the signal from our targets could be, given EM
 2495 observations. If we assume that all rotational energy losses, as observed in the frequency
 2496 derivative \dot{f}_\star , are converted into gravitational radiation, the indirect spin-down limit on
 2497 the maximum strain, $h_{0,\text{sd}}$, is [205]

$$h_{0,\text{sd}} = 4.0 \times 10^{-28} \left(\frac{8 \text{ kpc}}{D} \right) \times \left(\frac{600 \text{ Hz}}{f_{\text{GW}}} \right)^{1/2} \left(\frac{-\dot{f}_{\text{GW}}}{10^{-14} \text{ Hz s}^{-1}} \right)^{1/2}, \quad (4.12)$$

2498 where D is the distance to the target, f_{GW} is the gravitational wave frequency, and
 2499 \dot{f}_{GW} is its derivative. In Eq. (4.12) we assume $I_{zz}/I_0 \approx 1$, i.e. the zz component of the
 2500 moment-of-inertia tensor (I_{zz}) is very close to the moment-of-inertia of an undeformed
 2501 star (I_0). We assume $f_{\text{GW}} \approx 2f_\star$ when computing Eq. (4.12) for each of our targets. We
 2502 list the best estimates for the distance to each target in the second column of Table 4.4.

These estimates are typically poorly known, especially if there is no known counterpart observed in wavelengths other than X-ray for the target. We use the central estimate of the distance in Eq. (4.12).

For AMXPs, \dot{f}_\star is estimated by constructing a phase-connected timing solution when the target is in outburst, but estimates for \dot{f}_\star in quiescence are also possible for targets that have gone into outburst multiple times. The \dot{f}_\star observed during outburst can be either positive (corresponding to spin-up) or negative (corresponding to spin-down), while in quiescence \dot{f}_\star is typically (but not always) negative [214, 215]. The third column of Table 4.4 records \dot{f}_\star for each of our targets. When \dot{f}_\star has been measured in multiple outburst events, only the \dot{f}_\star from the most recent outburst is listed. For $\dot{f}_\star < 0$ we assume $\dot{f}_{\text{GW}} \approx 2\dot{f}_\star$ in Eq. (4.12). For targets with $\dot{f}_\star < 0$ (in either quiescent or active phases) we find $10^{-28} \lesssim h_{0,\text{sd}} \lesssim 10^{-27}$ (fourth column of Table 4.4), an order of magnitude lower than the estimated value of $h_0^{95\%}$.

As argued in Ref. [186], for $\dot{f}_\star > 0$ the torque due to gravitational radiation reaction may be masked by the accretion torque, allowing larger values of \dot{f}_{GW} , as long as one has $\dot{f}_\star = \dot{f}_{\text{acc}} + \dot{f}_{\text{GW}}$, where \dot{f}_{acc} is the spin-up rate due to accretion. A reasonable choice, without excessive fine-tuning, is to set $\dot{f}_{\text{GW}} \approx -\dot{f}_\star$, for an order-of-magnitude estimate in Eq. (4.12), i.e. assuming $|\dot{f}_{\text{acc}}| \approx 2|\dot{f}_{\text{GW}}|$. The resultant values for $h_{0,\text{sd}}$ for targets with $\dot{f}_\star > 0$ are all well below the estimates of $h_0^{95\%}$ set in Sec. 4.9.2, and fall in the range $10^{-28} \lesssim h_{0,\text{sd}} \lesssim 10^{-27}$.

Another avenue through which EM observations can constrain h_0 is by assuming that the X-ray flux is proportional to the mass accretion rate, and that the torque due to accretion balances the gravitational radiation reaction. The torque-balance limit is [171, 205]

$$h_{0,\text{torque}} = 5 \times 10^{-27} \left(\frac{600 \text{ Hz}}{\dot{f}_{\text{GW}}} \right)^{1/2} \times \left(\frac{F_X}{10^{-8} \text{ erg s}^{-1} \text{ cm}^{-2}} \right)^{1/2}, \quad (4.13)$$

where F_X is the observed bolometric X-ray flux. Eq. (4.13) has a few hidden assumptions, namely: i) that the mass of the neutron star is $1.4M_\odot$, ii) that all of the accretion luminosity is radiated as an X-ray flux, and iii) that the accretion torque is applied at the radius of the neutron star, which is set to 10 km. The exact dependence of the torque-balance limit on these assumptions is discussed in Ref. [171]. We take $\dot{f}_{\text{GW}} \approx 2\dot{f}_\star$ for each of our targets, as for Eq. (4.12). We take $F_X = F_{X,\text{max}}$, the maximum recorded X-ray flux from each target when it was in outburst (fifth column of Table 4.4), providing an upper limit on $h_{0,\text{torque}}$ (sixth column of Table 4.4). We find $5 \times 10^{-28} \lesssim h_{0,\text{torque}} \lesssim 1 \times 10^{-27}$ across all targets.

4.9. Astrophysical implications

The estimates of $h_0^{95\%}$ given in Sec. 4.9.2 can be converted into constraints on the physical parameters that govern the mechanism putatively generating continuous gravitational waves in each sub-band.

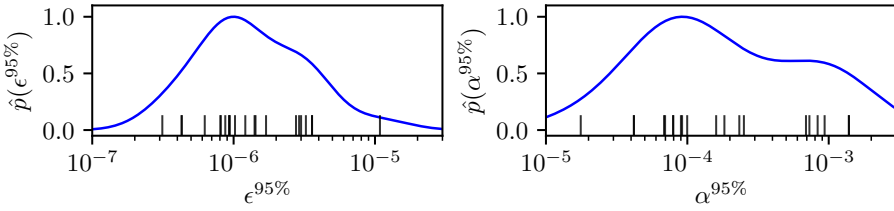


Figure 4.3: Kernel density estimate of the PDF of the constraints on ellipticity $\epsilon^{95\%}$ (left panel) and dimensionless r -mode amplitude $\alpha^{95\%}$ (right panel) via Eqs. (4.14) and (4.15) respectively. Both PDFs are normalized to a height of one. The black dashes in both panels correspond to the individual estimates of $\epsilon^{95\%}$ or $\alpha^{95\%}$ from each target.

2540 In the $2f_\star$ sub-band the simplest emission mechanism is that of a perpendicular bi-
 2541 axial rotator (using the language from Ref. [299]), for which we calculate the upper limit
 2542 of the ellipticity of the neutron star as [208]

$$\epsilon^{95\%} = 2.1 \times 10^{-6} \left(\frac{h_0^{95\%}}{10^{-25}} \right) \left(\frac{D}{8 \text{kpc}} \right) \left(\frac{600 \text{Hz}}{f_{\text{GW}}} \right)^2, \quad (4.14)$$

2543 assuming $I_{zz} = 10^{38} \text{ kg m}^2$. Using the central estimate for D (second column of Table
 2544 4.4), we find the strictest constraint, from all of our targets, $\epsilon^{95\%} = 3.1 \times 10^{-7}$ for IGR
 2545 J00291+5934. A kernel density estimate of the probability density function (PDF) of the
 2546 constraints $\epsilon^{95\%}$, $\hat{p}(\epsilon^{95\%})$, for all our targets, is shown in the left panel of Fig. 4.3. It is
 2547 peaked around $\epsilon^{95\%} \sim 10^{-6}$.

2548 In the $4f_\star/3$ sub-band the emission mechanism is via r -modes, the strength of which
 2549 is parametrized as [300]

$$\alpha^{95\%} = 1.0 \times 10^{-4} \left(\frac{h_0^{95\%}}{10^{-25}} \right) \left(\frac{D}{8 \text{kpc}} \right) \left(\frac{600 \text{Hz}}{f_{\text{GW}}} \right)^3. \quad (4.15)$$

2550 Eq. (4.15) assumes $f_{\text{GW}} \approx 4f_\star/3$, which may not be true, as discussed in Sec. 4.4 [262,
 2551 263]. The strictest constraint, from all of our targets, is $\alpha^{95\%} = 1.8 \times 10^{-5}$, again for IGR
 2552 J00291+5934. A kernel density estimate of the PDF of the constraints $\alpha^{95\%}$, $\hat{p}(\alpha^{95\%})$, for
 2553 all our targets, is shown in the right panel of Fig. 4.3. It is peaked around $\alpha^{95\%} \sim 10^{-4}$.

2554 The kernel density estimates of the PDFs $\hat{p}(\epsilon^{95\%})$ and $\hat{p}(\alpha^{95\%})$ in Fig. 4.3 are not
 2555 constraints on ϵ and α respectively, nor are they expressing the uncertainty in each
 2556 individual estimate of $\epsilon^{95\%}$ or $\alpha^{95\%}$ (which are dominated by the uncertainty in $h_0^{95\%}$,
 2557 and the distance, see column two of Table 4.4). They are instead presented to indicate
 2558 where the constraints on $\epsilon^{95\%}$ and $\alpha^{95\%}$ lie, given the strain upper limits calculated for
 2559 the targets in this search. That is, they are estimates of the true probability distribution
 2560 of the constraints one would obtain for ϵ and α , given a large population of AMXPs
 2561 (assuming the targets studied here are representative of this larger population). The
 2562 kernel density estimates are calculated by summing Gaussian kernels centered on each
 2563 data point, with bandwidth chosen to minimize the asymptotic mean integrated square
 2564 error [144].

2565 The physical mechanism for emission in the f_\star sub-band is less well-defined. A biaxial
 2566 non-perpendicular rotator emits gravitational radiation at both f_\star and $2f_\star$ [208, 256,

2567 [301]. The emission at f_\star dominates the $2f_\star$ emission for both $\theta \lesssim 20^\circ$ and $|\cos i| \lesssim 0.8$,
2568 where θ is the wobble angle (see figure 5 of Ref. [299] for details). The value of θ is
2569 low for certain models involving pinned superfluid interiors [54, 256]. Other possibili-
2570 ties exist, including a triaxial rotator [302–304]. We recommend future searches to also
2571 consider searching the f_\star sub-band, due to the wealth of information that a continuous
2572 gravitational wave detection at this frequency would provide regarding neutron star
2573 structure.

2574 4.10. CONCLUSIONS

2575 We present the results of a search for continuous gravitational waves from 20 accreting
2576 low-mass X-ray binaries in the Advanced LIGO O3 dataset. Five of these targets were
2577 searched before in O2 [186], and one was searched in S6 [203]. The search pipeline we use
2578 allows for spin-wandering and tracks the orbital phase of the binary via a hidden Markov
2579 model and the \mathcal{J} -statistic respectively. The targets have well-constrained rotational fre-
2580 quencies, f_\star , and orbital elements from electromagnetic observations of outburst events,
2581 restricting the parameter space. For each target we search three ~ 0.61 Hz-wide sub-
2582 bands centered on $\{1, 4/3, 2\}f_\star$. We also perform a target-of-opportunity search for emis-
2583 sion from SAX J1808.4–3658, which went into outburst during O3a.

2584 We find no candidates that survive our veto procedure and are above a threshold
2585 corresponding to a 1% false alarm probability per sub-band. We find 16 candidates that
2586 survive our astrophysical vetoes when we set the threshold to 30% false alarm probability
2587 per sub-band. As we search a total of 60 sub-bands, this number of surviving candidates
2588 is consistent with the expected number of false alarms. These candidates are systemat-
2589 ically investigated with further follow-up. In all cases, the follow-up does not provide
2590 convincing evidence that any are real astrophysical signals. However, they could not be
2591 convincingly ruled out, which is not surprising given their borderline significance. We
2592 record the orbital template and frequencies recovered for these candidates, and recom-
2593 mend that they are followed up in future gravitational wave data sets, and with different
2594 pipelines.

2595 The target-of-opportunity search returns one candidate above threshold that sur-
2596 vives our veto procedure. Additional, detailed follow-up of this candidate does not pro-
2597 duce convincing evidence that it is a true astrophysical signal rather than a noise fluc-
2598 tuation.

2599 Assuming all of the candidates are not astrophysical, we set upper limits on the
2600 strain at 95% confidence in each sub-band. Using these estimates, the strictest constraint
2601 on neutron star ellipticity is $\epsilon^{95\%} = 3.1 \times 10^{-7}$. The strictest constraint we place on
2602 the r -mode amplitude is $\alpha^{95\%} = 1.8 \times 10^{-5}$. Both of these constraints come from IGR
2603 J00291+5934.

2604 ACKNOWLEDGMENTS

2605 This material is based upon work supported by NSF’s LIGO Laboratory which is a ma-
2606 jor facility fully funded by the National Science Foundation. The authors also grate-
2607 fully acknowledge the support of the Science and Technology Facilities Council (STFC)

of the United Kingdom, the Max-Planck-Society (MPS), and the State of Niedersachsen/Germany for support of the construction of Advanced LIGO and construction and operation of the GEO600 detector. Additional support for Advanced LIGO was provided by the Australian Research Council. The authors gratefully acknowledge the Italian Istituto Nazionale di Fisica Nucleare (INFN), the French Centre National de la Recherche Scientifique (CNRS) and the Netherlands Organization for Scientific Research, for the construction and operation of the Virgo detector and the creation and support of the EGO consortium. The authors also gratefully acknowledge research support from these agencies as well as by the Council of Scientific and Industrial Research of India, the Department of Science and Technology, India, the Science & Engineering Research Board (SERB), India, the Ministry of Human Resource Development, India, the Spanish Agencia Estatal de Investigación, the Vicepresidència i Conselleria d'Innovació, Recerca i Turisme and the Conselleria d'Educació i Universitat del Govern de les Illes Balears, the Conselleria d'Innovació, Universitats, Ciència i Societat Digital de la Generalitat Valenciana and the CERCA Programme Generalitat de Catalunya, Spain, the National Science Centre of Poland and the Foundation for Polish Science (FNP), the Swiss National Science Foundation (SNSF), the Russian Foundation for Basic Research, the Russian Science Foundation, the European Commission, the European Regional Development Funds (ERDF), the Royal Society, the Scottish Funding Council, the Scottish Universities Physics Alliance, the Hungarian Scientific Research Fund (OTKA), the French Lyon Institute of Origins (LIO), the Belgian Fonds de la Recherche Scientifique (FRS-FNRS), Actions de Recherche Concertées (ARC) and Fonds Wetenschappelijk Onderzoek – Vlaanderen (FWO), Belgium, the Paris Île-de-France Region, the National Research, Development and Innovation Office Hungary (NKFIH), the National Research Foundation of Korea, the Natural Science and Engineering Research Council Canada, Canadian Foundation for Innovation (CFI), the Brazilian Ministry of Science, Technology, and Innovations, the International Center for Theoretical Physics South American Institute for Fundamental Research (ICTP-SAIFR), the Research Grants Council of Hong Kong, the National Natural Science Foundation of China (NSFC), the Leverhulme Trust, the Research Corporation, the Ministry of Science and Technology (MOST), Taiwan, the United States Department of Energy, and the Kavli Foundation. The authors gratefully acknowledge the support of the NSF, STFC, INFN and CNRS for provision of computational resources. This work was supported by MEXT, JSPS Leading-edge Research Infrastructure Program, JSPS Grant-in-Aid for Specially Promoted Research 26000005, JSPS Grant-in-Aid for Scientific Research on Innovative Areas 2905: JP17H06358, JP17H06361 and JP17H06364, JSPS Core-to-Core Program A. Advanced Research Networks, JSPS Grant-in-Aid for Scientific Research (S) 17H06133, the joint research program of the Institute for Cosmic Ray Research, University of Tokyo, National Research Foundation (NRF) and Computing Infrastructure Project of KISTI-GSDC in Korea, Academia Sinica (AS), AS Grid Center (ASGC) and the Ministry of Science and Technology (MoST) in Taiwan under grants including AS-CDA-105-M06, Advanced Technology Center (ATC) of NAOJ, and Mechanical Engineering Center of KEK.

This work is supported by NASA through the NICER mission and the Astrophysics Explorers Program and uses data and software provided by the High Energy Astrophysics Science Archive Research Center (HEASARC), which is a service of the Astrophysics Science Division at NASA/GSFC and High Energy Astrophysics Division of the

2655

4.A1. THRESHOLD SETTING

2656 In this Appendix we outline two alternative methods to set thresholds for the search.
 2657 In Appendix 4.A1.1 we detail the method in Ref. [185] to set thresholds by modeling
 2658 the tail of the log-likelihood distribution in noise as an exponential. In Appendix 4.A1.2
 2659 we review the non-parametric method in Refs. [172, 173, 186, 199, 305], which takes a
 2660 certain percentile detection statistic from noise-only realizations as the threshold. We
 2661 compare the methods in Appendix 4.A1.3. In Appendix 4.A1.4 we discuss generating
 2662 noise realizations using off-target searches, and justify the approach taken in this paper.
 2663 In Appendix 4.A1.5 we specify how to calculate p_{noise} , the probability that we see a value
 2664 of \mathcal{L} at least as high as a certain candidate in a given sub-band.

2665 Whatever the method, the threshold depends on both the target's projected semi-
 2666 major axis, a_0 , and the sub-band frequency, f , as log-likelihoods depend non-linearly on
 2667 $a_0 f$ as an increased number orbital sidebands are included in the \mathcal{J} -statistic at higher
 2668 $a_0 f$ [see equation (6) in Ref. [185] and Ref. [8] for details]. For this reason we set thresh-
 2669 olds independently for each target and sub-band.

2670

4.A1. Exponential tail method

2671 The PDF of the log-likelihood, $p(\mathcal{L})$, for the most likely path for a given template is
 2672 observed to have an exponentially distributed tail in noise,

$$p(\mathcal{L}) = A \lambda \exp[-\lambda(\mathcal{L} - \mathcal{L}_{\text{tail}})] \quad \text{for } \mathcal{L} > \mathcal{L}_{\text{tail}}, \quad (4.16)$$

2673 where A is a normalization constant, λ is a parameter to be found empirically, and $\mathcal{L}_{\text{tail}}$
 2674 is a cut-off that must also be determined empirically.

2675 For each target and sub-band we estimate λ and $\mathcal{L}_{\text{tail}}$ using a set of M sample log-
 2676 likelihoods, a subset of which have $\mathcal{L} > \mathcal{L}_{\text{tail}}$. This subset is denoted $S_{N_{\text{tail}}} \equiv \{\mathcal{L}_i\}$, $i \in$
 2677 $\{1, \dots, N_{\text{tail}}\}$. The entire set of M samples is generated by running the search on $N_G = 100$
 2678 realizations of Gaussian noise. To keep N_G small enough to be computationally feasible
 2679 we include log-likelihoods from all possible Viterbi paths through the sub-band for each
 2680 template, instead of just the log-likelihood from the most likely path. Thus, we have
 2681 $M = N_G N_f N_B$, where $N_f = 2^{20}$ is the number of frequency bins in each sub-band,
 2682 and N_B is the number of binary orbital templates needed for each individual sub-band,
 2683 as listed in Table 4.2. Separate tests, not shown here, indicate that including the log-
 2684 likelihoods from non-maximal paths does not change the shape of $p(\mathcal{L})$, and therefore
 2685 does not change the thresholds \mathcal{L}_{th} , if the appropriate trials factor is taken into account.

2686 Assuming each \mathcal{L}_i is independent, the maximum likelihood estimator, $\hat{\lambda}$, for λ is

$$\hat{\lambda} = \frac{N_{\text{tail}}}{\sum_{i=1}^{N_{\text{tail}}} (\mathcal{L}_i - \mathcal{L}_{\text{tail}})} . \quad (4.17)$$

2687 The normalization $A = N_{\text{tail}}/M$ is fixed via the fraction of total samples used to construct
 2688 $p(\mathcal{L})$. The cut-off $\mathcal{L}_{\text{tail}}$ is estimated in each sub-band as the smallest value \mathcal{L}^* where a
 2689 histogram of the samples $\mathcal{L}_i > \mathcal{L}^*$ has approximately constant slope when viewed on

2690 log-linear axes. Each \mathcal{L}_i is independent for the long coherence times ($T_{\text{drift}} = 10 \text{ d}$) used
 2691 in this search, as $N_T \ll N_f$ implies most optimal paths through the sub-band are not
 2692 correlated.

2693 The probability, α , that \mathcal{L} is above some threshold $\mathcal{L}_{\text{th}} > \mathcal{L}_{\text{tail}}$ if no signal is present
 2694 (i.e. in pure noise) is

$$\int_{\mathcal{L}_{\text{th}}}^{\infty} d\mathcal{L} p(\mathcal{L}) = \alpha. \quad (4.18)$$

2695 Combining Eqs. (4.8), (4.16), and (4.18) we solve for \mathcal{L}_{th} in a given sub-band, viz.

$$\mathcal{L}_{\text{th}} = -\frac{1}{\hat{\lambda}} \log \left(\frac{N_G \alpha_{N_{\text{tot}}}}{N_{\text{tail}}} \right) + \mathcal{L}_{\text{tail}}, \quad (4.19)$$

2696 where Eq. (4.8) is simplified via the binomial approximation ($N_{\text{tot}} = N_f N_B \gg 1$), and
 2697 $\alpha_{N_{\text{tot}}}$ is the desired false alarm probability for the search over the sub-band. Note Eq. (4.19)
 2698 depends implicitly on the sub-band frequency and N_B , through $\hat{\lambda}$ and N_{tail} .

2699 Across all targets and sub-bands we find $0.195 < \hat{\lambda} < 0.248$, with larger values
 2700 corresponding to higher frequency sub-bands, and those with larger N_B . A simple rule-
 2701 of-thumb is that, for a median value of $\hat{\lambda} = 0.218$, an increment of ≈ 3 in \mathcal{L} is $\approx 50\%$
 2702 less likely to occur in pure noise.

2703 4.A1. Percentile method

2704 Given a sorted set of most likely log-likelihoods $\{\mathcal{L}_i\}$, $i \in \{1, \dots, M\}$ with $M = N_G N_B$,
 2705 generated via running the search algorithm over N_G realizations of noise for a single
 2706 target and sub-band, one can pick as the threshold the \mathcal{L}_j corresponding to the percentile
 2707 equal to the desired false alarm probability, i.e.

$$\mathcal{L}_{\text{th}} = \mathcal{L}_j, \quad (4.20)$$

2708 with $j = \lfloor \alpha_{N_{\text{tot}}} M \rfloor$. As with the method described in Appendix 4.A1.1 we may opt to
 2709 use the log-likelihoods from all possible Viterbi paths through the sub-band for a given
 2710 orbital template, to reduce the number of realizations of noise we need to generate. With
 2711 this set of log-likelihoods, we have $M = N_G N_f N_B$.

2712 4.A1. Comparison of methods

2713 The two methods described in Appendices 4.A1.1 and 4.A1.2 give broadly similar results
 2714 for \mathcal{L}_{th} for a given probability of false alarm. Ref. [185] opts for the method in Appendix
 2715 4.A1.1. When Viterbi scores are used as the detection statistic, as in Ref. [185], the PDF
 2716 of the score in noise does not vary with frequency, and thus the thresholds in each sub-
 2717 band can be extrapolated from a small set of Gaussian noise realizations. If the PDF of the
 2718 detection statistic varies with target search parameters, then the method in Appendix
 2719 4.A1.2 is used, as in Refs. [172, 173, 186, 305]. The percentile method has inherently fewer
 2720 assumptions, as it does not fit a parametric model to $p(\mathcal{L})$. However it is not possible to
 2721 extrapolate thresholds calculated in one sub-band to other sub-bands.

2722 For our targets and sub-bands, we find $\mathcal{L}_{\text{th}}^e - \mathcal{L}_{\text{th}}^p \approx 2$, where the superscripts e and
 2723 p correspond to the exponential tail and percentile methods respectively. However the

exact difference depends on the realizations of Gaussian noise; Monte Carlo simulations indicate that with $N_G = 100$ the calculated threshold is usually within 2% of the true value, so thresholds should only be considered precise to 2%.

4.4.1. Off-target thresholds

Both methods derive \mathcal{L}_{th} based on realizations of Gaussian noise. However, the noise in real detector data is non-Gaussian in general [269]. To account for this we search O3 data at N_{OT} randomly chosen, but well-separated, off-target positions, to generate N_{OT} realizations of real detector noise, as originally done in Ref. [186]. We set N_{OT} such that $N_B N_{\text{OT}} > 500$, with a minimum value of $N_{\text{OT}} = 100$, to ensure enough samples are generated.

If there are no known noise lines in the sub-band, we find $4 < \mathcal{L}_{\text{th},G}^e - \mathcal{L}_{\text{th},\text{OT}}^p < 12$, where the subscripts G and OT correspond to thresholds calculated using Gaussian and off-target noise realizations respectively. That is, the thresholds calculated from Gaussian noise, using the exponential tail method are considerably more conservative than those calculated from off-target noise and the percentile method. If there are loud noise lines in the sub-band, $\mathcal{L}_{\text{th},\text{OT}}$ is often much higher, as these lines appear in the off-target noise realizations. Because off-target noise realizations are impacted by noise lines, $p(\mathcal{L})$ is not necessarily exponential in its tail. We thus opt to use the percentile method when calculating thresholds with off-target noise realizations. Table 4.5 contains the calculated $\mathcal{L}_{\text{th},G}^e$ and $\mathcal{L}_{\text{th},\text{OT}}^p$ for each target and sub-band.

As in Ref. [186] we consider \mathcal{L}_{th} for each sub-band to be the minimum of $\mathcal{L}_{\text{th},G}^e$ and $\mathcal{L}_{\text{th},\text{OT}}^p$, with $\alpha_{N_{\text{tot}}} = 0.3$. This choice minimizes the probability that we will miss a potential candidate due to inadvertently setting our threshold too high.

4.4.1. Probability that a candidate arises due to noise

As discussed in Sec. 4.4.3, when we set $\alpha_{N_{\text{tot}}} = 0.3$ we expect ~ 18 candidates above \mathcal{L}_{th} , across all targets and sub-bands. Let us quantify empirically the probability, p_{noise} , that, if the data in a given sub-band are pure noise, we see at least one template with log-likelihood higher than that of the candidate, $\mathcal{L}_{\text{cand}}$. We have

$$p_{\text{noise}} = \frac{\sum_{i=1}^M \mathbb{1}(\mathcal{L}_i > \mathcal{L}_{\text{cand}})}{M}, \quad (4.21)$$

where $\mathbb{1}(\dots)$ is the indicator function which returns 1 when the argument is true, otherwise 0. In this paper we calculate Eq. (4.21) for each candidate with $\mathcal{L} > \mathcal{L}_{\text{th}}$ using the set of log-likelihoods, $\{\mathcal{L}_i\}$, generated via off-target realizations as discussed in Appendix 4.A1.4. As in Appendix 4.A1.2, we set $M = N_G N_B$ to account for the extra “trials factor” needed for sub-bands with multiple templates.

4.4.2. FULL SEARCH RESULTS AND SURVIVOR FOLLOW-UP

This Appendix collates the full search results for reference and reproducibility for all targets in Figs. 4.4a–4.4s (except for IGR J18245–2452 which is shown in Fig. 4.2). Each of Figs. 4.4a–4.4s is laid out identically to Fig. 4.2.

2761 The orbital parameters (P , a_0 , and T_{asc}), terminating frequency bin [$f(N_T)$], log-
 2762 likelihood (\mathcal{L}), and p_{noise} , the probability that a search of that candidate's sub-band in
 2763 pure noise would return at least one candidate at least as loud as the one seen are shown
 2764 in Table 4.6, for each of the candidates that survive all vetoes and have $\mathcal{L} > \mathcal{L}_{\text{th}}$.

2765 4.4.2. Additional follow-up for survivors

2766 The full frequency paths, $f(t) - f(N_T)$, for all candidates with $p_{\text{noise}} \leq 0.1$ are shown in
 2767 the top panels of Figs. 4.5a–4.5e. The bottom panels of Figs. 4.5a–4.5e display the cumu-
 2768 lative log-likelihood along the frequency path relative to the average sum log-likelihood
 2769 needed to reach \mathcal{L}_{th} , namely $C\mathcal{L} \equiv \sum_{i=0}^{i=t} [\mathcal{L}(i) - \mathcal{L}_{\text{th}}/N_T]$, where $\sum_{i=0}^{i=t} \mathcal{L}(i)$ is $\ln P(Q^*|O)$
 2770 from Eq. (4.2) truncated after the t -th segment. Over-plotted (blue dashed line) is the
 2771 average cumulative log-likelihood needed at each data segment in order to reach \mathcal{L}_{th} .
 2772 This diagnostic indicates whether a handful of segments dominate in making the candi-
 2773 date's frequency path the optimal one for that template. If the candidate is a true signal,
 2774 we would expect the signal strength to be approximately constant, and thus the cumu-
 2775 lative log-likelihood should grow linearly as more data are considered. However, Monte
 2776 Carlo tests with injections show that the cumulative log-likelihood only becomes lin-
 2777 ear for $\mathcal{L} \gtrsim \mathcal{L}_{\text{th}} + 200$. This is not the case for any of the 16 survivor candidates, and
 2778 thus their cumulative log-likelihood cannot help us distinguish whether they are truly
 2779 astrophysical signals.

2780 The sky resolution of the algorithm described in Sec. 4.2 is roughly 2 arcmin in RA
 2781 and Dec., for an injection with $\mathcal{L}_{\text{th}} \lesssim \mathcal{L} \lesssim \mathcal{L}_{\text{th}} + 50$. The point-spread-function of an
 2782 injection is an ellipse, which has a varying orientation and eccentricity dependent on
 2783 the sky position. For each of our candidates we calculate \mathcal{L} at 440 regularly spaced
 2784 sky positions in a 100 arcmin^2 grid around the target's true location, using the template
 2785 recovered from the search and listed in Table 4.6. For almost all survivor candidates, the
 2786 distribution of \mathcal{L} values in the patch of sky around the candidate does not match the
 2787 elliptical point-spread-function we see in injections for their respective sky locations.
 2788 The sole exception is Candidate 2 from IGR J16597–3704. Figure 4.6 shows \mathcal{L} at 3721
 2789 regularly spaced sky positions in a 100 arcmin^2 grid around the target's true location,
 2790 again using the template as listed in Table 4.6. The roughly elliptical shape is consistent
 2791 with the point-spread-function of injections at this sky location. However, the region of
 2792 sky with $\mathcal{L} \gtrsim \mathcal{L}_{\text{th}}$ is centered ~ 1 arcmin lower in Dec. than the true declination of the
 2793 source, which is known to a precision of 0.01 arcmin [226].

2794 One final follow-up we perform for these candidates is to calculate \mathcal{L} in a small,
 2795 densely sampled patch of the $\{P, T_{\text{asc}}\}$ parameter space around each candidate's tem-
 2796 plate. Moderately loud injections ($\mathcal{L} \gtrsim \mathcal{L}_{\text{th}} + 100$) are seen to “spread out” in the $\{P, T_{\text{asc}}\}$
 2797 plane, and are detectable with $\mathcal{L} > \mathcal{L}_{\text{th}}$ even when searching a template that has a slightly
 2798 incorrect value of P and T_{asc} . However, none of our candidates are this loud, so this di-
 2799 agnostic does not help us distinguish whether they are truly astrophysical signals or
 2800 merely noise fluctuations.

2801 We do not use any data from LIGO's Observing Runs 1 or 2 (O1 and O2 respectively)
 2802 to aid in following up these candidates, as the detector is considerably more sensitive in
 2803 O3. The duration of O3 was also longer than the durations of O1 and O2. If a candidate is
 2804 only marginally above threshold in O3 data, it may be hidden in the noise in O1 and O2

2805 data, so including data from those observing runs is not likely to increase the candidate's
2806 signal-to-noise ratio.

2807 4.A3. SURVIVOR FOLLOW-UP FOR TARGET-OF-OPPORTUNITY 2808 SEARCH CANDIDATE

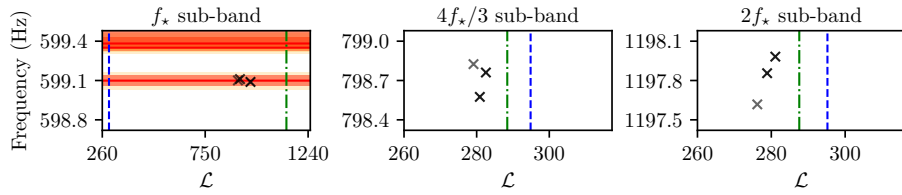
2809 For posterity, and to aid future follow-up with different pipelines, we record in Table 4.7
2810 the template, the frequency f , the log-likelihood \mathcal{L} , and p_{noise} , of the candidate from the
2811 target-of-opportunity search in Sec. 4.8 that survives all vetoes.

2812 As in Appendix 4.A2.1, we perform additional follow-up for this remaining candidate.
2813 With $T_{\text{obs}} = 24 \text{ d}$ the point-spread-function of a moderately loud injection ($\mathcal{L} \gtrsim \mathcal{L}_{\text{th}} + 20$),
2814 at the sky location of the target, is a narrow ellipse $\sim 2 \text{ arcmin}$ wide in RA, but over
2815 $\sim 30 \text{ arcmin}$ tall in Dec. When we search a 100 arcmin^2 patch of sky around the location
2816 of SAX J1808.4–3658 we do not see any evidence of this point-spread-function at the
2817 source location. There is an ellipse with $\mathcal{L} > \mathcal{L}_{\text{th}}$ roughly -2 arcmin away in RA from
2818 SAX J1808.4–3658, but as the location of the target is known to sub-arcsec precision
2819 [217], this ellipse is likely a noise fluctuation, rather than an astrophysical signal.

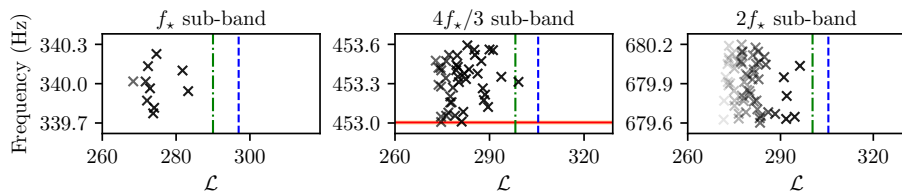
2820 We also calculate \mathcal{L} in a small, densely sampled patch of the $\{P, T_{\text{asc}}\}$ parameter
2821 space around the candidate's template. As discussed in Appendix 4.A2.1, moderately
2822 loud injections ($\mathcal{L} \gtrsim \mathcal{L}_{\text{th}} + 20$) “spread out” in the $\{P, T_{\text{asc}}\}$ plane. However, the candidate
2823 is not loud enough for this diagnostic to provide evidence for or against the hypothesis
2824 that the candidate is a noise fluctuation.

2825 If we assume that the remaining candidate is a false alarm, we calculate $h_0^{95\%}$ for
2826 the 24 d coherent search, using the procedure outlined in Sec. 4.9.1. We find $h_0^{95\%} =$
2827 1.3×10^{-25} for the sub-bands centered on f_\star and $4f_\star/3$, and $h_0^{95\%} = 1.7 \times 10^{-25}$ for
2828 the sub-band centered on $2f_\star$. These upper limits are higher than the ones listed in
2829 Sec. 4.9.2 because the longer coherence time does not completely compensate for the
2830 shorter observation time.

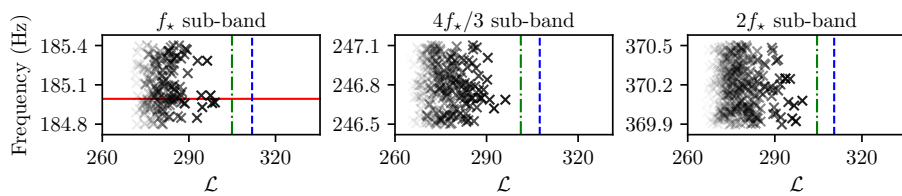
2831 Finally, we perform a complementary follow-up search using a deterministic signal
2832 template on the candidate of interest using PyFstat [306, 307]. The use of the PyFstat
2833 algorithm as a follow-up technique was applied to the last surviving outlier of Ref. [182]
2834 and previously in Refs. [177, 308]. The follow-up procedure, thoroughly described in
2835 Ref. [309], uses a Markov chain Monte Carlo (MCMC) sampler [310, 311] to explore a
2836 parameter-space region using the \mathcal{F} -statistic as log-likelihood [208]. Two coherence
2837 times are used here, namely $T_{\text{coh}} = 12 \text{ d}$ and $T_{\text{coh}} = 24 \text{ d}$. Prior distributions are Gaus-
2838 sian distributions centered at the outlier parameters (Table 4.7) using a standard devia-
2839 tion of one parameter-space bin with maximum mismatch $\mu_{\text{max}} = 1$ [268]. The results
2840 of the follow-up are evaluated using a Bayes factor, $\mathcal{B}_{\text{S/N}}$, that compares the evidence
2841 for a model that the data contain a coherent signal to the evidence for a model that the
2842 data contain only noise. The value of $\mathcal{B}_{\text{S/N}}$ is computed by comparing the change in
2843 the \mathcal{F} -statistic of the loudest candidate between the two follow-up stages with different
2844 coherence times: if a signal is present in the data, the \mathcal{F} -statistic should provide a con-
2845 sistent estimate of the signal-to-noise ratio; otherwise, the loudest candidate is a result
2846 of noise, the distribution of which follows a Gumbel distribution. This noise distribution
2847 is estimated using a similar method to the one described in Appendix 4.A1.4, with 600



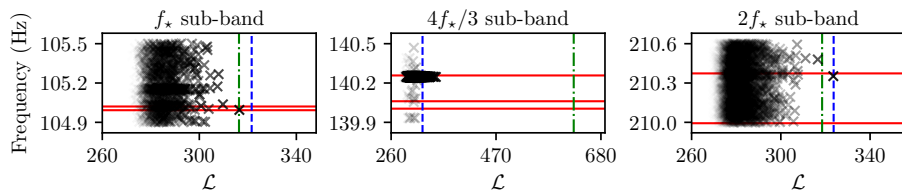
(a) Search results for IGR J00291+5934.



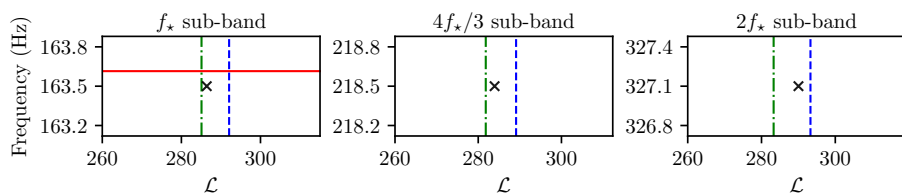
(b) Search results for MAXI J0911-655.



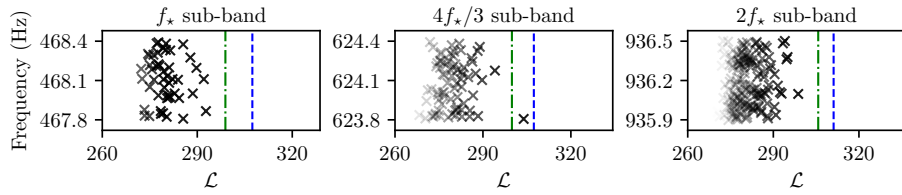
(c) Search results for XTE J0929-314.



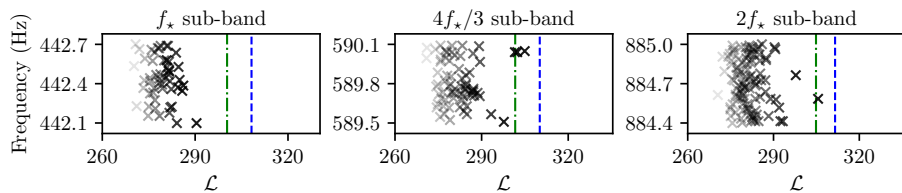
(d) Search results for IGR J16597-3704.



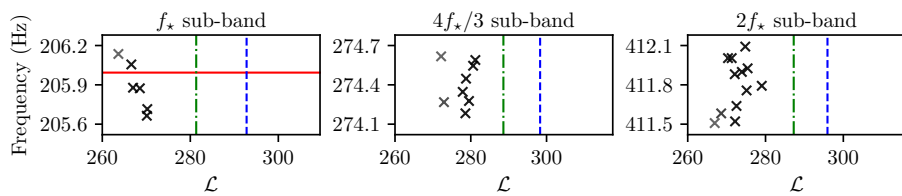
(e) Search results for IGR J17062-6143.



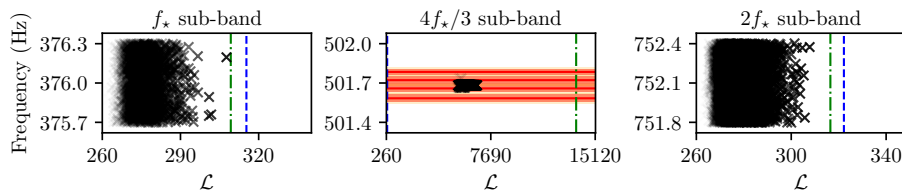
(f) Search results for IGR J17379–3747.



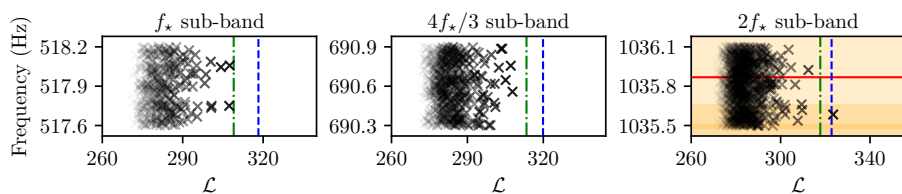
(g) Search results for SAX J1748.9–2021.



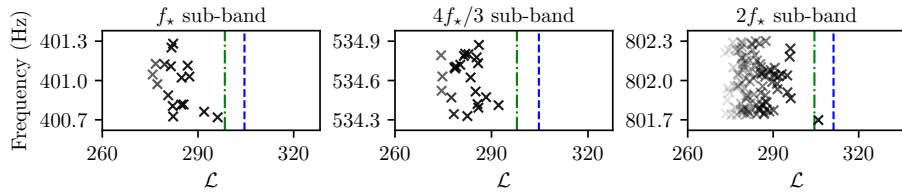
(h) Search results for NGC 6440 X–2.



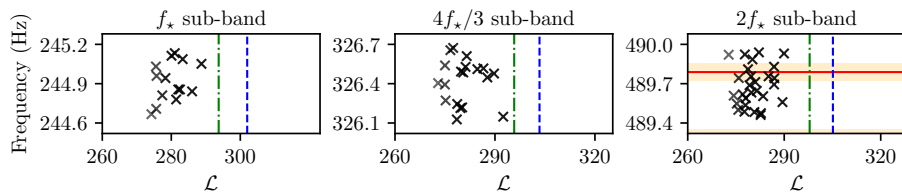
(i) Search results for IGR J17494–3030.



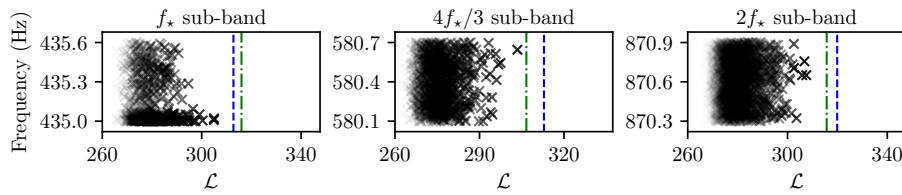
(j) Search results for Swift J1749.4–2807.



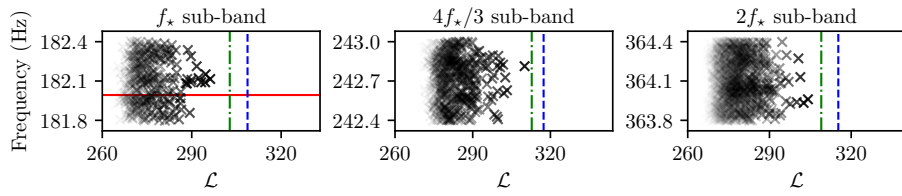
(k) Search results for IGR J17498–2921.



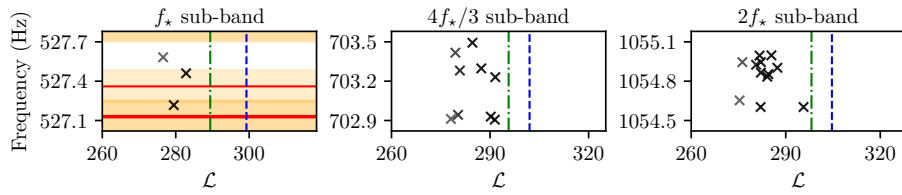
(l) Search results for IGR J17511–3057.



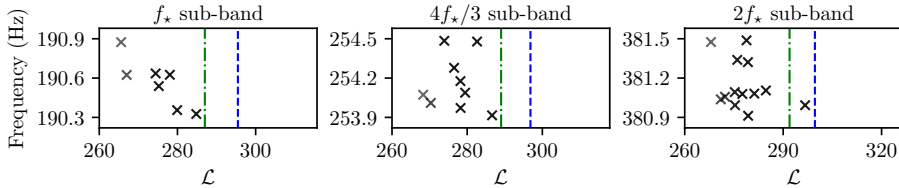
(m) Search results for XTE J1751–305.



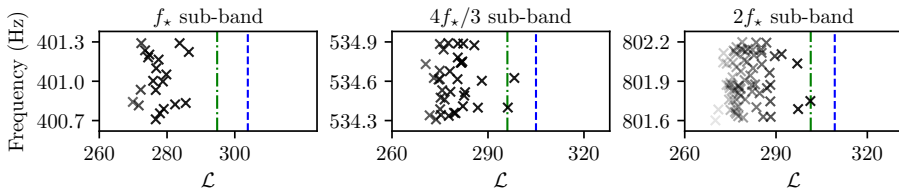
(n) Search results for Swift J1756.9–2508.



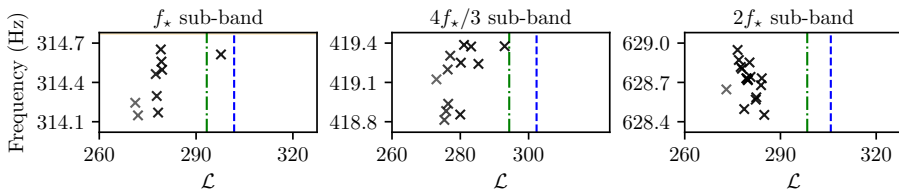
(o) Search results for IGR J17591–2342.



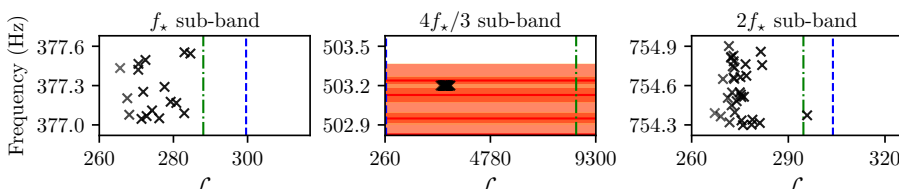
(p) Search results for XTE J1807–294.



(q) Search results for SAX J1808.4–3658.



(r) Search results for XTE J1814–338.



(s) Search results for HETE J1900.1–2455.

Figure 4.4: Search results for each target and sub-band, laid out as in Fig 4.2. Black crosses indicate the frequency and \mathcal{L} for the most likely path through the sub-band for each binary template. The vertical blue dashed (green dot-dashed) lines correspond to the threshold set via Gaussian (off-target) noise realizations, $\mathcal{L}_{\text{th},G}$ ($\mathcal{L}_{\text{th},\text{OT}}$), in each sub-band. Solid red lines indicate the peak frequency of known instrumental lines in the Hanford or Livingston detectors; the red band indicates the width of the line and the yellow band indicates the increased effective width due to Doppler broadening, as described in Sec. 4.6.1. Multiple overlapping orange bands creates the red bands. The transparency of crosses in sub-bands with many templates, e.g. the sub-bands of IGR J16597–3704, is adjusted relative to the maximum \mathcal{L} in that sub-band for clarity.

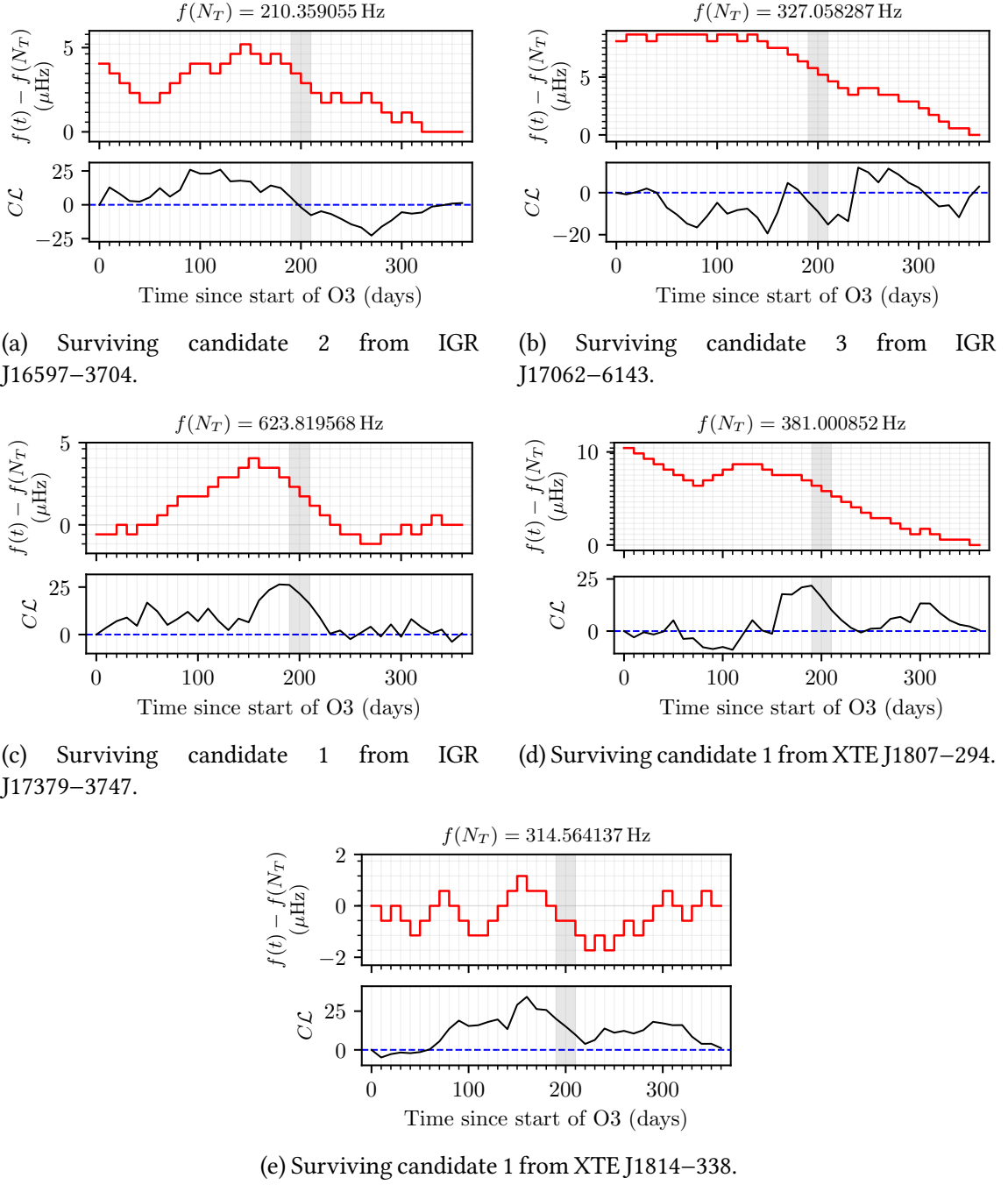


Figure 4.5: Top panels: frequency paths, $f(t)$, for candidates with $p_{\text{noise}} \leq 0.1$. The terminating frequency bin, $f(N_T)$, is subtracted and displayed in the title of each figure for clarity. Faint horizontal grey lines demarcate frequency bins of size $\Delta f = 5.787037 \times 10^{-7} \text{ Hz}$, while faint vertical grey lines demarcate chunks of length $T_{\text{drift}} = 10 \text{ d}$. Bottom panels: the cumulative log-likelihood along the frequency path relative to the average sum log-likelihood needed to reach \mathcal{L}_{th} , $C\mathcal{L} \equiv \sum_{i=0}^{t=t} [\mathcal{L}(i) - \mathcal{L}_{\text{th}}/N_T]$, where $\sum_{i=0}^{t=t} \mathcal{L}(i)$ is $\ln P(Q^*|O)$ from Eq. (4.2) truncated after the t -th segment. The horizontal blue dashed line corresponds to $\sum_{i=0}^{t=t} \mathcal{L}(i) = t\mathcal{L}_{\text{th}}/N_T$. The grey shaded regions in both top and bottom panels correspond to the segments which have no SFTs and are therefore filled with a uniform log-likelihood, as described in Sec. 4.5.

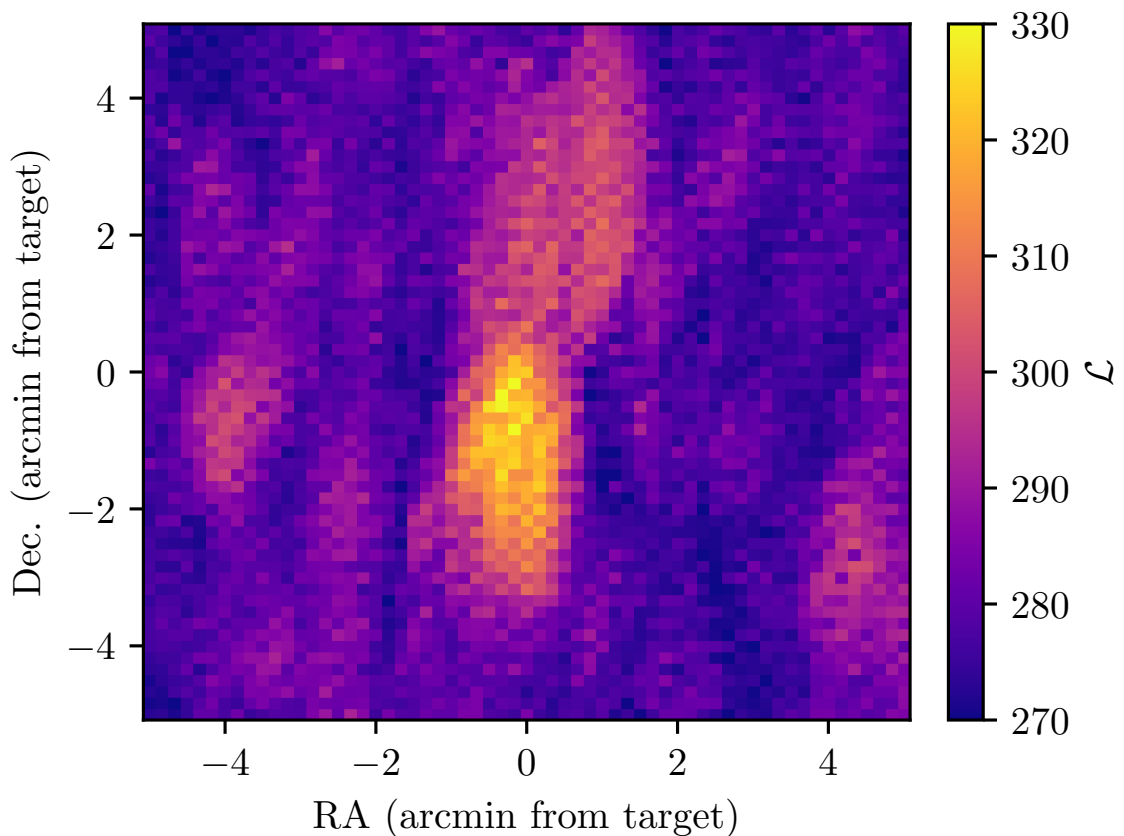


Figure 4.6: \mathcal{L} , as represented by the color of each pixel, calculated at 3721 regularly spaced sky locations in a 100 arcmin² patch of sky, centered on IGR J16597–3704. See text in Appendix 4.A2.1 for details.

2848 off-source calculations performed.

2849 The loudest candidate of the follow-up returns a log-Bayes factor of $\log_{10} \mathcal{B}_{S/N} =$
2850 1.45. We characterize the $\log_{10} \mathcal{B}_{S/N}$ distribution using 400 isotropically distributed
2851 sources injected into the real data with an amplitude of $h_0^{95\%}$. We obtain a 1% false
2852 dismissal threshold of 8.75, which is significantly larger than the candidate's log-Bayes
2853 factor of 1.45. That is, if this were a true signal, with $h_0 = h_0^{95\%}$, we would expect the
2854 log-Bayes factor to be higher than what we see in the real data by about 7. We conclude
2855 that there is no significant evidence of continuous gravitational wave emission from this
2856 target.

Table 4.4: Maximum expected strain from each target, as inferred from EM observations. The second estimate for the distance to the target. Targets with “-” listed as the frequency derivative (third column), \dot{f}_\star value during outburst, and also do not have a long-term (quiescent) \dot{f}_\star measured either. The labels (A) measured in outburst and quiescence respectively. The scaling equations used to estimate the maximum column), $h_{0,\text{sd}}$, and the maximum strain assuming torque-balance (sixth column), $h_{0,\text{torque}}$, are Eqs. (4.12) and (4.13). The $h_{0,\text{sd}}$ value is calculated using the central distance and \dot{f}_\star estimates. The $h_{0,\text{torque}}$ value is calculated using the X-ray flux measured during outburst (fifth column), $F_{X,\text{max}}$, which is typically measured to a precision of $\sim 10\%$. The value of $h_{0,\text{sd}}$ for each target in quiescence is not shown, as it is only measured for half of the targets, and is usually $\sim 1 - 2$ times smaller than $F_{X,\text{max}}$. The seventh column contains $h_0^{95\%}$ in the $2f_\star$ sub-band (fourth column of Table 4.3) to facilitate comparison with $h_0^{95\%}$ and $h_{0,\text{torque}}$ or $h_{0,\text{sd}}$.

Target	Distance (kpc)	\dot{f}_\star (Hz s ⁻¹)	$h_{0,\text{sd}}$ ($\times 10^{-26}$)	$F_{X,\text{max}}$ ($\times 10^{-8}$ erg s ⁻¹ cm ⁻²)	$h_{0,\text{torque}}$ ($\times 10^{-26}$)	$h_0^{95\%}$ ($\times 10^{-26}$)
IGR J00291+5934	4.2(5)	$-4.0(1.4) \times 10^{-15}$ (Q)	0.05	0.35	0.2	
MAXI J0911–655	9.45(15)	-	-	0.047	0.1	
XTE J0929–314	7.4 ^a	$-9.2(4) \times 10^{-14}$ (A)	0.2	0.1	0.2	
IGR J16597–3704	9.1 ^b	-	-	0.065	0.2	
IGR J17062–6143	7.3(5)	$+3.77(9) \times 10^{-15}$ (A)	0.04 ^f	0.006	0.05	
IGR J17379–3747	8 ^c	$-1.2(1.9) \times 10^{-14}$ (A)	0.05	0.04	0.08	
SAX J1748.9–2021	8.5 ^b	-	-	0.077	0.1	
NGC 6440 X–2	8.5 ^b	-	-	0.02	0.09	
IGR J17494–3030	8 ^c	$-2.1(7) \times 10^{-14}$ (Q)	0.07	0.0143	0.05	
Swift J1749.4–2807	6.7(1.3)	-	-	0.0352	0.07	
IGR J17498–2921	7.6(1.1)	$-6.3(1.9) \times 10^{-14}$ (A)	0.1	0.2	0.2	
IGR J17511–3057	3.6(5)	$+4.8(1.4) \times 10^{-14}$ (A)	0.2 ^f	0.2	0.2	
XTE J1751–305	6.7 ^d	$-5.5(1.2) \times 10^{-15}$ (Q)	0.04	0.29	0.2	
		$+3.7(1.0) \times 10^{-13}$ (A)	0.2 ^f			
Swift J1756.9–2508	8 ^c	$-4.8(6) \times 10^{-16}$ (Q)	0.02	0.288	0.3	
		$-4.3(2.1) \times 10^{-11}$ (A)	5			
IGR J17591–2342	7.6(7)	$-7.1(4) \times 10^{-14}$ (A)	0.1	0.0535	0.09	
XTE J1807–294	8 ^c	$+2.7(1.0) \times 10^{-14}$ (A)	0.08 ^f	0.2	0.3	
SAX J1808.4–3658	$3.3^{+0.3}_{-0.2}$	$-1.01(7) \times 10^{-15}$ (Q)	0.04	0.103	0.1	
		$-3.02(13) \times 10^{-13}$ (A)	0.7			
XTE J1814–338	10.25(1)	$-6.7(7) \times 10^{-14}$ (A)	0.1	0.069	0.1	
IGR J18245–2452	5.5 ^b	-	-	0.0466	0.1	
HETE J1900.1–2455	4.5(2)	$+4.2(1) \times 10^{-13}$ (A)	0.4 ^f	0.09	0.1	

^a Estimate assumes conservative mass transfer during accretion. An alternative estimate gives less than 10% of this.

^b Uncertainty not quoted as target located in a globular cluster.

^c Unknown, but as the target is in the direction of the galactic centre a fiducial value of 8 kpc is assumed.

^d Lower limit.

^e Estimate of \dot{f}_\star consistent with zero at a 3σ level.

^f Assumes $\dot{f}_{\text{GW}} \approx -\dot{f}_\star$, see text for details.

Table 4.5: Target, starting frequency, f_s , for each ~ 0.61 Hz-wide sub-band, threshold calculated using Gaussian noise realizations and the exponential tail method, $\mathcal{L}_{\text{th},G}^e$, and threshold calculated using off-target noise realizations and the percentile method, $\mathcal{L}_{\text{th},\text{OT}}^p$. All thresholds are calculated with $\alpha_{N_{\text{tot}}} = 0.3$.

Target	f_s (Hz)	$\mathcal{L}_{\text{th},G}^e$	$\mathcal{L}_{\text{th},\text{OT}}^p$	Target	f_s (Hz)	$\mathcal{L}_{\text{th},G}^e$
IGR J00291+5934	598.6	291.9	1136.7	IGR J17498–2921	400.7	304.
	798.2	294.9	288.4		534.4	304.
	1197.5	295.2	287.6		801.7	311.
MAXI J0911–655	339.7	297.0	290.0	IGR J17511–3057	244.5	302.
	453.0	305.4	298.2		326.1	303.
	679.6	305.5	300.4		489.4	305.
XTE J0929–314	184.8	311.9	304.9	XTE J1751–305	435.0	312.
	246.5	307.4	301.2		580.1	312.
	369.9	310.4	304.5		870.3	319.
IGR J16597–3704	104.9	321.6	316.4	Swift J1756.9–2508	181.8	308.
	139.9	322.9	625.5		242.5	317.
	210.0	323.7	318.5		363.8	315.
IGR J17062–6143	163.4	292.1	285.1	IGR J17591–2342	527.1	299.
	217.9	289.1	281.8		702.9	302.
	327.0	293.3	283.3		1054.5	304.
IGR J17379–3747	467.8	307.4	298.9	SAX J1808.4–3658	400.7	303.
	623.8	307.4	299.9		534.3	305.
	935.9	311.1	305.7		801.6	309.
SAX J1748.9–2021	442.1	308.2	300.3	XTE J1807–294	190.3	295.
	589.5	310.1	301.6		253.9	296.
	884.4	311.5	304.9		380.9	299.
NGC 6440 X–2	205.6	292.8	281.3	XTE J1814–338	314.1	301.
	274.2	298.3	288.6		418.8	302.
	411.5	295.9	287.2		628.4	305.
IGR J17494–3030	375.7	315.3	309.3	IGR J18245–2452	254.0	311.
	501.1	317.5	13763.8		338.8	312.
	751.8	322.2	316.5		508.4	317.
Swift J1749.4–2807	517.6	316.4	308.8	HETE J1900.1–2455	377.0	299.
	690.3	318.4	311.9		502.8	303.
	1035.5	321.0	316.3		754.3	303.

Table 4.6: Orbital template, (P , a_0 , T_{asc}), terminating frequency bin, $f(N_T)$, log-likelihood, \mathcal{L} , and the probability that a search of the candidate’s sub-band in pure noise would return a candidate just as loud, p_{noise} , for the 16 candidates with $\mathcal{L} > \mathcal{L}_{\text{th}}$ that cannot be eliminated by any of the vetoes detailed in Sec. 4.6.

Target	Candidate	P (s)	a_0 (lt-s)	T_{asc} (GPS time)	$f(N_T)$ (Hz)	\mathcal{L}	p_{noise}
MAXI J0911–655	1	2659.933	0.0176	1238165869.0437	453.309532	299.2	0.26
IGR J16597–3704	1	2758.61	0.0048	1238163275.6122	105.002195	316.5	0.30
	2	2757.90	0.0048	1238163010.7583	210.359055	323.5	0.09
IGR J17062–6143	1	2278.2112	0.0040	1238165942.2745	163.531805	286.4	0.24
	2	2278.2112	0.0040	1238165942.2745	218.452091	283.9	0.19
	3	2278.2112	0.0040	1238165942.2745	327.058287	290.0	0.05
IGR J17379–3747	1	6765.84	0.0770	1238162768.3832	623.819568	303.9	0.08
SAX J1748.9–2021	1	31555.29	0.3876	1238151700.2214	590.048237	304.9	0.12
	2	31555.30	0.3876	1238151760.9764	590.040010	302.3	0.27
	3	31555.31	0.3876	1238151710.6406	884.592276	305.6	0.22
IGR J17498–2921	1	13835.619	0.36517	1238164013.8774	801.703605	305.8	0.22
XTE J1807–294	1	2404.416	0.00483	1238165585.2721	381.000852	296.7	0.10
SAX J1808.4–3658	1	7249.15	0.0628	1238161168.0040	534.633578	298.2	0.16
	2	7249.16	0.0628	1238161183.0831	534.407934	296.2	0.30
XTE J1814–338	1	15388.723	0.3906	1238151585.3941	314.564137	297.7	0.08
HETE J1900.1–2455	1	4995.26	0.0184	1238161529.0866	754.378543	295.8	0.25

Table 4.7: Orbital template, (P , a_0 , T_{asc}), frequency, f , log-likelihood, \mathcal{L} , and the probability of seeing a candidate at least this loud in pure noise, p_{noise} , for the remaining candidate from the target-of-opportunity, 24 d coherent search when SAX J1808.4–3658 was in outburst. The candidate cannot be eliminated by any of the vetoes detailed in Sec. 4.6.

P (s)	a_0 (lt-s)	T_{asc} (GPS time)	f (Hz)	\mathcal{L}	p_{noise}
7249.155	0.062809	1249163578.03125	400.59656098	42.5	0.02

References

- ²⁸⁶⁰¹J. B. Carlin and A. Melatos, “Autocorrelations in pulsar glitch waiting times and sizes”,
²⁸⁶¹Monthly Notices of the Royal Astronomical Society **488**, 4890–4896 (2019).

²⁸⁶²²W. Fulgenzi, A. Melatos, and B. D. Hughes, “Radio pulsar glitches as a state-dependent
²⁸⁶³Poisson process”, Monthly Notices of the Royal Astronomical Society **470**, 4307–4329
²⁸⁶⁴(2017).

²⁸⁶⁵³J. B. Carlin and A. Melatos, “Generating quasi-periodic pulsar glitches using a state-
²⁸⁶⁶dependent Poisson process”, Monthly Notices of the Royal Astronomical Society **483**,
²⁸⁶⁷4742–4750 (2019).

²⁸⁶⁸⁴J. B. Carlin and A. Melatos, “Long-term statistics of pulsar glitches triggered by a
²⁸⁶⁹Brownian stress accumulation process”, Monthly Notices of the Royal Astronomical
²⁸⁷⁰Society **494**, 3383–3391 (2020).

²⁸⁷¹⁵J. B. Carlin and A. Melatos, “Long-term Statistics of Pulsar Glitches Due to History-
²⁸⁷²dependent Avalanches”, The Astrophysical Journal **917**, 1 (2021).

²⁸⁷³⁶LIGO Scientific Collaboration et al., “Search for continuous gravitational waves from
²⁸⁷⁴20 accreting millisecond x-ray pulsars in O3 LIGO data”, Physical Review D **105**,
²⁸⁷⁵022002 (2022).

²⁸⁷⁶⁷S. Suvorova, L. Sun, A. Melatos, W. Moran, and R. J. Evans, “Hidden Markov model
²⁸⁷⁷tracking of continuous gravitational waves from a neutron star with wandering spin”,
²⁸⁷⁸Physical Review D **93**, 123009 (2016).

²⁸⁷⁹⁸S. Suvorova, P. Clearwater, A. Melatos, L. Sun, W. Moran, and R. J. Evans, “Hidden
²⁸⁸⁰Markov model tracking of continuous gravitational waves from a binary neutron star
²⁸⁸¹with wandering spin. II. Binary orbital phase tracking”, Physical Review D **96**, 102006
²⁸⁸²(2017).

²⁸⁸³⁹M. Millhouse, A. Melatos, G. Howitt, J. B. Carlin, L. Dunn, and G. Ashton, “An updated
²⁸⁸⁴glitch rate law inferred from radio pulsars”, Monthly Notices of the Royal Astronomical
²⁸⁸⁵Society **511**, 3304–3319 (2022).

²⁸⁸⁶¹⁰D. Jones et al., “Validating continuous gravitational-wave candidates from a semi-
²⁸⁸⁷coherent search using Doppler modulation and an effective point spread function”,
²⁸⁸⁸Physical Review D **106**, 123011 (2022).

- 2889 ¹¹J. M. Cordes and D. J. Helfand, “Pulsar timing. III - Timing noise of 50 pulsars”, *The
2890 Astrophysical Journal* **239**, 640–650 (1980).
- 2891 ¹²S. Price, B. Link, S. N. Shore, and D. J. Nice, “Time-correlated structure in spin fluctua-
2892 tions in pulsars: Time-correlated structure in pulsars”, *Monthly Notices of the Royal
2893 Astronomical Society* **426**, 2507–2521 (2012).
- 2894 ¹³A. Parthasarathy et al., “Timing of young radio pulsars $\rm \{I\}$: Timing noise, pe-
2895 riodic modulation and proper motion.”, *Monthly Notices of the Royal Astronomical
2896 Society* **489**, 3810 (2019).
- 2897 ¹⁴A. Melatos, C. Peralta, and J. S. B. Wyithe, “Avalanche dynamics of radio pulsar glitches”,
2898 *The Astrophysical Journal* **672**, 1103–1118 (2008).
- 2899 ¹⁵C. M. Espinoza, A. G. Lyne, B. W. Stappers, and M. Kramer, “A study of 315 glitches in
2900 the rotation of 102 pulsars”, *Monthly Notices of the Royal Astronomical Society* **414**,
2901 1679–1704 (2011).
- 2902 ¹⁶J. R. Fuentes, C. M. Espinoza, and A. Reisenegger, “Glitch time series and size distri-
2903 butions in eight prolific pulsars”, *Astronomy and Astrophysics* **630**, A115 (2019).
- 2904 ¹⁷P. W. Anderson and N. Itoh, “Pulsar glitches and restlessness as a hard superfluidity
2905 phenomenon”, *Nature* **256**, 25–27 (1975).
- 2906 ¹⁸L. Warszawski and A. Melatos, “Gross-Pitaevskii model of pulsar glitches”, *Monthly
2907 Notices of the Royal Astronomical Society* **415**, 1611–1630 (2011).
- 2908 ¹⁹M. B. Larson and B. Link, “Simulations of glitches in isolated pulsars”, *Monthly Notices
2909 of the Royal Astronomical Society* **333**, 613–622 (2002).
- 2910 ²⁰J. Middleditch, F. E. Marshall, Q. D. Wang, E. V. Gotthelf, and W. Zhang, “Predicting
2911 the Starquakes in PSR J0537-6910”, *The Astrophysical Journal* **652**, 1531–1546 (2006).
- 2912 ²¹N. Andersson, G. L. Comer, and R. Prix, “Are Pulsar Glitches Triggered by a Superfluid
2913 Two-Stream Instability?”, *Physical Review Letters* **90**, 091101 (2003).
- 2914 ²²A. Mastrano and A. Melatos, “Kelvin-Helmholtz instability and circulation transfer at
2915 an isotropic-anisotropic superfluid interface in a neutron star”, *Monthly Notices of
2916 the Royal Astronomical Society* **361**, 927–941 (2005).
- 2917 ²³K. Glampedakis and N. Andersson, “Hydrodynamical Trigger Mechanism for Pulsar
2918 Glitches”, *Physical Review Letters* **102**, 141101 (2009).
- 2919 ²⁴B. Haskell and A. Melatos, “Models of Pulsar Glitches”, *International Journal of Mod-
2920 ern Physics D* **24**, 1530008 (2015).
- 2921 ²⁵A. Melatos, G. Howitt, and W. Fulgenzi, “Size-waiting-time Correlations in Pulsar
2922 Glitches”, *The Astrophysical Journal* **863**, 196 (2018).
- 2923 ²⁶J. Palfreyman, J. M. Dickey, A. Hotan, S. Ellingsen, and W. van Straten, “Alteration of
2924 the magnetosphere of the Vela pulsar during a glitch”, *Nature* **556**, 219–222 (2018).
- 2925 ²⁷G. Ashton, P. D. Lasky, V. Gruber, and J. Palfreyman, “Rotational evolution of the Vela
2926 pulsar during the 2016 glitch”, *Nature Astronomy* **3**, 1143–1148 (2019).
- 2927 ²⁸A. Melatos and C. Peralta, “Superfluid Turbulence and Pulsar Glitch Statistics”, *The
2928 Astrophysical Journal* **662**, L99–L102 (2007).

- 2929 ²⁹A. Melatos and B. Link, “Pulsar timing noise from superfluid turbulence”, *Monthly
2930 Notices of the Royal Astronomical Society* **437**, 21–31 (2014).
- 2931 ³⁰V. Khomenko, M. Antonelli, and B. Haskell, “Hydrodynamical instabilities in the su-
2932 perfluid interior of neutron stars with background flows between the components”,
2933 *Physical Review D* **100**, 123002 (2019).
- 2934 ³¹D. R. Cox and H. D. Miller, *The Theory of Stochastic Processes*, 1st (Chapman and Hall,
2935 London, 1965).
- 2936 ³²C. Gardiner, *Stochastic Methods: A Handbook for the Natural and Social Sciences*, Fourth
2937 (Springer-Verlag, Berlin Heidelberg, 2009).
- 2938 ³³A. L. Sweet and J. C. Hardin, “Solutions for Some Diffusion Processes with Two Bar-
2939 riers”, *Journal of Applied Probability* **7**, 423–431 (1970).
- 2940 ³⁴M. A. Alpar and A. Baykal, “Pulsar braking indices, glitches and energy dissipation
2941 in neutron stars”, *Monthly Notices of the Royal Astronomical Society* **372**, 489–496
2942 (2006).
- 2943 ³⁵O. Akbal, M. A. Alpar, S. Buchner, and D. Pines, “Nonlinear interglitch dynamics, the
2944 braking index of the Vela pulsar and the time to the next glitch”, *Monthly Notices of
2945 the Royal Astronomical Society* **469**, 4183–4192 (2017).
- 2946 ³⁶A. I. Chugunov and C. J. Horowitz, “Breaking stress of neutron star crust”, *Monthly
2947 Notices of the Royal Astronomical Society: Letters* **407**, 54–58 (2010).
- 2948 ³⁷G. Howitt, A. Melatos, and A. Delaigle, “Nonparametric Estimation of the Size and
2949 Waiting Time Distributions of Pulsar Glitches”, *The Astrophysical Journal* **867**, 60
2950 (2018).
- 2951 ³⁸M. J. Aschwanden et al., “Order out of Randomness: Self-Organization Processes in
2952 Astrophysics”, *Space Science Reviews* **214**, 55 (2018).
- 2953 ³⁹H. J. Jensen, *Self-Organized Criticality. Emergent Complex Behavior in Physical and
2954 Biological Systems*, Cambridge Lecture Notes in Physics (Cambridge University Press,
2955 Cambridge, 1998).
- 2956 ⁴⁰M. E. Lower et al., “The UTMOST pulsar timing programme – II. Timing noise across
2957 the pulsar population”, *Monthly Notices of the Royal Astronomical Society* **494**, 228–
2958 245 (2020).
- 2959 ⁴¹T. Celora, V. Khomenko, M. Antonelli, and B. Haskell, “The effect of non-linear mutual
2960 friction on pulsar glitch sizes and rise times”, *Monthly Notices of the Royal Astronom-
2961 ical Society* **496**, 5564–5574 (2020).
- 2962 ⁴²R. N. Manchester, G. B. Hobbs, A. Teoh, and M. Hobbs, “The Australia Telescope Na-
2963 tional Facility pulsar catalogue”, *The Astronomical Journal* **129**, 1993–2006 (2005).
- 2964 ⁴³H. Akaike, “A New Look at the Statistical Model Identification”, *IEEE Transactions on
2965 Automatic Control* **19**, 716 (1974).
- 2966 ⁴⁴D. Antonopoulou, C. M. Espinoza, L. Kuiper, and N. Andersson, “Pulsar spin-down:
2967 the glitch-dominated rotation of PSR J0537-6910”, *Monthly Notices of the Royal As-
2968 tronomical Society* **473**, 1644–1655 (2018).

- 2969 ⁴⁵R. D. Ferdman, R. F. Archibald, K. N. Gourgouliatos, and V. M. Kaspi, “The Glitches
2970 and Rotational History of the Highly Energetic Young Pulsar PSR J0537-6910”, *The
2971 Astrophysical Journal* **852**, 123 (2018).
- 2972 ⁴⁶A. G. Lyne, C. A. Jordan, F. Graham-Smith, C. M. Espinoza, B. W. Stappers, and P.
2973 Weltevrede, “45 Years of Rotation of the Crab Pulsar”, *Monthly Notices of the Royal
2974 Astronomical Society* **446**, 857–864 (2015).
- 2975 ⁴⁷C. M. Espinoza, D. Antonopoulou, B. W. Stappers, A. Watts, and A. G. Lyne, “Neu-
2976 tron star glitches have a substantial minimum size”, *Monthly Notices of the Royal
2977 Astronomical Society* **440**, 2755–2762 (2014).
- 2978 ⁴⁸M. Yu and Q.-J. Liu, “On the detection probability of neutron star glitches”, *Monthly
2979 Notices of the Royal Astronomical Society* **468**, 3031–3041 (2017).
- 2980 ⁴⁹M. Yu et al., “Detection of 107 glitches in 36 southern pulsars”, *Monthly Notices of the
2981 Royal Astronomical Society* **429**, 688–724 (2013).
- 2982 ⁵⁰G. H. Janssen and B. W. Stappers, “30 glitches in slow pulsars”, *Astronomy and As-
2983 trrophysics* **457**, 611–618 (2006).
- 2984 ⁵¹M. A. Alpar, S. A. Langer, and J. A. Sauls, “Rapid postglitch spin-up of the superfluid
2985 core in pulsars”, *The Astrophysical Journal* **282**, 533 (1984).
- 2986 ⁵²C. A. van Eysden and A. Melatos, “Pulsar glitch recovery and the superfluidity coef-
2987 ficients of bulk nuclear matter”, *Monthly Notices of the Royal Astronomical Society*
2988 **409**, 1253 (2010).
- 2989 ⁵³R. M. Shannon, L. T. Lentati, M. Kerr, S. Johnston, G. Hobbs, and R. N. Manchester,
2990 “Characterizing the rotational irregularities of the Vela pulsar from 21 yr of phase-
2991 coherent timing”, *Monthly Notices of the Royal Astronomical Society* **459**, 3104–3111
2992 (2016).
- 2993 ⁵⁴A. Melatos, J. A. Douglass, and T. P. Simula, “Persistent Gravitational Radiation from
2994 Glitching Pulsars”, *The Astrophysical Journal* **807**, 132 (2015).
- 2995 ⁵⁵N. Andersson, K. Glampedakis, W. C. G. Ho, and C. M. Espinoza, “Pulsar Glitches: The
2996 Crust is not Enough”, *Physical Review Letters* **109**, 241103 (2012).
- 2997 ⁵⁶J. Hooker, W. G. Newton, and B.-A. Li, “Efficacy of crustal superfluid neutrons in
2998 pulsar glitch models”, *Monthly Notices of the Royal Astronomical Society* **449**, 3559–
2999 3567 (2015).
- 3000 ⁵⁷B. Link, R. I. Epstein, and J. M. Lattimer, “Pulsar Constraints on Neutron Star Structure
3001 and Equation of State”, *Physical Review Letters* **83**, 3362–3365 (1999).
- 3002 ⁵⁸A. G. Lyne, S. L. Shemar, and F. G. Smith, “Statistical studies of pulsar glitches”,
3003 *Monthly Notices of the Royal Astronomical Society* **315**, 534–542 (2000).
- 3004 ⁵⁹R. M. Shannon and J. M. Cordes, “Assessing the Role of Spin Noise in the Precision
3005 Timing of Millisecond Pulsars”, *The Astrophysical Journal* **725**, 1607–1619 (2010).
- 3006 ⁶⁰B. K. Link and R. I. Epstein, “Mechanics and energetics of vortex unpinning in neutron
3007 stars”, *The Astrophysical Journal* **373**, 592–603 (1991).
- 3008 ⁶¹A. Melatos and C. Peralta, “Gravitational Radiation from Hydrodynamic Turbulence in
3009 a Differentially Rotating Neutron Star”, *The Astrophysical Journal* **709**, 77–87 (2010).

- 3010 ⁶²C. J. Horowitz and K. Kadau, “Breaking Strain of Neutron Star Crust and Gravitational
3011 Waves”, *Physical Review Letters* **102**, 10.1103/PhysRevLett.102.191102 (2009).
- 3012 ⁶³P. M. Morse and H. Feshbach, *Methods of Theoretical Physics* (McGraw-Hill, New York,
3013 1953).
- 3014 ⁶⁴L. Warszawski and A. Melatos, “Knock-on processes in superfluid vortex avalanches
3015 and pulsar glitch statistics”, *Monthly Notices of the Royal Astronomical Society* **428**,
3016 1911–1926 (2013).
- 3017 ⁶⁵L. Warszawski, A. Melatos, and N. G. Berloff, “Unpinning triggers for superfluid vortex
3018 avalanches”, *Physical Review B* **85**, 10.1103/PhysRevB.85.104503 (2012).
- 3019 ⁶⁶J. R. Lönnborn, A. Melatos, and B. Haskell, “Collective, glitch-like vortex motion in a
3020 neutron star with an annular pinning barrier”, *Monthly Notices of the Royal Astro-*
3021 *nical Society* **487**, 702–710 (2019).
- 3022 ⁶⁷V. Khomenko and B. Haskell, “Modelling Pulsar Glitches: The Hydrodynamics of Su-
3023 perfluid Vortex Avalanches in Neutron Stars”, *Publications of the Astronomical Soci-
3024 ety of Australia* **35**, e020 (2018).
- 3025 ⁶⁸G. Howitt, A. Melatos, and B. Haskell, “Simulating pulsar glitches: an N-body solver
3026 for superfluid vortex motion in two dimensions”, *Monthly Notices of the Royal As-
3027 trononical Society* **498**, 320–331 (2020).
- 3028 ⁶⁹S. Field, J. Witt, F. Nori, and X. Ling, “Superconducting Vortex Avalanches”, *Physical
3029 Review Letters* **74**, 1206–1209 (1995).
- 3030 ⁷⁰K. Sneppen and M. Newman, “Coherent noise, scale invariance and intermittency in
3031 large systems”, *Physica D: Nonlinear Phenomena* **110**, 209–222 (1997).
- 3032 ⁷¹M. E. J. Newman and K. Sneppen, “Avalanches, scaling, and coherent noise”, *Physical
3033 Review E* **54**, 6226–6231 (1996).
- 3034 ⁷²M. E. J. Newman, “Self-Organized Criticality, Evolution and the Fossil Extinction Record”,
3035 *Proceedings of the Royal Society of London, B* **263**, 1605–1610 (1996).
- 3036 ⁷³A. Melatos and L. Warszawski, “Superfluid Vortex Unpinning as a Coherent Noise
3037 Process, and the Scale Invariance of Pulsar Glitches”, *The Astrophysical Journal* **700**,
3038 1524 (2009).
- 3039 ⁷⁴B. Haskell, “The effect of superfluid hydrodynamics on pulsar glitch sizes and wait-
3040 ing times”, *Monthly Notices of the Royal Astronomical Society: Letters* **461**, L77–L81
3041 (2016).
- 3042 ⁷⁵P. M. Pizzochero, “Angular momentum transfer in Vela-like pulsar glitches”, *The As-
3043 trophysical Journal* **743**, L20 (2011).
- 3044 ⁷⁶B. Haskell and D. Antonopoulou, “Glitch recoveries in radio-pulsars and magnetars”,
3045 *Monthly Notices of the Royal Astronomical Society* **438**, L16–L20 (2014).
- 3046 ⁷⁷P. B. Jones, “The origin of pulsar glitches”, *Monthly Notices of the Royal Astronomical
3047 Society* **296**, 217–224 (1998).
- 3048 ⁷⁸P. Donati and P. M. Pizzochero, “Realistic energies for vortex pinning in intermediate-
3049 density neutron star matter”, *Physics Letters B* **640**, 74–81 (2006).

- 3050 ⁷⁹P. Avogadro, F. Barranco, R. A. Broglia, and E. Vigezzi, “Quantum calculation of vor-
3051 tices in the inner crust of neutron stars”, *Physical Review C* **75**, 012805 (2007).
- 3052 ⁸⁰M. Ruderman, T. Zhu, and K. Chen, “Neutron Star Magnetic Field Evolution, Crust
3053 Movement, and Glitches”, *The Astrophysical Journal* **492**, 267–280 (1998).
- 3054 ⁸¹M. A. Alpar, H. F. Chau, K. S. Cheng, and D. Pines, “Postglitch Relaxation of the Crab
3055 Pulsar after Its First Four Major Glitches: The Combined Effects of Crust Cracking,
3056 Formation of Vortex Depletion Region and Vortex Creep”, *The Astrophysical Journal*
3057 **459**, 706 (1996).
- 3058 ⁸²N. Chamel and P. Haensel, “Physics of Neutron Star Crusts”, *Living Reviews in Relativity* **11**, 10 (2008).
- 3060 ⁸³A. Melatos and L. V. Drummond, “Pulsar Glitch Activity as a State-dependent Poisson
3061 Process: Parameter Estimation and Epoch Prediction”, *The Astrophysical Journal* **885**,
3062 37 (2019).
- 3063 ⁸⁴P. M. McCulloch, P. A. Hamilton, D. McConnell, and E. A. King, “The Vela Glitch of
3064 Christmas 1988”, *Nature* **346**, 822 (1990).
- 3065 ⁸⁵R. G. Dodson, P. M. McCulloch, and D. R. Lewis, “High Time Resolution Observations
3066 of the January 2000 Glitch in the Vela Pulsar”, *The Astrophysical Journal Letters* **564**,
3067 L85–L88 (2002).
- 3068 ⁸⁶G. Srinivasan, D. Bhattacharya, A. G. Muslimov, and A. J. Tsygan, “A novel mechanism
3069 for the decay of neutron star magnetic fields”, *Current Science* **59**, 31–38 (1990).
- 3070 ⁸⁷P. M. Pizzochero, A. Montoli, and M. Antonelli, “Core and crust contributions in over-
3071 shooting glitches: the Vela pulsar 2016 glitch”, *Astronomy and Astrophysics* **636**, A101
3072 (2020).
- 3073 ⁸⁸B. Haskell and A. Melatos, “Pinned vortex hopping in a neutron star crust”, *Monthly
3074 Notices of the Royal Astronomical Society* **461**, 2200–2211 (2016).
- 3075 ⁸⁹D. R. Cox, “Some Statistical Methods Connected with Series of Events”, *Journal of the
3076 Royal Statistical Society, B* **17**, 129–164 (1955).
- 3077 ⁹⁰W. H. Press, S. A. Teukolsky, W. T. Vetterling, and B. P. Flannery, *Numerical Recipes
3078 3rd Edition: The Art of Scientific Computing* (Cambridge University Press, Sept. 2007).
- 3079 ⁹¹H. E. Hall and W. F. Vinen, “The Rotation of Liquid Helium II. II. The Theory of Mutual
3080 Friction in Uniformly Rotating Helium II”, *Proceedings of the Royal Society of London,*
3081 **A 238**, 215–234 (1956).
- 3082 ⁹²C. F. Barenghi, R. J. Donnelly, and W. F. Vinen, “Friction on quantized vortices in
3083 helium II. A review”, *Journal of Low Temperature Physics* **52**, 189–247 (1983).
- 3084 ⁹³N. Andersson, T. Sidery, and G. L. Comer, “Mutual friction in superfluid neutron stars”,
3085 *Monthly Notices of the Royal Astronomical Society* **368**, 162–170 (2006).
- 3086 ⁹⁴V. Graber, A. Cumming, and N. Andersson, “Glitch Rises as a Test for Rapid Superfluid
3087 Coupling in Neutron Stars”, *The Astrophysical Journal* **865**, 23 (2018).
- 3088 ⁹⁵C. Peralta, A. Melatos, M. Giacobello, and A. Ooi, “Transitions between Turbulent
3089 and Laminar Superfluid Vorticity States in the Outer Core of a Neutron Star”, *The
3090 Astrophysical Journal* **651**, 1079–1091 (2006).

- 3091 ⁹⁶M. S. Mongiovì, F. G. Russo, and M. Sciacca, “A mathematical description of glitches
 3092 in neutron stars”, *Monthly Notices of the Royal Astronomical Society* **469**, 2141–2150
 3093 (2017).
- 3094 ⁹⁷B. Haskell, D. Antonopoulou, and C. Barenghi, “Turbulent, pinned superfluids in neu-
 3095 tron stars and pulsar glitch recoveries”, *Monthly Notices of the Royal Astronomical
 3096 Society* **499**, 161–170 (2020).
- 3097 ⁹⁸Y. Y. Kagan and D. D. Jackson, “Long-Term Earthquake Clustering”, *Geophysical Jour-
 3098 nal International* **104**, 117–134 (1991).
- 3099 ⁹⁹T. Utsu, Y. Ogata, R. S, and Matsu’ura, “The Centenary of the Omori Formula for a
 3100 Decay Law of Aftershock Activity.”, *Journal of Physics of the Earth* **43**, 1–33 (1995).
- 3101 ¹⁰⁰E. Gügercinoğlu and M. A. Alpar, “The largest Crab glitch and the vortex creep model”,
 3102 *Monthly Notices of the Royal Astronomical Society* **488**, 2275–2282 (2019).
- 3103 ¹⁰¹C. M. Espinoza, D. Antonopoulou, R. Dodson, M. Stepanova, and A. Scherer, “Small
 3104 glitches and other rotational irregularities of the Vela pulsar”, *Astronomy and Astro-
 3105 physics* **647**, A25 (2021).
- 3106 ¹⁰²A. Melatos, L. M. Dunn, S. Suvorova, W. Moran, and R. J. Evans, “Pulsar Glitch Detec-
 3107 tion with a Hidden Markov Model”, *The Astrophysical Journal* **896**, 78 (2020).
- 3108 ¹⁰³F. Jankowski et al., “The UTMOST pulsar timing programme I: Overview and first
 3109 results”, *Monthly Notices of the Royal Astronomical Society* **484**, 3691–3712 (2019).
- 3110 ¹⁰⁴B. W. Stappers et al., “Observing pulsars and fast transients with LOFAR”, *Astronomy
 3111 and Astrophysics* **530**, A80 (2011).
- 3112 ¹⁰⁵E. Daly and A. Porporato, “Intertime jump statistics of state-dependent Poisson pro-
 3113 cesses”, *Physical Review E* **75**, 11119 (2007).
- 3114 ¹⁰⁶D. R. Cox and P. A. W. Lewis, *The Statistical Analysis of Series of Events* (Chapman and
 3115 Hall, 1966).
- 3116 ¹⁰⁷E. Çinlar, *Introduction to stochastic processes* (Englewood Cliffs, N.J. : Prentice-Hall,
 3117 1975).
- 3118 ¹⁰⁸J. F. C. Kingman, *Poisson processes* (Oxford: Clarendon Press; New York: Oxford Uni-
 3119 versity Press, 1993., 1993).
- 3120 ¹⁰⁹G. E. P. Box, G. M. Jenkins, G. C. Reinsel, and G. M. Ljung, *Time Series Analysis: Fore-
 3121 casting and Control* (John Wiley and Sons Inc., Hoboken, New Jersey, June 2015).
- 3122 ¹¹⁰E. D. Feigelson, G. J. Babu, and G. A. Caceres, “Autoregressive Times Series Methods
 3123 for Time Domain Astronomy”, *Frontiers in Physics* **6**, 80 (2018).
- 3124 ¹¹¹J. van der Hoek and R. J. Elliott, *Introduction to Hidden Semi-Markov Models*, London
 3125 Mathematical Society Lecture Note Series (Cambridge University Press, Cambridge,
 3126 2018).
- 3127 ¹¹²E. Priest and T. Forbes, “The magnetic nature of solar flares”, *The Astronomy and
 3128 Astrophysics Review* **10**, 313–377 (2002).
- 3129 ¹¹³A. O. Benz, “Flare Observations”, *Living Reviews in Solar Physics* **14**, 2 (2016).

- 3130 114 R. Rosner and G. S. Vaiana, "Cosmic flare transients - Constraints upon models for
3131 energy storage and release derived from the event frequency distribution", *The As-*
3132 *trophyical Journal* **222**, 1104 (1978).
- 3133 115 M. S. Wheatland and S. Glukhov, "Flare Frequency Distributions Based on a Master
3134 Equation", *The Astrophysical Journal* **494**, 858–863 (1998).
- 3135 116 M. S. Wheatland, "Do solar flares exhibit an interval-size relationship?", *Solar Physics*
3136 **191**, 381–389 (2000).
- 3137 117 M. S. Wheatland, "The Energetics of a Flaring Solar Active Region and Observed Flare
3138 Statistics", *The Astrophysical Journal* **679**, 1621–1628 (2008).
- 3139 118 M. Kanazir and M. S. Wheatland, "Time-Dependent Stochastic Modeling of Solar Ac-
3140 tive Region Energy", *Solar Physics* **266**, 301–321 (2010).
- 3141 119 H. S. Hudson, "A Correlation in the Waiting-time Distributions of Solar Flares", *Monthly*
3142 *Notices of the Royal Astronomical Society*, stz3121 (2019).
- 3143 120 E. T. Lu and R. J. Hamilton, "Avalanches and the Distribution of Solar Flares", *The*
3144 *Astroophysical Journal Letters* **380**, L89 (1991).
- 3145 121 E. T. Lu, R. J. Hamilton, J. M. McTiernan, and K. R. Bromund, "Solar Flares and Avalanches
3146 in Driven Dissipative Systems", *The Astrophysical Journal* **412**, 841 (1993).
- 3147 122 E. T. Lu, "The Statistical Physics of Solar Active Regions and the Fundamental Nature
3148 of Solar Flares", *The Astrophysical Journal* **446**, L109–L112 (1995).
- 3149 123 P. Bak, C. Tang, and K. Wiesenfeld, "Self-organized criticality: An explanation of the
3150 1/f noise", *Physical Review Letters* **59**, 381–384 (1987).
- 3151 124 P. Bak, C. Tang, and K. Wiesenfeld, "Self-organized criticality", *Physical Review A* **38**,
3152 364–374 (1988).
- 3153 125 E. T. Lu, "Constraints on Energy Storage and Release Models for Astrophysical Tran-
3154 sients and Solar Flares", *The Astrophysical Journal* **447**, 416 (1995).
- 3155 126 G. Boffetta, V. Carbone, P. Giuliani, P. Veltri, and A. Vulpiani, "Power Laws in Solar
3156 Flares: Self-Organized Criticality or Turbulence?", *Physical Review Letters* **83**, 4662–
3157 4665 (1999).
- 3158 127 E. Lippiello, L. de Arcangelis, and C. Godano, "Time-energy correlations in solar flare
3159 occurrence", *Astronomy and Astrophysics* **511**, L2 (2010).
- 3160 128 N. Farhang, M. S. Wheatland, and H. Safari, "Energy Balance in Avalanche Models for
3161 Solar Flares", *The Astrophysical Journal* **883**, L20 (2019).
- 3162 129 M. J. Aschwanden and J. R. Johnson, "The Solar Memory from Hours to Decades", *The*
3163 *Astroophysical Journal* **921**, 82 (2021).
- 3164 130 C. Verbeeck, E. Kraaijkamp, D. F. Ryan, and O. Podladchikova, "Solar Flare Distribu-
3165 tions: Lognormal Instead of Power Law?", *The Astrophysical Journal* **884**, 50 (2019).
- 3166 131 M. S. Wheatland, "The Origin of the Solar Flare Waiting-Time Distribution", *The As-*
3167 *trophyical Journal* **536**, L109 (2000).
- 3168 132 M. J. Aschwanden, J. R. Johnson, and Y. I. Nurhan, "The Poissonian Origin of Power
3169 Laws in Solar Flare Waiting Time Distributions", *The Astrophysical Journal* **921**, 166
3170 (2021).

- 3171 ¹³³F. Lepreti, V. Carbone, and P. Veltri, “Solar Flare Waiting Time Distribution: Varying-
3172 Rate Poisson or Lévy Function?”, *The Astrophysical Journal* **555**, L133 (2001).
- 3173 ¹³⁴A. Gorobets and M. Messerotti, “Solar Flare Occurrence Rate and Waiting Time Statis-
3174 tics”, *Solar Physics* **281**, 651–667 (2012).
- 3175 ¹³⁵D. A. Biesecker, “On the Occurrence of Solar Flares Observed with the Burst and
3176 Transient Source Experiment”, PhD thesis (University of New Hampshire, Jan. 1994).
- 3177 ¹³⁶H. S. Hudson, B. J. Labonte, A. C. Sterling, and T. Watanabe, “NOAA 7978: The Last
3178 Best Old-Cycle Region?”, in *Observational Plasma Astrophysics: Five Years of Yohkoh*
3179 and Beyond, Vol. 229, Space Science Library (Springer Dordrecht, 1998), p. 237.
- 3180 ¹³⁷N. Crosby, N. Vilmer, N. Lund, and R. Sunyaev, “Deka-keV X-ray observations of solar
3181 bursts with WATCH/GRANAT: frequency distributions of burst parameters”, *Astron-
3182 omy and Astrophysics* **334**, 299–313 (1998).
- 3183 ¹³⁸A. Lyne and F. Graham-Smith, *Pulsar Astronomy* (Cambridge University Press, Cam-
3184 bridge, UK, Mar. 2012).
- 3185 ¹³⁹L. Fletcher et al., “An Observational Overview of Solar Flares”, *Space Science Reviews*
3186 **159**, 19 (2011).
- 3187 ¹⁴⁰E. Daly and A. Porporato, “State-dependent fire models and related renewal pro-
3188 cesses”, *Physical Review E* **74**, 1–9 (2006).
- 3189 ¹⁴¹M. Wheatland, “Rates of Flaring in Individual Active Regions”, *Solar Physics* **203**, 87–
3190 106 (2001).
- 3191 ¹⁴²C. M. Hurvich and C.-L. Tsai, “Regression and time series model selection in small
3192 samples”, *Biometrika* **76**, 297–307 (1989).
- 3193 ¹⁴³E. L. Lehmann and H. J. M. D’Abrera, *Nonparametrics: Statistical Methods Based on*
3194 *Ranks* (Springer-Verlag, New York, 2006).
- 3195 ¹⁴⁴M. P. Wand and M. C. Jones, *Kernel Smoothing* (Chapman & Hall, London; New York,
3196 1995).
- 3197 ¹⁴⁵T. N. Woods et al., “New Solar extreme-ultraviolet irradiance observations during
3198 flares”, *The Astrophysical Journal* **739**, 59 (2011).
- 3199 ¹⁴⁶T. Török, B. Kliem, and V. S. Titov, “Ideal kink instability of a magnetic loop equilib-
3200 rium”, *Astronomy and Astrophysics* **413**, L27–L30 (2004).
- 3201 ¹⁴⁷C. R. Harris et al., “Array programming with NumPy”, *Nature* **585**, 357–362 (2020).
- 3202 ¹⁴⁸P. Virtanen et al., “SciPy 1.0: fundamental algorithms for scientific computing in Python”,
3203 *Nature Methods* **17**, 261–272 (2020).
- 3204 ¹⁴⁹J. D. Hunter, “Matplotlib: A 2D Graphics Environment”, *Computing in Science and*
3205 *Engineering* **9**, 90–95 (2007).
- 3206 ¹⁵⁰Stan Development Team, *Stan Modeling Language Users Guide and Reference Manual*,
3207 2.30, 2022.
- 3208 ¹⁵¹G. H. Fisher, B. T. Welsch, and W. P. Abbett, “Can We Determine Electric Fields and
3209 Poynting Fluxes from Vector Magnetograms and Doppler Measurements?”, *Solar Physics*
3210 **277**, 153–163 (2012).

- 3211 ¹⁵²X. Sun, J. T. Hoeksema, Y. Liu, T. Wiegmann, K. Hayashi, Q. Chen, and J. Thalmann,
 3212 “Evolution of Magnetic Field and Energy in a Major Eruptive Active Region Based on
 3213 SDO/HMI Observation”, *The Astrophysical Journal* **748**, 77 (2012).
- 3214 ¹⁵³X. Sun, J. T. Hoeksema, Y. Liu, M. Kazachenko, and R. Chen, “Investigating the Mag-
 3215 netic Imprints of Major Solar Eruptions with SDO/HMI High-cadence Vector Magne-
 3216 tograms”, *The Astrophysical Journal* **839**, 67 (2017).
- 3217 ¹⁵⁴S. Sahu, B. Joshi, A. Prasad, and K.-S. Cho, *Evolution of magnetic fields and energy*
 3218 *release processes during homologous eruptive flares*, Dec. 2022.
- 3219 ¹⁵⁵H. Ji and W. Daughton, “Phase diagram for magnetic reconnection in heliospherical,
 3220 astrophysical, and laboratory plasmas”, *Physics of Plasmas* **18**, 111207 (2011).
- 3221 ¹⁵⁶K. Shibata and S. Tanuma, “Plasmoid-induced-reconnection and fractal reconnection”,
 3222 *Earth, Planets and Space* **53**, 473–482 (2001).
- 3223 ¹⁵⁷P. H. Keys, M. Mathioudakis, D. B. Jess, S. Shelyag, P. J. Crockett, D. J. Christian,
 3224 and F. P. Keenan, “The Velocity Distribution of Solar Photospheric Magnetic Bright
 3225 Points”, *The Astrophysical Journal Letters* **740**, L40 (2011).
- 3226 ¹⁵⁸S. Shelyag, P. Keys, M. Mathioudakis, and F. P. Keenan, “Vorticity in the solar photo-
 3227 sphere”, *Astronomy and Astrophysics* **526**, A5 (2011).
- 3228 ¹⁵⁹S. Shelyag, V. Fedun, F. P. Keenan, R. Erdélyi, and M. Mathioudakis, “Photospheric
 3229 magnetic vortex structures”, *Annales Geophysicae* **29**, 883–887 (2011).
- 3230 ¹⁶⁰A. Gelman, J. B. Carlin, H. S. Stern, D. Dunson, A. Vehtari, and D. B. Rubin, *Bayesian*
 3231 *data analysis*, 3rd Editio (Chapman and Hall/CRC, New York, 2013).
- 3232 ¹⁶¹M. Betancourt, “A Conceptual Introduction to Hamiltonian Monte Carlo”, *arXiv e-*
 3233 *prints* (2018).
- 3234 ¹⁶²J. Aasi et al., “Advanced LIGO”, *Classical and Quantum Gravity* **32**, 074001 (2015).
- 3235 ¹⁶³F. Acernese et al., “Advanced Virgo: a second-generation interferometric gravitational
 3236 wave detector”, *Classical and Quantum Gravity* **32**, 024001 (2014).
- 3237 ¹⁶⁴LIGO Scientific Collaboration and Virgo Collaboration et al., “GWTC-1: A Gravitational-
 3238 Wave Transient Catalog of Compact Binary Mergers Observed by LIGO and Virgo
 3239 during the First and Second Observing Runs”, *Physical Review X* **9**, 031040 (2019).
- 3240 ¹⁶⁵LIGO Scientific Collaboration and Virgo Collaboration et al., “GWTC-2: Compact Bi-
 3241 nary Coalescences Observed by LIGO and Virgo during the First Half of the Third
 3242 Observing Run”, *Physical Review X* **11**, 021053 (2021).
- 3243 ¹⁶⁶The LIGO Scientific Collaboration et al., “GWTC-2.1: Deep Extended Catalog of Com-
 3244 pact Binary Coalescences Observed by LIGO and Virgo During the First Half of the
 3245 Third Observing Run”, *arXiv e-prints*, arXiv:2108.01045 (2021).
- 3246 ¹⁶⁷K. Glampedakis and L. Gualtieri, “Gravitational Waves from Single Neutron Stars:
 3247 An Advanced Detector Era Survey”, in *The Physics and Astrophysics of Neutron Stars*,
 3248 edited by L. Rezzolla, P. Pizzochero, D. I. Jones, N. Rea, and I. Vidaña, *Astrophysics and*
 3249 *Space Science Library* (Springer International Publishing, Cham, 2018), pp. 673–736.
- 3250 ¹⁶⁸M. Sieniawska and M. Bejger, “Continuous Gravitational Waves from Neutron Stars:
 3251 Current Status and Prospects”, *Universe* **5**, 217 (2019).

- 3252 169 B. Haskell and K. Schwenzer, “Isolated Neutron Stars”, in *Handbook of Gravitational*
3253 *Wave Astronomy*, edited by C. Bambi, S. Katsanevas, and K. D. Kokkotas (Springer,
3254 Singapore, 2021), pp. 1–28.
- 3255 170 B. P. Abbott et al., “Search for Gravitational Waves from a Long-lived Remnant of the
3256 Binary Neutron Star Merger GW170817”, *The Astrophysical Journal* **875**, 160 (2019).
- 3257 171 Y. Zhang, M. A. Papa, B. Krishnan, and A. L. Watts, “Search for Continuous Gravi-
3258 tational Waves from Scorpius X-1 in LIGO O2 Data”, *The Astrophysical Journal* **906**,
3259 **L14** (2021).
- 3260 172 D. Beniwal, P. Clearwater, L. Dunn, A. Melatos, and D. Ottaway, “Search for contin-
3261 uous gravitational waves from ten H.E.S.S. sources using a hidden Markov model”,
3262 *Physical Review D* **103**, 083009 (2021).
- 3263 173 D. Jones and L. Sun, “Search for continuous gravitational waves from Fomalhaut b
3264 in the second Advanced LIGO observing run with a hidden Markov model”, *Physical*
3265 *Review D* **103**, 023020 (2021).
- 3266 174 R. Abbott et al., “Gravitational-wave Constraints on the Equatorial Ellipticity of Mil-
3267 lisecond Pulsars”, *The Astrophysical Journal Letters* **902**, L21 (2020).
- 3268 175 V. Dergachev and M. A. Papa, “Search for continuous gravitational waves from small-
3269 ellipticity sources at low frequencies”, *Physical Review D* **104**, 043003 (2021).
- 3270 176 B. Rajbhandari, B. J. Owen, S. Caride, and R. Inta, “First searches for gravitational
3271 waves from \$r\$-modes of the Crab pulsar”, *Physical Review D* **104**, 122008 (2021).
- 3272 177 The LIGO Scientific Collaboration and the Virgo Collaboration et al., “All-sky search
3273 in early O3 LIGO data for continuous gravitational-wave signals from unknown neu-
3274 tron stars in binary systems”, *Physical Review D* **103**, 064017 (2021).
- 3275 178 K. Wette, L. Dunn, P. Clearwater, and A. Melatos, “Deep exploration for continuous
3276 gravitational waves at 171–172 Hz in LIGO second observing run data”, *Physical Re-*
3277 *view D* **103**, 083020 (2021).
- 3278 179 R. Abbott et al., “Diving below the Spin-down Limit: Constraints on Gravitational
3279 Waves from the Energetic Young Pulsar PSR J0537-6910”, *The Astrophysical Journal*
3280 *Letters* **913**, L27 (2021).
- 3281 180 R. Abbott et al., “Constraints from LIGO O3 Data on Gravitational-wave Emission Due
3282 to R-modes in the Glitching Pulsar PSR J0537–6910”, *The Astrophysical Journal* **922**,
3283 **71** (2021).
- 3284 181 LIGO Scientific Collaboration and Virgo Collaboration et al., “Narrow-band search
3285 for gravitational waves from known pulsars using the second LIGO observing run”,
3286 *Physical Review D* **99**, 122002 (2019).
- 3287 182 V. C. LIGO Scientific Collaboration and KAGRA Collaboration et al., “All-sky search
3288 for continuous gravitational waves from isolated neutron stars in the early O3 LIGO
3289 data”, *Physical Review D* **104**, 082004 (2021).
- 3290 183 R. Abbott et al., “Searches for Continuous Gravitational Waves from Young Super-
3291 nova Remnants in the Early Third Observing Run of Advanced LIGO and Virgo”, *The*
3292 *Astrophysical Journal* **921**, 80 (2021).

- 3293 ¹⁸⁴A. Ashok, B. Beheshtipour, M. A. Papa, P. C. C. Freire, B. Steltner, B. Machenschalk,
3294 O. Behnke, B. Allen, and R. Prix, “New Searches for Continuous Gravitational Waves
3295 from Seven Fast Pulsars”, *The Astrophysical Journal* **923**, 85 (2021).
- 3296 ¹⁸⁵LIGO Scientific Collaboration and Virgo Collaboration et al., “Search for gravitational
3297 waves from Scorpius X-1 in the second Advanced LIGO observing run with an im-
3298 proved hidden Markov model”, *Physical Review D* **100**, 122002 (2019).
- 3299 ¹⁸⁶H. Middleton, P. Clearwater, A. Melatos, and L. Dunn, “Search for gravitational waves
3300 from five low mass x-ray binaries in the second Advanced LIGO observing run with
3301 an improved hidden Markov model”, *Physical Review D* **102**, 023006 (2020).
- 3302 ¹⁸⁷M. A. Papa, J. Ming, E. V. Gotthelf, B. Allen, R. Prix, V. Dergachev, H.-B. Eggenstein,
3303 A. Singh, and S. J. Zhu, “Search for Continuous Gravitational Waves from the Central
3304 Compact Objects in Supernova Remnants Cassiopeia A, Vela Jr., and G347.3–0.5”, *The
3305 Astrophysical Journal* **897**, 22 (2020).
- 3306 ¹⁸⁸L. Fesik and M. A. Papa, “First Search for r-mode Gravitational Waves from PSR
3307 J0537–6910”, *The Astrophysical Journal* **895**, 11 (2020).
- 3308 ¹⁸⁹L. Fesik and M. A. Papa, “Erratum: “First Search for r-mode Gravitational Waves from
3309 PSR J0537–6910” (2020, ApJ, 895, 11)”, *The Astrophysical Journal* **897**, 185 (2020).
- 3310 ¹⁹⁰O. J. Piccinni, P. Astone, S. D’Antonio, S. Frasca, G. Intini, I. La Rosa, P. Leaci, S. Mas-
3311 trogiovanni, A. Miller, and C. Palomba, “Directed search for continuous gravitational-
3312 wave signals from the Galactic Center in the Advanced LIGO second observing run”,
3313 *Physical Review D* **101**, 082004 (2020).
- 3314 ¹⁹¹B. Steltner et al., “Einstein@Home All-sky Search for Continuous Gravitational Waves
3315 in LIGO O2 Public Data”, *The Astrophysical Journal* **909**, 79 (2021).
- 3316 ¹⁹²A. Patruno and A. L. Watts, “Accreting Millisecond X-ray Pulsars”, in *Timing Neutron
3317 Stars: Pulsations, Oscillations and Explosions*, edited by T. M. Belloni, M. Méndez, and C.
3318 Zhang, Astrophysics and Space Science Library (Springer, Berlin, Heidelberg, 2021),
3319 pp. 143–208.
- 3320 ¹⁹³J. W. T. Hessels, S. M. Ransom, I. H. Stairs, P. C. C. Freire, V. M. Kaspi, and F. Camilo,
3321 “*A Radio Pulsar Spinning at 716 Hz*”, *Science* **311**, 1901–1904 (2006).
- 3322 ¹⁹⁴G. B. Cook, S. L. Shapiro, and S. A. Teukolsky, “Rapidly rotating neutron stars in gen-
3323 eral relativity: Realistic equations of state”, *The Astrophysical Journal* **424**, 823–845
3324 (1994).
- 3325 ¹⁹⁵L. Bildsten, “Gravitational Radiation and Rotation of Accreting Neutron Stars”, *The
3326 Astrophysical Journal Letters* **501**, L89 (1998).
- 3327 ¹⁹⁶N. Andersson, K. D. Kokkotas, and N. Stergioulas, “On the Relevance of the R-Mode
3328 Instability for Accreting Neutron Stars and White Dwarfs”, *The Astrophysical Journal*
3329 **516**, 307–314 (1999).
- 3330 ¹⁹⁷J. Papaloizou and J. E. Pringle, “Gravitational radiation and the stability of rotating
3331 stars”, *Monthly Notices of the Royal Astronomical Society* **184**, 501–508 (1978).
- 3332 ¹⁹⁸R. V. Wagoner, “Gravitational radiation from accreting neutron stars”, *The Astrophys-
3333 ical Journal* **278**, 345–348 (1984).

- 3334 199 B. P. Abbott et al., "Search for gravitational waves from Scorpius X-1 in the first Ad-
3335 vanced LIGO observing run with a hidden Markov model", *Physical Review D* **95**,
3336 [122003 \(2017\)](#).
- 3337 200 B. P. Abbott et al., "Upper Limits on Gravitational Waves from Scorpius X-1 from a
3338 Model-based Cross-correlation Search in Advanced LIGO Data", *The Astrophysical
3339 Journal* **847**, 47 (2017).
- 3340 201 T. Di Salvo and A. Sanna, "Accretion Powered X-ray Millisecond Pulsars", in *Millisecond
3341 Pulsars*, edited by S. Bhattacharyya, A. Papitto, and D. Bhattacharya, *Astrophysics
3342 and Space Science Library* (Springer International Publishing, Cham, 2022), pp. 87–
3343 124.
- 3344 202 E. Goetz and K. Riles, "An all-sky search algorithm for continuous gravitational waves
3345 from spinning neutron stars in binary systems", *Classical and Quantum Gravity* **28**,
3346 [215006 \(2011\)](#).
- 3347 203 G. D. Meadors, E. Goetz, K. Riles, T. Creighton, and F. Robinet, "Searches for continu-
3348 ous gravitational waves from Scorpius X-1 and XTE J1751-305 in LIGO's sixth science
3349 run", *Physical Review D* **95**, 042005 (2017).
- 3350 204 A. Mukherjee, C. Messenger, and K. Riles, "Accretion-induced spin-wandering effects
3351 on the neutron star in Scorpius X-1: Implications for continuous gravitational wave
3352 searches", *Physical Review D* **97**, 043016 (2018).
- 3353 205 K. Riles, "Gravitational waves: Sources, detectors and searches", *Progress in Particle
3354 and Nuclear Physics* **68**, 1–54 (2013).
- 3355 206 B. Abbott et al., "Beating the Spin-Down Limit on Gravitational Wave Emission from
3356 the Crab Pulsar", *The Astrophysical Journal Letters* **683**, L45 (2008).
- 3357 207 A. Viterbi, "Error bounds for convolutional codes and an asymptotically optimum
3358 decoding algorithm", *IEEE Transactions on Information Theory* **13**, 260–269 (1967).
- 3359 208 P. Jaranowski, A. Królak, and B. F. Schutz, "Data analysis of gravitational-wave signals
3360 from spinning neutron stars: The signal and its detection", *Physical Review D* **58**,
3361 [063001 \(1998\)](#).
- 3362 209 LIGO Scientific Collaboration, "LIGO Algorithm Library - LALSuite", [10 . 7935 /
3363 GT1W-FZ16 \(2018\)](#).
- 3364 210 P. Casella, D. Altamirano, A. Patruno, R. Wijnands, and M. van der Klis, "Discovery
3365 of Coherent Millisecond X-Ray Pulsations in Aquila X-1", *The Astrophysical Journal
3366 Letters* **674**, L41 (2008).
- 3367 211 D. Mata Sánchez, T. Muñoz-Darias, J. Casares, and F. Jiménez-Ibarra, "The donor of
3368 Aquila X-1 revealed by high-angular resolution near-infrared spectroscopy", *Monthly
3369 Notices of the Royal Astronomical Society* **464**, L41–L45 (2017).
- 3370 212 A. L. Watts, B. Krishnan, L. Bildsten, and B. F. Schutz, "Detecting gravitational wave
3371 emission from the known accreting neutron stars", *Monthly Notices of the Royal As-
3372 tronomical Society* **389**, 839–868 (2008).
- 3373 213 A. Marino, T. Di Salvo, L. Burderi, A. Sanna, A. Riggio, A. Papitto, M. Del Santo, A. F.
3374 Gambino, R. Iaria, and S. M. Mazzola, "Indications of non-conservative mass transfer
3375 in AMXPs", *Astronomy and Astrophysics* **627**, 11 (2019).

- 3376 2¹⁴ A. Melatos and A. Mastrano, “Electromagnetic Spindown of a Transient Accreting
3377 Millisecond Pulsar During Quiescence”, *The Astrophysical Journal* **818**, 49 (2016).
- 3378 2¹⁵ P. Ghosh, F. K. Lamb, and C. J. Pethick, “Accretion by rotating magnetic neutron stars.
3379 I - Flow of matter inside the magnetosphere and its implications for spin-up and spin-
3380 down of the star”, *The Astrophysical Journal* **217**, 578–596 (1977).
- 3381 2¹⁶ P. M. Bult, K. C. Gendreau, Z. Arzoumanian, D. Chakrabarty, P. S. Ray, S. Guillot,
3382 M. T. Wolff, S. Bogdanov, and R. M. Ludlam, “NICER detects X-ray pulsations from
3383 the rapidly brightening SAX J1808.4-3658”, *The Astronomer’s Telegram* **3001** (2019).
- 3384 2¹⁷ P. Bult, D. Chakrabarty, Z. Arzoumanian, K. C. Gendreau, S. Guillot, C. Malacaria,
3385 P. S. Ray, and T. E. Strohmayer, “Timing the Pulsations of the Accreting Millisecond
3386 Pulsar SAX J1808.4-3658 during Its 2019 Outburst”, *The Astrophysical Journal* **898**,
3387 38 (2020).
- 3388 2¹⁸ A. J. Goodwin et al., “Enhanced optical activity 12 d before X-ray activity, and a 4 d
3389 X-ray delay during outburst rise, in a low-mass X-ray binary”, *Monthly Notices of the
3390 Royal Astronomical Society* **498**, 3429–3439 (2020).
- 3391 2¹⁹ B. Haskell and A. Patruno, “Are Gravitational Waves Spinning Down PSR J1023+0038?”,
3392 *Physical Review Letters* **119**, 161103 (2017).
- 3393 2²⁰ M. A. P. Torres et al., “Observations of the 599 Hz Accreting X-Ray Pulsar IGR J00291+5934
3394 during the 2004 Outburst and in Quiescence”, *The Astrophysical Journal* **672**, 1079–
3395 1090 (2008).
- 3396 2²¹ A. Patruno, “The Slow Orbital Evolution of the Accreting Millisecond Pulsar IGR
3397 J0029+5934”, *The Astrophysical Journal* **839**, 51 (2017).
- 3398 2²² J. Homan, G. Sivakoff, D. Pooley, C. Heinke, J. Strader, V. Tudor, and J. Miller-Jones,
3399 “Chandra identification of the X-ray transient MAXI J0911-635/Swift J0911.9-6452 in
3400 NGC 2808”, *The Astronomer’s Telegram* **8971** (2016).
- 3401 2²³ A. Sanna, A. Papitto, L. Burderi, E. Bozzo, A. Riggio, T. Di Salvo, C. Ferrigno, N. Rea,
3402 and R. Iaria, “Discovery of a new accreting millisecond X-ray pulsar in the globular
3403 cluster NGC 2808”, *Astronomy and Astrophysics* **598**, A34 (2017).
- 3404 2²⁴ D. K. Galloway, D. Chakrabarty, E. H. Morgan, and R. A. Remillard, “Discovery of a
3405 High-Latitude Accreting Millisecond Pulsar in an Ultracompact Binary”, *The Astro-
3406 physical Journal Letters* **576**, L137–L140 (2002).
- 3407 2²⁵ A. B. Giles, J. G. Greenhill, K. M. Hill, and E. Sanders, “The optical counterpart of XTE
3408 J0929-314: the third transient millisecond X-ray pulsar”, *Monthly Notices of the Royal
3409 Astronomical Society* **361**, 1180–1186 (2005).
- 3410 2²⁶ A. J. Tetarenko et al., “A Radio Frequency Study of the Accreting Millisecond X-ray
3411 Pulsar, IGR J16597-3704, in the Globular Cluster NGC 6256”, *The Astrophysical Jour-
3412 nal* **854**, 125 (2018).
- 3413 2²⁷ A. Sanna et al., “Discovery of 105 Hz coherent pulsations in the ultracompact binary
3414 IGR J16597-3704”, *Astronomy and Astrophysics* **610**, L2 (2018).
- 3415 2²⁸ P. Bult, T. E. Strohmayer, C. Malacaria, M. Ng, and Z. Wadiasingh, “Long-term Coher-
3416 ent Timing of the Accreting Millisecond Pulsar IGR J17062-6143”, *The Astrophysical
3417 Journal* **912**, 120 (2021).

- 3418 229 A. Sanna, E. Bozzo, A. Papitto, A. Riggio, C. Ferrigno, T. Di Salvo, R. Iaria, S. M. Maz-
3419 zola, N. D'Amico, and L. Burderi, "XMM-Newton detection of the 2.1 ms coherent
3420 pulsations from IGR J17379-3747", *Astronomy and Astrophysics* **616**, L17 (2018).
- 3421 230 P. Bult, C. B. Markwardt, D. Altamirano, Z. Arzoumanian, D. Chakrabarty, K. C. Gen-
3422 dreau, S. Guillot, G. K. Jaisawal, P. S. Ray, and T. E. Strohmayer, "On the Curious
3423 Pulsation Properties of the Accreting Millisecond Pulsar IGR J17379-3747", *The As-*
3424 *astrophysical Journal* **877**, 70 (2019).
- 3425 231 A. Sanna, L. Burderi, A. Riggio, F. Pintore, T. Di Salvo, A. F. Gambino, R. Iaria, M.
3426 Matranga, and F. Scarano, "Timing of the accreting millisecond pulsar SAX J1748.9-
3427 2021 during its 2015 outburst", *Monthly Notices of the Royal Astronomical Society*
3428 **459**, 1340–1349 (2016).
- 3429 232 C. O. Heinke et al., "Discovery of a Second Transient Low-Mass X-ray Binary in the
3430 Globular Cluster Ngc 6440", *The Astrophysical Journal* **714**, 894–903 (2010).
- 3431 233 P. Bult, A. Patruno, and M. van der Klis, "Coherent Timing of the Accreting Millisecond
3432 Pulsar NGC 6440 X-2", *The Astrophysical Journal* **814**, 138 (2015).
- 3433 234 M. Ng et al., "NICER Discovery of Millisecond X-Ray Pulsations and an Ultracompact
3434 Orbit in IGR J17494-3030", *The Astrophysical Journal Letters* **908**, L15 (2021).
- 3435 235 P. G. Jonker, M. A. P. Torres, D. Steeghs, and D. Chakrabarty, "Chandra X-ray and
3436 Gemini near-infrared observations of the eclipsing millisecond pulsar SWIFT J1749.4-
3437 2807 in quiescence", *Monthly Notices of the Royal Astronomical Society* **429**, 523–528
3438 (2013).
- 3439 236 P. M. Bult, D. Altamirano, A. C. Albayati, T. E. Strohmayer, P. S. Ray, D. Chakrabarty,
3440 M. Ng, K. C. Gendreau, Z. Arzoumanian, and A. Sanna, "NICER detects pulsations
3441 from Swift J1749.4-2807", *The Astronomer's Telegram* **4428** (2021).
- 3442 237 A. Sanna et al., "On the peculiar long-term orbital evolution of the eclipsing accreting
3443 millisecond X-ray pulsar SWIFT J1749.4 - 2807", *Monthly Notices of the Royal
3444 Astronomical Society* **514**, 4385–4397 (2022).
- 3445 238 A. Papitto, E. Bozzo, C. Ferrigno, T. Belloni, L. Burderi, T. di Salvo, A. Riggio, A. D'Aì,
3446 and R. Iaria, "The discovery of the 401 Hz accreting millisecond pulsar IGR J17498-
3447 2921 in a 3.8 h orbit", *Astronomy and Astrophysics* **535**, L4 (2011).
- 3448 239 M. Falanga, L. Kuiper, J. Poutanen, D. K. Galloway, E. Bozzo, A. Goldwurm, W. Hermsen,
3449 and L. Stella, "Spectral and timing properties of the accreting X-ray millisecond pulsar
3450 IGR J17498-2921", *Astronomy and Astrophysics* **545**, A26 (2012).
- 3451 240 A. Paizis, M. A. Nowak, J. Rodriguez, J. Wilms, S. Chaty, M. Del Santo, and P. Ubertini,
3452 "A Chandra Observation of the Bursting Millisecond X-Ray Pulsar IGR J17511-3057",
3453 *The Astrophysical Journal* **755**, 52 (2012).
- 3454 241 A. Riggio, A. Papitto, L. Burderi, T. di Salvo, M. Bachetti, R. Iaria, A. D'Aì, and M. T.
3455 Menna, "Timing of the accreting millisecond pulsar IGR J17511-3057", *Astronomy and
3456 Astrophysics* **526**, A95 (2011).
- 3457 242 C. B. Markwardt, J. H. Swank, T. E. Strohmayer, J. J. M. in 't Zand, and F. E. Marshall,
3458 "Discovery of a Second Millisecond Accreting Pulsar: XTE J1751-305", *The Astrophys-*
3459 *ical Journal Letters* **575**, L21–L24 (2002).

- 3460 243 A. Papitto, M. T. Menna, L. Burderi, T. di Salvo, and A. Riggio, “Measuring the spin
3461 up of the accreting millisecond pulsar XTEJ1751-305”, *Monthly Notices of the Royal*
3462 *Astronomical Society* **383**, 411–416 (2008).
- 3463 244 A. Sanna et al., “SWIFT J1756.9-2508: spectral and timing properties of its 2018 out-
3464 burst”, *Monthly Notices of the Royal Astronomical Society* **481**, 1658–1666 (2018).
- 3465 245 T. D. Russell, N. Degenaar, R. Wijnands, J. van den Eijnden, N. V. Gusinskaia, J. W. T.
3466 Hessels, and J. C. A. Miller-Jones, “The Radio-bright Accreting Millisecond X-Ray Pul-
3467 sar IGR J17591-2342”, *The Astrophysical Journal Letters* **869**, L16 (2018).
- 3468 246 A. Sanna et al., “Timing of the accreting millisecond pulsar IGR J17591-2342: evidence
3469 of spin-down during accretion”, *Monthly Notices of the Royal Astronomical Society*
3470 **495**, 1641–1649 (2020).
- 3471 247 C. B. Markwardt, M. Juda, and J. H. Swank, “XTE J1807-294”, *International Astronom-
3472 ical Union Circular* **8095**, 2 (2003).
- 3473 248 A. Patruno, J. M. Hartman, R. Wijnands, D. Chakrabarty, and M. van der Klis, “Ac-
3474 cretion Torques and Motion of the Hot Spot on the Accreting Millisecond Pulsar XTE
3475 J1807-294”, *The Astrophysical Journal* **717**, 1253–1261 (2010).
- 3476 249 M. I. Krauss, Z. Wang, A. Dullighan, A. M. Juett, D. L. Kaplan, D. Chakrabarty, M. H.
3477 van Kerkwijk, D. Steeghs, P. G. Jonker, and C. B. Markwardt, “The X-Ray Position and
3478 Optical Counterpart of the Accretion-powered Millisecond Pulsar XTE J1814-338”,
3479 *The Astrophysical Journal* **627**, 910–914 (2005).
- 3480 250 A. Papitto, T. di Salvo, L. Burderi, M. T. Menna, G. Lavagetto, and A. Riggio, “Timing
3481 of the accreting millisecond pulsar XTE J1814-338”, *Monthly Notices of the Royal*
3482 *Astronomical Society* **375**, 971–976 (2007).
- 3483 251 C. Pallanca, E. Dalessandro, F. R. Ferraro, B. Lanzoni, and G. Beccari, “The Optical
3484 Counterpart to the X-Ray Transient IGR J1824-24525 in the Globular Cluster M28”,
3485 *The Astrophysical Journal* **773**, 122 (2013).
- 3486 252 A. Papitto et al., “Swings between rotation and accretion power in a binary millisecond
3487 pulsar”, *Nature* **501**, 517–520 (2013).
- 3488 253 D. B. Fox, “HETE J1900.1-2455 Optical Counterpart”, *The Astronomer’s Telegram* **526**
3489 (2005).
- 3490 254 P. Kaaret, E. H. Morgan, R. Vanderspek, and J. A. Tomsick, “Discovery of the Mil-
3491 lisecond X-Ray Pulsar HETE J1900.1-2455”, *The Astrophysical Journal* **638**, 963–967
3492 (2006).
- 3493 255 A. Patruno, “Evidence of Fast Magnetic Field Evolution in an Accreting Millisecond
3494 Pulsar”, *The Astrophysical Journal Letters* **753**, L12 (2012).
- 3495 256 D. I. Jones, “Gravitational wave emission from rotating superfluid neutron stars”,
3496 *Monthly Notices of the Royal Astronomical Society* **402**, 2503–2519 (2010).
- 3497 257 N. Andersson, “A New Class of Unstable Modes of Rotating Relativistic Stars”, *The*
3498 *Astrophysical Journal* **502**, 708 (1998).
- 3499 258 J. L. Friedman and S. M. Morsink, “Axial Instability of Rotating Relativistic Stars”, *The*
3500 *Astrophysical Journal* **502**, 714 (1998).

- 3501 259 S. Yoshida and U. Lee, “R-Modes of Neutron Stars with a Solid Crust”, *The Astrophysical Journal* **546**, 1121–1125 (2001).
- 3502
- 3503 260 M. G. Alford, S. Mahmoodifar, and K. Schwenzer, “Viscous damping of r-modes: Small
3504 amplitude instability”, *Physical Review D* **85**, 024007 (2012).
- 3505 261 LIGO Scientific Collaboration and Virgo Collaboration et al., “First narrow-band search
3506 for continuous gravitational waves from known pulsars in advanced detector data”,
3507 *Physical Review D* **96**, 122006 (2017).
- 3508 262 A. Idrisy, B. J. Owen, and D. I. Jones, “R-mode frequencies of slowly rotating relativistic
3509 neutron stars with realistic equations of state”, *Physical Review D* **91**, 024001 (2015).
- 3510 263 S. Caride, R. Inta, B. J. Owen, and B. Rajbhandari, “How to search for gravitational
3511 waves from r-modes of known pulsars”, *Physical Review D* **100**, 064013 (2019).
- 3512 264 L. Sammut, C. Messenger, A. Melatos, and B. J. Owen, “Implementation of the frequency-
3513 modulated sideband search method for gravitational waves from low mass x-ray bi-
3514 naries”, *Physical Review D* **89**, 043001 (2014).
- 3515 265 C. Messenger et al., “Gravitational waves from Scorpius X-1: A comparison of search
3516 methods and prospects for detection with advanced detectors”, *Physical Review D* **92**,
3517 023006 (2015).
- 3518 266 LIGO Scientific Collaboration and Virgo Collaboration et al., “All-sky search for con-
3519 tinuous gravitational waves from isolated neutron stars using Advanced LIGO O2
3520 data”, *Physical Review D* **100**, 024004 (2019).
- 3521 267 A. Patruno, P. Bult, A. Gopakumar, J. M. Hartman, R. Wijnands, M. van der Klis, and
3522 D. Chakrabarty, “Accelerated Orbital Expansion and Secular Spin-down of the Ac-
3523 creting Millisecond Pulsar SAX J1808.4-3658”, *The Astrophysical Journal Letters* **746**,
3524 L27 (2012).
- 3525 268 P. Leaci and R. Prix, “Directed searches for continuous gravitational waves from bi-
3526 nary systems: Parameter-space metrics and optimal Scorpius X-1 sensitivity”, *Physical
3527 Review D* **91**, 102003 (2015).
- 3528 269 D. Davis et al., “LIGO detector characterization in the second and third observing
3529 runs”, *Classical and Quantum Gravity* **38**, 135014 (2021).
- 3530 270 J. Zweizig and K. Riles, *LIGO-T2000384-v4: Information on self-gating of h(t) used in O3*
3531 *continuous-wave and stochastic searches*.
- 3532 271 L. Sun et al., “Characterization of systematic error in Advanced LIGO calibration”,
3533 *Classical and Quantum Gravity* **37**, 225008 (2020).
- 3534 272 L. Sun et al., “Characterization of systematic error in Advanced LIGO calibration in
3535 the second half of O3”, *arXiv e-prints*, arXiv:2107.00129 (2021).
- 3536 273 LSC Instrument Authors et al., “Identification and mitigation of narrow spectral arti-
3537 facts that degrade searches for persistent gravitational waves in the first two observ-
3538 ing runs of Advanced LIGO”, *Physical Review D* **97**, 082002 (2018).
- 3539 274 E. Goetz et al., *LIGO-T2100200-v1: O3 lines and combs in found in self-gated C01 data*.
- 3540 275 M. M. Romanova, G. V. Ustyugova, A. V. Koldoba, and R. V. E. Lovelace, “Three-
3541 dimensional Simulations of Disk Accretion to an Inclined Dipole. II. Hot Spots and
3542 Variability”, *The Astrophysical Journal* **610**, 920 (2004).

- 3543 ²⁷⁶B. Haskell, M. Priymak, A. Patruno, M. Oppenorth, A. Melatos, and P. D. Lasky, “Detecting gravitational waves from mountains on neutron stars in the advanced detector era”, *Monthly Notices of the Royal Astronomical Society* **450**, 2393–2403 (2015).
- 3544
3545
- 3546 ²⁷⁷A. Papitto, A. Riggio, L. Burderi, T. di Salvo, A. D’Aì, and R. Iaria, “Spin down during quiescence of the fastest known accretion-powered pulsar”, *Astronomy and Astrophysics* **528**, A55 (2011).
- 3547
3548
- 3549 ²⁷⁸A. Sanna et al., “Spectral and timing properties of IGR J00291+5934 during its 2015 outburst”, *Monthly Notices of the Royal Astronomical Society* **466**, 2910–2917 (2017).
- 3550
- 3551 ²⁷⁹V. De Falco, L. Kuiper, E. Bozzo, D. K. Galloway, J. Poutanen, C. Ferrigno, L. Stella, and M. Falanga, “The 2015 outburst of the accretion-powered pulsar IGR J00291+5934: INTEGRAL and Swift observations”, *Astronomy and Astrophysics* **599**, A88 (2017).
- 3552
3553
- 3554 ²⁸⁰L. L. Watkins, R. P. van der Marel, A. Bellini, and J. Anderson, “Hubble Space Telescope Proper Motion (HSTPROMO) Catalogs of Galactic Globular Clusters. III. Dynamical Distances and Mass-to-Light Ratios”, *The Astrophysical Journal* **812**, 149 (2015).
- 3555
3556
- 3557 ²⁸¹A. Marino, T. Di Salvo, A. F. Gambino, R. Iaria, L. Burderi, M. Matranga, A. Sanna, and A. Riggio, “Evidence of a non-conservative mass transfer for XTE J0929-314”, *Astronomy and Astrophysics* **603**, A137 (2017).
- 3558
3559
- 3560 ²⁸²L. Keek, W. Iwakiri, M. Serino, D. R. Ballantyne, J. J. M. in’t Zand, and T. E. Strohmayer, “X-Ray Reflection and an Exceptionally Long Thermonuclear Helium Burst from IGR J17062-6143”, *The Astrophysical Journal* **836**, 111 (2017).
- 3561
3562
- 3563 ²⁸³J. van den Eijnden et al., “VLA radio detection of the very-faint X-ray transient IGR J17379-3747”, *The Astronomer’s Telegram* **1487** (2018).
- 3564
- 3565 ²⁸⁴H. Negoro et al., “MAXI/GSC detection of renewed activity from the gamma-ray source IGR J17379-3747”, *The Astronomer’s Telegram* **1447** (2018).
- 3566
- 3567 ²⁸⁵W. E. Harris, “A New Catalog of Globular Clusters in the Milky Way”, *arXiv e-prints*, arXiv:1012.3224 (2010).
- 3568
- 3569 ²⁸⁶R. Sharma, A. Beri, A. Sanna, and A. Dutta, “A broad-band look of the accreting millisecond X-ray pulsar SAX J1748.9-2021 using AstroSat and XMM-Newton”, *Monthly Notices of the Royal Astronomical Society* **492**, 4361–4368 (2020).
- 3570
3571
- 3572 ²⁸⁷R. Wijnands, E. Rol, E. Cackett, R. L. C. Starling, and R. A. Remillard, “GRB060602B = Swift J1749.4-2807: an unusual transiently accreting neutron-star X-ray binary”, *Monthly Notices of the Royal Astronomical Society* **393**, 126–132 (2009).
- 3573
3574
- 3575 ²⁸⁸M. Linares et al., “RXTE detection of a thermonuclear burst from IGR J17498-2921: distance estimate and burst oscillations”, *The Astronomer’s Telegram* **3568** (2011).
- 3576
- 3577 ²⁸⁹A. Riggio, L. Burderi, T. di Salvo, A. Papitto, A. D’Aì, R. Iaria, and M. T. Menna, “Secular spin-down of the AMP XTE J1751-305”, *Astronomy and Astrophysics* **531**, A140 (2011).
- 3578
3579
- 3580 ²⁹⁰N. V. Gusinskaia, T. D. Russell, J. W. T. Hessels, S. Bogdanov, N. Degenaar, A. T. Deller, J. van den Eijnden, A. D. Jaodand, J. C. A. Miller-Jones, and R. Wijnands, “Radio and X-ray monitoring of the accreting millisecond X-ray pulsar IGR J17591-2342 in outburst”, *Monthly Notices of the Royal Astronomical Society* **492**, 1091–1101 (2020).
- 3581
3582
3583

- 3584 291 L. Kuiper, S. S. Tsygankov, M. Falanga, I. A. Mereminskiy, D. K. Galloway, J. Poutanen,
 3585 and Z. Li, "High-energy characteristics of the accretion-powered millisecond pulsar
 3586 IGR J17591-2342 during its 2018 outburst. XMM-Newton, NICER, NuSTAR, and IN-
 3587 TEGRAL view of the 0.3-300 keV X-ray band", *Astronomy and Astrophysics* **641**, A37
 3588 (2020).
- 3589 292 A. Riggio, T. Di Salvo, L. Burderi, M. T. Menna, A. Papitto, R. Iaria, and G. Lavagetto,
 3590 "Spin-up and Phase Fluctuations in the Timing of the Accreting Millisecond Pulsar
 3591 XTE J1807-294", *The Astrophysical Journal* **678**, 1273–1278 (2008).
- 3592 293 D. K. Galloway and A. Cumming, "Helium-rich Thermonuclear Bursts and the Dis-
 3593 tance to the Accretion-powered Millisecond Pulsar SAX J1808.4-3658", *The Astro-*
 3594 *physical Journal* **652**, 559–568 (2006).
- 3595 294 A. J. Goodwin, D. K. Galloway, A. Heger, A. Cumming, and Z. Johnston, "A Bayesian
 3596 approach to matching thermonuclear X-ray burst observations with models", *Monthly*
 3597 *Notices of the Royal Astronomical Society* **490**, 2228–2240 (2019).
- 3598 295 P. D'Avanzo, S. Campana, J. Casares, S. Covino, G. L. Israel, and L. Stella, "The optical
 3599 counterparts of accreting millisecond X-ray pulsars during quiescence", *Astronomy*
 3600 *and Astrophysics* **508**, 297–308 (2009).
- 3601 296 S. Campana and T. Di Salvo, "Accreting Pulsars: Mixing-up Accretion Phases in Tran-
 3602 sitional Systems", in *The Physics and Astrophysics of Neutron Stars*, edited by L. Rez-
 3603 zolla, P. Pizzochero, D. I. Jones, N. Rea, and I. Vidaña, Astrophysics and Space Science
 3604 Library (Springer International Publishing, Cham, 2018), pp. 149–184.
- 3605 297 M. Suzuki et al., "Discovery of a New X-Ray Burst/Millisecond Accreting Pulsar, HETE
 3606 J1900.1-2455", *Publications of the Astronomical Society of Japan* **59**, 263–268 (2007).
- 3607 298 D. K. Galloway, M. P. Muno, J. M. Hartman, D. Psaltis, and D. Chakrabarty, "Ther-
 3608 monuclear (Type I) X-Ray Bursts Observed by the Rossi X-Ray Timing Explorer", *The*
 3609 *Astrophysical Journal Supplement Series* **179**, 360 (2008).
- 3610 299 L. Sun, A. Melatos, and P. D. Lasky, "Tracking continuous gravitational waves from
 3611 a neutron star at once and twice the spin frequency with a hidden Markov model",
 3612 *Physical Review D* **99**, 123010 (2019).
- 3613 300 B. J. Owen, "How to adapt broad-band gravitational-wave searches for r-modes", *Phys-*
 3614 *ical Review D* **82**, 104002 (2010).
- 3615 301 D. I. Jones, "Parameter choices and ranges for continuous gravitational wave searches
 3616 for steadily spinning neutron stars", *Monthly Notices of the Royal Astronomical So-*
 3617 *ciety* **453**, 53–66 (2015).
- 3618 302 M. Zimmermann, "Gravitational waves from rotating and precessing rigid bodies. II.
 3619 General solutions and computationally useful formulas", *Physical Review D* **21**, 891–
 3620 898 (1980).
- 3621 303 C. V. D. Broeck, "The gravitational wave spectrum of non-axisymmetric, freely pre-
 3622 cessing neutron stars", *Classical and Quantum Gravity* **22**, 1825–1839 (2005).
- 3623 304 P. D. Lasky and A. Melatos, "Tilted torus magnetic fields in neutron stars and their
 3624 gravitational wave signatures", *Physical Review D* **88**, 103005 (2013).

- 3625 305 M. Millhouse, L. Strang, and A. Melatos, “Search for gravitational waves from 12
3626 young supernova remnants with a hidden Markov model in Advanced LIGO’s sec-
3627 ond observing run”, *Physical Review D* **102**, 083025 (2020).
- 3628 306 G. Ashton and R. Prix, “Hierarchical multistage MCMC follow-up of continuous grav-
3629 itational wave candidates”, *Physical Review D* **97**, 103020 (2018).
- 3630 307 D. Keitel, R. Tenorio, G. Ashton, and R. Prix, “PyFstat: a Python package for continuous
3631 gravitational-wave data analysis”, *Journal of Open Source Software* **6**, 3000 (2021).
- 3632 308 P. B. Covas and A. M. Sintes, “First All-Sky Search for Continuous Gravitational-Wave
3633 Signals from Unknown Neutron Stars in Binary Systems Using Advanced LIGO Data”,
3634 *Physical Review Letters* **124**, 191102 (2020).
- 3635 309 R. Tenorio, D. Keitel, and A. M. Sintes, “Application of a hierarchical MCMC follow-
3636 up to Advanced LIGO continuous gravitational-wave candidates”, *Physical Review D*
3637 **104**, 084012 (2021).
- 3638 310 D. Foreman-Mackey, D. W. Hogg, D. Lang, and J. Goodman, “Emcee: The MCMC Ham-
3639 mer”, *Publications of the Astronomical Society of the Pacific* **125**, 306 (2013).
- 3640 311 W. D. Vausden, W. M. Farr, and I. Mandel, “Dynamic temperature selection for parallel
3641 tempering in Markov chain Monte Carlo simulations”, *Monthly Notices of the Royal
3642 Astronomical Society* **455**, 1919–1937 (2016).